



**HAL**  
open science

# Effect of electronic correlation on molecules adsorbed on metallic surfaces

Dimitra Xenioti

► **To cite this version:**

Dimitra Xenioti. Effect of electronic correlation on molecules adsorbed on metallic surfaces. Physics [physics]. Université de Strasbourg, 2015. English. NNT : 2015STRAE019 . tel-01330947

**HAL Id: tel-01330947**

**<https://theses.hal.science/tel-01330947>**

Submitted on 13 Jun 2016

**HAL** is a multi-disciplinary open access archive for the deposit and dissemination of scientific research documents, whether they are published or not. The documents may come from teaching and research institutions in France or abroad, or from public or private research centers.

L'archive ouverte pluridisciplinaire **HAL**, est destinée au dépôt et à la diffusion de documents scientifiques de niveau recherche, publiés ou non, émanant des établissements d'enseignement et de recherche français ou étrangers, des laboratoires publics ou privés.



ÉCOLE DOCTORALE DE PHYSIQUE ET CHIMIE-PHYSIQUE

DOMAINE DE RECHERCHE: PHYSIQUE

## THÈSE

Pour obtenir le grade de

DOCTEUR DE L'UNIVERSITÉ DE STRASBOURG

présenté par

**Dimitra XENIOTI**

---

# Effect of electronic correlation on molecules adsorbed on metallic surfaces

---

Date de soutenance le 25 Septembre 2015 devant le jury composé de :

### Directeur de thèse

M. Mébarek ALOUANI Professeur, Université de Strasbourg

### Rapporteurs

M. Xavier BLASE Directeur de Recherche, CNRS  
M. Michael ROHLFING Professeur, Université de Münster

### Autres membres du jury

M. Ferdinand EVERS Professeur, Université de Regensburg  
M. Eric BEAUREPAIRE Directeur de Recherche, CNRS  
M. Stefan BLÜGEL Professeur, Université de Aachen

---



# Contents

---

<b>Contents</b>	<b>i</b>
<b>List of Figures</b>	<b>iv</b>
<b>List of Tables</b>	<b>xi</b>
<b>Acknowledgments</b>	<b>xiii</b>
<b>General Introduction</b>	<b>1</b>
<b>1. Introduction</b>	<b>7</b>
1.1. The Schrödinger equation . . . . .	7
1.2. Born Oppenheimer Approximation . . . . .	8
1.3. Hartree-Fock Approximation . . . . .	9
1.4. Density Functional Theory . . . . .	9
1.4.1. Hohenberg - Kohn theorems . . . . .	9
1.4.2. Kohn-Sham equations . . . . .	12
1.4.3. Local Density Approximation . . . . .	13
1.4.4. Generalized Gradient Approximation . . . . .	14
1.4.5. DFT + U . . . . .	15
1.4.6. Hybrid functionals . . . . .	19
1.4.7. Dispersion Interactions . . . . .	19
1.5. Time-Dependent Density Functional Theory . . . . .	19
1.6. Electronic Correlation using Green Functions . . . . .	20
1.6.1. The Bandgap Problem within DFT . . . . .	20
1.6.2. The Green function . . . . .	21
1.6.3. Lehmann Representation . . . . .	24
1.6.4. Hedin's equations . . . . .	25
1.6.5. <i>GW</i> approximation . . . . .	30
1.6.6. Perturbative $G_0W_0$ . . . . .	31
1.6.7. Self-Consistent <i>GW</i> . . . . .	32

1.7.	Basis Sets . . . . .	33
1.7.1.	Projector Augmented Wave Method . . . . .	35
1.7.2.	Numeric Atom-Centered Orbitals . . . . .	38
1.8.	Solving the Electronic Problem . . . . .	40
1.9.	Implementation of <i>GW</i> within Projector Augmented Waves . . . . .	41
1.9.1.	Dielectric matrix evaluation . . . . .	42
1.9.2.	Self-energy evaluation . . . . .	43
<b>2.</b>	<b>Kondo Effect In Binuclear Metal-Organic Complexes</b>	<b>45</b>
2.1.	Introduction . . . . .	45
2.2.	Kondo's Approach . . . . .	45
2.2.1.	Anderson Model . . . . .	46
2.3.	Scanning Tunneling Microscopy and Spectroscopy . . . . .	48
2.3.1.	STM and STS . . . . .	48
2.3.2.	Bardeen Model . . . . .	49
2.3.3.	Tersoff-Hamman Model . . . . .	50
2.3.4.	Analyzing the Kondo Effect . . . . .	51
2.4.	Experimental Study of Metal-Organic Complexes . . . . .	51
2.5.	Computational Study . . . . .	54
2.5.1.	Molecular Atomic Structure . . . . .	54
2.5.2.	Computational Details . . . . .	54
2.5.3.	Gas Phase Molecule . . . . .	56
2.6.	Ni <sub>2</sub> Complex on Cu(001) . . . . .	57
2.6.1.	Computational Details . . . . .	57
2.6.2.	Spectral Function and Kondo Temperature . . . . .	58
2.7.	Fragments of Ni <sub>2</sub> Complex on Cu(001) . . . . .	59
2.7.1.	Computational Details . . . . .	59
2.7.2.	Calculated STM images . . . . .	60
2.7.3.	Kondo Temperature Estimation . . . . .	62
2.8.	Distorted Ni <sub>2</sub> Complex on Cu(001) . . . . .	64
2.8.1.	Computational Details . . . . .	64
2.8.2.	Calculated STM images . . . . .	66
2.8.3.	Kondo Temperature Estimation . . . . .	66
2.9.	Conclusions . . . . .	69
<b>3.</b>	<b>Study Of Linear Oligoacenes</b>	<b>71</b>
3.1.	Introduction . . . . .	71
3.2.	Gas Phase Oligoacenes . . . . .	72
3.2.1.	Computational Details . . . . .	72
3.2.2.	Density Functional Theory Calculations . . . . .	73
3.2.3.	Zone Folding . . . . .	74
3.2.4.	$G_0W_0$ Calculations . . . . .	77
3.2.5.	PBE0 Functional Calculations . . . . .	79

---

3.3. Oligoacenes On Au(111) . . . . .	81
3.3.1. Computational Details . . . . .	83
3.3.2. Workfunction and charge dipole . . . . .	85
3.3.3. Density of states . . . . .	91
3.3.4. Calculated Scanning Tunneling Microscopy (STM) images . . . . .	95
3.4. Oligoacenes on SiO <sub>2</sub> . . . . .	95
3.4.1. Computational Details . . . . .	98
3.4.2. Electronic Structure . . . . .	100
3.5. Conclusions . . . . .	102
<b>4. HOMO-LUMO Gaps of Molecules on Metallic Surfaces</b>	<b>105</b>
4.1. Introduction . . . . .	105
4.2. Computational Details . . . . .	107
4.3. Results . . . . .	109
4.4. Conclusions . . . . .	109
<b>General Conclusions</b>	<b>113</b>
<b>A. CH<sub>4</sub> and C<sub>2</sub>H<sub>4</sub> adsorbed on metallic surfaces</b>	<b>117</b>
<b>Bibliography</b>	<b>123</b>

# List of Figures

---

0.1. Schematic representation of the changes to molecular levels due to interaction with a substrate taken from Ref. [1]. HOMO and LUMO are well defined within the weak coupling regime (a). The band gap decreases and the resonances become broader when the coupling with the substrate increases (b). . . . .	3
0.2. Experimental and theoretical HOMO-LUMO gaps for a set of different organic molecules. Different methods were used for the evaluation of the theoretical band gaps; LDA (light blue triangles up), B3LYP (white triangle down), $G_0W_0$ with LDA as a starting point (green squares), $G_0W_0$ with HF as a starting point and self-consistent $GW$ (black diamonds). The graph was taken from Ref. [2]. . . . .	5
1.1. Feynman diagram representation of the Dyson equation, $G = G_0 + G_0\Sigma G$ . . . . .	24
1.2. Hedin's pentagon . . . . .	30
1.3. Graphical representation of the interstitial and the augmentation regions. . . . .	36
1.4. Simplified representation of the different approximations and numerical schemes applied in DFT to solve the electronic problem. The combination of choices determine the physical problems available and the phenomena that can be studied with the code and and the approximations employed. . . . .	41
2.1. Diagrammatic representation of spin-flip process in the Anderson model. In order for an impurity spin to flip from a down state, as shown in (a), to an up state, shown in (f), there is a virtual process that can occur in two different ways. The first one with the help of an empty orbital, (b) $\rightarrow$ (d), and the second with a doubly filled orbital, (c) $\rightarrow$ (e). The plot has been taken from [3]. . . . .	48
2.2. Structure of the $(\text{Me}(\text{hfacac})_2)_2(\text{bpym})$ complex. Each $\text{Me}^{2+}$ metal ion is linked to two hexafluoroacetylacetonate (hfacac) ligands by Me-O bonds. By forming N-Me bonds the aromatic 2,2'-bipyrimidine (bpym) ligand coordinates as bidentate chelate with two of the $\text{Me}(\text{hfacac})_2$ components. . . . .	52

---

2.3. Topography of (a) $\text{Mn}_2\text{-}\gamma$ , (b) $\text{Ni}_2\text{-}\alpha$ , (c) $\text{Ni}_2\text{-}\beta$ , (d) $\text{Zn}_2\text{-}\alpha$ , and (e) $\text{Zn}_2\text{-}\gamma$ obtained by low-temperature STM. In (f) the differential conductance $dI/dU$ near the Fermi-level is shown. The black dots are experimental data which were fitted with Fano-functions, presented in red lines. The figure is taken from [4]. . . . .	53
2.4. (a) STM topography of $\text{Ni}_2\text{-}\alpha$ and (b) STM topography of $\text{Ni}_2\text{-}\beta$ . (c) STS data on different position of the $\text{Ni}_2\text{-}\alpha$ . (d) $dI/dV$ map of $\text{Ni}_2\text{-}\beta$ . White and black areas indicate large and low differential conduction, respectively.	54
2.5. Ortep plot of the molecular structure of the $[(\text{Ni}(\text{hfacac})_2)_2(\text{bpym})]^{0}$ complex, obtained by single crystal X-ray diffraction. C atoms are represented in black, O in red, N in blue, F in light green, Ni in dark green and H in black circles. The figure was taken from [4]. . . . .	55
2.6. On the left the “standing” $\text{Ni}_2\text{-}\alpha$ complex bound to Cu(001) surface. On the right the $\text{Ni}_2\text{-}\beta$ complex “lies” on the Cu(001) surface. . . . .	57
2.7. The spectral function projected at the Ni atom which is closest to the surface, for the “standing” $\text{Ni}_2$ complex. The local DOS is shown in a logarithmic scale, while a ferromagnetic coupling of $S=1$ located in $\text{Ni}^{2+}$ ions is assumed. . . . .	59
2.8. $\text{Ni}(\text{hfacac})_2$ moiety bound to Cu(001) via a Ni atom placed at the hollow site.	60
2.9. (a) Experimental STM image of $\text{Ni}_2\text{-}\alpha$ configuration (same as in Figure 2.4(a)). The color coding is identical to Figure 2.9(c). (b): Simulated STM image of $\text{Ni}(\text{hfacac})_2$ , computed employing VASP package. (c) Simulated STM image of $\text{Ni}(\text{hfacac})_2$ , computed employing AITRANSS package. . . .	61
2.10. On the left: the optimal position of the $\text{Ni}(\text{hfacac})_2$ fragment on Cu(001). On the right: the estimated dependence of the binding energy of $\text{Ni}(\text{hfacac})_2$ to Cu(001) surface, on the angle that fixes the orientation of the fragment’s mirror planes vs the [001] direction of the fcc (001) surface. . . . .	61
2.11. Kohn-Sham wave functions corresponding to Ni $d_{z^2}$ and $d_{xy}$ orbitals of the free standing $\text{Ni}(\text{hfacac})_2$ fragment. . . . .	62
2.12. GGA+ $U$ calculated spin dependent local density of states projected on Ni atom of the $\text{Ni}(\text{hfacac})_2$ on Cu(001). Red and blue lines highlight contributions to the LDOS of Ni $d_{z^2}$ and $d_{xy}$ orbitals. . . . .	63
2.13. Graphical representations of the two “distorted” molecular configurations of $\text{Ni}_2$ complex adsorbed on Cu(001). The binding between the molecule and the substrate takes place via the central bpym unit. (a) shows the almost symmetric $C_{2\nu}$ -type structure with two mirror planes of the complex rotated by $45^\circ$ relative to fcc [001] and [010] directions, (b) shows the corresponding structure with broken local symmetry which is energetically more stable. . .	65

---

---

2.14. (a) Experimental STM image for the first configuration of $\text{Ni}_2 - \beta$ . (b) The corresponding simulated STM image for the first configuration of $\text{Ni}_2 - \beta$ , computed employing VASP package. (c) Simulated STM image of the first configuration of $\text{Ni}_2 - \beta$ , computed employing AITRANSS package. (d), (e), (f) calculated STM images of the “distorted” $\text{Ni}_2 - \beta$ compared to experiment. . . . .	66
2.15. Wave functions of $a, b, a', b'$ orbitals, which contribute to the LDOS projected on the Ni atom of the distorted $\text{Ni}_2$ complex, as presented in Figure 2.16. $a$ and $b$ orbitals are localized on the “left-hand” side, while $a'$ and $b'$ are localized on the “right-hand” side of the molecular complex. . . . .	68
2.16. Calculated DFT spin-dependent local density of states projected on one of Ni atoms of the distorted $\text{Ni}_2$ complexes adsorbed on Cu(001). The zoomed in plot shows the majority up-spin spectral function below the Fermi level, where contributions are highlighted arising from four orbitals ( $a, b, a', b'$ ). Each orbital is carrying one unpaired spin. The corresponding wave functions are presented in Figure 2.15. . . . .	70
3.1. Oligoacene molecule, consisting of a repeating benzene unit. As an example the molecule of pentacene is shown ( $N=5$ benzene rings). The hydrogen atoms are blue and the carbon red. . . . .	71
3.2. From left to right the HOMO-LUMO gap, $\Delta_g$ , of oligoacenes with respect to the number of rings $N$ , calculated within DFT and the orbital energies as a function of $1/N$ . The occupied orbitals are presented in blue, while the unoccupied are in red. Notice the repeating interchange of orbitals as the number of rings increases. The Figure was done by Richard Korytár, Ref. [5].	73
3.3. DFT calculated band structure of polyacene (infinite molecular chain). The valence and the conduction bands cross at $k_D = 0.9102 \pi/a$ , close to the Brillouin zone border, where $a = 2.462 \text{ \AA}$ is the unit cell length. . . . .	74
3.4. Zone folding for oligoacene with 9 rings. According to the rule, allowed wave numbers are given according to Eq. 3.2. Hence, the Brillouin zone is divided with 9 lines. The energy band gap is given as the difference between the energy of conduction band minus the corresponding energy of the valence band, closest to the crossing point. The value of this difference is shown as a green dot in the right graph. . . . .	75
3.5. The same as 3.4 but for 10 rings. At this point, the conduction and the valence bands interchange and the energy band gap reaches its minimum (green dot to the right). . . . .	75
3.6. The same as 3.4 but for 11 rings. In this case the conduction and the valence bands have already interchanged and the energy band gap starts to increase (green dot to the right). . . . .	76

---

3.7. DFT calculated band gaps of oligoacenes in natural units compared to the zone folding results. The gap energies are divided by the factor $\pi\hbar v_F/(N+1)/a$ . The horizontal axis is rescaled by the reciprocal space distance of the Dirac point to the zone border. Blue squares are calculated for a set of geometry-optimized molecules from DFT, whereas the red circles are given from the Bloch bands of the infinite chain by Brillouin zone folding. The Figure is taken from Ref. [5]. . . . .	76
3.8. $G_0W_0$ band structure of polyacene infinite chain compared to that obtained using PBE. Going from the $\Gamma$ -point through the corner of the first Brillouin zone, a crossing of the valence and the conduction bands occurs, at $k_D=0.89\pi/a$ . . . . .	78
3.9. Charge density at $\mathbf{k}$ points located around the crossing point of the bands, $k_D$ . The valence band that is increasing in energy, has an odd symmetry, whereas the conduction, decreasing band, has an even symmetry along the molecular axis. . . . .	78
3.10. HOMO and LUMO energies (dimensionless according to equation 3.3) with respect to the length of the oligoacene molecule. PBE results are shown in red symbols, while red lines represent the estimates from the Brillouin zone folding. PBE0 values are shown in green and $G_0W_0$ QP energies in magenta. In all cases, filled symbols show HOMO energies and empty ones their LUMO counterparts. . . . .	80
3.11. Band structure of polyacene infinite chain adsorbed on Au(111). The orbital of the molecule's contribution to the symmetry of the bands is highlighted with different colors. The band crossing occurs at $k_D=0.89 \pi/a$ as it can be seen for the bands which have a molecular orbital weight above 20%. . . . .	82
3.12. Band structure of polyacene infinite chain on Au(111) compared with the band structure of the molecular chain in the gas phase. The orbital weight of the adsorbed molecule is set above 20%. . . . .	83
3.13. A $(x, y)$ unit cell of oligoacene adsorbed on Au(111). As an example, we present the $xy$ plane of pentacene molecule adsorbed on Au(111). . . . .	84
3.14. From top to down, adsorption energy for naphthalene and pentacene, when adsorbed on Au(111) for different heights, $Z_{(C-Au)}$ . With red we present the results for GGA calculations. Van der Waals weak interactions are also taken into consideration and the corresponding adsorption energies are presented in blue. We highlight the final position of geometry optimization for both cases. . . . .	85
3.15. Electrostatic potential, integrated along $(x, y)$ directions of the unit cell and for different molecular coverages. $\Phi_0$ is the work function of Au(111) before the adsorption of the molecule, and $\Phi$ after adsorption. The vertical lines at positions $\sim 11 \text{ \AA}$ , $\sim 13 \text{ \AA}$ and $\sim 16 \text{ \AA}$ represent the positions of the layers of the substrate, while the line at $\sim 19 \text{ \AA}$ shows the position of the molecule. The inset shows the behavior of the potential as a function of coverage far from the molecule. . . . .	87

---

---

3.16. Change of the Au(111) work function as a function of naphthalene surface coverage. The solid line is a polynomial fit to the data. . . . .	88
3.17. Graphical representation of a electron energy levels with respect to the position, in the system of Au, vacuum and Au', where Au' denotes Au after adsorption of a molecule. The new system demonstrates an adsorption-induced reduction in the work function. . . . .	89
3.18. Variation of the charge density for naphthalene adsorbed on Au(111), (a) the first plane of the metal, (b) the plane of the molecule, (c) a plane at height $z \simeq 2\text{\AA}$ above the molecule, (d) a plane at height $z \simeq 3\text{\AA}$ above the molecule, (e) $(x, z)$ plane, (f) $(y, z)$ plane. . . . .	90
3.19. Difference of charge density integrated along the $x$ and $y$ directions and represented along $z$ direction (see Eq.3.8). We present also the dependence of this quantity for different surface coverages. The unit of $n'(z)$ is $- e $ , with $e$ being the charge of electron. . . . .	91
3.20. Difference of charge density for different coverages integrated along the $z$ direction using equation 3.9. The maximum error of this calculation is of the order of $5 \times 10^{-3} e$ . . . . .	92
3.21. Charge dipole moment for naphthalene adsorbed on Au(111) for different surface coverages. The units of $\Delta\mu$ given here are $ e  \cdot \text{\AA}$ . The electronic charge transfer from the molecule to the substrate is implied. . . . .	93
3.22. Density of states (DOS) of oligoacene molecules. Top to bottom, projected DOS on the C atoms of naphthalene, pentacene, hexacene and heptacene. Blue represents the structures where the molecules stands $8 \text{\AA}$ away of Au(111), while red corresponds to the adsorbed molecules. The gray shaded areas represent the DOS of the first layer of the Au(111) substrate. The Fermi level of the relaxed structures has been shifted to 0 (red solid line), while the HOMO level of the structures with $Z_{(C-Au)}=8 \text{\AA}$ is represented with dashed blue lines. . . . .	94
3.23. The decay of the energy band gap for the $C_{4N+2}H_{2N+4}$ molecules at $8 \text{\AA}$ away from the surface (circles) and for their adsorbed counterparts (squares) (see also Table 3.3). . . . .	95
3.24. Density of states (DOS) of heptacene at $8 \text{\AA}$ (top), $4 \text{\AA}$ (middle) and completely adsorbed (bottom) on Au(111) surface. The DOS of the first monolayer of Au below the molecule is represented in grey. With solid red line the Fermi level for the relaxed molecule is denoted. With dashed lines the Fermi level for the molecule at $8 \text{\AA}$ (top), $4 \text{\AA}$ (middle) are shown with respect to the Fermi level of the relaxed molecule. . . . .	96
3.25. Calculated STM images for the relaxed $C_{4N+2}H_{2N+4}$ , for $N = 2, 5, 6, 7$ molecules adsorbed on Au(111) surface. Top to bottom naphthalene, pentacene, hexacene and heptacene. On the left column we present the HOMO of each molecule and on the right the LUMO. . . . .	97

---

3.26. Schematic representation of pentacene molecule adsorbed on $\text{SiO}_2$ $\alpha$ -quartz. The carbon atoms are shown in red, the hydrogen in blue, oxygen in brown and silicon in grey. The coordinates of the substrate have been taken from [6] and are the result of molecular dynamics in the initial O-terminated structure of $\text{SiO}_2$ $\alpha$ -quartz. . . . .	98
3.27. The unfolded band structure of polyacene relaxed on the reconstructed “dense” $\alpha$ - $\text{SiO}_2$ surface, is shown on the left. The color bar on the bottom denotes the values of $\delta N(\mathbf{k}_i; \epsilon_i)$ , given in equation 3.15. On the right, the total DOS of the structure is presented. . . . .	101
3.28. Total density of states of pentacene relaxed on the reconstructed $\alpha$ - $\text{SiO}_2$ surface. The HOMO-LUMO gap originated from the molecule states is about 1.15 eV. . . . .	102
4.1. Schematic representation of energy levels indicating the shifts of HOMO and LUMO of a gas phase molecule upon its adsorption on a metallic surface. The figure has been taken from [7]. . . . .	106
4.2. Graphical representation of the molecules of methane, ethylene and ethane adsorbed on a Cu(001) or Co(001) substrates. . . . .	107
4.3. DFT (up) and $G_0W_0$ (down) calculated DOS for ethane adsorbed on Cu(001). The colorbar indicates the projected DOS on the molecule in states/eV/cell. The red arrows indicate the changes in HOMO and LUMO levels while the molecule approaches the substrate, from distance $d=8 \text{ \AA}$ to the final adsorbed configuration at $d=3.1 \text{ \AA}$ . The Fermi level of the adsorbed molecule within DFT is shown in a black line. . . . .	110
4.4. Up downwards DFT and $G_0W_0$ calculated DOS for ethane molecule adsorbed on Co(001), same as in Figure 4.3. The arrows $\uparrow$ and $\downarrow$ indicate, respectively, the up and down spins. . . . .	111
A.1. DFT and $G_0W_0$ calculated DOS for methane adsorbed on Cu(001), respectively, first and second subfigure. The colorbar indicates the projected DOS on the molecule in states/eV/cell. The red arrows indicate the shifts in HOMO and LUMO levels while the molecule approaches the substrate, from distance $d=8 \text{ \AA}$ to the final adsorbed configuration at $d=2.5 \text{ \AA}$ . The Fermi level of the adsorbed molecule calculated within PBE is also shown (black line). . . . .	118
A.2. DFT and $G_0W_0$ calculated DOS for methane adsorbed on Co(001), in analogy to Figure A.1. The arrows $\uparrow$ and $\downarrow$ indicate, respectively, the up and down spins. . . . .	119
A.3. From top to bottom DFT and $G_0W_0$ calculated PDOS for ethylene adsorbed on Cu(001). The height of the resonances is shown in different colors according to the colorbar on the right. The shifts of the HOMO and LUMO energies are indicated with red arrows and the Fermi level of the final structure with a black line (within DFT). . . . .	120

---

A.4. Similar to Figure A.3 for ethylene adsorbed on Co(001). The up and down spins are indicated, respectively, with  $\uparrow$  and  $\downarrow$ . . . . . 121

# List of Tables

---

2.1.	Selected bond lengths and bond angles of $[(\text{Ni}(\text{hfacac})_2)_2(\text{bpym})]^{0}$ obtained from single crystal X-ray diffraction data, [4]. . . . .	55
2.2.	DFT calculated relative energies of the low-energy spin configurations in the gas-phase of $\text{Ni}_2$ complex. The estimations are obtained using PBE exchange-correlation functional on TURBOMOLE [8] and FHI-aims [9]. . . . .	56
2.3.	DFT calculated relative energies of the low-energy spin configurations realized in $\text{Ni}_2$ complexes. Considered molecules are: (i) gas-phase relaxed $\text{Ni}_2$ complex, with $\text{Ni}^{2+}$ ions found in distorted octahedral environment, (ii) free but distorted $\text{Ni}_2$ complex, where local $C_{2v}$ symmetry is kept, (iii) free but distorted $\text{Ni}_2$ complex, where symmetry constraint is released. The two latter molecules were first relaxed on top of Cu(001). Last column refers to magnetically excited zero-spin state at one of the $\text{Ni}^{2+}$ ions. . . . .	67
3.1.	Comparison of the band crossing wave number, $k_D$ , the Fermi velocity, $v_F$ and the oscillation period, as computed within DFT and $G_0W_0$ . . . . .	79
3.2.	Number of electrons of oligoacene molecules, given by Bader analysis, for the gas phase and when adsorbed on Au(111). . . . .	90
3.3.	HOMO - LUMO gaps for the molecules in the gas phase, 8 Å above the substrate and that of the molecule adsorbed on Au(111) surface. . . . .	92
3.4.	MBJ functional calculated HOMO - LUMO gaps of the free and adsorbed molecules on Au(111). . . . .	94
4.1.	DFT-calculated distances of adsorbed molecules on Cu(001) or Co(001) substrates. . . . .	108
4.2.	DFT and $G_0W_0$ calculated HOMO and LUMO energies for methane, ethylene and ethane molecules in the gas phase. The experimental value of the ionization potential (IE) is also given. All the energies are given in units of eV. . . . .	108



# Acknowledgments

---

I remember clearly that day in the beginning of February 2012 when I was leaving Greece for the first time to visit the University of Strasbourg, carrying lots of wonder and dreams. I remember people welcoming me with a warm smile and helping me to deal with everything new. I remember letting fear go and starting to feel again at home surrounded by friends from all over the world. During the past three years I experienced various feelings ranging from sadness and frustration to joy and pure happiness. I guess it is all part of life and I can say now I am grateful for every single moment I spent during this PhD.

First of all, I want to thank my supervisor Mébarek Alouani for believing in me and giving me the opportunity to do this PhD. There are not enough words to acknowledge his support, help and care throughout this time. In parallel, I would like to deeply thank my co-supervisor Ferdinand Evers. Working with him taught me more than I could ever imagine in a scientific but also in a personal level. He has the wonderful skill to show affection and care for his students and their scientific development. I will keep our discussions in mind because they made me, I think, a better scientist and a better person.

I would also like to thank the Franco-German University and Eric Beaurepaire for giving me the opportunity to perform half of my thesis in Strasbourg and half to the other side of the border, in Karlsruhe, Germany. I also thank Veronique Wernher for her help through all the administration procedures always with a warm smile. This thesis would have no results without the IT support of HPC meso centre of Strasbourg, GENSI-CINES and Steinbuch Centre for Computing (SCC).

I cannot forget Alexej Bagrets and Richard Korytár, the post-docs in Evers group in Karlsruhe, who trained me, helped me and taught me so much with patience and encouragement. A huge thank you goes also to Saber Gueddida, Anant Dixit, Beata Taudul, Michal Studniarek, Etienne Urbain, Filip Schleicher, Ufuk Halisdemir, Christian Seiler, Paul Schnäbele, Ferdinand Kaplan, Christian Günthner, Michael Walz and Jan Wilhelm for our discussions, co-operation and the great time we had working together.

Last but not least I want to thank my dear friends for all the great time we had together the laughs and joy we shared. Thank you Silvia Zanettini, Vina Faramarzi, Christian

## Acknowledgments

---

Andreas, Manuel Gruber, Céline Etrillard, Ondrej Vlasin, Gael Reecht, Michael Chong, Tindara Verduci, Kerstin Bücken, Nicolas Bachellier, Florian Godel, Dominik Metten, Guillaume Froehlicher, Francois Federspiel, Olga Gladii and Vadym Iurchuk. Nothing compares to the time around Place du Café. I also thank Anastasia Skilitsi and Damianos Agathangelou for the unforgettable few months spent together. Thank you Coral Herranz Lancho, Senthil Kavin, Andrea Magri, Veronica Gomez Piedrafita and of course Fabrizio Franza. KIT Campus Nord was much more enjoyable with you inside. I thank from the bottom of my heart Tasos Papaioannou, Eleni Graikou, Dora Manika for our friendship no matter how far we are from each other.

I dedicate this work and title to my parents, Charalambos Xeniotis and Areti Doulaveri. Nothing could be started or fulfilled without their unlimited love. They know how to encourage me to chase my dreams, knowing that no matter what, their hug is open for me back home. To that village of 180 inhabitants, in the mountains of central Greece...

# General Introduction

---

The technology based on silicon microelectronics is reaching its performance limits, leading to the development of new electrical, technological and computational paradigms. After the discovery of tunneling magnetoresistance (TMR) and giant magnetoresistance (GMR), we are facing a great revolution of magnetic memory and storage capacities of modern hard drives, in the two novel fields of spintronics [10] and molecular electronics [11]. At the same time, new research is focusing on organic materials as possible candidates to replace silicon technology, since they are cheap to produce, flexible and diverse in their applications. The combination of spintronics and organic electronics is believed to lead to a new generation of spin based devices, which would most likely open a new broad range of applications and a new generation of products in organic spintronics [12]. For such applications in the nanoscale, the behavior of these materials is defined by their electronic structure.

The electronic structure of a system can be investigated experimentally with distinct experimental setups, for instance, scanning tunneling microscopy and spectroscopy, direct and inverse photoemission, optical adsorption, etc. In analogy, the theoretical description and the prediction of an electronic system's properties can be achieved with different theoretical frameworks. The understanding of characteristic properties of materials and the interpretation of experimentally observable phenomena, from first-principles, has become an extremely efficient tool for theoretical physicists. The study of materials with *ab-initio* methods can be done using different approximations to the many body problem depending on the properties that need to be addressed. One of them is the widely known density functional theory (DFT), which in some cases succeeds to describe material properties in good agreement with experiment. It also predicts the atomic geometries of the structures with great accuracy. In other situations when DFT is not accurate enough, a many body perturbation theory, like the *GW* approximation (where  $G$  is a Green function and  $W$  the screened dynamical interaction) is more effective for the evaluation of the electronic correlation effects, and the description of dynamical effects like the screening of the electrons.

The work presented in this manuscript focuses on organic molecules adsorbed on metallic surfaces, and more specifically on the electronic structure changes due to the screening

of the metallic environment. As one realizes immediately, there is a plethora of different systems that can be studied in this context. The choice of the diverse systems, contained in this thesis, was motivated by mainstream experimental and theoretical research on highly promising subjects.

A challenge in the field of organic spintronics or in general organic electronics is the use of only one molecule as the main protagonist defining the desirable properties in electronic devices. In this context, a new field of molecular spintronics is emerging. In particular, compounds of the single molecule magnet (SMM) class [1, 13] have attracted a lot of attention, since their magnetic relaxation time at low temperatures is of the order of years. Many applications have been proposed using SMMs like memory elements [14, 15], rectifiers and transistors [16–18]. In such devices, the external control of electron spins can be achieved through temperature, pressure, light or electron charging, if the so-called “spin-transition” complexes are used [19–21]. The behavior of the system in these complexes is defined by a single spin. Intensive work has been done in such systems, with increasing complexity ranging from  $3d$  or  $4f$  adatoms on metallic surfaces [22–27], through molecules with extended  $\pi$  orbitals [28–31], to carbon nanotubes [32, 33]. In addition, different systems like a hybrid spinterface of an organic magnetic molecule and a ferromagnetic substrate have brought interesting new aspects to this field [34]. Naturally, for such applications, the molecules should be deposited on a supportive substrate or in a junction. Therefore, not only the properties of the gas-phase molecules, but also the properties of the adsorbed molecules in different types of substrates should be investigated. The interaction of the electrons of the molecule with those of the substrate will change considerably the properties of the molecular system. Thus, its deep understanding is imperative for further progress in the field of molecular electronics.

When a molecule is in a typical break-junction or a scanning tunneling microscope (STM) setup, the low-temperature transport at low bias is governed by the Kondo effect [35], which gives rise to a sharp Kondo resonance in the spectrum of the differential conductance, hence opening a new way of coherent transport in molecular electronics. Nowadays, it is possible to tune the system in a controlled way from the Kondo regime to the uncorrelated one. For instance, this can be achieved by changing the molecular atomic configuration without altering the chemical composition. Switching the Kondo effect on and off provides means to exert spin control which is of utmost interest to spintronics. The sensitivity of the Kondo resonance to spin polarization of the surface electrons offers the possibility to “tune” the source and drain magnetization, something that would have great implications to information storage and processing. The Kondo effect, nowadays, has been revived in the context of molecular adsorbates and molecular junctions. Many cases have been extensively studied, so far, especially when the adsorbed molecule carries one spin. However, further investigation is required on this direction, especially when the candidate molecule carries two spins. The physics in play is intriguing, because Kondo effect occurs in the presence of two spins that can also be magnetically coupled to each other. *Ab initio* methods can shed light on the problem, giving a good prediction of the atomic structures,

---

and providing an insight of the appearing Kondo effect mechanism. This subject will be analyzed in chapter 2 of this thesis.

Except the Kondo effect, other physical phenomena also take place when a molecule is adsorbed on a substrate, even in the absence of an active spin. The adsorption of a molecule on a metallic substrate, for example, might lead to a modification in the electron density of the substrate and the molecule, the electronic coupling of the molecular states with the extended states of the metal, or the polarization of the metal due to adsorption. Charge transfer between the molecule and the substrate may alter the properties of the system. Indeed, an electron or a hole can be added into the molecular orbitals, due to the Coulomb interaction with the substrate. These phenomena are interpreted as changes in the electronic structures of both the molecule and the substrate, such as the rearrangement of the molecular orbitals or widening of the resonances in their density of states. It can also lead to the change in the energy needed to extract an electron from the system (its ionization energy) or the energetic gain when an electron is added to the system (its electron affinity). Figure 0.1 shows some of these basic processes occurring in non-magnetic molecular electronics [1]. In the weak coupling regime (when the molecule does not interact strongly with the substrate), the highest occupied molecular orbital (HOMO) and the lowest unoccupied molecular orbital (LUMO) are well defined. HOMO-LUMO gap decreases and the resonances become broader and closer to the Fermi level, as the coupling is increased. For the adsorbed molecule the energy gap is further reduced. Note that in the case that the molecule carries an unpaired spin a multi-peaked structure appears at the Fermi level for strong coupling (Kondo effect).

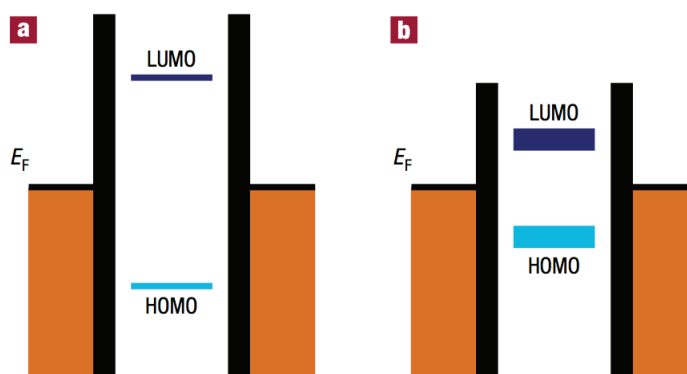


Figure 0.1.: Schematic representation of the changes to molecular levels due to interaction with a substrate taken from Ref. [1]. HOMO and LUMO are well defined within the weak coupling regime (a). The band gap decreases and the resonances become broader when the coupling with the substrate increases (b).

Such changes in the HOMO-LUMO gap is of fundamental interest in the research of

molecular electronics and photovoltaics. In these cases, it is not the spin, but the energy band gaps that can be manipulated in order to give desirable properties to specific devices. Analogous to the molecular electronics, the existence of a supportive substrate is also a prerequisite for photovoltaics and organic solar cells. Especially in the field of organic photovoltaics (OPVs) a lot of studies have been conducted on polymers and oligomers like alkanes and oligoacenes due to their mechanical flexibility and their ability to harvest light [36–38]. In OPVs a bilayered donor-acceptor heterojunction exists and such molecules are proposed as acceptors in the photoactive heterojunction. Oligoacenes, in particular, consist of one repeated benzene ring and form candidates for several applications in organic electronics [39–41]. In spite of the intensive research in this direction, oligoacene molecules have not been investigated adequately above pentacene, mainly because their synthesis has not yet been achieved [42]. Experimentally, the synthesis of larger gas-phase oligoacenes is under investigation to increase their stability [43, 44]. In addition, the on-substrate synthesis provides hope to these achievements [45]. Furthermore, great progress has been achieved in scanning probe microscopy in imaging organic molecules with high resolution [46, 47]. Oligoacenes exhibit pronounced properties, like the oscillation of their HOMO-LUMO gaps with respect to their molecular length [5, 48]. Investigation is required to define the origin of such a property, its survival under the screening of a supporting substrate, as long as its possible adjustment in alternative applications, like the tuning of a semiconductor’s energy band gap. *Ab-initio* methodologies form a powerful tool to carry out such a study that will be presented in detail in chapter 3 of the present manuscript.

Finally, focusing on the theoretical research on molecular electronics, a question that arises is the adequacy of each theoretical framework to describe the properties of matter. Although DFT methods succeed to describe certain properties, like total energies or atomic structures, in good agreement with experiment, they fail to give good results for energy band gaps and band structures [49]. Indeed, DFT has the tendency to underestimate the experimental values of the band gaps for solids and surfaces [50, 51]. In certain cases, like Germanium, DFT gives a qualitatively wrong result, predicting the materials to be metallic while they have a finite gap [52]. These limits of DFT can be overcome with the many-body *GW* approximation [53, 54]. *GW* has also been successful in the description of transition metals [55, 56], *f*-electron systems [57], surfaces [58] and interfaces [7]. In particular in the case of molecules, extensive research has been done to obtain good agreement between theory and photoemission experiments [2, 59–62]. Figure 0.2 shows the results of such a study for several organic molecules in the gas-phase [2]. The HOMO-LUMO gaps are obtained with different functionals within DFT methods, and *GW* techniques using a different starting-point calculation (DFT or Hartree-Fock). A more detailed description of the methods mentioned here will be presented in chapter 1 of this manuscript.

Several studies have also been done for the description of electronic structure of adsorbed molecules on metallic surfaces. These studies indicate that certain phenomena arising from the interaction between the molecule and the substrate can be captured within DFT to a certain extent. Such phenomena are the rearrangement of HOMO and

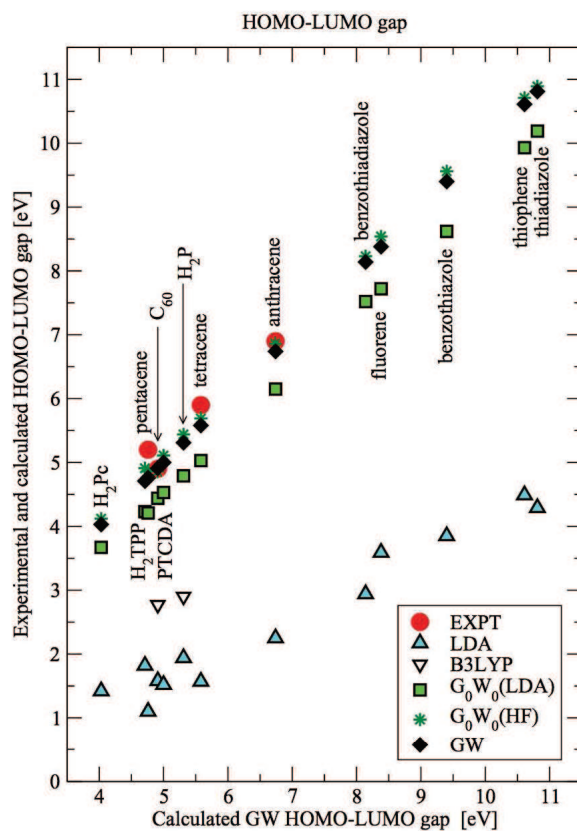


Figure 0.2.: Experimental and theoretical HOMO-LUMO gaps for a set of different organic molecules. Different methods were used for the evaluation of the theoretical band gaps; LDA (light blue triangles up), B3LYP (white triangle down),  $G_0W_0$  with LDA as a starting point (green squares),  $G_0W_0$  with HF as a starting point and self-consistent  $GW$  (black diamonds). The graph was taken from Ref. [2].

LUMO, the broadening of their resonances in the density of states or the shift of the orbital energies [63, 64]. However, the polarization of the substrate cannot be described within single-particle methodologies. During the adsorption of a molecule the electrons of the substrate will screen the added electrons or holes in the interface, an effect which is dynamical and can be described within the *GW* approximation [7]. It has been proved that the quasiparticle gap of the adsorbed molecule is reduced with respect to its gas phase counterpart [7, 65–67]. Nonetheless, further examination is necessary, in particular, in cases where the substrate is magnetic, for example ferromagnetic like cobalt. Such an examination will be presented in chapter 4.

This manuscript is structured as follows. In the Chapter 1, an overview of the fundamental theory is given. In particular, a description of the main principles behind DFT and *GW* methods are provided along with several supporting ideas necessary to some calculations, such as the van der Waals dispersion forces and the Hubbard U term. Besides, the possible basis sets that can be used in the DFT codes are illustrated, focusing on the projector augmented wave method and the numeric atom-centered orbitals. Chapter 2 is dedicated to the study of Kondo effect in binuclear metal-organic molecules adsorbed on a Cu(001) surface. Firstly an introduction to the theory of the Kondo effect and the STM principles is provided, followed by the observations of STM experiments. Lastly, the theoretical results are presented, for the free and the adsorbed molecular complexes. Chapter 3 presents a complete study of oligoacene molecules. It starts by drawing the properties of the molecular chain in the gas-phase and continues by giving evidence for the survival of these properties in adsorbed molecules. The end of the chapter suggests a possible application for oligoacene molecules on a semiconductor substrate. Chapter 4 is dedicated to the investigation of DFT and *GW*-evaluated properties of three different molecules adsorbed on a paramagnetic and a ferromagnetic substrate. Namely, methane ( $\text{CH}_4$ ), ethane ( $\text{C}_2\text{H}_6$ ) and ethylene ( $\text{C}_2\text{H}_4$ ) are adsorbed on a Cu(001) or a Co(001) surface. The results obtained from each method are compared and discussed. The manuscript ends by highlighting the main conclusions of this thesis and providing perspectives for further investigation on the subjects discussed.

# Introduction 1

---

The understanding and the description of matter has been an issue for thought and wonder since the age of the ancient Greeks, when Demokritos developed his theory of atom, the piece of which the matter consists and can not be divided further. Throughout the centuries, since then, scientists have built a completely different picture of matter, consisting of atoms which contain a number  $Z$  of electrons, each of them carrying the elementary charge  $-e$  and orbiting around a nucleus of charge  $Ze$ .

Quantum mechanics, the field describing the laws in the small scale started to be developed in 1913, by Bohr. Bohr described the electronic orbitals of the hydrogen atom with great success and laid the foundations for the Schrödinger equation to come in 1926. Schrödinger equation became the mathematical language of quantum mechanics. In principle this, one and only, equation can describe entirely the physical properties of matter, multi-electronic atoms, molecules and solids.

## 1.1. The Schrödinger equation

If we imagine a piece of matter as an ensemble of interacting atoms, we can describe the system as a set of atomic nuclei and electrons interacting via electrostatic Coulomb forces. The Hamiltonian describing this system should look like:

$$\begin{aligned} \hat{H} = & - \sum_{I=1}^{N_Z} \frac{\hbar^2}{2M_I} \nabla_I^2 - \sum_{i=1}^{N_e} \frac{\hbar^2}{2m} \nabla_i^2 + \frac{e^2}{2} \sum_{I=1}^{N_Z} \sum_{J \neq I}^{N_Z} \frac{Z_I Z_J}{|\mathbf{R}_I - \mathbf{R}_J|} \\ & + \frac{e^2}{2} \sum_{i=1}^{N_e} \sum_{j \neq i}^{N_e} \frac{1}{|\mathbf{r}_i - \mathbf{r}_j|} - e^2 \sum_{I=1}^{N_Z} \sum_{i=1}^{N_e} \frac{Z_I}{|\mathbf{R}_I - \mathbf{r}_i|}, \end{aligned} \quad (1.1)$$

where  $\mathbf{R}_I$  for  $I = 1, \dots, N_Z$  is the set of  $N_Z$  nuclear coordinates,  $\mathbf{r}_i$  for  $i = 1, \dots, N_e$  is the set of  $N_e$  electronic coordinates,  $Z_I$  is the nuclear charge,  $M_I$  the nuclear mass and  $e$  the electronic charge. Therefore, the properties of the system can be derived by solving the time-independent Schrödinger equation:

$$\hat{H}\Psi_n(\mathbf{R}, \mathbf{r}) = \epsilon_n \Psi_n(\mathbf{R}, \mathbf{r}), \quad (1.2)$$

where  $\mathbf{R} = (R_1, R_2, \dots, R_{N_Z})$  and  $\mathbf{r} = (r_1, r_2, \dots, r_{N_e})$  are the position vectors of the  $N_Z$  nuclei and  $N_e$  electrons, respectively,  $\epsilon_n$  are the energy eigenvalues and  $\Psi_n(\mathbf{R}, \mathbf{r})$  the corresponding eigenstates, or wave functions. Since the electron is a fermion, the wave function must be antisymmetric with respect to the exchange of electronic coordinates in  $\mathbf{r}$ , whereas it can be symmetric or antisymmetric with respect to exchange of nuclear variables in  $\mathbf{R}$ , depending on the spin of the nucleus. If the nucleus has a half-integer spin it is also a fermion (antisymmetric wave function due to Pauli exclusion principle), while if it has spin integer, it is a boson (symmetric wave function).

In practice, the Schrödinger equation is impossible to be solved analytically due to its complexity, except from the case of hydrogen or hydrogenoid atoms. In order to overcome this complexity but still give a reliable description of matter, some approximations had to be introduced. The first approximation, to lead a pool of other approximations, still developing nowadays, was the adiabatic or Born-Oppenheimer approximation.

## 1.2. Born Oppenheimer Approximation

Born and Oppenheimer [68] proposed that the movement of the atomic nuclei can be neglected in the evaluation of the electronic properties of matter. This assumption was very reasonable since the electrons are much lighter than the nuclei and therefore move much faster. Thus, one can focus only on the electrons, which interact with the positive atomic nuclei and with each other via Coulomb forces. The former interaction can be treated, even if it is not simple, whereas the latter interaction is far complicated to calculate and more approximations are needed.

Hence, the complexity of the problem after the Born-Oppenheimer approximation resides in the electron-electron interactions. There are two different kinds of such interactions that should be treated. First, the exchange interaction which is the outcome of Pauli exclusion principle for fermions. Then, there is the correlation interaction, where each electron is affected by the motion of the rest of the electrons in the system.

An idea that can simplify the problem even more, is the one-electron picture in a mean field approximation. This way, the system is described by a single electron interacting with a collection of classical ions via an effective potential, where the exchange and correlation interactions are taken into account in an average or effective way. The mean-field theory is the basis for theories like Hartree-Fock and density functional theory, which have been the main approaches to solve the electronic structure problem in condensed matter physics.

### 1.3. Hartree-Fock Approximation

Within the Hartree-Fock (HF) approximation [69], [70] the wave function of the many-body system is an antisymmetric product of single particle wave functions each of which satisfies an one-particle Schrödinger equation. It is worth noting that the Hartree-Fock approximation is based on the assumption of Hartree that the electron is moving in an effective field, interacting with the rest of electrons only via Coulomb forces.

The HF method fully accounts for the electronic exchange interaction of the electrons and provides its exact value. However, the correlation energy is neglected, a fact that leads to the breakdown of the theory for metallic and bulk systems. It produces overestimated band gaps and underestimated binding energies. A more detailed description of the HF method is given in [71]. Since, the HF method completely neglects the correlation effects, another methodology was necessary, which would provide an estimation for both exchange and correlation contributions to the Hamiltonian of the electronic system. This need triggered the development of the famous density functional theory.

### 1.4. Density Functional Theory

In parallel with the Hartree theory a different approach was developed by Thomas (1927) and independently Fermi (1928), for the calculation of an electronic system's energy in terms of the electronic density. In their work, Thomas and Fermi gave a prescription of the total electronic energy taking into account the kinetic, exchange and correlation contributions from the homogeneous electron gas. The idea was, with this starting point, to construct the same quantities for the inhomogeneous system, read as

$$E_\alpha[\rho] = \int \rho(\mathbf{r})\epsilon_\alpha[\rho(\mathbf{r})] d\mathbf{r}, \quad (1.3)$$

where  $\epsilon_\alpha[\rho(\mathbf{r})]$  is the energy density of contribution  $\alpha$ .  $\alpha$  can represent the kinetic, exchange or correlation contribution, calculated locally at every point in space.

This was the first time that the total energy of an electronic system was proposed as a functional of the electronic density of the system, and set up the basis for the later development of the density functional theory (DFT) which has been the most extensively used method in electronic structure calculations in condensed matter physics during the past five decades.

#### 1.4.1. Hohenberg - Kohn theorems

The hopes to describe the energy exclusively in terms of the electronic density, were realized by the formulation and proof of Hohenberg-Kohn theorems in 1964, thirty years after Thomas-Fermi approach.

- **Theorem I** The external potential of an electronic system is univocally determined by its electronic density up to a constant value.

*Proof:* The proof of this theorem in the original paper [72] is made *ad absurdum*, i.e. it can not be otherwise. Indeed, if we suppose the opposite statement to hold, which means the external potential is not univocally determined by the density, we can find two potentials,  $v$  and  $v'$ , such that their ground state density  $\rho$  is the same.

Let  $\Phi$  be the ground wave function and  $E_0 = \langle \Phi | \hat{H} | \Phi \rangle$  the corresponding ground state energy of the Hamiltonian  $\hat{H} = \hat{T} + \hat{V}_{ext} + \hat{U}_{ee}$ . Likewise, we assume  $\Phi'$  and  $E'_0 = \langle \Phi' | \hat{H}' | \Phi' \rangle$  a second wave function and ground state energy, respectively, corresponding to the Hamiltonian  $\hat{H}' = \hat{T} + \hat{V}'_{ext} + \hat{U}_{ee}$ . According to Rayleigh-Ritz's variational principle and using the fact that different Hamiltonians necessarily correspond to different ground states,  $\Phi \neq \Phi'$  we have:

$$\begin{aligned} E_0 < \langle \Phi' | \hat{H} | \Phi' \rangle &= \langle \Phi' | \hat{H}' | \Phi' \rangle + \langle \Phi' | \hat{H} - \hat{H}' | \Phi' \rangle \\ &= E'_0 + \int \rho(\mathbf{r}) [v_{ext}(\mathbf{r}) - v'_{ext}(\mathbf{r})] d\mathbf{r} \end{aligned} \quad (1.4)$$

If we exchange the roles of  $\Phi$  and  $\Phi'$  and consequently also  $\hat{H}$  and  $\hat{H}'$  we obtain:

$$\begin{aligned} E'_0 < \langle \Phi | \hat{H}' | \Phi \rangle &= \langle \Phi | \hat{H} | \Phi \rangle + \langle \Phi | \hat{H}' - \hat{H} | \Phi \rangle \\ &= E_0 + \int \rho(\mathbf{r}) [v'_{ext}(\mathbf{r}) - v_{ext}(\mathbf{r})] d\mathbf{r} \end{aligned} \quad (1.5)$$

Adding the two inequalities, 1.4 and 1.5 we readily obtain:

$$E_0 + E'_0 < E'_0 + E_0 \quad (1.6)$$

which is of course absurd. Therefore, our initial hypothesis is wrong and there cannot be  $v_{ext}(\mathbf{r}) \neq v'_{ext}(\mathbf{r})$  that correspond to the same electronic density for the ground state, unless they differ only by a constant.

- **Theorem II** There is a variational principle on the density stating that the ground-state energy  $E_0$  has its global minimum for the true ground-state density  $\rho$ .

*Proof:* Let  $\tilde{\rho}(\mathbf{r})$  be a non-negative density normalized to N. We can define the variational energy  $E_v$  as a functional of the density due to the previous theorem:

$$E_v[\tilde{\rho}] = F[\tilde{\rho}] + \int \tilde{\rho}(\mathbf{r}) v_{ext}(\mathbf{r}) d\mathbf{r} \quad (1.7)$$

with

$$F[\tilde{\rho}] = \langle \Phi[\tilde{\rho}] | \hat{T} + \hat{U}_{ee} | \Phi[\tilde{\rho}] \rangle \quad (1.8)$$

Here  $\Phi[\tilde{\rho}]$  is the ground state of a potential which has  $\tilde{\rho}$  as its ground state density. If  $E_0 = E_v[\rho]$  is the ground state energy we have:

$$\begin{aligned} \langle \Phi[\tilde{\rho}] | \hat{H} | \Phi[\tilde{\rho}] \rangle &= F[\tilde{\rho}] + \int \tilde{\rho}(\mathbf{r}) v_{ext}(\mathbf{r}) \, d\mathbf{r} \\ E_v[\tilde{\rho}] &\geq E_v[\rho] = E_0 = \langle \Phi[\rho] | \hat{H} | \Phi[\rho] \rangle. \end{aligned} \quad (1.9)$$

The inequality comes from the Rayleigh-Ritz's variational principle for the wave function, applied to the electronic density in this case. The variational principle, therefore, states that

$$\delta \{ E_v[\rho] - \mu \left( \int \rho(\mathbf{r}) \, d\mathbf{r} - N \right) \} = 0, \quad (1.10)$$

which leads to

$$\mu = \frac{\delta E_v[\rho]}{\delta \rho} = v_{ext}(\mathbf{r}) + \frac{\delta F[\rho]}{\delta \rho}, \quad (1.11)$$

where  $F[\rho] = \langle \Phi | \hat{T} + \hat{U}_{ee} | \Phi \rangle$  with  $\Phi$  being the ground state many-body wave function. Thus,  $F[\rho]$  is a universal functional and does not depend explicitly on the external potential, but only on the electronic density. Its knowledge would imply the exact knowledge of the solution of the full many-body Schrödinger equation.

Hohenberg-Kohn theorems form the mathematical basis of the density functional theory (DFT). Their power underlies the fact that a simple quantity like the density can give access to all ground-state properties of a system and especially the kinetic energy.

Since the total energy is a functional of the density, if we extract some known parts out of it, the remainder will also be a density-functional:

$$\begin{aligned} E_0[\rho] &= \langle \Psi_0 | H | \Psi_0 \rangle \\ &= \langle \Psi_0 | T + U_{ee} | \Psi_0 \rangle + \int v_{ext}(\mathbf{r}) \rho(\mathbf{r}) \, d\mathbf{r}. \end{aligned} \quad (1.12)$$

$U_{ee}$  can be further split up into two parts, the classical electronic energy, known also as the Hartree term and the remainder  $E_{xc}$ , referred to as the exchange correlation energy. The

contribution of the Hartree term is by far the most important from the energetic point of view, while the exchange-correlation contribution follows with decreasing importance, as they can be further split into the exchange and the correlation part. Therefore we have for the total energy:

$$E_0[\rho] = \langle \Psi_0 | T | \Psi_0 \rangle + \frac{1}{2} \int \int \frac{\rho(\mathbf{r})\rho(\mathbf{r}')}{|\mathbf{r} - \mathbf{r}'|} d\mathbf{r} d\mathbf{r}' + \int v_{\text{ext}}(\mathbf{r})\rho(\mathbf{r}) d\mathbf{r} + E_{\text{xc}}[\rho].$$

The exchange energy is known and can be calculated exactly as in the Hartree-Fock theory. This calculation though is very expensive computationally and therefore the exchange part is frequently approximated. The correlation part on the other hand is completely unknown. In fact all the unknown of the many-body problem is gathered there. And this is not the only problem one has to face. The kinetic energy is in principle a function of the electronic density, but its explicit dependence to the density is not known.

### 1.4.2. Kohn-Sham equations

In 1965, Kohn and Sham in a very interesting paper [73] tried to minimize the unknown part of the kinetic energy. They introduced the kinetic energy of a fictitious system of non-interacting electrons that can feel an external potential  $v_{\text{xc}}$ , such that it has the same ground state density as the interacting system. They did that by assuming that the non-interacting system of electrons can be described exactly by an antisymmetric wave function of the Slater determinant type, which is made of one-electron orbitals.

The real kinetic energy, in this case, can be split to the kinetic energy of the non-interacting system plus the correlation contribution to the kinetic energy of the interacting system. The correlation part of the kinetic energy derives from the fact that the real many-body wave function is not a Slater determinant and can be added in the initial correlation part that is unknown,  $E_c$ . Following the above methodology, the Kohn-Sham energy can now be read as:

$$E_{KS} = - \sum_{i=1}^N \int \phi_i^*(\mathbf{r}) \frac{\nabla_r^2}{2} \phi_i(\mathbf{r}) d\mathbf{r} + \frac{1}{2} \int \int \frac{\rho(\mathbf{r})\rho(\mathbf{r}')}{|\mathbf{r} - \mathbf{r}'|} d\mathbf{r} d\mathbf{r}' + \int v_{\text{ext}}(\mathbf{r})\rho(\mathbf{r}) d\mathbf{r} + E_{\text{xc}}[\rho], \quad (1.13)$$

where  $\phi_i(\mathbf{r})$  is the wave function of the non-interacting system. Note that now the  $E_{\text{xc}}$  term includes the correlated part of the kinetic energy. The Kohn-Sham potential can be read as:

$$v_{KS}(\mathbf{r}) = v_{\text{ext}}(\mathbf{r}) + \int \frac{\rho(\mathbf{r}')}{|\mathbf{r} - \mathbf{r}'|} d\mathbf{r}' + v_{\text{xc}}[\rho](\mathbf{r}), \quad (1.14)$$

where the second term represents the Hartree term and  $v_{\text{xc}}$  the new exchange-correlation potential:

$$v_{\text{xc}}(\mathbf{r}) = \frac{\delta E_{\text{xc}}}{\delta \rho(\mathbf{r})}. \quad (1.15)$$

The one-electron orbitals have the one and only required property to yield the correct ground state density and can be defined as:

$$\rho(\mathbf{r}) = \sum_{i=1}^N |\phi_i(\mathbf{r})|^2. \quad (1.16)$$

In contrast to the Hartree and Hartree-Fock theories, where the reference potential depends on the solutions of the one-electron Schrödinger equation, the Kohn-Sham orbitals are defined only by the electronic density. For the closed shell situation, where no spin polarisation is taken into account, the Kohn-Sham orbitals are obtained by the self-consistent solution of the independent particle problem:

$$\left( -\frac{\nabla^2}{2} + v_{KS}(\mathbf{r}) \right) \phi_i(\mathbf{r}) = \epsilon_i \phi_i(\mathbf{r}) \quad (1.17)$$

The next step is then to find sensible approximations for the exchange-correlation potential,  $v_{\text{xc}}$ .

### 1.4.3. Local Density Approximation

The exchange-correlation energy,  $E_{\text{xc}}$ , is unknown, as mentioned before, and has to be approximated in such a way that the results obtained from the calculations are reliable. At the same time the computational expenses have always to be taken into account. The first approximation, introduced, was proposed by Kohn and Sham [73] in 1965 and is called the local density approximation (LDA). The exchange-correlation energy in the LDA formulation can be read as

$$E_{\text{xc}}[n(\mathbf{r})] = \int \rho(\mathbf{r}) \epsilon_{\text{xc}}^{\text{hom}}[\rho](\mathbf{r}) \, d\mathbf{r}, \quad (1.18)$$

where  $\epsilon_{\text{xc}}^{\text{hom}}$  is the exchange-correlation energy density in a homogeneous gas of electrons. Exact data of the exchange-correlation energy per particle, in the homogeneous electron gas regime,  $\epsilon_{\text{xc}}$  was obtained, by Ceperley and Adler, using Quantum Monte Carlo calculations [74].

LDA can also be generalized to the case of spin-polarized calculations, where spin up and spin down electrons are treated separately, in an approximation called the local spin density approximation (LSDA). The exchange-correlation energy in this case can be represented as:

$$E_{xc}^{\sigma,\text{LSDA}}(\mathbf{r}) = \frac{d}{d\rho_{\sigma}(\mathbf{r})} \{[\rho_{\uparrow}(\mathbf{r}), \rho_{\downarrow}(\mathbf{r})] \epsilon_{xc}[\rho_{\uparrow}(\mathbf{r}), \rho_{\downarrow}(\mathbf{r})]\}. \quad (1.19)$$

LDA considers a general inhomogeneous electronic system as locally homogeneous. This assumption has the natural outcome that any inhomogeneities in the density are completely neglected. As a consequence, LDA tends to overestimate the binding energy of molecules and the cohesive energy of solids. Dispersion interactions, like the weak van der Waals forces, and the bond lengths of weakly coupled systems are poorly reproduced. Non-local exchange and correlation effects are also not included. Therefore, strong local correlation effects cannot be treated within LDA. Furthermore, LDA and LSDA underestimate significantly the energy bandgap of semiconductors or molecules, by more than 50% with respect to the experimental values. Moreover, some semiconductors with small gaps like Ge are predicted to be metallic within LDA. This fact reflects also to an overestimation of the dielectric constant.

Despite its weaknesses, LDA can predict with high precision the geometries of systems with strong chemical or ionic bonds. It is computationally relatively cheap and can give good predictions of the electronic structure of many systems with up to hundreds of atoms unit cell. This is the reason it has been the first choice for ab initio calculations among the condensed matter community for the past fifty years.

The problems LDA suffers from are intrinsic and differ for each type of materials. Therefore, there is no unique recipe to improve upon them. Scientists have been trying to address the diverse weaknesses of LDA developing different kind of approximations and methods, some of which will be presented below.

#### 1.4.4. Generalized Gradient Approximation

A kind of natural improvement to the LDA to complete homogeneity is to assume a dependence of the exchange-correlation density,  $\epsilon_{xc}$  on the derivatives of the density. The approximation is called generalized gradient approximation (GGA) [75]. The dependence of the exchange-correlation energy,  $E_{xc}$ , to the density is still local, but improves the results with respect to LDA, in many cases [76].

The GGA, in general, attempts to make corrections to each part of exchange and correlation energies of the exchange-correlation energy. By definition,  $E_{xc}$  can be analyzed, into the exchange part plus the correlation part as follows:

$$E_{xc} = E_x + E_c \quad (1.20)$$

For the exchange part separately we have within this formalism:

$$E_{x\sigma}^{\text{GGA}} = E_{x\sigma}^{\text{LDA}} - \int d\mathbf{r} \rho_{\sigma}(r)^{\frac{4}{3}} F_x \left( \frac{|\nabla \rho_{\sigma}|}{\rho_{\sigma}(\mathbf{r})^{\frac{4}{3}}} \right), \quad (1.21)$$

where  $\sigma$  is the spin index. Different approximations have been proposed to get an expression for the last part of the above equation [77].

For the correlation energy  $E_c$  there are also diverse approximations. The equations describing these methods are extended and difficult, whereas they don't add much to the understanding of the underlying physics so they won't be presented in this manuscript. It is mentioned though that throughout the work presented here, whenever GGA is mentioned, we have used the functional proposed by Perdew, Burke and Ernzerhof (PBE) [78].

It should be mentioned that GGA improves the binding energies, the atomic energies, the bond lengths and angles with respect to LDA, but has a tendency to overestimate them. There is also a better prediction of the energy band gap and the dielectric constant, but it is not significant. Good results in this respect can only be taken if the screening of the exchange hole is taken into account when an electron is removed from the system. As we will see later, this happens in the *GW* approximation.

The GGA is supposed to improve upon the outcomes of LDA, but this is not always the case. For example, semiconductors are slightly better described within LDA except for the binding energies. Likewise, the lattice constants of noble metals (Ag, Au, Pt) are overestimated in GGA. In this case, LDA values are closer to experiment. It is noted though that the superiority of LDA in such cases is attributed to fortunate error cancellations, since as an approximation LDA is inferior to GGA.

### 1.4.5. DFT + U

One of the biggest failures of LDA and similar functionals comes in the description of strongly-correlated materials. These contain in addition to the delocalized *s*- and *p*-electrons, the localized partially filled *d*- or *f*-shells. The attempt to treat the different shells with the same single-particle mean-field functional, like LDA, leads to the majority of cases in unreliable results and even to the wrong ground state. To this problem, an often practiced way is to add an orbital-dependent single-particle potential to describe better the localized, strong-correlated electrons. This potential includes explicitly the information about the strength of the Coulomb interaction within the set of problematic states. The method which we will describe is the so-called LDA+*U*.

We consider a subspace of  $d$ -states (a similar approach is valid for  $f$ -electrons) to which we want to introduce a  $d$ - $d$  Coulomb interaction via the Hamiltonian

$$E[n_i] = \frac{1}{2}U \sum_{i \neq j} n_i n_j, \quad (1.22)$$

where  $U$  is a parameter, known as Hubbard  $U$  parameter, and  $n_i$  is the occupation number of orbital  $i$  of the  $d$ -electrons. The total number of electrons will be then in the subspace

$$N = \sum_i n_i \quad (1.23)$$

The total Coulomb energy due to  $d$ - $d$  interactions can now be read

$$E_{dd} = \frac{1}{2}U(N-1)N \quad (1.24)$$

The energy described by (1.24) depends on the total occupation of  $d$  orbitals. One has to be careful to avoid double counting errors, since the Coulomb energy is already described by the LDA. Thus, to introduce a new total energy functional which will depend on the set of  $n_i$ , one has to subtract (1.24) from the LDA total energy, and take the LDA+ $U$  total energy functional as

$$E^{\text{LDA}+U}[n, n_i] = E^{\text{LDA}}[n] + \frac{1}{2}U \sum_{i \neq j} n_i n_j - \frac{1}{2}U(N-1)N \quad (1.25)$$

Within the above functional, equation 1.25, the sphericity and the exchange of the  $d-d$  interactions are not taken into account. The resulting total energy will be correct, but the single particle energies will be modified as

$$\epsilon_i = \frac{\partial E^{\text{LDA}+U}}{\partial n_i} = \epsilon_i^{\text{LDA}} + U \left( \frac{1}{2} - n_i \right) \quad (1.26)$$

The above equation represents physically a splitting between the occupied and the unoccupied states. This splitting is proportional to  $U$  and is analogous to the lower and upper Hubbard bands in the Hubbard model [79].

The potential of each orbital reads

$$V_i(\mathbf{r}) = V^{\text{LDA}}(\mathbf{r}) + U \left( \frac{1}{2} - n_i \right). \quad (1.27)$$

In order to determine the total energy of LDA+ $U$ , [80], one needs to define a localized orthonormal basis  $|inlm\sigma\rangle$  inside an atomic sphere, where  $i$  denotes the atom,  $n$  is the principal quantum number,  $l$  the angular quantum number,  $m$  the magnetic quantum number and  $\sigma$  the spin index. To make the notation simple, we suppose only one correlated atom  $i$  and orbital  $l$  and we ignore the  $n$  and  $l$  indices. Then, the density matrix is given as:

$$n_{m,m'}^\sigma = -\frac{1}{\pi} \int^{E_F} \text{Im} G_{m,m'}^\sigma(E) dE, \quad (1.28)$$

where  $G^\sigma$  is the Green function. To simplify the expression of the density matrix let us assume, without loss of generality, that  $l = 2$ . At this point, the exchange between the localized  $3d$  electrons of the same spin  $\sigma$ , can be taken into account, using the Hamiltonian:

$$H = \frac{1}{2}U \sum_{m,m',\sigma} n_{m,\sigma} n_{m',-\sigma} + \frac{1}{2}(U - J) \sum_{m \neq m',\sigma} n_{m,\sigma} n_{m',\sigma}, \quad (1.29)$$

where  $J$  is the exchange parameter and  $n_{m,\sigma}$  denotes the number of electrons as:

$$n_{m,\sigma} = c_{m,\sigma}^\dagger c_{m,\sigma}. \quad (1.30)$$

The Hamiltonian in equation 1.29 consists of two terms. The first describes the Coulomb interaction between the electrons carrying opposite spins. The second term describes the interaction between the electrons of the same spin. Therefore, the first term describes the repulsion of the electrons and can be written as  $U n_{m,\sigma} n_{m,-\sigma}$ . This term can be approximated within the mean field theory and be rewritten as  $U n_{m,\sigma} n_{-\sigma}$ , where the mean value of  $n_\sigma$  is given as

$$n_\sigma = \sum_m n_{m,\sigma}. \quad (1.31)$$

The mean value of the Hamiltonian describing the total number of  $d$ -electrons, within LDA is given as:

$$\langle H \rangle^{\text{LDA}} = \frac{1}{2}U \sum_\sigma n_\sigma n_{-\sigma} + \frac{1}{2}(U - J) \sum_\sigma n_\sigma (n_\sigma - 1), \quad (1.32)$$

where  $n_\sigma$  is the number of  $d$ -electrons of spin  $\sigma$ .

The mean value of the Hamiltonian derived from the mean field formalism reads:

$$\langle H \rangle^{\text{MF}} = \frac{1}{2}U \sum_{m,m',\sigma} n_{m,\sigma} n_{m',-\sigma} + \frac{1}{2}(U - J) \sum_{m \neq m',\sigma} n_{m,\sigma} n_{m',\sigma}, \quad (1.33)$$

where  $n_{m,\sigma}$  is the occupation number of the  $d$ -electron with magnetic quantum number  $m$ .

Subtracting equation 1.32 from equation 1.33 and adding the LDA functional, one can extract the LDA+ $U$  functional as:

$$E^{\text{LDA}+U} = E^{\text{LDA}} + \frac{1}{2}(U - J) \sum_{m,\sigma} (n_{m,\sigma} - n_{m,\sigma}^2), \quad (1.34)$$

where the terms  $\sum_{m,\sigma} n_{m,\sigma}$  and  $\sum_{m,\sigma} n_{m,\sigma}^2$  represent the traces of the electronic density operators  $\rho^\sigma$  and  $(\rho^\sigma)^2$ , respectively. Hence, the  $E^{\text{LDA}+U}$  functional can be written in a rotationally invariant form with respect to an orbital unitary transformation. The axis-system independent form is written as:

$$E^{\text{LDA}+U} = E^{\text{LDA}} + \frac{1}{2}(U - J) \sum_{\sigma} [\text{Tr} \rho^\sigma - \text{Tr}(\rho^\sigma \rho^\sigma)]. \quad (1.35)$$

At this point, the effects of non-sphericity of the  $d$ -orbitals, the Coulomb interaction and the exchange interaction can be introduced as following:

$$\langle \chi_{m_1}^\alpha; \chi_{m_3}^\alpha | V_{ee} | \chi_{m_2}^\alpha; \chi_{m_4}^\alpha \rangle = \int \int dr_1 dr_2 \chi_{m_1}^{\alpha*}(r_1) \chi_{m_3}^{\alpha*}(r_2) v_{ee}(r_1, r_2) \chi_{m_2}^\alpha(r_1) \chi_{m_4}^\alpha(r_2). \quad (1.36)$$

The above coefficients represent the Coulomb energy in the case where  $m_1 = m_2$  and  $m_3 = m_4$ . In the case where  $m_1 = m_4$  and  $m_3 = m_2$  the coefficients represent the exchange energy. Finally, the total LDA+ $U$  energy is given as:

$$E^{\text{LDA}+U} = E^{\text{LDA}} + E^{e-e} - E_{\text{dc}}^{\text{LDA}}, \quad (1.37)$$

where

$$E^{e-e} = \frac{1}{2} \sum_{\sigma, \sigma'} \sum_{\substack{m_1, m_2 \\ m_3, m_4}} n_{m_1, m_2}^\sigma \times [\langle \chi_{m_1}^\alpha; \chi_{m_3}^\alpha | V_{ee} | \chi_{m_2}^\alpha; \chi_{m_4}^\alpha \rangle - \delta_{\sigma, \sigma'} \langle \chi_{m_1}^\alpha; \chi_{m_3}^\alpha | V_{ee} | \chi_{m_2}^\alpha; \chi_{m_4}^\alpha \rangle] n_{m_3, m_4}^{\sigma'}, \quad (1.38)$$

and where the double counting energy  $E_{\text{dc}}^{\text{LDA}}$  is given by:

$$E_{\text{dc}}^{\text{LDA}} = \frac{1}{2} U n(n-1) - \frac{1}{2} J \sum_{\sigma} n^\sigma (n^\sigma - 1). \quad (1.39)$$

### 1.4.6. Hybrid functionals

In the limit of weak interaction the exchange energy is the exact Hartree-Fock exchange energy. Therefore, it is reasonable, in some cases, to add a certain fraction of the HF exchange to the LDA or GGA exchange-correlation functionals. This thought led to the development of the hybrid exchange-correlation functionals where

$$E_{xc}^{\text{HYB}} = E_{xc}^{\text{LDA}} + \lambda(E_x^{\text{HF}} - E_x^{\text{LDA}}). \quad (1.40)$$

If PBE is used as the local functional and  $\lambda=0.25$  is assumed, the resulting hybrid functional is called PBE0.

During the past years many other hybrid functionals have been proposed and used for the description of various systems.

### 1.4.7. Dispersion Interactions

Dispersion interactions, mostly referred to as van der Waals weak interactions, form a difficult benchmark within DFT. These interactions describe a dynamical correlation effect that takes place between two non-chemically bonded fragments. Its origin is the coupling of the electric field generated by fluctuations in the electronic density of the one fragment with the density of the other fragment. Naturally, the usual local and semi-local functionals cannot capture this phenomenon and other approximations have to be taken into account. At long distances the van der Waals interactions should approach the classical dipole-dipole interaction, with a decay of

$$E_{\text{vdW}} = -\frac{C_6}{R^6}, \quad (1.41)$$

where  $C_6$  is a constant and  $R$  is the distance between the two fragments.

Many approximations have been proposed for the description of the dispersion interactions and they are included in many codes as post-DFT correction to the total energy of the system, like the Grimme's DFT-D2 scheme [81] and the Tkatchenko Scheffler scheme [82].

## 1.5. Time-Dependent Density Functional Theory

DFT can be extended to include time-dependent external potentials, which frequently occur, when for example the system is exposed to an external laser field. Such an extension leads to the time-dependent density functional theory (TDDFT) formalism. TDDFT gives a good estimation of the excitation energies of the system, which can be compared to experimental photo-absorption spectra. The accordance of these theoretical estimations with experimental values depends on the approximations used, just as in static DFT calculations. TDDFT is based on the Runge-Gross theorem [83], the equivalent of the Hohenberg-Kohn theorem in static DFT. Its fundamental theory can cover almost any kind of time-dependent external potential, whereas it can also include spin degrees of freedom. Further analysis of TDDFT formalism and applications can be found in [84].

## 1.6. Electronic Correlation using Green Functions

### 1.6.1. The Bandgap Problem within DFT

Within HF theory, the eigenvalues of the Hamiltonian,  $\epsilon_i^{\text{HF}}$  are given, according to the Koopman's theorem [85], as:

$$\epsilon_i^{\text{HF}} = E(n_1, n_2, \dots, n_i, \dots, n_N) - E(n_1, n_2, \dots, n_i - 1, \dots, n_N) \quad (1.42)$$

where  $E(n_1, n_2, \dots, n_N)$  is the ground state energy of the system and  $n_1, n_2, \dots, n_N$  the occupation number. Koopman's theorem ensures that in case of reduction of the occupation, the orbitals remain unchanged and defines the required energy  $\epsilon_i^{\text{HF}}$  needed to eject an electron from orbital  $i$ .

Within DFT formalism, an analog of Koopman's theorem is valid, the Janak theorem [86]. However, the interpretation of the eigenvalues is different. In fact, the Janak theorem proves that the variation of the KS total energy with respect to an orbital occupation is equal to the eigenvalue of that orbital, such that:

$$\frac{\partial E}{\partial n_i} = \epsilon_i \quad (1.43)$$

At zero temperature for a large system, the chemical potential,  $\mu$ , is given as the variation of the total energy with respect to the total occupation number,  $\frac{\partial E}{\partial N} = \mu$ . Therefore, one can conclude that  $\epsilon_i = \mu$ , a fact that proves the physical meaning of the highest occupied molecular orbital (HOMO) within KS theory. The rest eigenvalues, however, cannot be interpreted with a physical analog.

If we assume the ionization energy (IE) and the electron affinity (AE) the bandgap of the system will be given as:

$$\begin{aligned} E_{\text{gap}} &= \text{IE} - \text{AE} \\ &= [E_{N-1} - E_N] - [E_N - E_{N+1}], \end{aligned} \quad (1.44)$$

where  $E_M$  is the total energy of a system with  $M$  electrons. In the thermodynamic limit it is  $E_N - E_{N-1} = \epsilon_N^N$  and  $E_{N+1} - E_N = \epsilon_{N+1}^{N+1}$ , with  $\epsilon_m^M$  being the  $m$ -state of the system with  $M$  electrons. Therefore, from equation 1.44 we have:

$$E_{\text{gap}} = \epsilon_{N+1}^{N+1} - \epsilon_N^N \quad (1.45)$$

The bandgap obtained within DFT though will be given as:

$$E_{\text{gap}}^{\text{DFT}} = \epsilon_{N+1}^N - \epsilon_N^N, \quad (1.46)$$

which differs from equation 1.45 by a quantity  $\Delta$ :

$$\begin{aligned}\Delta &= E_{\text{gap}} - E_{\text{gap}}^{\text{DFT}} \\ &= \epsilon_{N+1}^{N+1} - \epsilon_{N+1}^N\end{aligned}\tag{1.47}$$

Thus, it is evident that DFT fails to evaluate the band gaps of real systems with good accuracy, and tends to underestimate them. Even for the IE, in practice, there is only a qualitative agreement with experiments, mainly because of self-interaction errors in the single-particle eigenvalues. Hybrids can partially alleviate these errors and give in general better agreement with experiments. This however is not adequate and another approximation is needed to evaluate the energy band gaps with better accuracy.

### 1.6.2. The Green function

In order to attack the many-body problem and estimate its properties with good accuracy, a very successful idea is to assume that the system consists of weakly interacting fictitious particles, instead of real strongly interacting particles. The fictitious system of particles took the name quasiparticles and possess two properties, a lifetime and an effective mass. The calculation of these properties is done with the use of quantum field theoretical quantities, widely known as Green functions [87].

The time-ordered one-particle equilibrium Green's function  $G$  is defined as:

$$\begin{aligned}iG(1, 2) &= \langle \Psi | T \left[ \hat{\psi}(1) \hat{\psi}^\dagger(2) \right] | \Psi \rangle \\ &= \begin{cases} \langle \Psi | \left[ \hat{\psi}(1) \hat{\psi}^\dagger(2) \right] | \Psi \rangle, & t_1 > t_2 \\ - \langle \Psi | \left[ \hat{\psi}^\dagger(2) \hat{\psi}(1) \right] | \Psi \rangle, & t_2 > t_1 \end{cases}\end{aligned}\tag{1.48}$$

The ket  $|\Psi\rangle$  labels the normalized many-body wave function of the  $N$ -electron ground state. Index 1 is a shortcut for the representation of the position, the time and the spin variables, i.e  $(\mathbf{r}_1, t_1, \sigma_1)$  of the particle 1. The same is valid for the particle 2 and so forth.  $T$  is the Wick's time-ordering operator, which orders the operators in time, with the largest time on the left, as it is shown in the equation 1.48. With  $\psi, \psi^\dagger$  in equation 1.48 we declare the annihilation and the creation field operations, respectively, within the Heisenberg representation, which obey the fermionic anti-commutation relations:

$$\begin{aligned}\left[ \hat{\psi}_a(\mathbf{r}), \hat{\psi}_b^\dagger(\mathbf{r}') \right]_+ &= \delta(\mathbf{r}, \mathbf{r}') \delta_{ab} \\ \left[ \hat{\psi}_a(\mathbf{r}), \hat{\psi}_b(\mathbf{r}') \right]_+ &= \left[ \hat{\psi}_a^\dagger(\mathbf{r}), \hat{\psi}_b^\dagger(\mathbf{r}') \right]_+ = 0\end{aligned}\tag{1.49}$$

The physical interpretation of equation 1.48 should be emphasized. If an electron is added to the system in its ground state, at the position  $\mathbf{r}_2$  and at time  $t_2$  carrying a spin

$\sigma_2$ , the Green's function gives the probability for an electron to be found at  $\mathbf{r}_1$  with spin  $\sigma_1$  at time  $t_1$ . This declaration stands when  $t_1 > t_2$ . On the other hand, when  $t_2 > t_1$ , the Green's function gives the probability to find a hole at position  $\mathbf{r}_2$  at time  $t_2$ , with spin  $\sigma_2$ , if an electron was previously, at time  $t_1$ , from the position  $\mathbf{r}_1$  with spin  $\sigma_1$ .

The one-particle Green's function gives the expectation value of any single-particle operator in the ground state of a system, the total energy of the system in the ground state and its single-particle excitation spectrum. However powerful the one-particle Green function is not the answer to every question on the many-body electron system. For instance, it cannot describe the optical absorption of materials. Optical absorption refers to a low energy excitation according to which a photon excites an electron into a low-lying empty state. Then, the motion of the excited electron can not be decoupled from the hole created in the occupied states. This motion requires the description of the full motion of the electron and the hole, which cannot be done with the one-particle Green's function. Thus, the two-particle Green's function is introduced and defined as:

$$i^2 G_2(1, 2; 1', 2') = \langle \Psi | T \left[ \hat{\psi}(1) \hat{\psi}(2) \hat{\psi}^\dagger(2') \hat{\psi}^\dagger(1') \right] | \Psi \rangle. \quad (1.50)$$

The Green function can be also generalized to the  $N$  particles case as:

$$i^N G^N(1, \dots, N; 1', \dots, N') = \langle \Psi | \hat{T} \left[ \hat{\psi}(1) \dots \hat{\psi}(N) \hat{\psi}^\dagger(N') \dots \hat{\psi}^\dagger(1') \right] | \Psi \rangle. \quad (1.51)$$

Starting from the equation of motion for the Heisenberg creation and annihilation field operations, equations 1.49, and the definition of the one- and two-particle Green functions, equations 1.48 and 1.50, a group of equations of motion for the Green function can be derived. The detailed derivation can be found in [88] or [89]. The outcome of these equations is that the one-particle Green function depends on the two-particle one, according to:

$$\left[ i \frac{\partial}{\partial t_1} - h(1) \right] G(1, 2) + i \int d3 v(1, 3) G_2(1, 3^+; 2, 3^{++}) = \delta(1, 2), \quad (1.52)$$

where  $h(1) = h_0(\mathbf{r}_1) \delta(t_1)$  is the single-particle term of the electronic Hamiltonian,  $v(1, 2) = v(\mathbf{r}_1, \mathbf{r}_2) \delta(t_1 - t_2) = \delta(t_1 - t_2) / |\mathbf{r}_1 - \mathbf{r}_2|$  the repulsive Coulomb interaction between electrons and  $1^+ \equiv \{\mathbf{r}_1, t_1 + \eta, \sigma_1\}$ ,  $\eta$  being a positive infinitesimal, with additional indexes of plus indicating further addition of  $\eta$ .

Similarly, the two-particle Green function depends on the three-particle one and so on. In such a way any calculation is still very complicated since the estimation of a quantity depends upon the evaluation of a more complex counterpart. However, at this point the fundamental idea of many-body perturbation theory is introduced: for the calculation of e.g the one-particle Green function, the only thing that should be needed is the one-particle

Green function. Therefore, an approximation of higher-particle Green functions in terms of the lower ones is needed.

This approximation is achieved with the definition of a quantity called the self-energy of the system and it is defined, for the two-particle Green function case, as:

$$\int d3 [v_H(3)\delta(3, 1) + \Sigma(1, 3)] G(3, 2) = -i \int d3 v(1, 3)G_2(1, 3^+; 2, 3^{++}), \quad (1.53)$$

where  $v_H(1) = v_H(\mathbf{r}_1)\delta(t_1)$  is the Hartree potential.

The self-energy  $\Sigma$  is in general a complex, non-local and non-Hermitian operator. Its real part is related to the exchange and correlation contributions to the quasiparticle energies. Its imaginary part is related with the excitation lifetimes. The self-energy accounts for every event a particle experiences during its propagation in a many-electron system, under the Born-Oppenheimer approximation. An example of such interactions can be the formation of electron-hole pairs, which interact with the propagating particle. The lowest-order processes are the free propagation of the particle through the system or the bare Coulomb interaction. Such events affect the propagation of the particle and hence form the Green function that describes it.

The replacement of the self-energy definition (equation 1.53) in equation 1.52 yields the famous Dyson equation in form:

$$\left[ i \frac{\partial}{\partial t_1} - h(1) - v_H(1) \right] G(1, 2) - \int d3 \Sigma(1, 3)G(3, 2) = \delta(1, 2). \quad (1.54)$$

Hence, the purpose of the many-body perturbation theory is to find appropriate approximations for the self-energy operator,  $\Sigma$ , as a function of the one-particle Green function. In the case of non-interacting fermions, the equation of motion of the Green function  $G_0$  becomes:

$$\left[ i \frac{\partial}{\partial t_1} - h(1) - v_H(1) \right] G_0(1, 2) = \delta(1, 2), \quad (1.55)$$

such that the Dyson equation can be rewritten in terms of the non-interacting Green function,  $G_0$ , and the interacting one,  $G$  as:

$$[G_0^{-1}(1, 3) - \Sigma(1, 3)]G(3, 2) = \delta(1, 2). \quad (1.56)$$

The latter equation is usually represented in a symbolic way:

$$G_0 + G_0 \Sigma G = G, \quad (1.57)$$

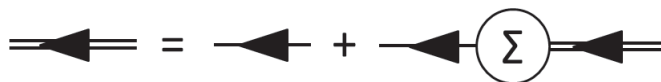


Figure 1.1.: Feynman diagram representation of the Dyson equation,  $G = G_0 + G_0 \Sigma G$ .

which shows that all the effects beyond non-interacting particles are included in the self-energy. The Dyson equation can also be represented in terms of Feynman diagrams, shown in Figure 1.1. A simple introduction to Feynman diagrams is given in [90].

### 1.6.3. Lehmann Representation

A different representation of the Green function can be derived if one introduces the time-dependent field operations in the Heisenberg picture,  $\hat{\psi}_n(\mathbf{r}, t) = e^{i\hat{H}t} \hat{\psi}(\mathbf{r}) e^{-i\hat{H}t}$ , in equation 1.48:

$$iG(\mathbf{r}, t; \mathbf{r}', t') = \langle \Psi | e^{i\hat{H}t} \hat{\psi}(\mathbf{r}) e^{-i\hat{H}(t-t')} \hat{\psi}(\mathbf{r}') e^{-i\hat{H}t'} | \Psi \rangle \theta(t - t'), \quad (1.58)$$

where it has been assumed that  $t > t'$  (electron propagation). An analogous derivation can be done for  $t' > t$ , describing the propagation of a hole. The integral representation of the step-function as was also introduced in equation 1.58 and is defined as:

$$\theta(t - t') = - \int_{-\infty}^{+\infty} \frac{d\omega}{2\pi i} \frac{e^{-i\omega(t-t')}}{\omega + i\eta}. \quad (1.59)$$

If the completeness relation  $\sum_s |\Psi_s^{N+1}\rangle \langle \Psi_s^{N+1}| = 1$  is introduced to equation 1.58, one gets:

$$iG(\mathbf{r}, t; \mathbf{r}', t') = \sum_n e^{i(E_0 - E_n^{N+1})(t-t')} \langle \Psi | \hat{\psi}(\mathbf{r}) | \Psi_n^{N+1} \rangle \langle \Psi_n^{N+1} | \hat{\psi}^\dagger(\mathbf{r}') | \Psi \rangle \theta(t - t') \quad (1.60)$$

where  $\Psi_s^{N+1}$  is the  $n$ -th excited state of the  $N + 1$  particle system, and  $E_s^{N+1}$  the corresponding energy. We can now introduce certain definitions:

$$\epsilon_s = E_s^{N+1} - E_0^N \quad (1.61)$$

$$f_n(\mathbf{r}) = \langle \Psi | \hat{\psi}(\mathbf{r}) | \Psi_n^{N+1} \rangle \quad (1.62)$$

$$f_n^*(\mathbf{r}') = \langle \Psi_n^{N+1} | \hat{\psi}^\dagger(\mathbf{r}') | \Psi \rangle, \quad (1.63)$$

where  $f_n$  and  $f_n^*$  are referred to as Lehmann amplitudes and describe the overlap between the ground state and an excited state of the system, carrying an extra electron. That

means that  $f_n$  give the probability amplitude for an electron to be added to the system, for  $t > t'$ . We introduce the definitions in equation 1.61 in equation 1.60 and we get:

$$iG(\mathbf{r}, t; \mathbf{r}', t') = \sum_n e^{-i\epsilon_n(t-t')} f_n(\mathbf{r}) f_n^*(\mathbf{r}') \theta(t-t'), \quad (1.64)$$

By performing a Fourier transformation to frequency of equation 1.64, one obtains the Lehmann representation of the Green function [91]:

$$G(\mathbf{r}, \mathbf{r}', \omega) = \sum_n \frac{f_n(\mathbf{r}) f_n^*(\mathbf{r}')}{\omega - \epsilon_n + i\eta}. \quad (1.65)$$

The Lehmann representation shows that the Green function has poles at the single-particle excitation energies,  $\epsilon_n = E_n^{N+1} - E_0^N$ . This proves that the Green function is a quantity that can describe correctly the photoemission events, i.e the experimental processes where the system is driven to an excited state, through the removal (direct photoemission) or the addition of an electron (inverse photoemission).

Replacing the Green function in equation 1.64 in the Dyson equation 1.56, the quasiparticle equation can be derived:

$$[h_0(\mathbf{r}) + v_H(\mathbf{r})] f_n(\mathbf{r}) + \int d\mathbf{r}' \Sigma(\mathbf{r}, \mathbf{r}', \epsilon_n) f_n(\mathbf{r}') = \epsilon_n f_n(\mathbf{r}). \quad (1.66)$$

The quasiparticle equation is an alternative expression of the Dyson equation, actually turning the latter to a single-particle eigenvalue problem. In the case where the self-energy is exact, it is possible to access all single-particle excitation energies of the system,  $\epsilon_n$  and the corresponding probability amplitude,  $f_n$ . However, this problem is difficult to solve, because the self-energy is non-Hermitian and frequency-dependent. Thus, one needs to make a few approximations to compute the self-energy.

#### 1.6.4. Hedin's equations

Lars Hedin (1965) proposed a set of self-consistent equations that provide an exact solution for the Green function and the self-energy of a many-body electron system [92]. Hedin's equations, as they are called, express the many-body problem in terms of quantities with a physical meaning, like the screened Coulomb interaction  $W$  and the polarizability,  $P$ . The goal of the derivation presented in the following is to transform the Dyson equation into a closed set of integro-differential equations. But firstly one should decouple a hierarchy of equations for obtaining the Green function. This is achieved with the Schwinger derivative technique [93].

Schwinger introduced a small external potential,  $U$  as a perturbation to the system and derived the following identity for the two-electron Green function:

$$G_2(1, 4; 2, 3) = G(1, 2)G(4, 3) - \frac{\delta G(1, 2)}{\delta U(3, 4)}. \quad (1.67)$$

With this equation it is obvious we can express the two-particle Green function only in terms of the one-particle Green function.

Let us rewrite at this point the equation of motion of the one-particle Green function 1.52:

$$\left[ i \frac{\partial}{\partial t_1} - h(1) \right] G(1, 2) + i \int d3 v(1, 3) G_2(1, 3^+; 2, 3^{++}) = \delta(1, 2), \quad (1.68)$$

If we use the Schwinger's formula 1.67 and introduce it to equation 1.68 for a local  $U(3)\delta(3, 4)$  we get:

$$\begin{aligned} \left[ i \frac{\partial}{\partial t_1} - h(1) \right] G(1, 2) + i \int d3 v(1, 3) G(3, 3^+) G(1, 2) \\ - i \int d3 v(1^+, 3) \frac{\delta G(1, 2)}{\delta U(3)} = \delta(1, 2). \end{aligned} \quad (1.69)$$

Multiplying the above equation on the right by  $\int d5 G^{-1}(4, 5) G(5, 2) = \delta(4, 2)$  we have:

$$\begin{aligned} \left[ i \frac{\partial}{\partial t_1} - h(1) + i \int d3 v(1, 3) G(3, 3^+) \right] G(1, 2) \\ - i \left[ \int d345 v(1^+, 3) \frac{\delta G(1, 4)}{\delta U(3)} G^{-1}(4, 5) \right] = \delta(1, 2) \end{aligned} \quad (1.70)$$

Since  $-iG(3, 3^+)$  is the electronic density, one can realize that  $-i \int d3 v(1, 3) G(3, 3^+)$  in equation 1.70 is the Hartree potential. The last term of the equation 1.70 gives the self-energy operator as:

$$\Sigma(1, 2) = i \left[ \int d345 v(1^+, 3) \frac{\delta G(1, 4)}{\delta U(3)} G^{-1}(4, 2) \right] \quad (1.71)$$

Using the derivative of the inverse identity:

$$\frac{\delta F(1, 2)}{\delta G(3)} = - \int d45 F(1, 4) \frac{\delta F^{-1}(4, 5)}{\delta G(3)} F(5, 2), \quad (1.72)$$

in equation 1.71, one gets for the self-energy:

$$\Sigma(1, 2) = -i \int d345 v(1^+, 3) G(1, 4) \frac{\delta G^{-1}(4, 2)}{\delta U(3)}, \quad (1.73)$$

which accounts for all the many-body effects beyond the Hartree potential.

At this point one can introduce the local classical potential  $V$ :

$$V(1) = U(1) - i \int d2 v(1, 2) G(2, 2^+), \quad (1.74)$$

which is the sum of the external perturbation  $U$  and the Hartree potential.

Using the chain rule:

$$\frac{\delta F[G[H]](1)}{\delta H(2)} = \int d3 \frac{\delta F[G](1)}{\delta G(3)} \frac{\delta G[H](3)}{\delta H(2)} \quad (1.75)$$

via  $V$  in the equation 1.73, one gets:

$$\Sigma(1, 2) = -i \int d345 v(1^+, 3) \frac{\delta G^{-1}(1, 4)}{\delta V(5)} \frac{\delta V(5)}{\delta U(3)} G(4, 2), \quad (1.76)$$

where the definitions of the dielectric function:

$$\epsilon^{-1}(1, 2) = \frac{\delta V(1)}{\delta U(2)} \quad (1.77)$$

and the irreducible vertex function:

$$\Gamma(1, 2; 3) = -\frac{\delta G^{-1}(1, 2)}{\delta V(3)}, \quad (1.78)$$

and the dynamical screened Coulomb interaction:

$$W(1, 2) = \int d3 v(1, 3) \epsilon^{-1}(3, 2) \quad (1.79)$$

can be introduced. By the term irreducible the differentiation upon  $V$  and not  $U$ , is implied.

According to the above definitions, the self-energy (equation 1.73) can be written as:

$$\Sigma(1, 2) = i \int d34 G(1, 4) W(3, 1^+) \Gamma(4, 2; 3). \quad (1.80)$$

Let us start from the vertex function definition, equation 1.78, introducing the Dyson equation 1.56. Then we get:

$$\begin{aligned}
 \Gamma(1, 2; 3) &= -\frac{\delta}{\delta V(3)}[G_0^{-1}(1, 2) - v_H(1, 2)\delta(1, 2) - \Sigma(1, 2) - U(1)\delta(1, 2)] \\
 &= \delta(1, 2)\delta(1, 3) + \int d45 \frac{\delta\Sigma(1, 2)}{\delta G(4, 5)} \frac{\delta G(4, 5)}{\delta V(3)} \\
 &= \delta(1, 2)\delta(1, 3) + \int d4567 \frac{\delta\Sigma(1, 2)}{\delta G(4, 5)} G(4, 6)G(7, 5)\Gamma(6, 7; 3),
 \end{aligned} \tag{1.81}$$

where the chain rule 1.75 was used in the first step and the derivative of the inverse 1.72 as well as the definition of  $\Gamma$ , on the second.

Concerning the inverse dielectric function,  $\epsilon^{-1}$ , using the definition of  $V$  (1.74), we get:

$$\begin{aligned}
 \epsilon^{-1}(1, 2) &= \frac{\delta(U(1) - i \int d3 v(1, 3)G(3, 3^+))}{\delta U(2)} \\
 &= \delta(1, 2) + \int d3 v(1, 3)\chi(3, 2),
 \end{aligned} \tag{1.82}$$

where

$$\chi(1, 2) = -i \frac{\delta G(1, 1^+)}{\delta U(2)} \tag{1.83}$$

is the so-called reducible polarizability of the system. With the term reducible the dependence on the bare external potential  $U$  is implied. One can also define the irreducible polarizability as:

$$P(1, 2) = -i \frac{\delta G(1, 1^+)}{\delta V(2)}. \tag{1.84}$$

The irreducible and the reducible polarizabilities are linked through the following equation:

$$\begin{aligned}
 \chi(1, 2) &= -i \int d3 \frac{G(1, 1^+)}{V(3)} \frac{\delta V(3)}{\delta U(2)} \\
 &= P(1, 2) + \int d34 P(1, 3)v(3, 4)\chi(4, 2),
 \end{aligned} \tag{1.85}$$

where the relation 1.82 and the chain rule 1.75 were used.

The reducible polarizability can be further determined in terms of  $G$  and  $\Gamma$ , using 1.72, as:

$$\begin{aligned}
 P(1, 2) &= i \int d34 G(1, 3) \frac{\delta G^{-1}(3, 4)}{\delta V(2)} G(4, 1) \\
 &= -i \int d34 G(1, 3) G(4, 1) \Gamma(3, 4; 2).
 \end{aligned} \tag{1.86}$$

The dynamical screened Coulomb interaction, defined in 1.79, using equations 1.82, 1.83 and 1.84 is read:

$$\begin{aligned}
 W(1, 2) &= \int d3 v(1, 3) \frac{\delta}{\delta U(2)} [U(3) - iG(4, 4^+)v(4, 3)] \\
 &= v(1, 2) + \int d34 v(1, 3) \chi(4, 2) v(4, 3) \\
 &= v(1, 2) + \int d34 v(1, 3) \chi_0(3, 4) W(4, 2),
 \end{aligned} \tag{1.87}$$

where to obtain the last line the relation  $\chi(1, 2) = \int d3 \chi_0(1, 3) \epsilon^{-1}(3, 2)$  is used, which is implied by the first part of equation 1.85.

The five Hedin's equations can be summarized as shown below:

$$G(1, 2) = G_0(1, 2) + \int d34 G_0(1, 3) \Sigma(3, 4) G(4, 2) \tag{1.88}$$

$$P(1, 2) = -i \int d34 G(2, 3) G(4, 2) \Gamma(3, 4; 1) \tag{1.89}$$

$$W(1, 2) = v(1, 2) + \int d34 v(1, 3) P(3, 4) W(4, 2) \tag{1.90}$$

$$\Sigma(1, 2) = i \int d34 G(1, 4) W(3, 1^+) \Gamma(4, 2; 3) \tag{1.91}$$

$$\Gamma(1, 2; 3) = \delta(1, 2) \delta(1, 3) + \int d4567 \frac{\delta \Sigma(1, 2)}{\delta G(4, 5)} G(4, 6) G(7, 5) \Gamma(6, 7; 3) \tag{1.92}$$

Each Hedin equation, 1.88-1.92, is dependent of the other four, a fact that transforms the problem of the calculation of the single-particle Green function to a self-consistent problem.

The solution of the self-consistent problem can be approached by an iterative scheme:

1. Initialize of a first self-consistent calculation with a non-interacting Green function  $G_0$ .
2. Evaluate  $P$ ,  $W$ ,  $\Sigma$  and  $\Gamma$ , taking  $\Gamma(1, 2; 3) = \delta(1, 2) \delta(1, 3)$ .

3. Construct the vertex  $\Gamma$ .
4. Update the Green function  $G$ .
5. Iterate the five equations 1.88-1.92 until the convergence criterion is satisfied.

The structure of this self-consistent loop is usually shown as a sketch known as the Hedin pentagon, see Figure 1.2.

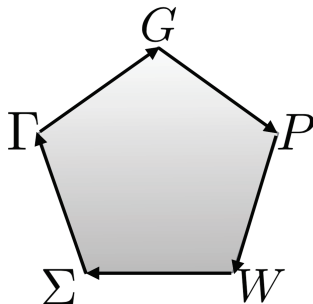


Figure 1.2.: Hedin's pentagon

It is useful to note that by setting  $\Sigma=0$ , in the Hedin equations, the Hartree approximation can be recovered [69]. Therefore, assuming a zero self-energy is equivalent to an independent move of the particles, which interact only through the mean electrostatic field, generated by the rest of the electrons. This gives naturally a poor description to the nature of the fermions, which is partially reconstructed with the Hartree-Fock approximation. The Hartree-Fock approximation is reproduced by the Hedin's equations by neglecting polarization effects, i.e. setting  $P = 0$  and restricting the vertex  $\Gamma$  to its zero-th order component, i.e.  $\Gamma(1, 2; 3) = \delta(1, 2)\delta(1, 3)$ . Notice that in absence of polarization effects, there is no screening to renormalize the Coulomb interaction. It is therefore  $W(1, 2) = v(1, 2)$ .

### 1.6.5. $GW$ approximation

The use of the screened Coulomb interaction  $W$  instead of the bare Coulomb interaction  $v$ , is the heart of the  $GW$  approximation. Such a screening between electrons is motivated mainly by the expectation that the perturbation theory can converge faster in powers of  $W$  than with respect to  $v$ . Therefore, Hedin proposed a first-order perturbative expansion of the self-energy  $\Sigma$  in terms of  $W$ , which starts from an initialization of the Hedin pentagon assuming  $\frac{\delta\Sigma}{\delta G} = 0$  in the vertex equation. Thus, we have:

$$\Gamma(1, 2; 3) = \delta(1, 2)\delta(1, 3). \quad (1.93)$$

Substituting the above equation 1.93 in Hedin's equations 1.88-1.91, one obtains the so-called  $GW$  approximation equation's, read:

$$G(1, 2) = G_0(1, 2) + \int d34 G_0(1, 3)\Sigma(3, 4)G(4, 2) \quad (1.94)$$

$$P(1, 2) = -iG(1, 2)G(2, 1) \quad (1.95)$$

$$W(1, 2) = v(1, 2) + \int d34 v(1, 3)P(3, 4)W(4, 2) \quad (1.96)$$

$$\Sigma(1, 2) = iG(1, 2)W(1, 2) \quad (1.97)$$

$GW$  approximation has been the state of the art methodology to evaluate energy band gaps and band structures, in solids and molecules with very good agreement with experiments, see for example [51]. It has to be emphasized, however, that it assumes the sum of higher-order terms in  $W$  to be small compared to the first-order perturbation. Such an assumption is not always adequate, since many times higher-order terms are indispensable, for example in the calculation of optical properties. In such cases, one needs to take into account Bethe-Salpeter equation, which is described in details in [94].

### 1.6.6. Perturbative $G_0W_0$

As we have seen so far, the  $GW$  approximation has been a very successful method to attack the many-body problem, giving reasonable results for observable quantities. Nevertheless, the  $GW$  approximation is very demanding in computational resources, even for relatively small systems of few atoms. Therefore, the necessity to simplify the complexity of equations 1.93-1.96 is an active field of research, in order to treat systems like solids or molecules with hundreds of atoms. A simple way is to treat the self-energy and the Green function in a non-self-consistent manner. The more applicable method, called  $G_0W_0$ , was first applied to the electron gas by Hedin *et al.* in 1969 [95], while it was extended to real semiconductor calculations by Hybertsen and Louie about 20 years later [96, 97].

The heart of  $G_0W_0$  method is the replacement of the the self-consistent cycle, implied in equations 1.93-1.96, by a perturbation scheme. Within  $G_0W_0$  the Green function  $G$  is replaced with a Green function obtained from a preliminary density-functional or Hartree-Fock calculation in order to evaluate equations 1.94-1.96. Therefore, the polarizability,  $P$ , is estimated in terms of the single-particle orbitals and eigenvalues obtained in this preliminary calculation. Moreover, the screened interaction  $W_0$  is evaluated from the non-interacting response function and the self-energy can be expressed as:

$$\Sigma(1, 2) = iG_0(1, 2)W_0(1, 2). \quad (1.98)$$

$G_0W_0$  method nowadays has been implemented in most mainstream DFT codes and has become the reference method for the estimation of band gaps and band structures for

solids [50], [51] and for molecules [2, 59–62]. It has also been successful in describing transition metals [55, 56], *f*-electron systems [57], surfaces [58] and interfaces [7]. Throughout this thesis,  $G_0W_0$  calculations have been performed for gas-phase and surface-adsorbed molecules, using the VASP package [98–100].

Despite its success in diverse systems,  $G_0W_0$  approximation suffers from some shortcomings, due to the non-self-consistent calculation of the self-energy and the perturbative evaluation of the quasi-particle energies. The most problematic shortcoming is the dependence of the results upon the preliminary reference calculation. Indeed, the starting point calculation, i.e. density-functional or Hartree-Fock, gives different  $G_0W_0$  energy and band gap results, up to several eV [101]. Furthermore, the screening properties of the Coulomb interactions can be over- or under-estimated depending on the preliminary calculation, DFT or HF respectively. Finally, it should be emphasized that within  $G_0W_0$  the conservation laws of number of particles, momentum and total energy are violated. These conservation laws can be reformulated in terms of Green functions, as shown by Baym and Kadanoff [102]. They actually proved that the conservation laws are satisfied in this representation if and only if there exists a functional of the Green function,  $\Phi[G]$  [103], such that:

$$\Sigma(1, 2) = \frac{\delta\Phi[G]}{\delta G(1, 2)}. \quad (1.99)$$

Within  $G_0W_0$  there is no such a functional; the above condition is not satisfied and therefore the conservation laws are violated. However, this deficiency of  $G_0W_0$  is not affecting the results for the spectral properties, but it can be important for non-equilibrium systems and transport phenomena.

### 1.6.7. Self-Consistent $GW$

In order to improve the shortcomings of  $G_0W_0$  except the fully self-consistent scheme of  $GW$  some partially self-consistent methods have also been proposed. Here we will present the most popular of such attempts, highlighting their main principles and the quality of their outcome.

- Eigenvalue self-consistent  $GW$  (ev-sc $GW$ ): Within this scheme the self-energy and the quasi-particle equation are iterated self-consistently. At each iteration the input eigenvalues are replaced by the real part of the quasi-particle energies. The method was introduced by Hybertsen and Louie [96] and has been investigated further ever since, see for example [2, 104]. ev-sc $GW$  reduces the starting-point dependence of  $G_0W_0$  and improves in some cases the estimation of the first ionization energies. However, it often deteriorates the lower lying quasi-particle states. In general, there is no proof of some significant quantitative improvement in the description of the excitation energies of molecules using ev-sc $GW$  [105]. Besides, the problems appearing within  $G_0W_0$  are not fixed.

- Quasi-particle self-consistent  $GW$  (QP-sc $GW$ ): Here, the main idea is to find a ground state that minimizes the  $G_0W_0$  quasi-particle correction [106, 107]. QP-sc $GW$  has been applied with success to localized  $d$ - and  $f$ -electron systems, greatly improving the starting-point dependence of  $G_0W_0$  [108, 109]. The computational cost of the method, though, is high and comparable to the fully self-consistent  $GW$ .
- Fully self-consistent  $GW$ (sc $GW$ ): Naturally, the sc $GW$  scheme comes down to the iteration of the Hedin equations, according to Hedin's pentagon. Apart from the expecting computational cost, sc $GW$  is expected to eliminate  $G_0W_0$  problems, i.e the dependence on the preliminary calculation and of course the validation of the conservation laws. Nonetheless, the results obtained within sc $GW$  have lead to conflicting conclusions on their quality. Indeed, the spectral properties have been shown to be improved or sometimes deteriorated compared to  $G_0W_0$  based on LDA [110–112]. The total energies obtained within sc $GW$ , though, are found to be improved, compared to  $G_0W_0$  [113, 114]. In general, there is the impression that self-consistency does not improve considerably the quality upon the non-self-consistent results of  $G_0W_0$ . It is true that the studies supporting this idea are not abundant, but the computational cost as well as the not extremely encouraging results, coming from self-consistency, can dissuade one from using the sc $GW$  methodology.

## 1.7. Basis Sets

To study the electronic structure of a system the first step is to choose the most appropriate method. The next step is related to the choice of the basis set to represent the orbitals in terms of analytic functions with known properties. A good choice of the basis set will make the representation of the charge density and the potential of the system more adequate.

In general, we can distinguish three types of basis sets that are widely used for the solution of the electronic problem in mainstream ab-initio codes.

### 1. All-electron methods

Within these methodology, the electrons of the system are separated in different groups: the core, the semi-core and the valence electrons. The core electrons are close enough to the nuclei so that they are considered tightly bound to it, while the valence electrons participate actively to the chemical bonding, so they define also the properties of the system. The semi-core electrons, do not participate actively in the chemical bonding, but they are close in energy to the valence states, they can polarize and cannot be treated as frozen orbitals. Naturally the electrons cannot be distinguished and this is only a nomenclature. What is, in reality, distinguished is the characteristics of the orbitals which are occupied by these electrons. Therefore, the different orbitals are treated in different ways, although the methods deal with

all the electrons of the system explicitly.

The core states are calculated by solving an atomic problem, usually including relativistic effects with a Dirac equation form of the KS equations. The valence states are calculated separately by solving the KS equations in all space. For the semi-core states one has to be careful to include them either as valence states or as core states. In the first case, however, the calculation becomes more difficult since the semi-core states are relatively localized and different from the valence states, while in the latter case the states should not be confined artificially.

The advantage of all-electron methods is the access to the core states, which does not exist in other basis sets. The wavefunctions and energies of core states give access to hyperfine quantities, hyperfine fields, electric field gradient as well as chemical shifts of core levels. The drawback of such methods is the high computational cost they require to treat real systems.

## 2. Plane wave pseudopotentials

As mentioned already, the chemical properties of a material are mostly controlled by its valence electrons, whereas the core electrons are essentially inert. Practically, this can lead to the exclusion of the innermost electrons out of explicit calculations. Therefore, they can be presented by a smooth and nodeless effective potential, known as pseudopotential. The resulting pseudo wavefunction is made as smooth as possible close to the nuclear core region.

Plane waves of the form  $e^{i\mathbf{k}\cdot\mathbf{r}}$ ,  $\mathbf{k}$  being the wave vector, can be used as a complete and orthonormal set of basis functions to describe the valence electron wave functions. Note that the plane waves do not depend on the positions of the nuclei. The periodic potential is produced by the periodicity of the underlying lattice. This potential imposes also a periodicity on the electron density through periodic boundary conditions. The use of Born von Karman boundary conditions and Bloch's theorem facilitate the solution of the Kohn-Sham equations for solids and other periodic systems.

The pseudopotential can be generated from an atomic calculation. Then it is used to compute properties of the valence electrons only, since the core states are considered frozen and unchanged [115]. It should be noticed that many different forms of pseudo-potentials have been suggested and constructed, which are used to calculate a huge variety of systems. However, one should know that there is no single best pseudo-potential to treat successfully any kind of calculations. In fact, many reference calculations are needed to verify the good behavior of a potential, the accuracy of the results it gives and its transferability to other materials.

In the following we will focus on a method combining the all-electron and the pseudopotential methods, known as the projector augmented wave (PAW) method.

### 3. Local basis sets

The local basis sets adopt the idea to mimic the properties of the final solution of the electronic problem, by expanding the wavefunctions into localized functions, which are solutions of an approximate local KS equation. The basis functions centered at different atoms have to overlap but this overlap can vanish with distance and goes to zero at some point.

Such basis sets are explicitly atom centered, a fact that makes them very successful to describe open systems with a large vacuum space, such as molecules or surfaces with vacuum. On the contrary, periodic systems are not treated naturally as in methods using explicitly only plane waves.

A different set of functions can be chosen to build local basis sets, like Gaussian functions, Wannier functions or numerical atom-centered orbitals (NAOs). Such basis functions are usually efficient because accuracy can be achieved with relatively small basis functions. Especially in the case of NAOs, which we will analyze more in detail in the following. The basis functions are constructed by numerical integration of the atomic KS equations. Although local basis sets can be very efficient, they show an unsystematic convergence behavior. Unlike the plane waves, where the number of basis functions can be systematically increased to study the convergence, in this case, the accuracy achieved cannot be estimated in most cases. Therefore, the choice of the basis functions gets more complicated and requires experience to avoid errors.

#### 1.7.1. Projector Augmented Wave Method

The projector augmented wave method (PAW), introduced by Blochl [116], is a combination of the all-electron methods and the plane wave pseudopotential approach and offers great computational efficiency to DFT calculations.

The idea behind this approach is that the wave functions describing the electronic behavior have different behavior in different regions of space. Indeed, the wave functions vary smoothly between the atoms, in a region that can be called the interstitial region, while they oscillate rapidly near the nuclei, due to the strong potential of the nuclei and to Pauli exclusion principle. Therefore, the space can be divided in two regions, where the wave function is described by two different expressions. This is the main principle of augmented wave methods. In all-electron methods a division of the all electron basis set into core and valence states can be problematic due to the rapid oscillations of the valence wave function near the ion cores. These oscillations are a result of the requirement for the valence wave functions to be orthogonal to core states. The problem can be coped with using many Fourier components or a very fine mesh to describe the wave functions accurately.

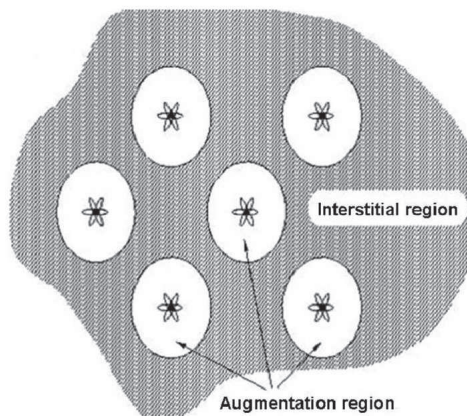


Figure 1.3.: Graphical representation of the interstitial and the augmentation regions.

The idea of the PAW method is to transform the all-electron wave function into a pseudo wave function that has no oscillation in the augmentation region. Once this pseudo wave function,  $\tilde{\psi}$ , is known the all-electron wave function can be obtained from it by a linear transformation  $\hat{T}$  as:

$$|\psi_n\rangle = \hat{T}|\tilde{\psi}_n\rangle, \quad (1.100)$$

where  $n$  is the band index. The operation  $\hat{T}$  is defined as  $\hat{T} = 1 + \sum_{\alpha} \hat{T}^{\alpha}$ , where  $\hat{T}^{\alpha}$  are the local atom-centered operators that act only in the augmentation region,  $\Omega^{\alpha}$ , where  $\alpha$  is a combined index for the atomic site,  $\mathbf{R}$ , the angular momentum number  $l, m$  and additional index for the energies for which the atomic Schrödinger equation is solved.

In order to define the  $\hat{T}^{\alpha}$ , the all-electron wave function  $|\psi_n\rangle$  is expanded into all-electron partial waves,  $|\phi_{\alpha}\rangle$  in  $\Omega_{\alpha}$ . Here we assume only one energy per orbital. There is therefore one to one correspondence between each partial wave and each smooth pseudo partial wave  $|\tilde{\phi}_{\alpha}\rangle$  as:

$$|\phi_{\alpha}\rangle = (1 + \hat{T}^{\alpha})|\tilde{\phi}_{\alpha}\rangle. \quad (1.101)$$

Outside  $\Omega_{\alpha}$ ,  $|\phi_{\alpha}\rangle = |\tilde{\phi}_{\alpha}\rangle$ . The pseudo partial waves form a complete set in the augmentation region so that:

$$|\tilde{\psi}_n\rangle = \sum_{\alpha} c_{\alpha,n}|\tilde{\phi}_{\alpha}\rangle, \quad (1.102)$$

where  $c_{\alpha,n}$  are expansion coefficients for the band  $n$  and combined index  $\alpha$ . If we return now to the all-electron wave function we have:

$$|\psi_n\rangle = \hat{T}|\tilde{\psi}_n\rangle \stackrel{1.102}{=} \hat{T} \left( \sum_{\alpha} c_{\alpha,n} |\tilde{\phi}_{\alpha}\rangle \right) \stackrel{1.101}{=} \sum_{\alpha} c_{\alpha,n} |\phi_{\alpha}\rangle. \quad (1.103)$$

The linearity of the transformation  $\hat{T}$  implies that the coefficients  $c_{\alpha,n}$  are linear functionals of the pseudo wave functions  $|\tilde{\psi}_n\rangle$ :

$$c_{\alpha,n} = \langle \tilde{p}_{\alpha} | \tilde{\psi}_n \rangle, \quad (1.104)$$

where  $|\tilde{p}_{\alpha}\rangle$  are fixed functions called projector functions. In each augmentation region, the projector functions fulfill the condition:

$$\sum_{\alpha} |\tilde{\phi}_{\alpha}\rangle \langle \tilde{p}_{\alpha}| = 1 \quad (1.105)$$

which also implies

$$\langle \tilde{p}_{\alpha} | \tilde{\phi}_{\beta} \rangle = \delta_{\alpha,\beta}. \quad (1.106)$$

There are no restrictions on the choice of the projector functions outside the augmentation regions but for convenience they can be chosen to be localized in the augmentation region. Therefore, the linear transformation between the valence wave functions and the pseudo wave functions reads as:

$$\hat{T} = 1 + \sum_{\alpha} (|\phi_{\alpha}\rangle - |\tilde{\phi}_{\alpha}\rangle) \langle \tilde{p}_{\alpha}|. \quad (1.107)$$

Thus, the all-electron KS wave function can be obtained from the pseudo wave function as:

$$|\psi_n\rangle = |\tilde{\psi}_n\rangle + \sum_{\alpha} (|\phi_{\alpha}\rangle - |\tilde{\phi}_{\alpha}\rangle) \langle \tilde{p}_{\alpha} | \tilde{\psi}_n \rangle. \quad (1.108)$$

Equation 1.108 shows that the transformation is determined by the all-electron partial waves,  $|\phi_{\alpha}\rangle$ , the pseudo partial waves  $|\tilde{\phi}_{\alpha}\rangle$  and a projector function  $|\tilde{p}_{\alpha}\rangle$ , localized within the augmentation region associated with each pseudo partial wave.  $|\phi_{\alpha}\rangle$  is determined by solving the radial Schrödinger equation for the isolated atom and is orthogonalized to the core states.  $|\tilde{\phi}_{\alpha}\rangle$  are expanded into planewaves and  $|\tilde{p}_{\alpha}\rangle$  are calculated as a radial function multiplied by spherical harmonics and then transformed to plane wave representation.

The expectation values of any operator, within PAW, is defined as:

$$\langle A \rangle = \sum_n f_n \langle \psi_n | A | \psi_n \rangle, \quad (1.109)$$

where  $f_n$  is the occupation number of state  $n$ . Notice that the observables are given as expectation values of the pseudo wave functions, therefore they can be considered as pseudo operators. To find an expression for the pseudo operator, let us use the definition of the linear transformation  $\hat{T}$  such that:

$$\langle A \rangle = \sum_n f_n \langle \tilde{\psi}_n | \tilde{A} | \tilde{\psi}_n \rangle. \quad (1.110)$$

In the case of local operators, the pseudo operator  $\tilde{A}$  can be expressed as:

$$\tilde{A} = \hat{T}^\dagger A \hat{T} = A + \sum_{\alpha, \beta} |\tilde{p}_\alpha\rangle (\langle \phi_\alpha | A | \phi_\beta \rangle - \langle \tilde{\phi}_\alpha | A | \tilde{\phi}_\beta \rangle) \langle \tilde{p}_\beta|. \quad (1.111)$$

Therefore, to take an estimation for the pseudo operator, the second term of the summation in equation 1.111, has to be added to the value of the observable  $A$ .

In the case of nonlocal operators an additional term  $\Delta A$  has to be added to the above expression,  $\Delta A$  as given by:

$$\Delta A = \sum_\alpha |\tilde{p}_\alpha\rangle (\langle \phi_\alpha | - \langle \tilde{\phi}_\alpha |) A \left( 1 - \sum_\beta |\tilde{\phi}_\beta\rangle \langle \tilde{p}_\beta| \right) + (1 - |\tilde{p}_\beta\rangle \langle \tilde{\phi}_\beta|) A (|\phi_\alpha\rangle - |\tilde{\phi}_\alpha\rangle) \langle \tilde{p}_\alpha|. \quad (1.112)$$

### 1.7.2. Numeric Atom-Centered Orbitals

Another approach to the basis set, a local one, is numeric atom-centered orbital (NAO) basis functions of the form:

$$\phi_i(\mathbf{r}) = \frac{u_i(r)}{r} Y_{lm}(\Omega), \quad (1.113)$$

where  $|\phi_i\rangle, i = 1, \dots, N$  defines the Hilbert space of the electrons.  $u_i(r)$  are radial functions of occupied free-atom orbitals, numerically tabulated and fully flexible.  $Y_{lm}(\Omega)$  denotes the spherical harmonics, where  $l, m$  are implicit functions of the basis function index  $i$ .

The shape of the basis functions given in equation 1.113 include both analytically and numerically defined functions of Gaussian or Slater type. Numerical solutions of Schrödinger-like radial equations can be read as:

$$\left[ -\frac{1}{2} \frac{d^2}{dr^2} + \frac{l(l+1)}{r^2} + v_i(r) + v_{\text{cut}}(r) \right] u_i(r) = \epsilon_i u_i(r), \quad (1.114)$$

where  $v_i(r)$  is the potential that defines the main behavior of  $u_i(r)$  and  $v_{\text{cut}}(r)$  is a steeply increasing confining potential that ensures a smooth decay of each radial function to be zero outside a confining radius. This radius is defined as  $r_{\text{cut}}$ .

In practice, in the case of non spin-polarized free atoms, a minimal basis set is assumed, consisting of the core and the valence functions of spherically symmetric free atoms. This is done by setting  $v_i(r)$  to the self-consistent free-atom radial potential  $v_{\text{at}}^{\text{free}}$ . The basis sets are transferable to spin-polarized systems. This minimal basis takes into account the wave function oscillations near the nucleus.

The introduction of the confining potential  $v_{\text{cut}}$  prevents the appearance of slow-decaying analytical or numerical radial function tails. Thus, there is a strict separation of basis functions in distant spatial regions which is important for the computational efficiency for large structures. The form of  $v_{\text{cut}}$  can be chosen according to:

$$v_{\text{cut}} = \begin{cases} 0 & \text{if } r \leq r_{\text{onset}} \\ s \cdot \exp\left(\frac{w}{r-r_{\text{onset}}}\right) \cdot \frac{1}{(r-r_{\text{cut}})^2} & \text{if } r_{\text{onset}} < r < r_{\text{cut}}, \\ \infty & \text{if } r \geq r_{\text{cut}} \end{cases} \quad (1.115)$$

where  $r_{\text{onset}}$  is the position where the potential  $v_{\text{cut}}$  begins smoothly and then increases gradually to infinity at position  $r_{\text{cut}}$ . The width of the function is  $w = (r_{\text{cut}} - r_{\text{onset}})$  and  $s$  is a scaling parameter. For more details the reader is referred to [9].

In the implementation framework, different basis set hierarchies of increasing accuracy are constructed, which are called *tiers*. For the construction of the basis set, there is a large amount of NAOs of the form 1.113, defined. For each element of the periodic table, the simplest closed-shell optimization target can be chosen. The basis functions are added to the optimization target, one by one and the basis functions that induce the minimum total energy are kept. The procedure is iterated until the addition of further basis functions does not cause any changes to the total energy.

The basis sets constructed, according to this procedure, are transferable to any system and can be employed to a wide range of local and non-local DFT exchange-correlation functionals. Furthermore, NAOs permit the systematic convergence of the calculations with different accuracy depending on the choice of higher-order *tiers*. NAO basis sets

can be also used for many-body perturbation approaches, such as RPA or *GW* calculations [117].

The NAO representation of any non-local single-particle operator  $\hat{A}$  and the corresponding real-space representation  $A(\mathbf{r}, \mathbf{r}')$  are given as:

$$\begin{aligned} A_{ij} &= \int \int d\mathbf{r} d\mathbf{r}' \phi_i(\mathbf{r}) \hat{A}(\mathbf{r}, \mathbf{r}') \phi_j(\mathbf{r}'), \\ A(\mathbf{r}, \mathbf{r}') &= \sum_{ijlm} \phi_i(\mathbf{r}) s_{ij}^{-1} A_{jl} s_{lm}^{-1} \phi_m(\mathbf{r}'). \end{aligned} \quad (1.116)$$

The method of NAOs has been implemented in the Fritz Haber Institute *ab initio* molecular simulations (FHI-aims) package [9]. In this implementation the so-called resolution of identity (RI) technique is also used, for the treatment of the two-electron Coulomb repulsion integrals [117]. Such implementation makes FHI-aims package faster and capable of treating systems with hundreds atoms.

## 1.8. Solving the Electronic Problem

In conclusion, in this chapter we have presented a theoretical introduction of the methods and techniques to attack the electronic problem in condensed matter. The heart of such a problem is a Schrödinger equation of the simplified form:

$$\left(-\frac{1}{2}\nabla^2 + V_{\text{eff}}\right)\psi = \epsilon\psi, \quad (1.117)$$

where the first term defines the kinetic energy, the second the effective potential, including all kind of interactions,  $\psi$  the wave function and  $\epsilon$  the eigenvalues of the problem.

Defining the problem according to the above equation, we can represent diagrammatically the tactic of choice of different approximations and numerical schemes applied in DFT codes, to solve this problem in practice.

As presented in the above scheme, to solve the electronic problem, one has to choose the most suitable basis set to define the orbitals. It is also essential to find the appropriate approximation to the effective potential to describe different properties of the system.

The practical of the many-body problem of a real system, even after a series of approximations, is not an easy task. In addition, the computational cost of the calculations should be also considered. However, thanks to powerful algorithms, massive parallelization and supercomputers, the DFT can be performed for systems of hundreds of atoms with great accuracy. The results presented within this thesis are obtained using three different codes, FHI-aims [9, 117], VASP [98, 99], and less extensively TURBOMOLE [8].

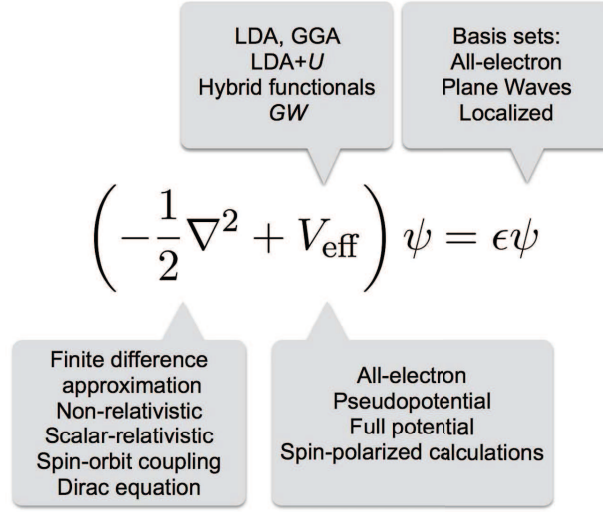


Figure 1.4.: Simplified representation of the different approximations and numerical schemes applied in DFT to solve the electronic problem. The combination of choices determine the physical problems available and the phenomena that can be studied with the code and the approximations employed.

## 1.9. Implementation of $GW$ within Projector Augmented Waves

In the present thesis for the  $G_0W_0$  calculation, the VASP package was used [98]. VASP uses the projector augmented wave (PAW) basis set [99]. Therefore, it is important to see some of the numerical aspects of the  $GW$  implementation in VASP code [118], [104].

The quasiparticle energies,  $E_{n\mathbf{k}}$  can be calculated by solving the nonlinear system of equations:

$$(T + V_{n-e} + V_H - E_{n\mathbf{k}})\psi_{n\mathbf{k}}(\mathbf{r}) + \int d^3\mathbf{r}' \Sigma(\mathbf{r}, \mathbf{r}', E_{n\mathbf{k}})\psi_{n\mathbf{k}}(\mathbf{r}'), \quad (1.118)$$

where  $T$  is the kinetic energy operator,  $V_{n-e}$  the operator accounting for the nuclear-electron interactions,  $V_H$  the Hartree potential and  $\Sigma$  the self-energy operator within  $GW$  approximation given as:

$$\Sigma(\mathbf{r}, \mathbf{r}', \omega) = \frac{i}{4\pi} \int_{-\infty}^{\infty} e^{i\omega'\delta} G(\mathbf{r}, \mathbf{r}', \omega + \omega') W(\mathbf{r}, \mathbf{r}', \omega') d\omega'. \quad (1.119)$$

The screened Coulomb interaction is constructed using the polarizability within the random phase approximation (RPA). A detailed review of RPA can be found in [119]. Within

the non-self-consistent  $G_0W_0$  approximation the  $G_0$  and  $W_0$  are given by a starting point DFT calculation (usually LDA or GGA). Therefore, the eigenstates of equation 1.118 can be approximated by DFT wave functions. In that case, the eigenvalues of equation 1.118 can be calculated to first order from the diagonal matrix elements of the QP equation as:

$$E_{n\mathbf{k}} = \text{Re}[\langle \psi_{n\mathbf{k}} | T + V_{n-e} + V_H + \Sigma(E_{n\mathbf{k}}) | \psi_{n\mathbf{k}} \rangle]. \quad (1.120)$$

Equation 1.120 must be solved iteratively in order to obtain the values of  $E_{n\mathbf{k}}$ . Using the Newton-Raphson method for root finding the previous equation can be rewritten as:

$$E_{n\mathbf{k}} \leftarrow E_{n\mathbf{k}} + Z_{n\mathbf{k}} \text{Re}[\langle \psi_{n\mathbf{k}} | T + V_{n-e} + V_H + \Sigma(E_{n\mathbf{k}}) | \psi_{n\mathbf{k}} \rangle - E_{n\mathbf{k}}], \quad (1.121)$$

where  $Z$  is a normalization factor given as:

$$Z_{n\mathbf{k}} = \left( 1 - \text{Re} \langle \psi_{n\mathbf{k}} | \frac{\partial}{\partial \omega} \Sigma(\omega) | \psi_{n\mathbf{k}} \rangle \right)^{-1}, \quad (1.122)$$

where the derivative of  $\Sigma$  is calculated at the quasiparticle energies  $E_{n\mathbf{k}}$ . The iteration in equation 1.121 starts from the DFT calculated eigenvalues  $\epsilon_{n\mathbf{k}}$ .

### 1.9.1. Dielectric matrix evaluation

If the bare Coulomb kernel is multiplied with the inverse dielectric matrix, it gives the dynamically screened Coulomb interaction as:

$$W_{\mathbf{q}}(\mathbf{G}, \mathbf{G}', \omega) = 4\pi e^2 \frac{1}{|\mathbf{q} + \mathbf{G}|} \epsilon_{\mathbf{q}}^{-1}(\mathbf{G}, \mathbf{G}', \omega) \frac{1}{|\mathbf{q} + \mathbf{G}'|}, \quad (1.123)$$

where  $\mathbf{q}$  is the Bloch wave vector and  $\mathbf{G}$  the reciprocal space vector. The symmetric dielectric matrix appearing in equation 1.123 is calculated within RPA as:

$$\epsilon_{\mathbf{q}}(\mathbf{G}, \mathbf{G}', \omega) = \delta_{\mathbf{G}, \mathbf{G}'} - \frac{4\pi e^2}{|\mathbf{q} + \mathbf{G}| |\mathbf{q} + \mathbf{G}'|} \chi_{\mathbf{q}}^0(\mathbf{G}, \mathbf{G}', \omega), \quad (1.124)$$

where  $\chi_{\mathbf{q}}^0(\mathbf{G}, \mathbf{G}', \omega)$  is the time-ordered independent particle polarizability, which reads as:

$$\chi_{\mathbf{q}}^0(\mathbf{G}, \mathbf{G}', \omega) = \frac{1}{\Omega} \sum_{nn'\mathbf{k}} 2w_{\mathbf{k}} (f_{n'\mathbf{k}-\mathbf{q}} - f_{n\mathbf{k}}) \frac{\langle \psi_{n'\mathbf{k}-\mathbf{q}} | e^{-i(\mathbf{q}+\mathbf{G})\cdot\mathbf{r}} | \psi_{n\mathbf{k}} \rangle \langle \psi_{n\mathbf{k}} | e^{i(\mathbf{q}+\mathbf{G}')\cdot\mathbf{r}'} | \psi_{n'\mathbf{k}-\mathbf{q}} \rangle}{\omega + \epsilon_{n'\mathbf{k}-\mathbf{q}} - \epsilon_{n\mathbf{k}} + i\eta \text{sgn}[\epsilon_{n'\mathbf{k}-\mathbf{q}} - \epsilon_{n\mathbf{k}}]}, \quad (1.125)$$

where  $w_{\mathbf{k}}$  is the  $\mathbf{k}$ -point weight,  $f_{n'\mathbf{k}-\mathbf{q}}$  and  $f_{n\mathbf{k}}$  are, respectively, the one electron occupancies of the corresponding states and  $\eta$  an infinitesimal complex shift.

The exchange charge density,  $\langle \psi_{n\mathbf{k}} | e^{-i(\mathbf{q}+\mathbf{G})\cdot\mathbf{r}} | \psi_{n\mathbf{k}} \rangle$  within VASP is approximated as [118]:

$$\begin{aligned} \langle \psi_{n\mathbf{k}} | e^{-i(\mathbf{q}+\mathbf{G})\cdot\mathbf{r}} | \psi_{n\mathbf{k}} \rangle &\approx \langle \tilde{u}_{n'(\mathbf{k}-\mathbf{q})} | e^{-i\mathbf{G}\cdot\mathbf{r}} | \tilde{u}_{n\mathbf{k}} \rangle + \\ &\sum_{i,j,R,L,M} \langle \tilde{u}_{n'(\mathbf{k}-\mathbf{q})} | p_{i(\mathbf{k}-\mathbf{q})} \rangle \langle p_{i\mathbf{k}} | \tilde{u}_{n\mathbf{k}} \rangle \\ &\times \int d^3r (e^{-i\mathbf{q}\cdot(\mathbf{r}-\mathbf{R}_i)} \hat{Q}_{ij}^{LM}(\mathbf{r}-\mathbf{R}_i) e^{-i\mathbf{G}\cdot\mathbf{r}}), \end{aligned} \quad (1.126)$$

where  $\tilde{u}_{n\mathbf{k}}$  is the cell periodic part of the one-electron pseudo wave function,  $|\tilde{\psi}_{n\mathbf{k}}\rangle = e^{i\mathbf{k}\cdot\mathbf{r}}|\tilde{u}_{n\mathbf{k}}\rangle$ ,  $p_{i\mathbf{k}}$  is the  $\mathbf{k}$ -dependent projector function, related to the PAW projector function  $p_i$ , centered on the atom with coordinated  $\mathbf{R}_i$ , and  $\hat{Q}_{ij}^{LM}(\mathbf{r}-\mathbf{R}_i)$  the multipole expansions of the compensation charges ( see Ref. [118] and the references therein).

The calculation of the polarizability matrix given in equation 1.125 is very time consuming, because the summation has to be carried out over all the occupied and unoccupied states. Furthermore, the summations are performed for all the frequencies in the frequency grid. Therefore, instead of equation 1.125 the spectral representation of the polarizability can be calculated as:

$$\begin{aligned} \chi_{\mathbf{q}}^S(\mathbf{G}, \mathbf{G}', \omega') &= \frac{1}{\Omega} \sum_{nn'\mathbf{k}} 2w_{\mathbf{k}} \operatorname{sgn}(\omega') \delta(\omega' + \epsilon_{n\mathbf{k}} - \epsilon_{n'\mathbf{k}-\mathbf{q}}) \\ &(f_{n\mathbf{k}} - f_{n'\mathbf{k}-\mathbf{q}}) \langle \psi_{n'\mathbf{k}-\mathbf{q}} | e^{-i(\mathbf{q}+\mathbf{G})\cdot\mathbf{r}} | \psi_{n\mathbf{k}} \rangle \\ &\langle \psi_{n\mathbf{k}} | e^{i(\mathbf{q}+\mathbf{G}')\cdot\mathbf{r}'} | \psi_{n'\mathbf{k}-\mathbf{q}} \rangle, \end{aligned} \quad (1.127)$$

where the spectral function is related to the imaginary part of the polarizability:

$$\chi_{\mathbf{q}}^S(\mathbf{G}, \mathbf{G}', \omega') = \frac{1}{\pi} \operatorname{Im} \chi_{\mathbf{q}}^0(\mathbf{G}, \mathbf{G}', \omega). \quad (1.128)$$

The only pairs of states  $n\mathbf{k}, n'\mathbf{k}-\mathbf{q}$  that contribute to  $\chi$  are those at frequency  $\omega' = \epsilon_{n'\mathbf{k}-\mathbf{q}} - \epsilon_{n\mathbf{k}}$ . This procedure makes the evaluation of the spectral function rather efficient.

### 1.9.2. Self-energy evaluation

The diagonal matrix elements of the self-energy  $\Sigma(\omega)_{n\mathbf{k},n\mathbf{k}}$  are calculated within VASP as:

$$\begin{aligned}
 \widetilde{\Sigma}(\omega)_{n\mathbf{k},n\mathbf{k}} &= \frac{1}{\Omega} \sum_{\mathbf{q}\mathbf{G}\mathbf{G}'} \sum_{n'} \frac{i}{2\pi} \int_0^\infty d\omega' W_{\mathbf{q}}(\mathbf{G}, \mathbf{G}', \omega') \\
 &\times \langle \psi_{n\mathbf{k}} | e^{i(\mathbf{q}+\mathbf{G})\cdot\mathbf{r}} | \psi_{n'\mathbf{k}-\mathbf{q}} \rangle \langle \psi_{n'\mathbf{k}-\mathbf{q}} | e^{-i(\mathbf{q}+\mathbf{G}')\cdot\mathbf{r}'} | \psi_{n\mathbf{k}} \rangle \\
 &\times \left[ \frac{1}{\omega + \omega' - \epsilon_{n'\mathbf{k}-\mathbf{q}} + i\eta \operatorname{sgn}(\epsilon_{n'\mathbf{k}-\mathbf{q}} - \mu)} \right. \\
 &\left. + \frac{1}{\omega - \omega' - \epsilon_{n'\mathbf{k}-\mathbf{q}} + i\eta \operatorname{sgn}(\epsilon_{n'\mathbf{k}-\mathbf{q}} - \mu)} \right],
 \end{aligned} \tag{1.129}$$

where  $\mu$  is the Fermi energy.

The bare Coulomb kernel  $v_{\mathbf{q}}^{\text{bare}}$  has to be subtracted from the dynamically screened Coulomb interaction such as:

$$\widetilde{W}_{\mathbf{q}}(\mathbf{G}, \mathbf{G}', \omega') = W_{\mathbf{q}}(\mathbf{G}, \mathbf{G}', \omega') - v_{\mathbf{q}}^{\text{bare}}(\mathbf{G}, \mathbf{G}') \tag{1.130}$$

which makes the self-energy integral behave well, when  $W(\omega)$  approaches  $v^{\text{bare}}$  at large frequencies. In order to obtain the final self-energy the exact Fock exchange term has to be added as:

$$\Sigma(\omega)_{n\mathbf{k},n\mathbf{k}} = \widetilde{\Sigma}(\omega)_{n\mathbf{k},n\mathbf{k}} + \langle \psi_{n\mathbf{k}} | v_x | \psi_{n\mathbf{k}} \rangle. \tag{1.131}$$

The evaluation of the self-energy is very time consuming. Different methods can be used to limit such a computational cost using Hilbert transforms which are presented in detail in Ref. [118].

# Kondo Effect In Binuclear Metal-Organic Complexes 2

---

## 2.1. Introduction

The motivation for the work presented in this chapter is to address the physics of molecules adsorbed on surfaces which carry more than one active spins. If we consider two exchange coupled spins, we anticipate the case of single molecule magnets (SMMs) [1], [120]. Even in the case of binuclear magnets [121, 122], interesting aspects can arise like Kondo screening and intermolecular exchange coupling.

Before we pass into the analysis of the results, it is useful to describe the Kondo effect and how the experiments can detect its features and analyze them. Hence, we begin with presenting the basic theory of Kondo effect and the principles of scanning tunneling microscopy (STM). Then, we pass to the STM results for the system under study and finally we present our theoretical analysis.

## 2.2. Kondo's Approach

Generally speaking, the electrical resistance of pure metals is expected to decrease as temperature decreases. This happens due to the gradual freeze out of the lattice vibrations when the temperature is reduced. However, it was discovered experimentally, already in the 1930's, in certain metals carrying magnetic impurities, that the electrical resistance increases again below a certain temperature [123, 124]. This observation remained a mystery up to the theoretical explanation given by Kondo in 1964 [35, 125].

Kondo attributed the experimental observations to scattering events on the magnetic impurities. Within his model the interaction of the spins of the conduction electrons of the host metal with the localized spin of the magnetic impurities is taken into account, through perturbation theory. For a single impurity, the Hamiltonian describing this interaction is read:

$$H = \sum_{k,s} \epsilon_k \alpha_{ks}^* \alpha_{ks} - J \sum_{k,k'} (\alpha_{k'\uparrow}^* \alpha_{k\uparrow} - \alpha_{k'\downarrow}^* \alpha_{k\downarrow}) - J \sum_{k,k'} (\alpha_{k'\uparrow}^* \alpha_{k\downarrow} S^- - \alpha_{k'\downarrow}^* \alpha_{k\uparrow} S^+), \quad (2.1)$$

where  $\epsilon_k$  is the one-electron energy of the conduction electron,  $k$  its wave number and  $s$  its spin component along the  $z$ -direction,  $\alpha_{ks}$  the annihilation and  $\alpha_{ks}^*$  the creation operator,  $S$  is the spin operator of the impurity,  $S_z$  its projection along the  $z$ -axis and  $S^\pm = S_x \pm iS_y$ , with  $S_x$  and  $S_y$  the projections of  $S$  in the  $x$ - and  $y$ -direction respectively. The Hamiltonian is separated in three terms: the first represents the conduction electrons that do not interact with the impurity. The second and third terms describe the scattering of the conduction electrons with the magnetic impurity. The second without taking account the spin-flip process, which are given in the third term.

Using the Hamiltonian expressed in equation 2.1, Kondo derived the resistivity of a system with a certain concentration of impurities as:

$$\rho(T) = \rho_0 + \alpha T^5 + bJ \text{Ln} \left( \frac{T}{c} \right), \quad (2.2)$$

where  $\alpha$ ,  $b$  and  $c$  are constant numbers. At high temperatures the phonon scattering dominates following a  $T^5$  dependence, whereas at low temperatures impurity scattering prevails with logarithmic dependence of  $T$ . Note that Kondo effect arises only if the impurities hosted on the metal are magnetic. This means that the total spin of all electrons surrounding the impurity atom has to be unequal to zero. For  $J > 0$ , the ferromagnetic coupling creates a screening cloud of spins aligned parallel to the spin of the impurity. This spin becomes asymptotically free at low temperatures. For ferromagnetic coupling or at temperatures  $T \gg T_K$ , the system is in the weak coupling regime and can be treated using the perturbation theory proposed by Kondo. On the contrary, for antiferromagnetic spin alignment of the conduction electrons and the localized electrons, i.e. exchange interaction  $J < 0$ , an entangled many-body state emerges. In this strong coupling regime, the antiparallel alignment of the spins of the conduction electrons effectively screen the spin of the impurity.

### 2.2.1. Anderson Model

In 1961, Anderson described the conditions under which a single magnetic impurity embedded in a metal can retain its magnetic moment [126]. Although this is a prerequisite for a Kondo state, the link between Anderson's model and the Kondo effect was discovered some years later, by Shrieffer and Wolff [127].

The so-called Anderson single-impurity model [126] takes into account only a single  $d$  or  $f$  orbital state that can be filled with 0, 1 or 2 electrons. Let us assume a  $d$ -localized

orbital and describe its interaction with the conduction electrons of the host metal. Since the orbital has to be magnetic, we consider a singly occupied  $d$  orbital which will lie below the Fermi energy with a binding energy  $\epsilon$ . If we add a second electron to the orbital, the energy will be increased by the Coulomb repulsion  $U$ . Now the fully occupied orbital  $d^2$  will lie above the Fermi energy to ensure again the existence of an unpaired spin. A broadening of the  $d$  states is expected because of their hybridization with the continuum of the metal's electronic states. This broadening is equal to  $\Delta = \sigma|V|^2$ , where  $\sigma$  is the density of states of the metal at the Fermi level and  $V$  the matrix element describing the interaction of the  $d$  state with the bath of the conduction electrons of the metal.

Schrieffer and Wolff [127] proved the equivalence of the Anderson model with the Kondo's scattering process in the limit of a small  $s$ - $d$  hybridization,  $\Delta$ . In this case, the interaction  $J$  appearing in the Kondo Hamiltonian can be given as a function of Anderson variables:

$$J = 2|V|^2 \frac{U}{\epsilon(\epsilon + U)}. \quad (2.3)$$

According to the Anderson model, there are two possible ways to flip the spin of the singly occupied  $d$  state, through its interaction with a bulk electron of the opposite spin, Figure 2.1. On the one hand, the  $d$  orbital can be first emptied and afterwards be re-filled with a conduction electron carrying opposite spin, Figure 2.1,(b) $\rightarrow$ (d). On the other hand, the  $d^1$  orbital can be fully occupied with 2 electrons, and then the initial electron can be transferred to the metal, leaving the electron with opposite spin on its position, Figure 2.1,(c) $\rightarrow$ (e). Note that in order to bring the electron from the  $d$ -orbital to an empty state in the bulk, above the Fermi energy (Figure 2.1(b)), an energy equal or greater than  $\epsilon$  is needed. Likewise, to refill the  $d$ -orbital with an electron of opposite spin, below the Fermi energy, Figure 2.1(c)), at most the energy  $\epsilon$  can be gained. The same is valid for the case of temporarily doubly occupied orbital, where an initial energy of at least  $2U-\epsilon$  is required (Figure 2.1(d)). Of course in the continuous spin-flip process of the Kondo effect there is no external energy available. That means that the bulk electrons involved in the process must be located exactly at the Fermi energy. The Kondo problem of heavy fermions is well explained in [128]. In the following we will take into account that the Kondo temperature can be estimated according to the Anderson model, reading specific parameters from the density of states localized on the ion contributing to the Kondo effect. The Anderson model formula for the estimation of the Kondo temperature, in this case, is given as:

$$k_B T_K \simeq 0.41U \sqrt{\frac{\Gamma}{4U}} e^{-\pi(U-\epsilon_d)\epsilon_d/U\Gamma}, \quad (2.4)$$

where  $-\epsilon_d < 0$  is the position of the occupied resonance level measured versus the Fermi energy,  $\Gamma$  the width of the Kondo resonance, and  $U$  the Coulomb on-site interaction.

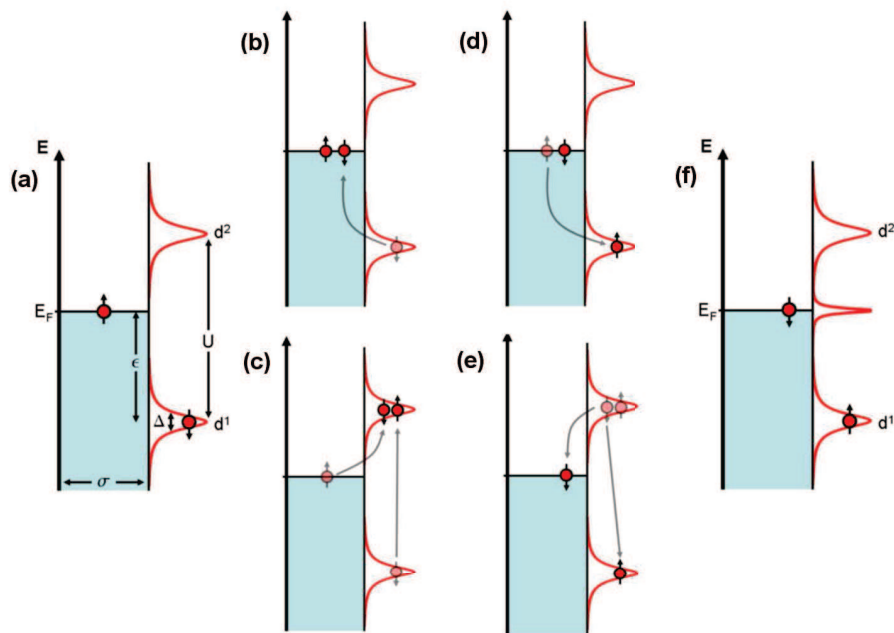


Figure 2.1.: Diagrammatic representation of spin-flip process in the Anderson model. In order for an impurity spin to flip from a down state, as shown in (a), to an up state, shown in (f), there is a virtual process that can occur in two different ways. The first one with the help of an empty orbital, (b)→(d), and the second with a doubly filled orbital, (c)→(e). The plot has been taken from [3].

## 2.3. Scanning Tunneling Microscopy and Spectroscopy

### 2.3.1. STM and STS

Scanning Tunneling Microscopy (STM), is a tool that shaped nanoscience and nanotechnology during the last three decades. It represents a powerful tool, giving access to atomic scale structures, with high resolution. It was invented in 1982 by Binnig and Rohrer [129], [130], [131] for which they were awarded the Nobel prize in Physics in 1986. At the early days of its invention, STM was used as a visualization tool for surface topography [132]. However, it was developed quickly into a tool that allows access to occupied and unoccupied states, a procedure known as scanning tunneling spectroscopy (STS) [133]. Nowadays, even atomic manipulation has been achieved and magnetic contrasts were realized with the spin-polarized STM [134].

According to the STS concept, the electronic states of a sample can be investigated experimentally at the atomic scale. STS can measure the local density of states (LDOS)

of a sample as any inelastic process deriving by the tunneling electrons. STS has been used with great success in the observation of spin-flip of an atomic spin [135], the lifetime of an excited electron state [136] and the Kondo-resonance of a single atom [23].

The further description of STM and STS goes beyond the purposes of the present thesis. The principles and its concepts are described in great detail in many reviews and books, see for example [137–139]. Herein, we present the two basic methods to model the tunneling currents between the surface and the tip of an STM.

### 2.3.2. Bardeen Model

The tunneling junction problem treated by Bardeen, also mentioned as the transfer Hamiltonian problem [140], gives a fundamental understanding of the ability of STM to reach high space and energy resolution. However, it adopts several assumptions which lead to some limitations of the model. The electron tunneling is treated as a one-particle process, which means that the mutual interaction between electrons during tunneling is neglected. Furthermore, a direct interaction of the tip and the sample is neglected, which avoids the formation of coupled electronic states. The latter assumption is valid if the distance between the tip and the sample is large enough, i.e. above  $\sim 4 \text{ \AA}$ . In the case of elastic tunneling, i.e. when no energy loss of the electrons with quasi-particles of the electrons is assumed, and at low temperatures, it comes out that the current is given as:

$$I = \frac{4\pi e}{\hbar} \int_0^{eV} n^T(E_F^T - eV + \epsilon) n^S(E_F^S + \epsilon) |M|^2, \quad (2.5)$$

where  $T$  and  $S$  refer to the unperturbed substrate and the unperturbed electrode respectively,  $n$  is the density of states, and  $E_F$  the Fermi energy.  $M$  is the tunneling matrix element defined by  $\langle \psi^T | U_T | \psi^S \rangle$ , with  $\psi^S$  the wave function of the electrode  $S$  (substrate),  $\psi^T$  the wave function of the electrode  $T$  (tip) and  $U_T$  the potential function of the tip.

Therefore, Bardeen's model states that the tunneling current depends explicitly on the electronic states of both the tip and the substrate. The differential conductivity, which is also measured experimentally, is given as:

$$\frac{dI}{dV} = \frac{4\pi e}{\hbar} n^T(E_F^T) n^S(E_F^S + eV) |M(E_F^S + eV, E_F^T)|^2, \quad (2.6)$$

where  $V$  is the applied bias voltage. The equation 2.6 explains the unique power of STM to access the occupied and unoccupied electronic states of the substrate, simply by changing the sign of the bias voltage  $V$ .

In Bardeen's model the electronic states of both electrodes contribute equally. However, the STM measurements' aim is to resolve the topography of the sample, taking for granted that the exact atomic configuration of the tip is unknown as well. Therefore, the use of a more simplified model is necessary, where the tip configuration can be neglected, but still giving acceptable results for the tunnel current.

### 2.3.3. Tersoff-Hamman Model

Tersoff and Hamann (TH) [141], [142] gave a solution to the above problem, by focusing on the difficulty to access the tip states. Indeed, in the TH model, the tip states are represented with arbitrarily localized wave functions and potential. In practice this means, that the tip is modeled as one geometrical point. As a consequence, the STM image is related only to the properties of the surface. Hence, they assumed a spherical  $s$ -type wave function for the tip and a plane wave approximation for the sample. In the limit of low temperature and a small bias voltage  $V$ , they obtained the tunneling current as:

$$I(\mathbf{R}_T, V) = \frac{16\pi^3 C^2 \hbar^3 e^2}{\kappa^2 m^2} V n^T n^S(\mathbf{R}_T, E_F^S), \quad (2.7)$$

where  $R_T$  is the curvature of the tip,  $C$  is a normalization constant,  $n^T$  and  $n^S$  the density of states of the tip and the sample respectively and  $E_F^S$  the Fermi energy for the sample,  $\kappa$  the decay constant that describes an electron penetrating through a barrier into the  $+z$  direction. The decay constant  $\kappa$  is derived from the one dimensional tunneling model and is given as  $\sqrt{2m(|U| - E)}/\hbar$ , where  $U$  is the potential that the electron feels,  $m$  its mass and  $E$  its energy.

The differential conductivity given by the TH model is:

$$\frac{dI(\mathbf{R}_T, V)}{dV} = \frac{16\pi^3 C^2 \hbar^3 e}{\kappa^2 m^2} n^T n^S(\mathbf{R}_T, E_F^S + eV). \quad (2.8)$$

It is clear from the above equations that the current and the differential conductivity are proportional to the density of states of the sample in the vacuum,  $n^S(\mathbf{R}_T, E_F^S + eV)$ .

Despite its drastic simplification of neglecting the tip's states, apart from an  $s$  wave function, the TH model has proved to be very successful in the simulation and prediction of STM images in realistic problems. Furthermore, it is extremely valuable in interpreting STM images with characteristic feature sizes of  $\geq 10 \text{ \AA}$ , like the profiles of superstructures of surface reconstruction, the scattered waves of surface states, as well as defects, adsorbates and substitution atoms on the surface. However, it can also fail to explain some experimental observations, because of neglecting the tip electronic states.

### 2.3.4. Analyzing the Kondo Effect

We have to mention at this point that the Kondo effect is detectable within STS measurements. In case of appearance of the Kondo effect, characteristic peaks are resolved in the  $dI/dV$  curves near the Fermi level. The shape of the zero-bias anomaly in STS caused by the Kondo effect can be described by a Fano resonance [143–145] as:

$$\frac{dI}{dV}(V) \propto \frac{(\epsilon + q)^2}{1 + \epsilon^2}, \quad (2.9)$$

where

$$\epsilon = \frac{eV - \epsilon_0}{\Gamma}, \quad (2.10)$$

with  $\epsilon_0$  the energy shift of the resonance from the Fermi level and  $\Gamma$  the width of the resonance. The Fano parameter  $q$  characterizes the interference of the tunneling between the tip and the sample [146]. The Kondo resonance can be approximated by a Lorentzian resonance, taking into account the temperature dependence [147]. Hence, the full width at half maximum of a Kondo resonance,  $2\Gamma(T)$  reads as:

$$2\Gamma(T) = 2\sqrt{(\pi k_B T)^2 + 2(k_B T_K)^2}, \quad (2.11)$$

with  $k_B$  the Boltzmann constant,  $T$  the environment temperature and  $T_K$  the Kondo temperature. By fitting the experimental STS with the equations 2.9-2.11, the Kondo temperature  $T_K$  can be extracted.

It is true that, the information offered by STM and STS about the properties and functionality of atoms or molecules are essential for perspective applications like molecular electronics. That is the reason why STM and STS are the mainstream experimental methods to study systems anticipated for single molecule magnets (SMM's) [1], like the one we study in the following.

## 2.4. Experimental Study of Metal-Organic Complexes

A series of binuclear metal-organic complexes of the form  $[(\text{Me}(\text{hfacac})_2)_2(\text{bpym})]^{0}$  were synthesized, by Ruben's group, Figure 2.2 [4]. "Me" can be Mn, Zn or Ni atoms.

These complexes were deposited, by Wulfhekel's group, on a clean Cu(001) surface and studied with low-temperature STM and analyzed with STS [4]. The STM images and STS were measured at 4.2 K and their outcome is presented in Figure 2.3. The spectra are normalized and a linear background was considered to obtain reasonable fitting results.

As can be noticed in Figure 2.3, in the case of  $\text{Zn}_2$ , no feature of Kondo effect was detected in the STS analysis. Such a fact can be explained due to the closed-shell  $3d$

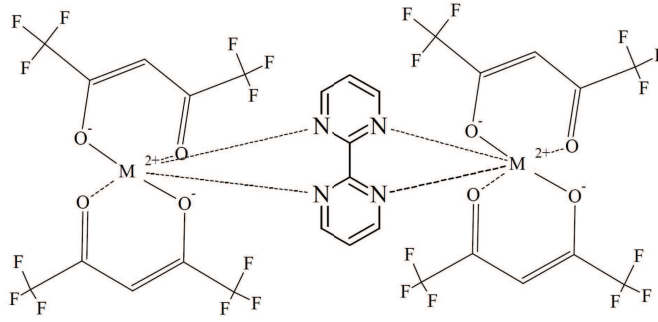


Figure 2.2.: Structure of the  $(\text{Me}(\text{hfacac})_2)_2(\text{bpym})$  complex. Each  $\text{Me}^{2+}$  metal ion is linked to two hexafluoroacetylacetonate (hfacac) ligands by Me-O bonds. By forming N-Me bonds the aromatic 2,2'-bipyrimidine (bpym) ligand coordinates as bidentate chelate with two of the  $\text{Me}(\text{hfacac})_2$  components.

$\text{Zn}^{2+}$  ions in the molecule. Since, no spin is unpaired there is no possibility for a spin to be coupled with the conduction electrons of the metal. Kondo effect in this case, would appear only if the interaction of the adsorbed molecule with the substrate leads to an electron transfer and the acquisition of a magnetic moment on the molecule. Since, the measurements do not indicate any Kondo resonance, we can conclude that the interaction between the  $\text{Zn}_2$  complex and the  $\text{Cu}(001)$  substrate is weak for such an electron transfer to take place.

On the contrary, in the case of  $\text{Mn}_2$  and  $\text{Ni}_2$  complexes, the characteristic Kondo resonance is clearly resolved in the STS data, at zero bias. Both  $\text{Mn}^{2+}$  and  $\text{Ni}^{2+}$  ions exhibit a partially filled  $3d$  shell and therefore carry a finite magnetic moment. Hence, the coupling of their uncoupled spins with the conduction electrons of the substrate is expected. For  $\text{Mn}_2$  a Kondo temperature of 15 K is determined by fitting to a Fano resonance, see equations 2.9-2.11.

Additionally, the  $\text{Ni}_2$  complex showed an intriguing unexpected feature. Unlike  $\text{Mn}_2$ ,  $\text{Ni}_2$  appears in two variants with different STM images and STS characteristics. The two adsorption geometries are referred to as  $\text{Ni}_2 - \alpha$  and  $\text{Ni}_2 - \beta$ . The Kondo temperatures determined for  $\text{Ni}_2 - \alpha$  and  $\text{Ni}_2 - \beta$  are  $T_K = 5.8$  K and 16 K, respectively. Another difference between the two adsorption geometries comes out by a site-dependent STS measurement, performed on  $\text{Ni}_2 - \alpha$  and  $\text{Ni}_2 - \beta$  (Figure 2.4). For the  $\text{Ni}_2 - \alpha$  complex, the STS measurement shows that the Kondo resonance has a single maximal amplitude at the center of the molecule (Figure 2.4(a) and 2.4(c)). In the case of  $\text{Ni}_2 - \beta$ , however, two spots with maximal amplitude of  $dI/dU$  signal appear, separated by a distance of 4 Å (Figure 2.4(b) and 2.4(d)). These maxima match the two  $\text{Ni}^{2+}$  ions and their expected distance in the molecule.

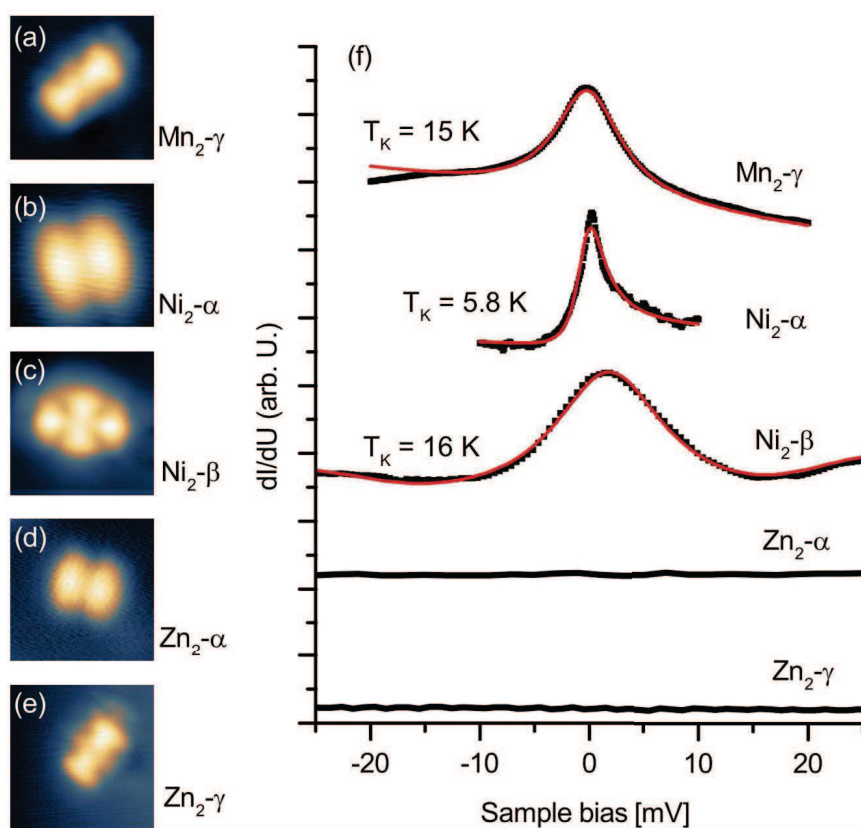


Figure 2.3.: Topography of (a)  $\text{Mn}_2\text{-}\gamma$ , (b)  $\text{Ni}_2\text{-}\alpha$ , (c)  $\text{Ni}_2\text{-}\beta$ , (d)  $\text{Zn}_2\text{-}\alpha$ , and (e)  $\text{Zn}_2\text{-}\gamma$  obtained by low-temperature STM. In (f) the differential conductance  $dI/dU$  near the Fermi-level is shown. The black dots are experimental data which were fitted with Fano-functions, presented in red lines. The figure is taken from [4].

Since for the complexes of  $\text{Zn}_2$  and  $\text{Mn}_2$  the experimental results were expected, we focus only on the intriguing behavior of  $\text{Ni}_2$  complex embedded on  $\text{Cu}(001)$ . Our target in the following is to rationalize the experimental observations for the  $\text{Ni}_2$  complex, by performing DFT calculations.

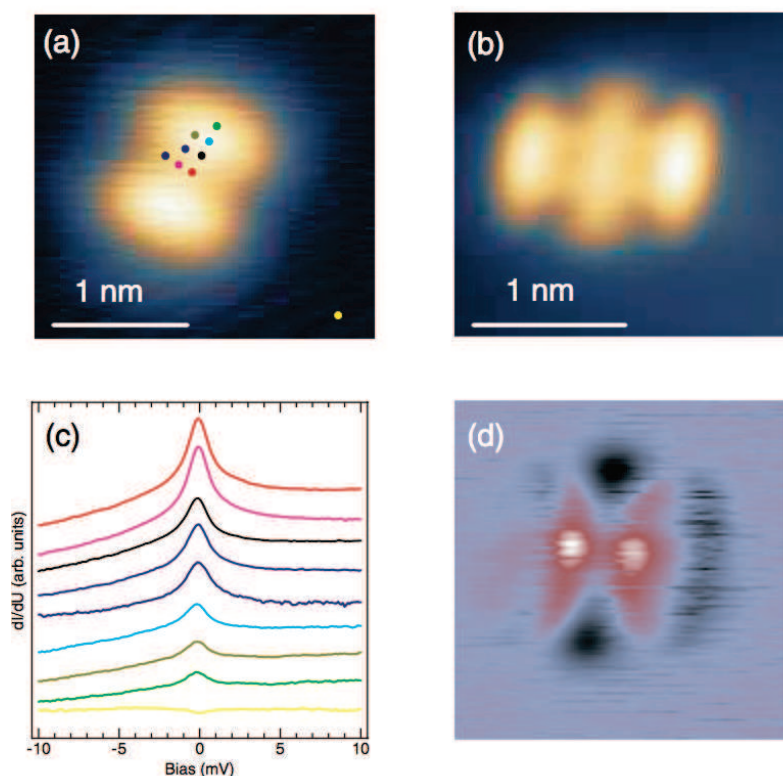


Figure 2.4.: (a) STM topography of  $\text{Ni}_2 - \alpha$  and (b) STM topography of  $\text{Ni}_2 - \beta$ . (c) STS data on different position of the  $\text{Ni}_2 - \alpha$ . (d)  $dI/dV$  map of  $\text{Ni}_2 - \beta$ . White and black areas indicate large and low differential conduction, respectively.

## 2.5. Computational Study

### 2.5.1. Molecular Atomic Structure

The  $\text{Ni}_2$  complex,  $(\text{Ni}(\text{hexafluoroacetylacetonate})_2)_2\text{bipyrimidine}$ , was synthesized at Karlsruhe Institute of Technology at Institute of Nanotechnology (INT), [4]. We present in Table 2.1 some characteristic values of the bond lengths and bond angles, between the Ni atoms and the atoms around it, obtained by single-crystal X-ray diffraction (for further details see [4]). In Figure 2.5 the Ortep representation of the gas phase molecules is displayed.

### 2.5.2. Computational Details

For the analysis of the electronic structure and the magnetic properties of free-standing and adsorbed metal-organic complexes, we have employed quantum chemistry packages FHI-aims [9] and TURBOMOLE [8]. The atomic structure of  $\text{Ni}_2$  complex has been relaxed

Table 2.1.: Selected bond lengths and bond angles of  $[(\text{Ni}(\text{hfacac})_2)_2(\text{bpym})]^0$  obtained from single crystal X-ray diffraction data, [4].

Bond	Distance (Å)	Bond Angle	Degrees
Ni(1)-O(4)	2.000	O(4)-Ni(1)-O(2)	91.84
Ni(1)-O(2)	2.025	O(4)-Ni(1)-O(1)	86.12
Ni(1)-O(1)	2.034	O(2)-Ni(1)-O(1)	90.57
Ni(1)-O(3)	2.038	O(4)-Ni(1)-O(3)	90.00
Ni(1)-N(1)	2.086	O(2)-Ni(1)-O(3)	86.65
Ni(1)-N(3)	2.112	O(1)-Ni(1)-O(3)	176.12
Ni(2)-O(5)	2.028	O(4)-Ni(1)-N(1)	172.41
Ni(2)-O(6)	2.029	O(2)-Ni(1)-N(1)	94.98
Ni(2)-O(7)	2.031	O(1)-Ni(1)-N(1)	90.49
Ni(2)-O(8)	2.031	O(3)-Ni(1)-N(1)	93.35
Ni(2)-N(4)	2.112	O(4)-Ni(1)-N(3)	93.82
Ni(2)-N(2)	2.113	O(2)-Ni(1)-N(3)	174.26
		O(1)-Ni(1)-N(3)	88.94
		O(3)-Ni(1)-N(3)	91.23
		N(1)-Ni(1)-N(3)	79.31
		O(4)-Ni(1)-O(2)	91.84

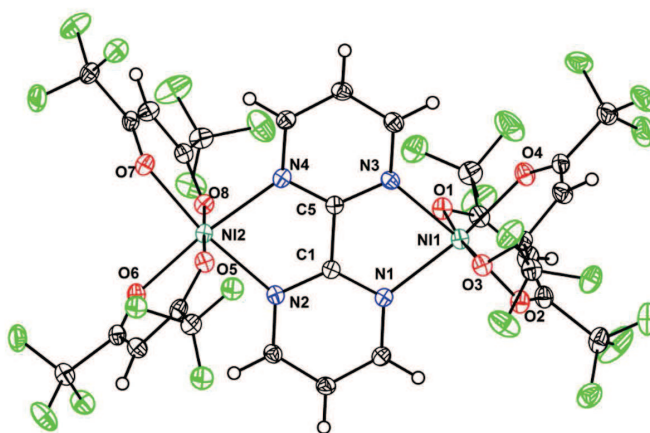


Figure 2.5.: Ortep plot of the molecular structure of the  $[(\text{Ni}(\text{hfacac})_2)_2(\text{bpym})]^0$  complex, obtained by single crystal X-ray diffraction. C atoms are represented in black, O in red, N in blue, F in light green, Ni in dark green and H in black circles. The figure was taken from [4].

Table 2.2.: DFT calculated relative energies of the low-energy spin configurations in the gas-phase of Ni<sub>2</sub> complex. The estimations are obtained using PBE exchange-correlation functional on TURBOMOLE [8] and FHI-aims [9].

		AF: ↑↑ ↓↓	F: ↑↑ ↑↑	↑↑ ↑↓
relaxed Ni <sub>2</sub>	fhi-aims	0.000 eV	15.8 meV	0.500 eV
complex	turbomole	0.000 eV	14.9 meV	0.522 eV

following the data obtained by the single-crystal X-ray diffraction, presented previously. All calculations were performed using the PBE exchange-correlation functionals [78]. In the case of FHI-aims package, a *tier1* basis set composed of numerical atom-centered orbitals has been used. In the case of TURBOMOLE [8], we employed a basis set of contracted Gaussian-type basis of split-valence quality with polarization functions (def-SVP) [148]. The corresponding Coulomb-fitting basis sets have been used within the resolution of identity approximation [149].

### 2.5.3. Gas Phase Molecule

The electron configuration of Ni atom is [Ar]4s<sup>2</sup>3d<sup>8</sup> so the local magnetic moments of  $2\mu_B$  is due to two unpaired *d*-electrons. These magnetic moments can be coupled ferro- (FM) or antiferro-magnetically (AFM) for the Ni<sub>2</sub> complex.

In order to find which magnetic configuration is the most favorable, we have performed “constrained” DFT calculations. We first prepare an initial guess for the electron density, reflecting the presence of two unpaired electrons in the *d*-shell of each Ni<sup>2+</sup> ion. Kohn-Sham (KS) equations are then solved iteratively assuming that the number of unpaired electrons in the system is constrained to four in the case of FM coupled spins, or to zero for the AFM coupled spins. Similarly, we assume another case of magnetic coupling, where the initial state corresponds to zero magnetic moment at each Ni<sup>2+</sup> ion. In this case, though, the KS equations are converged to an excited state of the closed *d*-shell of Ni<sup>2+</sup> ion, breaking the first Hund’s rule for spin coupling. The results of the constrained DFT calculations are presented in Table 2.2, for the three different mentioned configurations. It shows that the DFT ground state corresponds to two unpaired spins located in each Ni<sup>2+</sup> ion, while the two pairs of electrons between the Ni<sup>2+</sup> ions are AF coupled. The FM configuration is higher in energy by  $\sim 15.4$  meV, while the closed shell conformation is higher by  $\sim 0.5$  eV.

## 2.6. Ni<sub>2</sub> Complex on Cu(001)

For the Ni<sub>2</sub> complex on a clean Cu(001) surface, STM shows two different adsorption-type dependent STM images. Therefore, one expects there are two possible adsorption configurations, as presented in Figure 2.6. The first configuration, the Ni<sub>2</sub> –  $\alpha$  “standing” on Cu(001), possesses two symmetric upper parts (the hfacac ligand) which could be seen in the STM image 2.4(a), due to electrons passing from the substrate to the upper part of the complex. Likewise, in the second configuration Ni<sub>2</sub> –  $\beta$ , electrons pass from the substrate to the upper part of the molecule, which “lies” on the surface with both its hfacac ligands. In this case, however, the central bipyrimidine part of the molecule can be pictured on the STM image, giving the central globe seen in Figure 2.4(b).

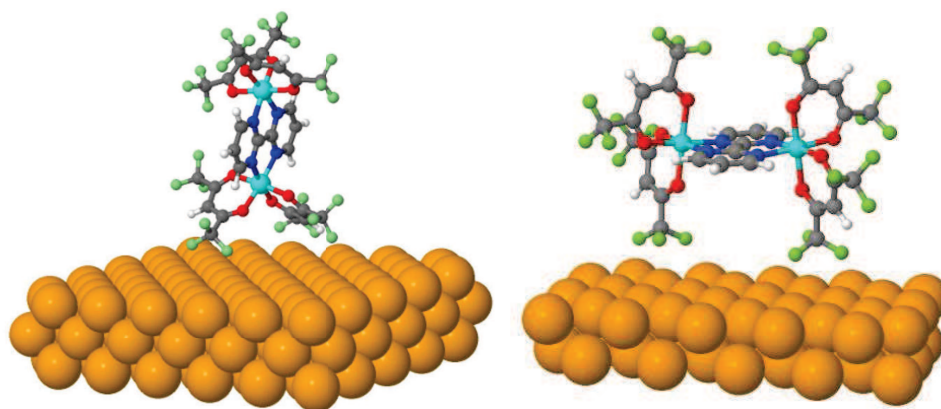


Figure 2.6.: On the left the “standing” Ni<sub>2</sub> –  $\alpha$  complex bound to Cu(001) surface. On the right the Ni<sub>2</sub> –  $\beta$  complex “lies” on the Cu(001) surface.

Following the intuitive picture of the problem, we analyze the adsorption geometries schematically illustrated in Figure 2.6. First the gas-phase “standing” Ni<sub>2</sub> –  $\alpha$  complex adsorbed on Cu(001) surface, and then the embedded “lying” Ni<sub>2</sub> –  $\beta$  complex.

### 2.6.1. Computational Details

In order to optimize the atomic structures of the adsorbed molecules we have used FHI-aims package [9]. The copper surface has been modeled by finite-size fcc(001) atomic clusters with three atomic layers for the Ni<sub>2</sub> –  $\alpha$  complex and two atomic layers for the Ni<sub>2</sub> –  $\beta$  complex. The calculations have been performed using the PBE exchange-correlation functional [78]. The basis set of numerical atom-centered orbitals used is the *tier1*. The van der Waals (vdW) dispersive forces have been taken within Tkatchenko-Scheffler model [82], which relies on the inter-atomic dispersion coefficients derived from electron density. The degrees of freedom for the atoms of the molecule and a few copper atoms of the surface layer, in the nearest vicinity of the molecules, have been fully relaxed. The coordinates

of the rest of the copper atoms are fixed to the bulk values. Relaxation steps have been carried out until the residual forces acting on atoms have reached values below 0.01 eV/Å.

The spectral functions of molecular complexes adsorbed on Cu(001) were calculated within the non-equilibrium Green's function (NEGF) formalism merged with DFT, as implemented in the simulation code AITRANSS [150–152]. Within AITRANSS, a metal-organic complex bound to an atomic Cu cluster is considered as an “extended molecule”. This extended molecule is coupled to an infinite “reservoir” of electrons. The Cu(001) clusters used in these simulations are smaller compared to the ones used for the relaxation of the structures. The copper clusters are limited in this case to two atomic layers.

A self-consistent set of KS orbitals is found for the “extended molecule” and then its interaction with the infinite reservoir of electrons is accounted for within the Green's function formalism. The KS Hamiltonian is supplemented by the parameter-dependent local self-energy,  $\Sigma^{\text{surface}}(\mathbf{x}, \mathbf{x}') = [\lambda - i\eta]\delta(\mathbf{x} - \mathbf{x}')$ , where  $\eta$  is the level broadening and  $\lambda$  the contribution to the real part of the self-energy.  $\Sigma^{\text{surface}}$  is ascribed to the “surface-1” atomic layer of the simulation clusters. For the chosen value of the parameter  $\eta$ , the contribution  $\lambda$  is obtained by imposing the charge neutrality condition within the “extended molecule”. For the present calculations we have  $\eta = 2.7$  eV. The Green function describing the system can be further projected on the basis functions associated with a selected atom, i.e. Ni<sup>2+</sup> ions in our case, thus allowing to compute the local density of states.

### 2.6.2. Spectral Function and Kondo Temperature

Our simulation results indicate that the final distance between fluorine and copper is above 3 Å. This distance suggests a binding between the molecule and the surface through weak van der Waals forces. This means, there is only a weak hybridization between molecular and substrate states, which translates into narrow molecular resonances in the density of states projected on the Ni<sup>2+</sup> ion, shown in Figure 2.7.

Reading the Anderson model parameters from the spectral function  $A(E)$ , namely, the single occupied resonance level width  $\Gamma \approx 10^{-2}$  eV, the on-site Coulomb repulsion energy  $U \approx 2$  eV and the position of the resonance level  $\epsilon_d \approx U/2 \approx 1$  eV relative to the Fermi energy, and replacing in equation 2.4, we get an estimation of the Kondo temperature:

$$k_B T_K \approx U \sqrt{\frac{\Gamma}{4U}} e^{-\pi U/4\Gamma} \approx 0.1 e^{-10^2 \pi/2} \approx 0. \quad (2.12)$$

It is clear that this result contradicts the experimental value of  $k_B T_K \sim 10$  meV. Hence, we have to exclude the primarily assumed adsorption geometries (Figure 2.6) and define alternative geometries. The prerequisite for possible adsorption geometries is the stronger binding between the molecular complex and the substrate, with strong hybridization that can give a measurable Kondo temperature.

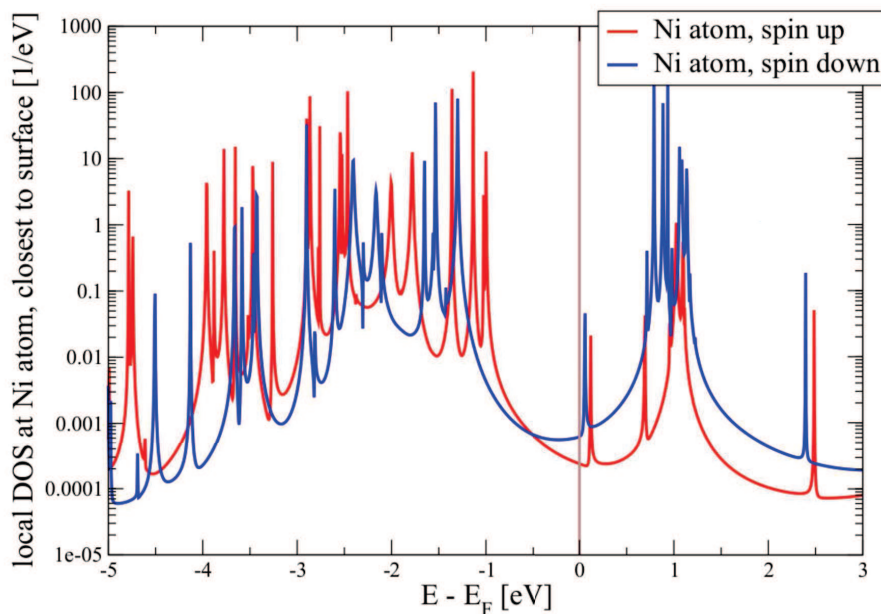


Figure 2.7.: The spectral function projected at the Ni atom which is closest to the surface, for the “standing” Ni<sub>2</sub> complex. The local DOS is shown in a logarithmic scale, while a ferromagnetic coupling of  $S=1$  located in Ni<sup>2+</sup> ions is assumed.

## 2.7. Fragments of Ni<sub>2</sub> Complex on Cu(001)

In our first assumption of a strong bonded configuration, we consider the extreme case of molecular fragmentation 2.9a. Here we assume that bonds between Ni<sup>2+</sup> ion and nitrogen are broken and a Ni(hfacac)<sub>2</sub> moiety is created. Thus, we enforce a much larger coupling of the molecular complex to the substrate through the Ni<sup>2+</sup> ion. In that situation the coupling of the spin to the Cu surface is comparable to the case of single Ni adatom (no ligands attached). Kondo temperatures, in such cases, are expected to be in the order of a tenth of meV, according to earlier experiments, [25,26], in good agreement with the recent measurements [4].

### 2.7.1. Computational Details

For the relaxation of the molecular structure embedded on Cu(001), we have used FHI-aims package [9]. The copper surface has been modeled by finite-size fcc(001) atomic clusters with three atomic layers. The degrees of freedom for the atoms of the molecule and a few copper atoms of the surface layer, in the nearest vicinity of the molecules, were fully relaxed. Relaxation steps were carried out until the residual forces acting on atoms reached values below 0.01 eV/Å. The basis set of numerical atom-centered orbitals used is

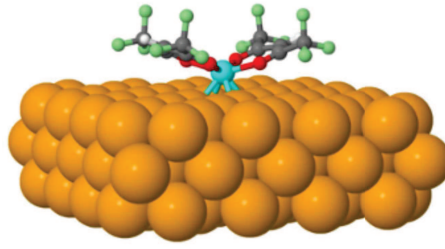


Figure 2.8.:  $\text{Ni}(\text{hfacac})_2$  moiety bound to  $\text{Cu}(001)$  via a Ni atom placed at the hollow site.

the *tier1*. The van der Waals (vdW) dispersive forces have been taken within Tkatchenko-Scheffler model [82]. The spectral functions were calculated using the NEGF method as implemented in AITRANSS [150] interfaced with FHI-aims package [9]. Calculated STM images were approximated by the space-resolved local density of states, according to Tersoff and Hamann [141]. In our simulations, we have used two different methods, following the Tersoff and Hamann approach, as implemented in the AITRANSS package interfaced with TURBOMOLE [8] and in VASP.

In the first method, we employ the Green's function formalism linked to the quantum-chemical cluster calculations [151]. We can further plot a space-resolved spectral function, in the vicinity of the molecular complex, which has been integrated over an energy window of 0.1 eV around the Fermi level. In the second method, we employ the PAW method [99] as implemented in VASP code [98]. In these calculations, we used plane waves with an energy cutoff of 500 eV. A repeated slab model is used to represent the metal surface, where a slab consists of three atomic layers. A vacuum region of 20 Å was inserted between the slabs. To sample the surface Brillouin-zone, a mesh of  $4 \times 4 \times 1$   $\mathbf{k}$  points was used. To represent the van der Waals weak interactions, in this case, we employed the semi-empirical DFT- D2 method, proposed by Grimme [81].

### 2.7.2. Calculated STM images

In order to show that the fragmentation scenario is consistent with the experimental findings, we start by presenting the calculated STM images of the fragmented molecules. The result is shown in Figure 2.9.

The calculated STM images (Figure 2.9) reproduce the most important characteristics of the experimental ones for  $\text{Ni}_2 - \alpha$  (Figure 2.4a). More specifically, the outermost contours have a butterfly shape, two mirror planes exist and the size of the experimental and computational images are consistent.

Furthermore, we estimated the optimal position of the  $\text{Ni}(\text{hfacac})_2$  fragment on  $\text{Cu}(001)$ , with respect to the angle that fixes the orientation of the fragment's mirror planes with respect to the [001] direction of the fcc (001) surface. The results predict a non-zero op-

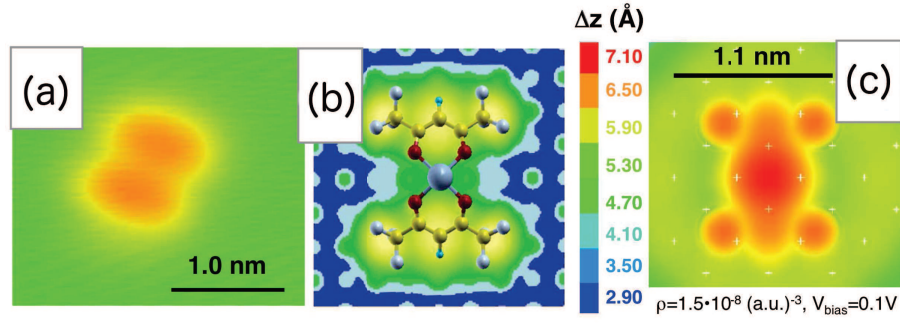


Figure 2.9.: (a) Experimental STM image of Ni<sub>2</sub> –  $\alpha$  configuration (same as in Figure 2.4(a)). The color coding is identical to Figure 2.9(c). (b): Simulated STM image of Ni(hfacac)<sub>2</sub>, computed employing VASP package. (c) Simulated STM image of Ni(hfacac)<sub>2</sub>, computed employing AITRANSS package.

timal angle of 45° for the above orientation (Figure 2.10). A non-zero angle  $\approx 25^\circ$ , is also observed in the representative experimental images of Ni<sub>2</sub> –  $\alpha$ .

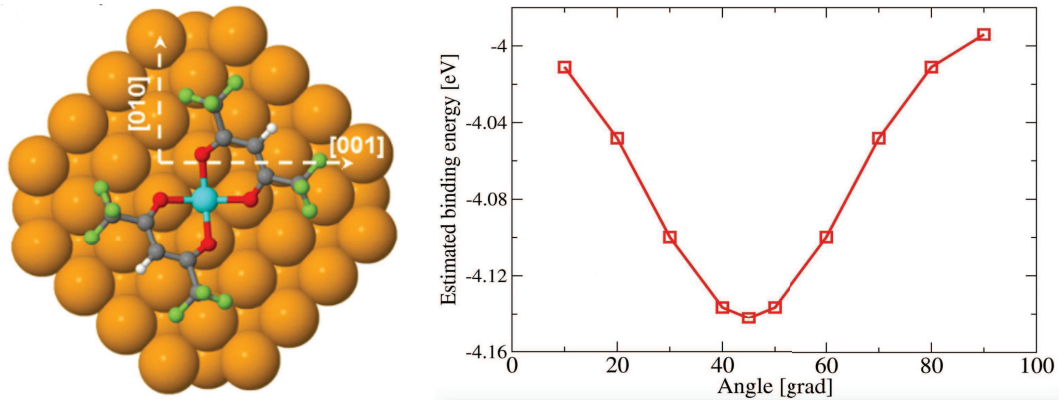


Figure 2.10.: On the left: the optimal position of the Ni(hfacac)<sub>2</sub> fragment on Cu(001). On the right: the estimated dependence of the binding energy of Ni(hfacac)<sub>2</sub> to Cu(001) surface, on the angle that fixes the orientation of the fragment’s mirror planes vs the [001] direction of the fcc (001) surface.

Another detail also reproduced in this configuration is the spatial dependency of the Kondo amplitude. The fragment’s geometry is such that the associated Kondo resonance would have its maximum amplitude with the STM tip located in the center of the image, at the Ni atom. That is consistent with the structure of the spatially resolved Kondo resonance of Ni<sub>2</sub> –  $\alpha$  observed experimentally (Figure 2.4c).

One can still be skeptical about the extreme assumption of the fragmentation of the

$\text{Ni}_2 - \alpha$  complex. However, we should not underestimate the effect of temperature during the adsorption. Experimental STM images characterizing adsorption of  $\text{Ni}_2$  complexes on Cu(001) surface suggest that molecular fragmentation at surface is likely triggered by the temperature. Namely, experimental data reveal that when  $\text{Ni}_2$  complexes are evaporated on the substrates at room temperature, two species,  $\text{Ni}_2 - \alpha$  and  $\text{Ni}_2 - \beta$  are found, while  $\text{Ni}_2 - \alpha$  which we attribute to molecular fragments, is not found after deposition onto pre-cooled substrates (77 K).

Therefore the fragmentation scenario is consistent with the experimental phenomenology. We can now proceed with the goal to understand the molecular magnetism and eventually estimate the Kondo temperature for the  $\text{Ni}(\text{hfacac})_2$  on Cu(001).

### 2.7.3. Kondo Temperature Estimation

We consider the atomic configuration of Ni atom as  $[\text{Ar}]4s^23d^8$ . In the simplified picture of a free  $\text{Ni}(\text{hfacac})_2$  fragment, the  $4s$ -states hybridize so strongly with the ligands, that the  $s$ -electrons are effectively transferred to ligand orbitals. Therefore, the metal ion takes the  $\text{Ni}^{2+}$  configuration and exhibits two unpaired spins. Our DFT results confirm the above picture. We find a spin-polarized ground state with a magnetic moment of  $2\mu_B$ . The magnetization is largely due to two orbitals ( $a$  and  $b$  shown in Figure 2.11), that are populated with up-spin electrons only, and that contribute substantial weight to both Ni  $d_{z^2}$  and  $d_{xy}$  atomic states.

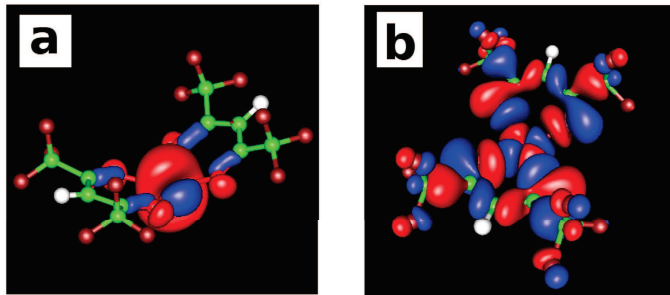


Figure 2.11.: Kohn-Sham wave functions corresponding to Ni  $d_{z^2}$  and  $d_{xy}$  orbitals of the free standing  $\text{Ni}(\text{hfacac})_2$  fragment.

The question to address, is whether the fragment keeps its magnetic moment when adsorbed on the substrate or not. To answer this question, we performed another spin-polarized DFT study. In essence, the substrate further breaks the residual degeneracy of the  $d$ -orbitals splitting  $d_{z^2}$  and  $d_{xy}$  by 1.4 eV. As a result,  $d_{z^2}$  is nearly full (0.4 eV below  $E_F$ ), while  $d_{xy}$  is nearly empty (1 eV above  $E_F$  with resonance  $\Gamma_b \approx 10^{-2}$  eV). The magnetization drops after adsorption by about a factor of two, down to  $1.2 \mu_B$ . The net

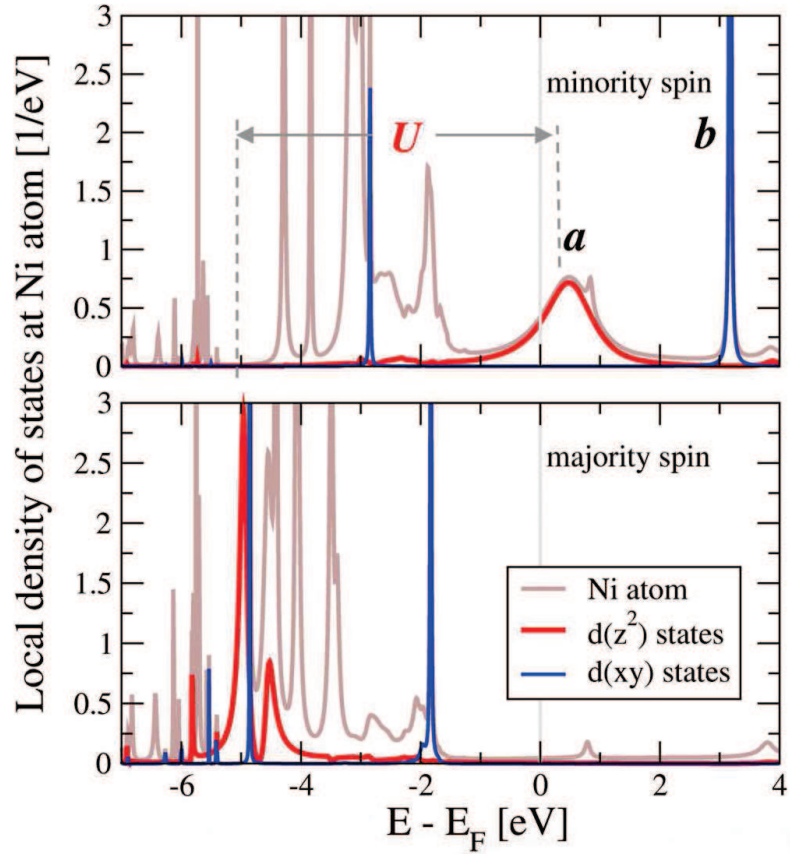


Figure 2.12.: GGA+ $U$  calculated spin dependent local density of states projected on Ni atom of the Ni(hfacac)<sub>2</sub> on Cu(001). Red and blue lines highlight contributions to the LDOS of Ni  $d_{z^2}$  and  $d_{xy}$  orbitals.

electron transfer to the molecule in the adsorption process is 0.4 e.

The GGA-type calculation leaves us with a situation where a localized  $3d_{z^2}$  orbital is only partially occupied. In DFT with conventional local exchange-correlation functionals (LDA, GGA) this is typically an indication of correlation physics, such as the Coulomb blockade [16, 153]. The Coulomb-blockade is not described by conventional DFT-functionals, but it can be captured on the level of GGA+ $U$  [80].

Therefore, we performed a GGA+ $U$  calculation placing a repulsive on-site term with relatively large strength  $U=6$  eV on the metal site. The interaction shifts the spin-down resonance  $\alpha$  from 0.4 eV below to 0.5 eV above  $E_F$ . Hence, the magnetic moment increases up to  $1.62 \mu_B$  thus suggesting the picture of the  $S=1$  Kondo effect.

So far we have ignored the spatial structure of the two molecular orbitals involved, orbital

$a$  with substantial contribution from Ni  $d_{z^2}$  atomic state, and orbital  $b$  with substantial contribution from Ni  $d_{xy}$  atomic state. As can be seen in Figure 2.11, the  $a$  orbital (first quantum dot,  $\Gamma_a$ ) is directed towards the surface. Hence, it hybridizes with the substrate much stronger than the  $b$  orbital (second dot  $\Gamma_b$ ). This means that  $\Gamma_b \ll \Gamma_a$  which is interpreted in the LDOS of Ni as a wider resonance for the  $a$  orbital (Figure 2.12). Each level has a single occupancy and the electrons populating them are coupled ferromagnetically. Note that the exchange interaction is around 0.5 eV (see Table 2.2), which is much larger compared to the expected Kondo energy scale around 10 K. In this case, both spins form a triplet,  $S=1$ . Reading parameters from the spectral function

$$\Gamma_a \simeq 0.8eV \gg \Gamma_b; \epsilon_d \simeq 0.5eV; U \simeq 5.5eV \gg \epsilon_d, \quad (2.13)$$

and modifying slightly the formula for the Kondo temperature in equation 2.4 for the case of double-dot system, we have:

$$k_B T_K \simeq 0.41U \sqrt{\frac{\Gamma^*}{4U}} e^{-\pi\epsilon_d/\Gamma}, \quad (2.14)$$

where  $U \gg \epsilon_d$  and  $\Gamma^* = \Gamma_a/2$ .

Hence, we obtain  $k_B T_K \simeq 5.84 \times 10^{-3}$  eV. This gives us a Kondo temperature  $T_K \simeq 70$  K. Such a result is in qualitative agreement with the experiment.

We emphasize that a more precise estimation of the Kondo-temperature is extremely difficult due to the exponential dependence of  $T_K$  on the model parameters. If, for example, we take into account that DFT has a tendency to overestimate resonance line-widths, we may assume a slightly smaller  $\Gamma_a \simeq 0.6$  eV. This reduces  $T_K$  down to approximately 16 K, which is in good agreement with the experimentally observed value.

## 2.8. Distorted Ni<sub>2</sub> Complex on Cu(001)

The existence of the Ni<sub>2</sub> -  $\beta$  images in experiments suggests that also a molecular complex with two Ni ions are expected to be found on the Cu surface. To rationalize this observation, we tried to find an intact but strongly distorted molecular configuration by means of DFT methodology. The distortion has to be such that the molecule establishes a chemical bond to the Cu(001) surface. Such a strong hybridization is an important prerequisite for observable Kondo temperatures. We assume this bond to be realized via the delocalized  $\pi$  orbitals of the central bpym unit overlapping with the electron density extending from the surface.

### 2.8.1. Computational Details

As before, we used FHI-aims package [9] for the relaxation of the molecular structure embedded on Cu(001). The copper surface has been modeled by finite-size fcc(001) atomic

clusters with two atomic layers. Similarly to the previous study, the molecular atomic coordinates and a few copper atoms of the surface layer were fully relaxed. Relaxation was stopped with the residual forces acting on atoms reached values being below 0.01 eV/Å.

We mention that even for the modern *ab initio* methods, finding the relaxed ground-state structure of a large organic molecule, such as the Ni<sub>2</sub> complex, on a surface, is a nontrivial procedure. Due to the many atomic degrees of freedom involved, relaxation can end up in different molecular configurations with energies differing by only 100 meV, as was shown by simulations. To be specific in the following discussion, we focus on two representative but slightly different configurations of “distorted” Ni<sub>2</sub> complex, shown in Figure 2.13.

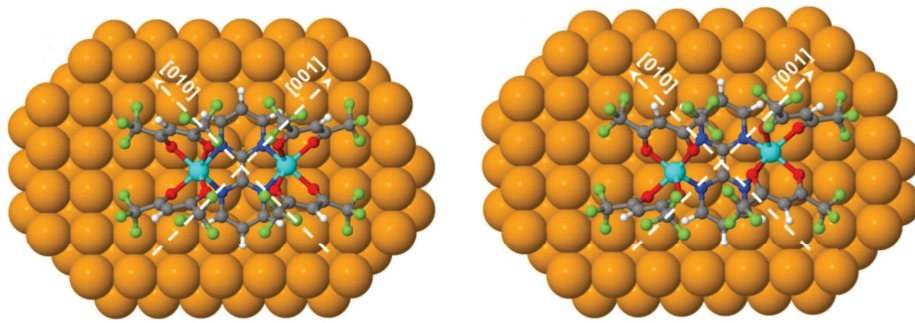


Figure 2.13.: Graphical representations of the two “distorted” molecular configurations of Ni<sub>2</sub> complex adsorbed on Cu(001). The binding between the molecule and the substrate takes place via the central bpym unit. (a) shows the almost symmetric  $C_{2v}$ -type structure with two mirror planes of the complex rotated by  $45^\circ$  relative to fcc [001] and [010] directions, (b) shows the corresponding structure with broken local symmetry which is energetically more stable.

The first atomic structure of the complex has an approximate  $C_{2v}$  symmetry, in registry with the underlying Cu(001) surface. Further relaxation steps result in an energy gain of about 0.25 eV. Then, the local symmetry of the molecular complex is broken resulting in the second configuration. Both configurations are shown in Figure 2.13.

The spectral functions were calculated using the NEGF method as implemented in AITRANSS [150] interfaced with FHI-aims package [9]. Calculated STM images were approximated according to Tersoff and Hamann method [141], as implemented in the AITRANSS package [150] interfaced with TURBOMOLE [8] and in VASP [98]. Within FHI-aims, the van der Waals (vdW) dispersion forces have been taken into account within Tkatchenko-Scheffler model [82]. Within VASP calculations, vdW corrections were added according to Grimme’s semi-empirical DFT- D2 method [81].

### 2.8.2. Calculated STM images

For the first configuration, shown in Figure 2.13, the simulated STM image of the complex reveals a “crosslike” structure (Figures 2.14(c) and 2.14(e)), resembling  $\text{Ni}_2 - \beta$  experimental images, shown in Figure 2.14(a). For the second “distorted”  $\text{Ni}_2$  complex adsorption structure, the former STM images are transformed to the ones with broken symmetry (Figures 2.14(d) and 2.14(f)), which were also experimentally observed 2.14(b).

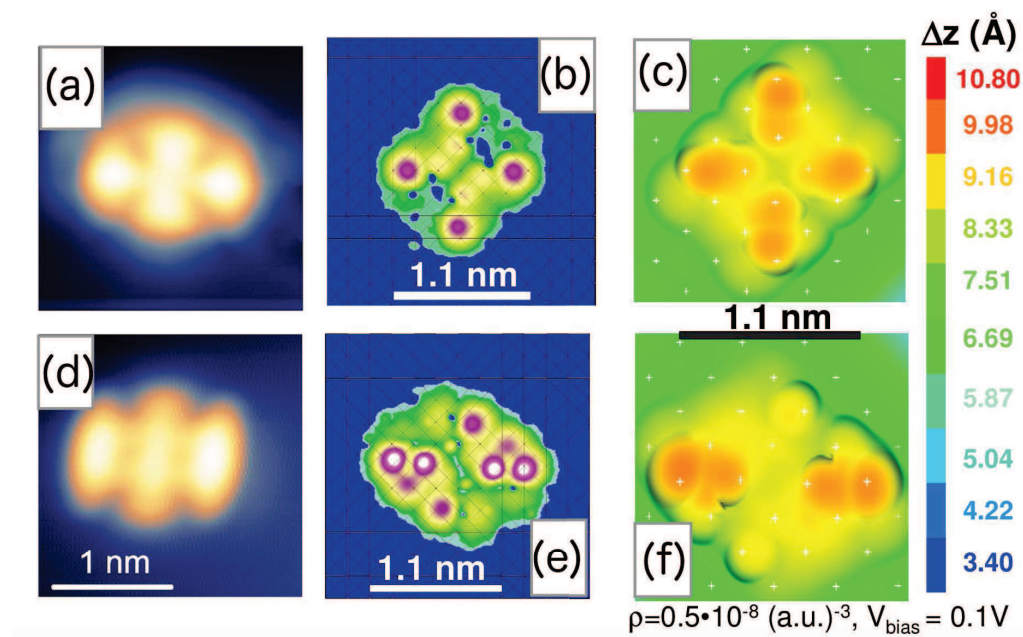


Figure 2.14.: (a) Experimental STM image for the first configuration of  $\text{Ni}_2 - \beta$ . (b) The corresponding simulated STM image for the first configuration of  $\text{Ni}_2 - \beta$ , computed employing VASP package. (c) Simulated STM image of the first configuration of  $\text{Ni}_2 - \beta$ , computed employing AITRANSS package. (d), (e), (f) calculated STM images of the “distorted”  $\text{Ni}_2 - \beta$  compared to experiment.

Once more, the phenomenology of our simulations agrees with the experimental data and we can proceed to a more detailed spin-dependent DFT analysis to get an estimation for the Kondo temperature.

### 2.8.3. Kondo Temperature Estimation

Our calculations indicate that a fractional charge of approximately 0.5 e leaks out from the surface to the molecule, populating partially the LUMO of the  $\text{Ni}_2$  complex and the LUMO\* of the bpym moiety. Also, a magnetic moment carried by the complex is slightly reduced, compared to the gas-phase molecule, from  $4.0 \mu_B$  to  $3.3 \mu_B$ .

Table 2.3.: DFT calculated relative energies of the low-energy spin configurations realized in Ni<sub>2</sub> complexes. Considered molecules are: (i) gas-phase relaxed Ni<sub>2</sub> complex, with Ni<sup>2+</sup> ions found in distorted octahedral environment, (ii) free but distorted Ni<sub>2</sub> complex, where local  $C_{2v}$  symmetry is kept, (iii) free but distorted Ni<sub>2</sub> complex, where symmetry constraint is released. The two latter molecules were first relaxed on top of Cu(001). Last column refers to magnetically excited zero-spin state at one of the Ni<sup>2+</sup> ions.

		AF: $\uparrow\uparrow\downarrow\downarrow$	F: $\uparrow\uparrow\uparrow\uparrow$	$\uparrow\uparrow\downarrow\downarrow$
(i) relaxed Ni <sub>2</sub> complex	fhi-aims	0.000 eV	15.8 meV	0.500 eV
	turbomole	0.000 eV	14.9 meV	0.522 eV
(ii) distorted Ni <sub>2</sub> complex with two symmetry planes	fhi-aims	0.000 eV	6.9 meV	0.396 eV
	turbomole	0.000 eV	6.1 meV	0.390 eV
(iii) distorted Ni <sub>2</sub> complex	fhi-aims	0.000 eV	2.5 meV	0.456 eV
	turbomole	0.000 eV	1.9 meV	0.361 eV

The structure of the binuclear complex suggests that the molecular spins should reside on the Ni(hfacac)<sub>2</sub> units, where each unit could accept two unpaired electrons owing to [Ar]3d<sup>8</sup> electronic configuration of the Ni<sup>2+</sup> ion. Each unpaired electron subsystem is referred to as  $S=1$ . The two  $S=1$  subsystems are magnetically nearly decoupled, due to their weak indirect interaction via the  $\pi$  orbitals of the bpym unit. Thus, we anticipate that each subsystem will develop a Kondo effect, independently of the other, as the molecular complex provides two parallel conduction paths for the tunneling electron, one for each spin.

We confirmed these expectations by performing constrained DFT calculations. The results are shown in Table 2.3 where the relative energies of the low-energy spin configurations are presented for three different gas-phase Ni<sub>2</sub> complexes. These results are for the Ni<sup>2+</sup> complexes in the gas-phase, with Ni<sup>2+</sup> ions found in distorted octahedral environment. For the first configuration of the “distorted” Ni<sub>2</sub> complex, the local  $C_{2v}$  symmetry has been kept, but the Cu(001) substrate has been removed, and for the second “distorted” Ni<sub>2</sub> complex, the symmetry constraint has been released. This calculation predicts a “singlet” ground state with antiferromagnetically (AFM) coupled  $S=1$  spins. For the distorted Ni<sub>2</sub> complex, the state with ferromagnetically (FM) coupled  $S=1$  spins is approximately 2 meV above the AFM state.

If we consider FM coupling between  $S=1$  subsystems, the frontier molecular orbitals (see Figure 2.15) carry unpaired spins confirming the above picture. Two out of four orbitals,  $a$  and  $b$ , are primarily localized on the left-hand side of the Ni<sub>2</sub> complex, while their counterparts,  $a'$  and  $b'$ , are localized on the right-hand side. When the Ni<sub>2</sub> complex

is brought in contact with the Cu surface, these molecular orbitals are transformed to resonances ( $a, b, a', b'$ ) in the spectral function centered around  $-1.5$  eV below the Fermi level  $E_F$ , while the upper Hubbard band ( $\epsilon_d$ ) is placed just above  $E_F$ . Furthermore, since the wave functions  $a$  and  $a'$  involve larger contributions from  $\pi$  orbitals of the central bpym unit, the corresponding resonances  $\alpha$  and  $\alpha'$  are much broader than the  $b$  and  $b'$  ones, Figure 2.16.

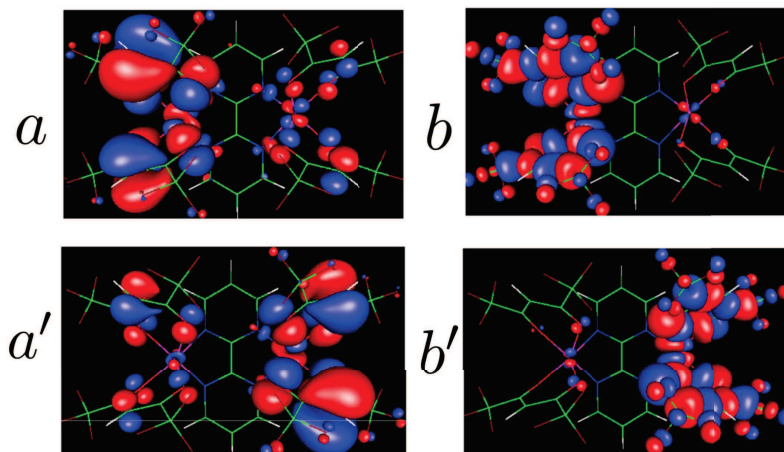


Figure 2.15.: Wave functions of  $a, b, a', b'$  orbitals, which contribute to the LDOS projected on the Ni atom of the distorted  $\text{Ni}_2$  complex, as presented in Figure 2.16.  $a$  and  $b$  orbitals are localized on the “left-hand” side, while  $a'$  and  $b'$  are localized on the “right-hand” side of the molecular complex.

The AFM singlet ground state of the system, would be incompatible with the Kondo effect, unless we assume that the weak AFM coupling between the two subsystems is below the Kondo temperature,  $J_{AF}=(E_{AF}-E_F)/2 \simeq 12 \text{ K} \leq T_K$ . Under this assumption, each subsystem will undergo Kondo screening by the conduction electron of Cu(001) independently of the other, below the Kondo temperature.

We now use the modified Anderson equation 2.14, where  $U \gg \epsilon_d$  and read the parameters from the computed spectral function (Figure 2.16). Hence, we get

$$\begin{aligned} 2\Gamma^* &= \Gamma_{\alpha,\alpha'} \simeq 0.1\text{eV} \gg \Gamma_{b,b'} \\ \epsilon_d &\sim 0.06 - 0.125\text{eV}, U \simeq 1.5\text{eV} \gg \epsilon_d, \end{aligned} \quad (2.15)$$

and we can estimate the Kondo temperature as  $T_K \sim 0.4 - 20 \text{ K}$ . The upper limit is taken above  $J_{AF}$  and is in the range of experimental values.

## 2.9. Conclusions

In conclusion, in this chapter, we presented a thorough DFT study of binuclear metal-organic complexes deposited on a Cu(001) surface. Our target was to explain the low-temperature STS measurements which revealed that the systems undergo the Kondo effect with the Kondo resonances located in the transition-metal atoms. The STM and STS data were found to be adsorption-type dependent and the Kondo temperatures in the order of 10 K.

We managed to rationalize the experimental observations by assuming appropriate adsorption geometries, where the molecules could be strongly hybridized with the substrate. Namely, we attributed the first set of STM images and STS data to molecular fragments and the second to a distorted complex with partially weakened internal chemical bonds.

In both cases, our calculations showed that an  $S=1$  Kondo effect is emerging from the open  $3d$  shells of the individual  $\text{Ni}^{2+}$  ions. Using the appropriate Anderson model formula for the  $S=1$  Kondo effect and reading parameters from the local density of states projected on the Ni atoms, we managed to estimate Kondo temperatures in the same order of magnitude as the experimentally measured ones.

In general, binuclear complexes form a great candidate for studying fundamental aspects of magnetic double impurity or double quantum dot systems. Furthermore, understanding the interaction between the spins located in different functional units is very important in the field of spintronics for quantum information storage and processing with molecules adsorbed on surfaces.

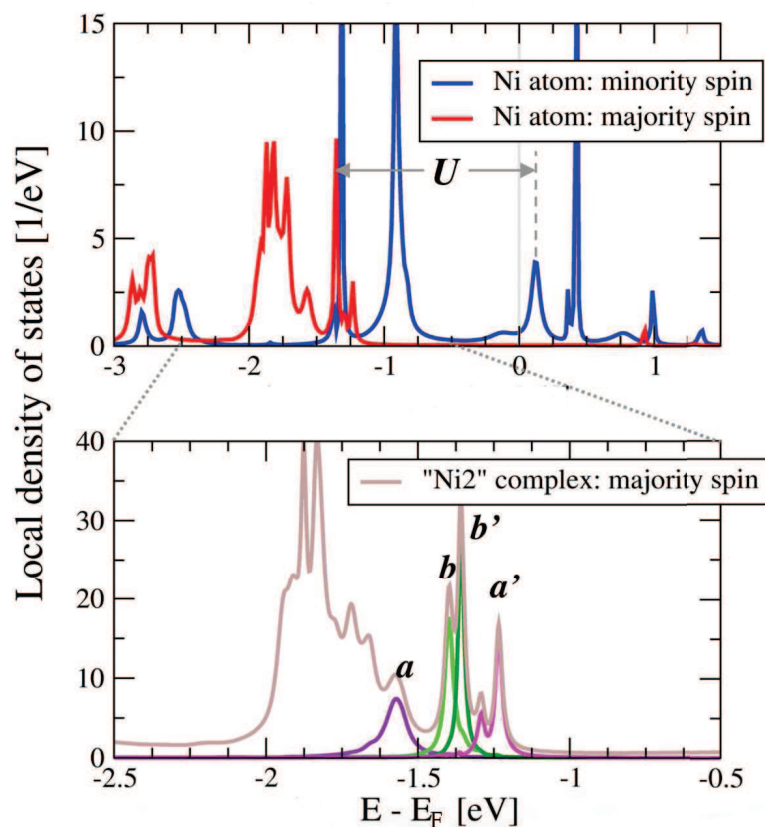


Figure 2.16.: Calculated DFT spin-dependent local density of states projected on one of Ni atoms of the distorted  $\text{Ni}_2$  complexes adsorbed on  $\text{Cu}(001)$ . The zoomed in plot shows the majority up-spin spectral function below the Fermi level, where contributions are highlighted arising from four orbitals ( $a$ ,  $b$ ,  $a'$ ,  $b'$ ). Each orbital is carrying one unpaired spin. The corresponding wave functions are presented in Figure 2.15.

# Study Of Linear Oligoacenes 3

---

## 3.1. Introduction

In this chapter we will study the behavior of the HOMO-LUMO gaps of various oligoacene molecules. Oligoacenes are linear polycyclic hydrocarbons consisting of a repeated benzene ring unit (Figure 3.1). They exhibit profound mechanical flexibility and ability to harvest light [36–38]. They also form ideal examples of quantum wires and the simplest realisation of the so-called nanographene. For details about the actual research and applications on graphene and nanographene, there are numerous reviews and publications, see for example [154–156].

Oligoacenes form ideal candidates for several applications in organic electronics [39–41]. From the theoretical point of view, the physical properties of oligoacenes have attracted much attention for many years [157–160]. However, up to now most theoretical studies about their energy gaps were limited to relatively small chains, usually up to pentacene, with five repeated benzene-type rings.

In the following we present a complete inspection of the HOMO-LUMO gaps of oligoacene chains in the gas phase but also when they are adsorbed on a metallic surface of Au(111) and on an insulator such as SiO<sub>2</sub>. The latter study is important because the interaction of the molecule with a substrate is a prerequisite for any technological application.

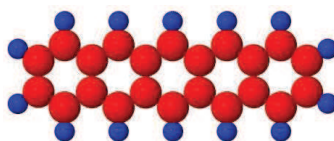


Figure 3.1.: Oligoacene molecule, consisting of a repeating benzene unit. As an example the molecule of pentacene is shown (N=5 benzene rings). The hydrogen atoms are blue and the carbon red.

## 3.2. Gas Phase Oligoacenes

Using common sense, one expects that the band gap of a molecular wire approaches a constant if the infinite chain is a band insulator, or vanishes if it is a metal. In the latter case, the metallic behavior is demonstrated by a single, partially filled band that crosses the Fermi energy. Then, the gaps of finite-length chains tend to zero as  $1/N$ , where  $N$  is the number of fused units. The  $1/N$  behavior reminds us of the level spacing of the particle-in-a-box model, where the energy levels are given by:

$$E_n = \frac{n^2 \hbar^2 \pi^2}{2mL}, \quad (3.1)$$

where  $m$  is the mass and  $L$  the molecular length.

Therefore, the expecting behavior of the energy gap as a function of the molecular length is a monotonous decay. In this chapter we present the study of the band gaps of oligoacenes versus their length using Kohn-Sham (KS) density functional methods (DFT) and the post-DFT,  $G_0W_0$  method, to show that this simple expectation is untrue. In fact, we will show that the band gap will oscillate as a function of the molecular size.

### 3.2.1. Computational Details

For the DFT results presented in this work, the Fhi-aims package [9] and the PBE functional [78] were implemented. The spin-restricted (closed shell) Kohn-Sham equations are solved in the non-relativistic form. Relativity is included *a posteriori* by rescaling the Hamiltonian eigenlevels, according to the zeroth order regular approximation [161]. The basis set used is the *tier2* [9]. For non-periodic calculations, the ground state was reached with strict convergence criteria for the difference in electron density change,  $10^{-6}$ , for the total energy  $10^{-6}$  eV/Å<sup>3</sup> and for forces,  $10^{-5}$  eV Å<sup>-1</sup>. Geometries were considered optimized only after the maximum residual force dropped below  $10^{-3}$  eV Å<sup>-1</sup>.

For the DFT band structure, quasiparticle (QP) band structure and QP spectra of finite chains, we used Vienna Ab initio Simulation Package (VASP) [98]. The one-electron orbitals are expressed using the projector augmented wave basis set (PAW) [99]. In these calculations, we used plane waves with 400 eV energy cutoff for the DFT starting calculation, and a cutoff of 300 eV for the response functions. First, standard Kohn-Sham DFT calculations were performed, using the PBE exchange-correlation functional [78], with a mesh of  $100 \times 1 \times 1$   $\mathbf{k}$  points in the Brillouin zone. Then, QP corrections were included on top of the Kohn-Sham states at the non-self-consistent, single-shot,  $G_0W_0$  level. After convergence checks, a frequency grid of 80 points and 600 bands in total were used. The QP energies were represented on a mesh of 11  $\mathbf{k}$  points in the Brillouin zone.

### 3.2.2. Density Functional Theory Calculations

The DFT calculations for the HOMO-LUMO gaps (Figures 3.2 and ) were performed by Richard Korytár and are presented in this manuscript for purposes of completeness. The energy band gap calculated within DFT, using a PBE functional, is shown in Figure 3.2a for oligoacenes. Contrary to held beliefs, what we observe, is the oscillation of the energy band gap as a function of the number of benzene-type rings.

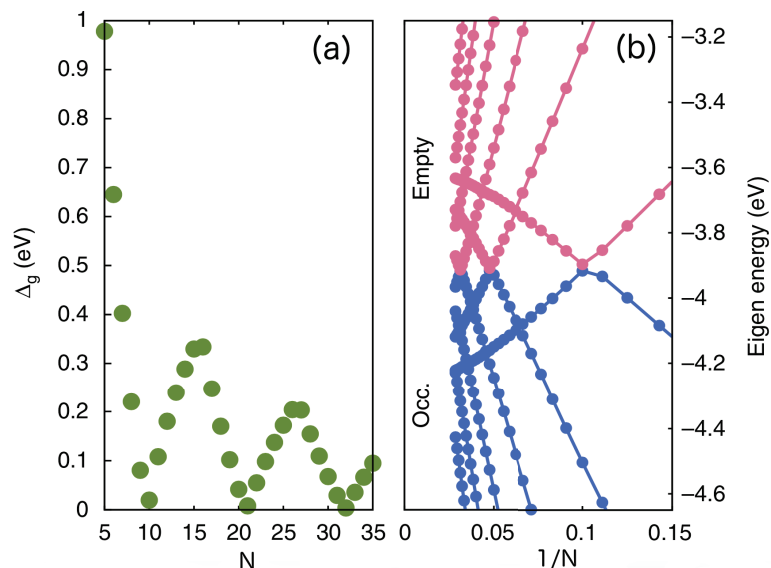


Figure 3.2.: From left to right the HOMO-LUMO gap,  $\Delta_g$ , of oligoacenes with respect to the number of rings  $N$ , calculated within DFT and the orbital energies as a function of  $1/N$ . The occupied orbitals are presented in blue, while the unoccupied are in red. Notice the repeating interchange of orbitals as the number of rings increases. The Figure was done by Richard Korytár, Ref. [5].

The gap  $\Delta_g$  drops quickly to zero for the first 10 oligoacenes, but then rises again, and drops repeatedly, with a period of 11. Figure 3.2b presents the orbital energies as a function of  $1/N$ . As the number of rings increases, a repeating interchange of orbitals occurs. This observation gives the possibility to tailor the gaps of these molecules by changing their length. Notice also that molecules with similar excitation gaps can have very different lengths. To understand the origin of these oscillations further analysis is required. To understand the gap oscillations, we first invoke the DFT calculated band structure of the infinite molecular chain, called polyacene, Figure 3.3.

As we pass from the  $\Gamma$  point to the edge of the first Brillouin zone we encounter a crossing of the conduction and the valence bands, at  $\mathbf{k}$  point,  $k_D=0.9102 \pi/a$ . This band crossing is reminiscent of the Dirac cones in graphene. Such peculiar band structure of polyacene wires was first discussed by Kivelson and Chapman [48] based on an analysis

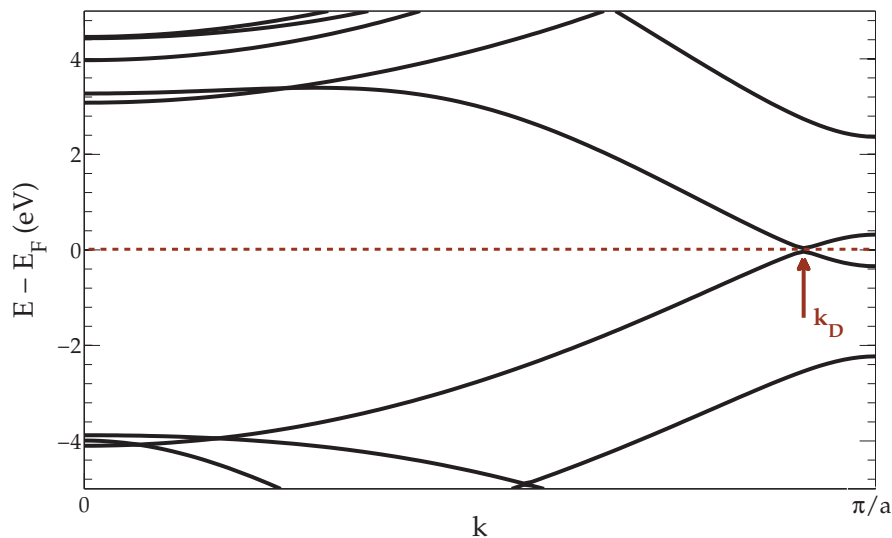


Figure 3.3.: DFT calculated band structure of polyacene (infinite molecular chain). The valence and the conduction bands cross at  $k_D = 0.9102 \pi/a$ , close to the Brillouin zone border, where  $a = 2.462 \text{ \AA}$  is the unit cell length.

of a tight-binding Hamiltonian with up to third nearest neighbor hopping and predicted a possible non-avoided band crossing.

### 3.2.3. Zone Folding

To understand the appearance of such oscillations, let us focus on sufficiently long oligoacenes. In this case, we should be able to derive their spectrum from the polyacene band structure by imposing selection rules for wave numbers due to hard-wall boundary conditions, a method known as zone folding.

For a given number of rings,  $N$ , only selected wave numbers are allowed. We can choose the set of selection rules that applies to a guitar string with length  $a(N+1)$ . The rule reads

$$k_m^N = \frac{m}{N+1} \frac{\pi}{a}, \quad m = 1, \dots, N, \quad (3.2)$$

where  $a$  is the length of one ring. We show examples of this approach in Figure 3.4, Figure 3.5 and Figure 3.6 for 9, 10 and 11 rings, respectively.

We denote the energy band gap as  $E_g(k) = \epsilon_c(k) - \epsilon_v(k)$ , where  $\epsilon_c$  and  $\epsilon_v$  are respectively the conduction and the valence band energies. The gap  $\Delta_g^N$  is given approximately by the

energy  $E_g(\bar{k}^{(N)})$ , with  $\bar{k}^{(N)}$  the wave number from the allowed set, that is closest to the Dirac point,  $k_D$ . Therefore,  $\bar{k}^{(N)}$  labels the HOMO/LUMO pair.

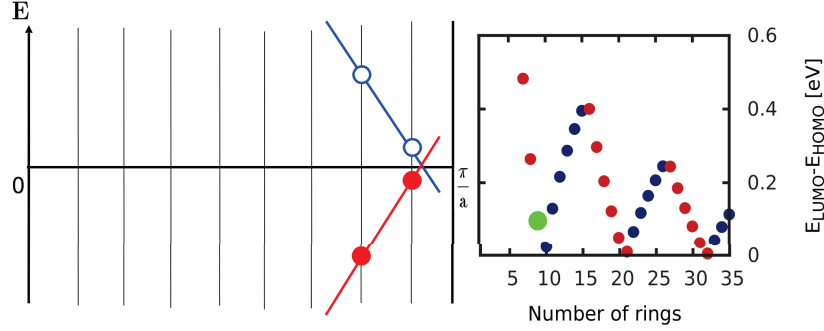


Figure 3.4.: Zone folding for oligoacene with 9 rings. According to the rule, allowed wave numbers are given according to Eq. 3.2. Hence, the Brillouin zone is divided with 9 lines. The energy band gap is given as the difference between the energy of conduction band minus the corresponding energy of the valence band, closest to the crossing point. The value of this difference is shown as a green dot in the right graph.

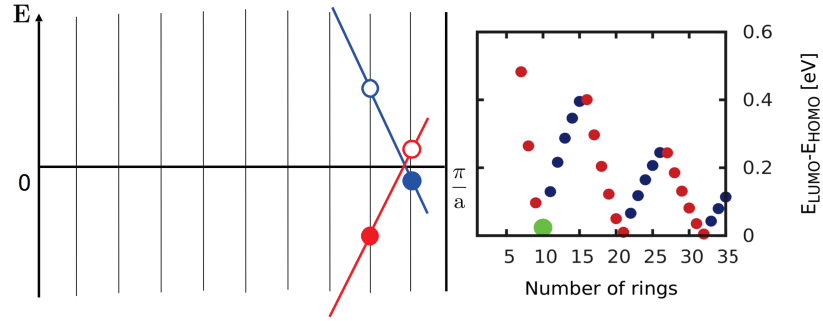


Figure 3.5.: The same as 3.4 but for 10 rings. At this point, the conduction and the valence bands interchange and the energy band gap reaches its minimum (green dot to the right).

As one increases the number of rings,  $\bar{k}^{(N)}$  will move and eventually cross the Dirac point, where the HOMO and LUMO interchange. This fact gives an explanation for the periodicity of the gap oscillations of oligoacenes.

This band gap is controlled by the position of the Dirac cone in the Brillouin zone. The period should be then inversely proportional to the distance from the zone boundary,  $\pi/a - k_D$ . The maxima of the gap occurs when the Dirac point lies in the middle between two consecutive wave numbers from the allowed set. If a local maximum occurs at  $N_0$  with value  $\Delta_g^{N_0}$ , its upper bound must be  $\hbar v_F \pi / a / (N_0 + 1)$ , where  $v_F$  is the Fermi velocity.

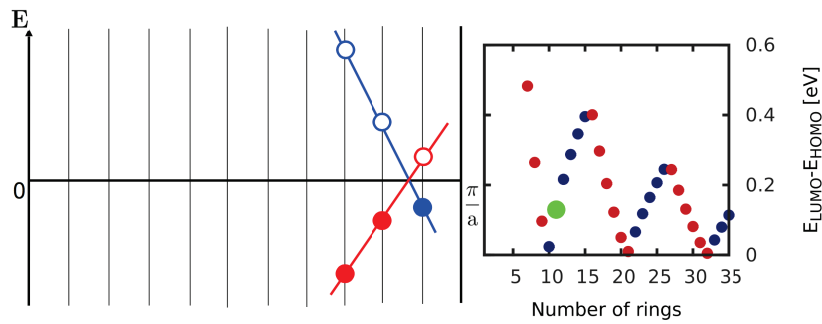


Figure 3.6.: The same as 3.4 but for 11 rings. In this case the conduction and the valence bands have already interchanged and the energy band gap starts to increase (green dot to the right).

Numerically we have within DFT  $v_F \pi/a = 6.485$  eV.

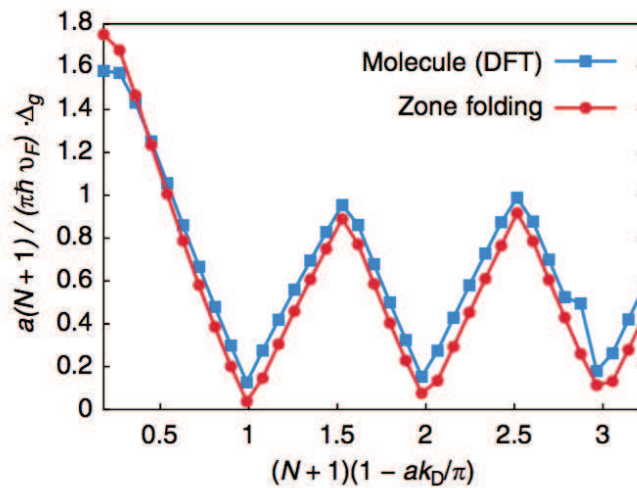


Figure 3.7.: DFT calculated band gaps of oligoacenes in natural units compared to the zone folding results. The gap energies are divided by the factor  $\pi \hbar v_F/(N+1)/a$ . The horizontal axis is rescaled by the reciprocal space distance of the Dirac point to the zone border. Blue squares are calculated for a set of geometry-optimized molecules from DFT, whereas the red circles are given from the Bloch bands of the infinite chain by Brillouin zone folding. The Figure is taken from Ref. [5].

In Figure 3.7, in blue, we show the gap  $\Delta_g^{(N)}$  obtained from DFT, expressed in natural units. In the same plot we show the gaps reconstructed from zone folding,  $E_g(\bar{k}^{(N)})$ , in red. The agreement of the zone folding with the DFT results is excellent. Naively, corrections of the order of  $1/N$  to the zone-folding procedure should be expected. However, for benzene the deviation is only 11%. Similarly, we get a correction of 1% for tetracene and 8% for hexacene. We should emphasize that the DFT molecular gaps  $\Delta_g^{(N)}$ , shown in Figure 3.7, already involve relaxation effects. Notice that  $\Delta_g^{(N)}$  is always higher than  $E_g(\bar{k}^{(N)})$  for  $N > 4$ . This is due to the relaxation effects that compress the length of the rings at molecule's edges. When the total length shrinks, the gap increases, because the level spacing increases.

Hence, we have seen that at the DFT-level the band structure effects control the excitation gaps of oligoacenes. We continue with a comparison of the DFT predictions with post-DFT or hybrid methods to show the robustness of the results.

### 3.2.4. $G_0W_0$ Calculations

In DFT, there is not an analog of the Koopmans' theorem [85], stating that the first ionization energy of a molecular system is equal to the negative of the HOMO energy. However, experiment shows that the differences between the KS single particle energies can be interpreted as physical excitation energies, and often the results can be compared to experimental results, although underestimated in most cases. Within DFT, the ionization potential  $I$  agrees with the highest occupied molecular orbital (HOMO) energy of the charge-neutral molecule with  $N_{\text{el}}$  electrons as  $I = -\epsilon_{\text{HOMO}}(N_{\text{el}})$ . However, the corresponding electron affinity of the system,  $A$ , is obtained from a reference calculation by adding one electron to the system,  $A = -\epsilon_{\text{HOMO}}(N_{\text{el}} + 1)$ .

A method that is widely used to improve upon DFT's outcome for the ionization potential and the electron affinity, is the  $GW$  method [51], [92]. In the following we use the less computationally demanding,  $G_0W_0$  method, where only one iteration over the Green function and the screened Coulomb interaction is taken into account.

In contrast to DFT, in  $G_0W_0$ , the energies of charged excitations are already incorporated in the QP energies. The question we want to answer is whether the ionization energies and electron affinities also inherit the oscillatory behavior of the Dirac cone. The answer is not trivial since post-DFT methods can deviate significantly from the DFT results and correct any artifacts of approximate exchange-correlation functionals [2], [59].

We employ the  $G_0W_0$  method for the infinite chain of polyacene and we extract the corresponding band structure, which is presented in Figure 3.8 compared with its PBE counterpart. The band pattern shown within  $G_0W_0$  is very similar to the PBE result. To find the crossing point we can inspect the symmetry of the four Bloch states around the

crossing point, as shown in Figure 3.9.

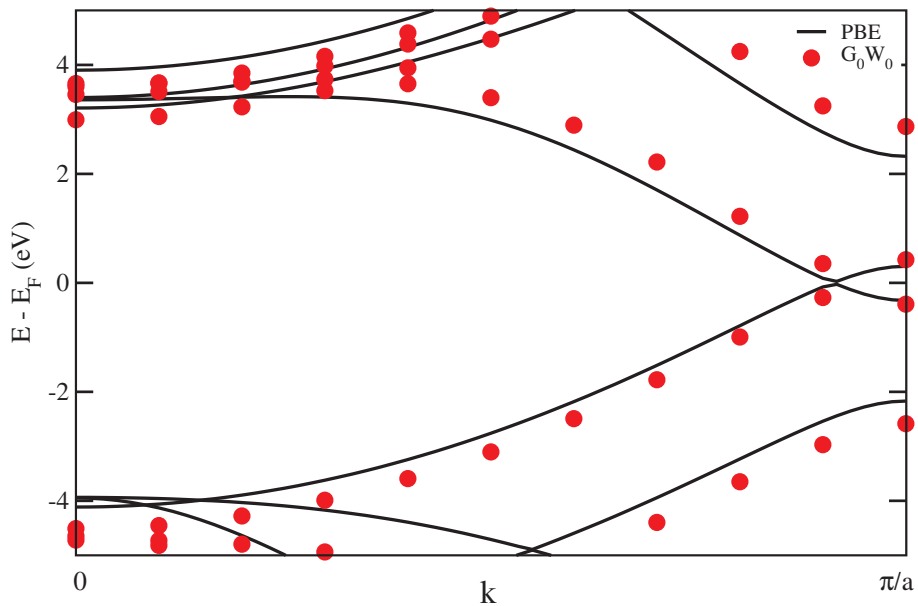


Figure 3.8.:  $G_0W_0$  band structure of polyacene infinite chain compared to that obtained using PBE. Going from the  $\Gamma$ -point through the corner of the first Brillouin zone, a crossing of the valence and the conduction bands occurs, at  $k$ -point,  $k_D=0.89\pi/a$ .

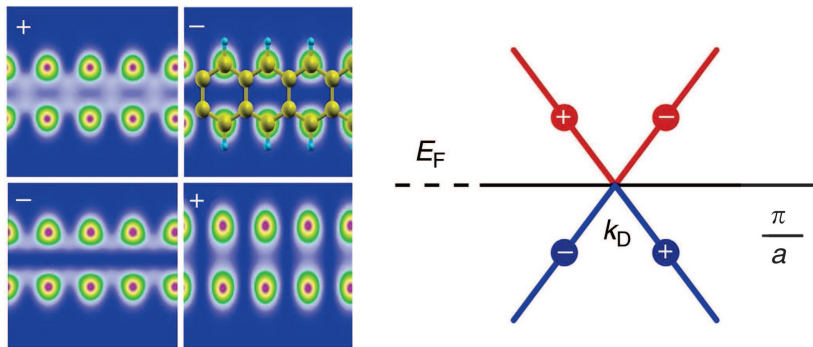


Figure 3.9.: Charge density at  $k$  points located around the crossing point of the bands,  $k_D$ . The valence band that is increasing in energy, has an odd symmetry, whereas the conduction, decreasing band, has an even symmetry along the molecular axis.

In Figure 3.9, the charge density at the four  $\mathbf{k}$  points around the crossing point,  $k_D$  is shown. We observe that the QP band whose energy grows with  $k$  has a nodal plane along the long molecular axis and we indicate it with the minus sign, denoting odd symmetry. The other two states of the band decreasing with energy, lack this nodal plane, so they have an even symmetry, noted with the plus sign. Such a distinct symmetry of the QP bands around the Fermi energy provides evidence of band crossing within  $G_0W_0$ . Therefore, we expect the charged excitations to support oscillations analogous to the ones already observed within PBE.

Table 3.1.: Comparison of the band crossing wave number,  $k_D$ , the Fermi velocity,  $v_F$  and the oscillation period, as computed within DFT and  $G_0W_0$ .

	PBE	$G_0W_0$	Units
Wave number	0.9102	0.9356	$\pi/a$
Fermi velocity	6.485	8.3883	$(a/\pi\hbar)$ eV
Oscillation period	11.14	15.533	rings

The parameters of the Dirac cone, estimated from  $G_0W_0$ , are compared to the results derived from DFT, in Table 3.1. We observe the increase in the wave number within  $G_0W_0$  compared with the one within DFT, by approximately 2.8%. This change leads to an increase in the Fermi velocity and the oscillation period expected, within  $G_0W_0$ , from 11 to 15 rings.

### 3.2.5. PBE0 Functional Calculations

If we ignore the effects of the derivative discontinuity in DFT [162], we can introduce the LUMO energy within DFT not by  $\epsilon_{\text{HOMO}}(N_{\text{el}}+1)$ , but by  $\epsilon_{\text{LUMO}}(N_{\text{el}})$ . Figure 3.10 shows the behavior of the HOMO (red filled) and LUMO (open circle) energies within PBE with respect to the oligoacene length and is compared with PBE0 (triangles),  $G_0W_0$  (diamonds) and the Brillouin zone folding counterparts (solid lines). Note that the quantities presented in Figure 3.10 are dimensionless. We achieve this by replacing the number of rings  $N$  by a dimensionless number  $\xi = (N + 1)(1 - ak_D/\pi)$ . Hence, the zone folding will predict gap minima at integer  $\xi$ . The orbital energies  $E_{\text{HOMO/LUMO}}$  are then represented by the dimensionless quantity:

$$\epsilon_{\text{HOMO/LUMO}} = \frac{a(N + 1)}{\pi\hbar v_F} [E_{\text{HOMO/LUMO}} - E_F], \quad (3.3)$$

where  $E_F$ ,  $v_F$ ,  $a$ ,  $k_D$  are, respectively, the Fermi level, the Fermi velocity, the length of one ring and the crossing point. Note that the frontier orbitals cross near  $\xi = 1$  with increasing number of rings, linearly.

The calculated PBE0 HOMO and LUMO energies are shown in Figure 3.10 with filled and open green symbols respectively. As presented in the first chapter, PBE0 is a hybrid density functional where a certain fraction  $\lambda$  of the PBE exchange is replaced by an exact Hartree-Fock (HF) exact exchange. In this study we consider the conventional version of PBE0 with  $\lambda = 25\%$ . Therefore, the PBE derivative discontinuity is partially restored. The PBE0 results deviate significantly from the PBE calculated energies. This difference is due to the finite value of the parameter  $\lambda$ . If  $\lambda \rightarrow 0$  the difference vanishes. As one notices, at  $\xi = 1$ , which corresponds to  $N = 11$  rings, there is a sudden “jump” of the PBE0 energy values.

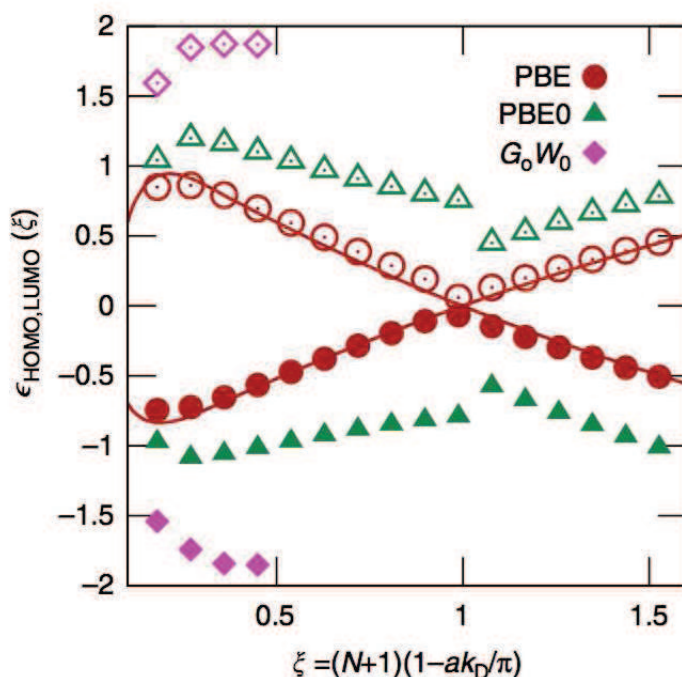


Figure 3.10.: HOMO and LUMO energies (dimensionless according to equation 3.3) with respect to the length of the oligoacene molecule. PBE results are shown in red symbols, while red lines represent the estimates from the Brillouin zone folding. PBE0 values are shown in green and  $G_0W_0$  QP energies in magenta. In all cases, filled symbols show HOMO energies and empty ones their LUMO counterparts.

In order to explain this “jump” we have to consider about the symmetries of the frontier orbitals. Within PBE, the frontier orbitals can be symmetric or antisymmetric with respect to a mirror plane, normal to the molecular plane that cuts the molecular long axis into two identical pieces. The energy of symmetric orbitals decreases as a function

of  $\xi$ , whereas the energy of antisymmetric orbitals increases with  $\xi$ . This means that at  $\xi=1$  the symmetry of the frontier orbitals changes. PBE0 results from a PBE reference result plus a corrective perturbative term, which depends on  $\lambda$ . These correction terms contain Coulomb-matrix elements of the PBE calculation. Since at  $N=11$  the symmetry of the frontier orbitals changes, the Coulomb-matrix elements react and the PBE0 energies exhibit such a jump.

Another feature observed in Figure 3.10, is the slowly increasing deviation between the HOMO-LUMO energies within PBE and PBE0, for the first 10 molecules. In PBE0 the charging energy of HOMO and LUMO energies is given by the HF exchange. HF does not take into account the screening of the interaction. This means, that for long linear molecular chains, the charging energy is dominated by logarithmic length dependence. This dependence results in the deviation with respect to PBE energies.

In Figure 3.10 the  $G_0W_0$  QP energies for the first four oligoacene chains are also presented. Due to computational cost we did not study longer molecules. The obvious differences are explained by considering that within  $G_0W_0$  the charging energies are included entirely. Notice that within PBE0 the charging energies are included fractionally, as 25%. Therefore for benzene the difference  $E_{\text{HOMO}}^{G_0W_0} - E_{\text{HOMO}}^{\text{PBE}}$  is approximately four times the difference  $E_{\text{HOMO}}^{\text{PBE0}} - E_{\text{HOMO}}^{\text{PBE}}$ . The same is valid for LUMO energies. The relative difference drops for longer molecules, because  $G_0W_0$  includes also screening effects contrary to PBE0.

In conclusion, we predicted the behavior of large oligoacenes by means of density functional theory (DFT) and post-DFT methods. In particular, we showed that the energy band gap of oligoacenes exhibits oscillations with increasing molecular length and this effect emanates from a “Dirac-type” band crossing at the Fermi level [5]. However, with an eye in prospective technological applications, the survival of these properties under the screening of a metallic surface is indispensable. Hence, we continue by studying oligoacenes adsorbed on a metallic substrate, within the framework of ab initio electronic structure methodology.

### 3.3. Oligoacenes On Au(111)

In the following we focus on how the physical properties will be altered with respect to those of the gas-phase, when oligoacenes are adsorbed on a clean Au(111) surface. To this end, one has to show that the band crossing remains in the case of the infinite chain of polyacene adsorbed on Au(111).

The lattice parameter of Au(111) and the molecule is, respectively, 2.88 Å and 2.44 Å. Because of such a mismatch in the lattice constant along the long molecular axis, a modification of 9% (decrease) and 7% (increase), respectively, in the lattice constants of Au and the molecule, has been made. Notice that such a modification in the lattice constant is not physical. Therefore, an agreement with experiment is not expected. In order to

have a smallest modification of the lattice parameters more unit cells should be used. The purpose here is to find out whether the band crossing remains for the adsorbed molecular chain.

Figure 3.11 shows the band structure calculated from the  $\Gamma$  point toward the corner of the Brillouin zone,  $\pi/a$ , along the long molecular axis. The polyacene is adsorbed at a distance of  $2.8 \text{ \AA}$  away from the metallic surface. The different orbital symmetries of molecular contribution to the bands are shown with different colors. It is clear that for an orbital contribution above 20%, the crossing of the molecule's bands is still occurring, at about  $k_D=0.89 \pi/a$ .

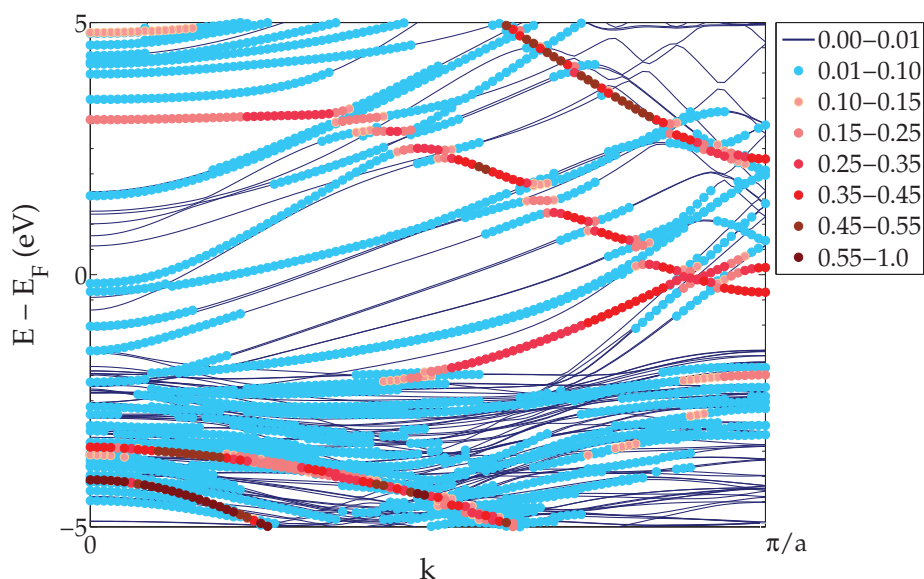


Figure 3.11.: Band structure of polyacene infinite chain adsorbed on Au(111). The orbital of the molecule's contribution to the symmetry of the bands is highlighted with different colors. The band crossing occurs at  $k_D=0.89 \pi/a$  as it can be seen for the bands which have a molecular orbital weight above 20%.

To show better the band crossing, we compare, in Figure 3.12, the band structure of the adsorbed chain with the band structure of the gas phase polyacene. The weight of the adsorbed molecule's contribution to the band structure is set above 20%. The figure shows that the two band structures are very similar.

Since the band structure calculation for polyacene adsorbed on Au(111) showed the band crossing we can proceed to the physical systems of some finite-length molecules adsorbed on Au(111). Because of the limited computational resources, we investigated only

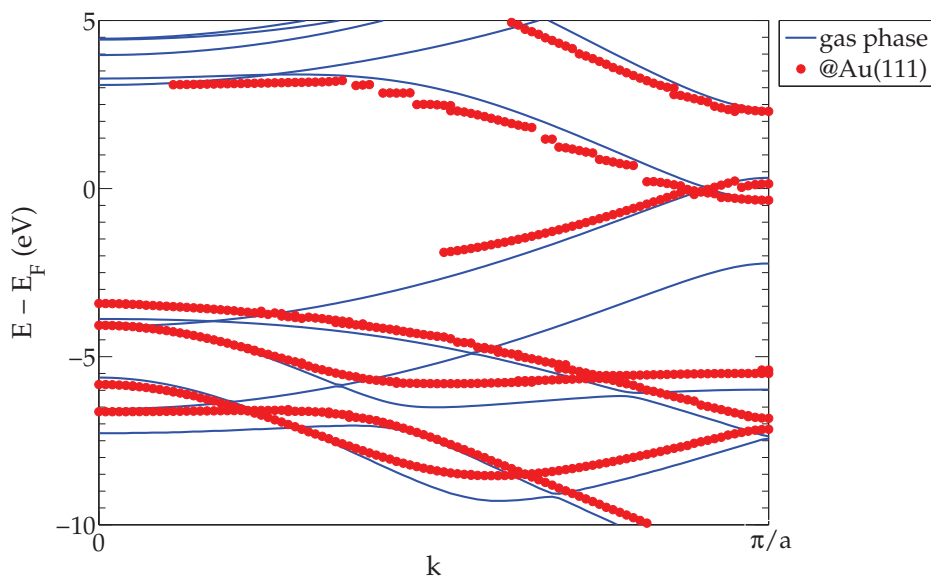


Figure 3.12.: Band structure of polyacene infinite chain on Au(111) compared with the band structure of the molecular chain in the gas phase. The orbital weight of the adsorbed molecule is set above 20%.

naphthalene ( $C_{10}H_8$ ), pentacene ( $C_{22}H_{14}$ ), hexacene ( $C_{26}H_{16}$ ) and heptacene ( $C_{30}H_{18}$ ), adsorbed on Au(111). We fully relaxed the molecules deposited on a metallic Au(111) surface and analyzed the behavior of their electronic structure.

### 3.3.1. Computational Details

For all the calculations, presented in this section, we used the VASP package [98], [99]. Standard DFT calculations were performed, using the PBE exchange-correlation functional [78]. In all the calculations, the plane wave basis set energy cutoff is 500 eV and is sufficient for describing the electronic structure of oligoacenes on surfaces. To represent the van der Waals weak interactions, we employed the semi-empirical DFT-D2 method, proposed by Grimme [81]. The necessary coefficients of the Grimme's scheme,  $C_6$  and  $R_0$  for Au, are taken equal to  $47.81 \text{ J nm}^6/\text{mol}$  and  $1.497 \text{ \AA}$ , respectively [163], while these of other elements are taken from Grimme paper [81].

A repeated slab model is used to represent the metal surface, where a slab consists of four atomic layers. A vacuum region of  $20 \text{ \AA}$  was inserted between the slabs. To sample the surface Brillouin-zone a mesh of  $4 \times 4 \times 1$   $\mathbf{k}$  points was used. The surface slab dimensions used for naphthalene and pentacene is  $(7 \times 3)$  and  $(9 \times 3)$  Au atoms, respectively, while for hexacene and heptacene is  $(11 \times 3)$ .

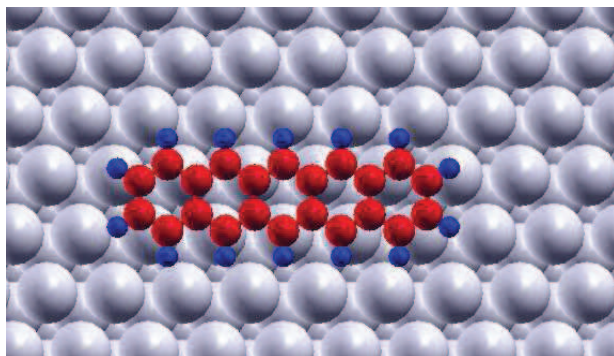


Figure 3.13.: A  $(x, y)$  unit cell of oligoacene adsorbed on Au(111). As an example, we present the  $xy$  plane of pentacene molecule adsorbed on Au(111).

The center of the molecules is located at an hcp-hollow site of Au(111) with the long molecular axis aligned with the close-packed metal atom rows. It has been proved theoretically and experimentally that this adsorption geometry is preferable for pentacene when relaxed on a (111) metallic surface [163, 164]. The same has been shown for benzene [165]. Thus, we choose the same geometry as an initial state of all our calculations, as showed, for instance, for pentacene in Figure 3.13.

For a first geometry optimization, we calculate the adsorption energies of naphthalene and pentacene on Au(111) for different distances from the substrate. We first fix the substrate slabs at their bulk positions and the molecule at a certain height above them. The only degrees of freedom fully optimized in this first procedure are the carbon positions parallel to the surface. The stopping criterion used for this geometry optimization is a difference of  $10^{-4}$  eV in the energy between two ionic relaxation steps. The adsorption energies are defined as

$$E_{ad} = E(C_xH_y/metal) - E(C_xH_y) - E(metal), \quad (3.4)$$

where  $E(C_xH_y/metal)$  is the total energy of the adsorbed system,  $E(C_xH_y)$  the total energy of the isolated molecule and  $E(metal)$  the total energy of the clean Au(111) surface. The results are presented in Figure 3.14, for PBE calculations with and without van der Waals corrections.

Figure 3.14 shows that the adsorption of the two molecules is stable at a distance of 2.70 Å for naphthalene and of 2.87 Å for pentacene, when van der Waals weak interactions are included. Note that, in the case where van der Waals corrections are not included, the adsorption of both molecules is not stable. Because of this fact we included van der Waals weak interactions throughout our calculations.

To fully optimize the structures on top of Au(111), we then relaxed all the degrees of freedom of the molecules, as well as the first layer of the substrate, while the other three

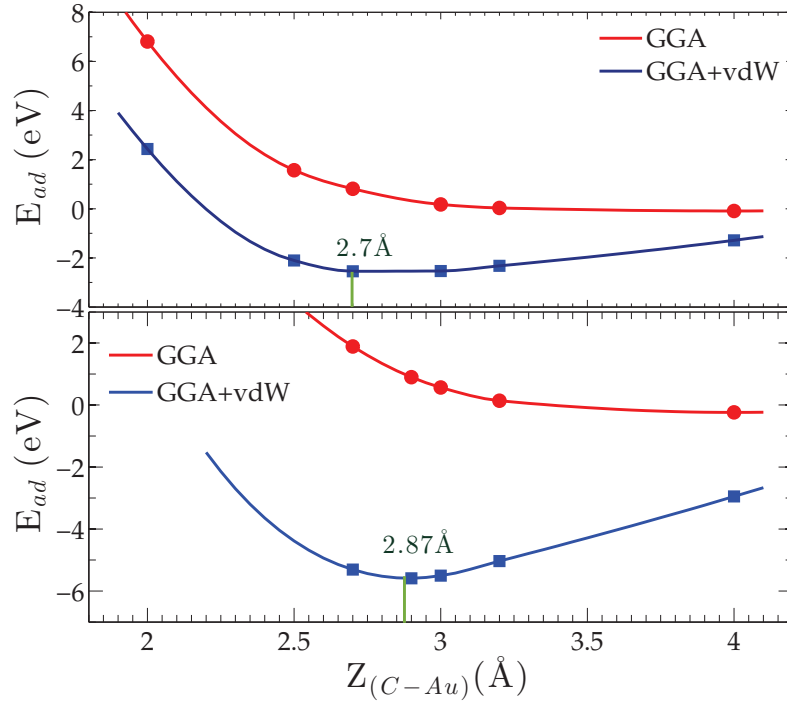


Figure 3.14.: From top to down, adsorption energy for naphthalene and pentacene, when adsorbed on Au(111) for different heights,  $Z_{(C-Au)}$ . With red we present the results for GGA calculations. Van der Waals weak interactions are also taken into consideration and the corresponding adsorption energies are presented in blue. We highlight the final position of geometry optimization for both cases.

layers are set to their bulk positions. We followed the same procedure for hexacene and heptacene, starting from the initial position of 3 Å. The relaxation processes until the difference of total energy between two consecutive relaxation steps is smaller than  $10^{-4}$  eV. For the relaxed structure, the absolute values of the total forces acting on the molecule are less than  $0.02$  eV/Å.

### 3.3.2. Workfunction and charge dipole

In photoemission experiments of an interface, where the band gap of a molecule can be measured, there is no way to distinguish the energy states of the substrate and the adsorbed molecule. A signature of the substrate, though, is given by its workfunction. Identifying the substrate, the molecular energy levels can be extracted.

The work function of the clean metal is defined as the difference between the electrostatic potential energy in the vacuum minus the Fermi energy,  $\Phi_0 = V(\infty) - E_F$  and is characteristic of a metal. The work function defines the minimum energy needed to remove an electron from the metal to the vacuum level. This will help us understand the electron transfer from the substrate to the molecule. It is also intriguing to investigate the changes in the workfunction for different oligoacene molecules, with oscillated band gaps. For simplicity, however, for this study we focus only on the molecule of naphthalene, adsorbed on Au(111) surface composed of three layers.

For Au(111), we find  $\Phi_0$  equal to  $5.0 \pm 0.2$  eV in a very good agreement with the experimental value [166]. The electrostatic potential  $V(x, y, z)$  integrated along the  $(x, y)$  directions of the unit cell is given as

$$V(z) = \frac{1}{A} \int_0^a \int_0^b V(x, y, z) dx dy, \quad (3.5)$$

where  $A$  is the area of the unit cell in the  $x$ - $y$ . The variation of  $V(z)$  along  $z$  direction is shown in Figure 3.15, with respect to the coverage, for naphthalene. As coverage we define, the surface covered by the molecule in the unit cell divided by the surface of the Au substrate.

We notice a reduction of the work function, induced by the adsorption of the molecule. The difference in  $\Phi$  versus the coverage, is presented in Figure 3.16, for naphthalene. This behavior is reminiscent of a conductor shown in Figure 3.17. In this representation the initial work function of Au is reduced to a new value due to the adsorption of the molecule.

The adsorption-induced reduction in the work function is intriguing and requires further analysis. It is known that the change in the surface work function, after adsorption,  $\Delta\Phi$  is related to the dipole moment through the Helmholtz equation [167]. In atomic units this relationship reads

$$\Delta\Phi = -4\pi\theta\Delta\mu, \quad (3.6)$$

where  $\Delta\Phi$  denotes the difference  $\Phi - \Phi_0$  between the work function after the molecule's adsorption and the work function of the clean metal,  $\Phi_0$ , in Hartree.  $\Delta\mu$  is the induced electric dipole due to the adsorption of the molecule and is in electron Bohr, and  $\theta$  is the fractional coverage over the area of the surface.

To study the electric dipole we start from another quantity that can provide an insight of the charge transfer mechanism. This is the difference of the charge density  $\Delta n(x, y, z)$  given as:

$$\Delta n(x, y, z) = n_{\text{mol+sub}}(x, y, z) - n_{\text{mol}}(x, y, z) - n_{\text{sub}}(x, y, z), \quad (3.7)$$

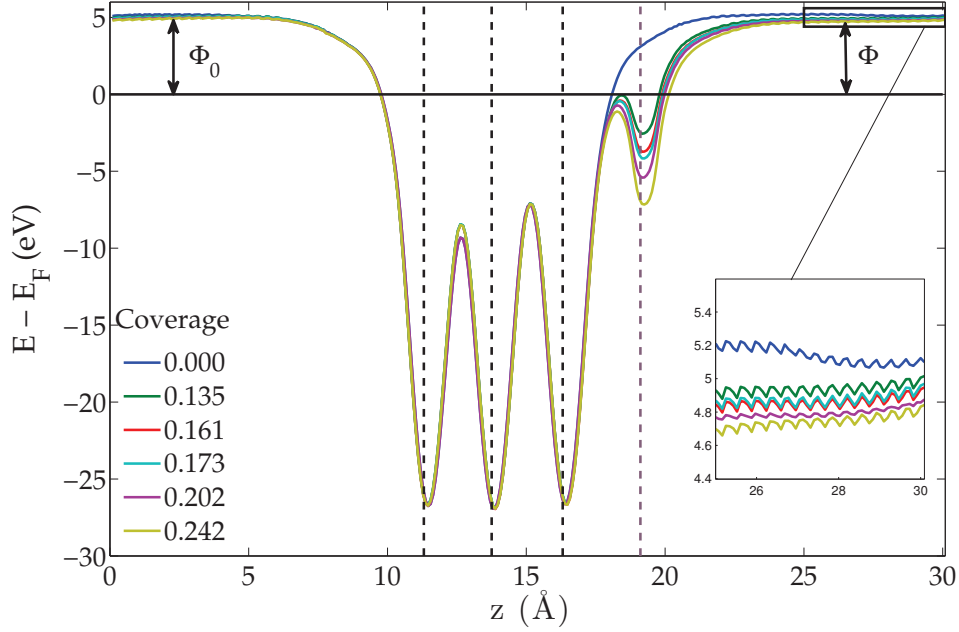


Figure 3.15.: Electrostatic potential, integrated along  $(x, y)$  directions of the unit cell and for different molecular coverages.  $\Phi_0$  is the work function of Au(111) before the adsorption of the molecule, and  $\Phi$  after adsorption. The vertical lines at positions  $\sim 11$  Å,  $\sim 13$  Å and  $\sim 16$  Å represent the positions of the layers of the substrate, while the line at  $\sim 19$  Å shows the position of the molecule. The inset shows the behavior of the potential as a function of coverage far from the molecule.

where  $n_{\text{mol}+\text{sub}}(x, y, z)$  is the charge density of the whole system (molecule + substrate),  $n_{\text{mol}}(x, y, z)$  and  $n_{\text{sub}}(x, y, z)$  are, respectively, the charge density of the molecule in the gas phase and the substrate alone.

$\Delta n(x, y, z)$  takes negative and positive values, at different positions, given in units of  $e/\text{Å}^3$ . This means that, negative values show a loss of electrons and positive values a gain of electrons. Figures 3.18 shows  $\Delta n(x, y, z)$  on different planes of the unit cell.

Furthermore, we can integrate the difference of charge density along  $x$  and  $y$ , in order to determine its behavior along the  $z$  axis. This charge density can now be read as

$$n'(z) = \int_0^a \int_0^b \Delta n(x, y, z) dx dy, \quad (3.8)$$

where  $a$  and  $b$  are the unit cell lattice parameters along  $x$  and  $y$  axis.

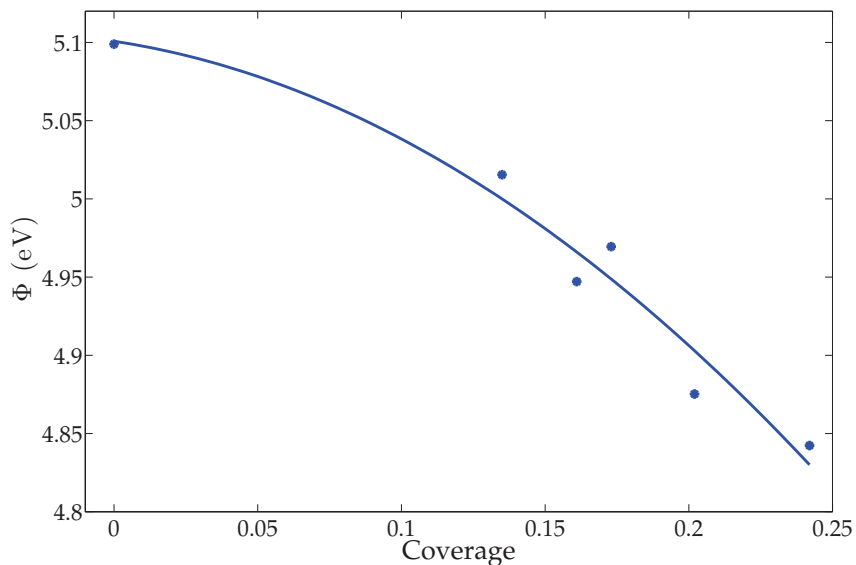


Figure 3.16.: Change of the Au(111) work function as a function of naphthalene surface coverage. The solid line is a polynomial fit to the data.

Figure 3.19 shows  $n'(z)$  for different values of surface coverage. Note that, the vertical lines at positions  $\sim 11 \text{ \AA}$ ,  $\sim 13 \text{ \AA}$  and  $\sim 16 \text{ \AA}$  represent the positions of the layers of the substrate, while the line at  $\sim 19 \text{ \AA}$  shows the position of the molecule.

Taking into account the units of the charge density, as mentioned before, it is clear that the space above the molecule is hosting holes, while electrons seem to be transferred to the region of the metal just below the molecule.

If we now integrate the above charge density,  $n'_z$  along the  $z$  direction according to the equation

$$N(z) = \int_0^z n'(z') dz', \quad (3.9)$$

we find the curves shown in Figure 3.20 as a function of the surface coverage.

It is clear, in this case, that positive charge density is gathered in the region of the substrate just below the molecule, which is then canceled out by negative charge density in the region of the molecule. At the edge of the unit cell along the  $z$  direction, the difference of the charge density goes to zero, as expected. Such a result, implies that the charge is

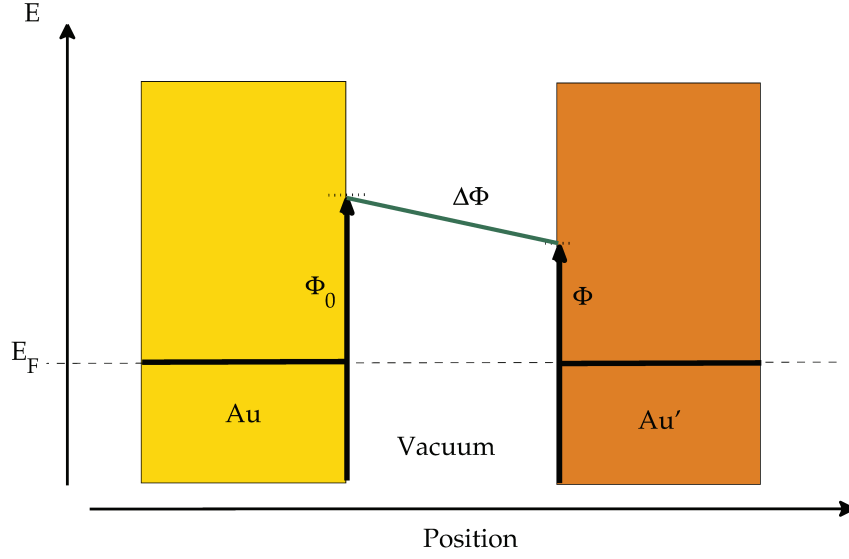


Figure 3.17.: Graphical representation of a electron energy levels with respect to the position, in the system of Au, vacuum and Au', where Au' denotes Au after adsorption of a molecule. The new system demonstrates an adsorption-induced reduction in the work function.

conserved within the unit cell.

The adsorption-induced electric dipole of the system,  $\Delta\mu(z)$ , can be now estimated as:

$$\Delta\mu(z) = - \int_{z_0}^z (z' - z_0)n'(z')dz', \quad (3.10)$$

The result for the adsorption-induced dipole is shown in Figure 3.21. It is noted that the dipole demonstrates the movement of electronic charge. The positive values in the edge of the unit cell shows the direction of the electron transfer from the molecule to the substrate. This adsorption-induced electric dipole explains the reduction of the workfunction noticed previously.

To verify the outcome of the dipole moment study, we determine the charge transfer between the molecule and the substrate by means of Bader analysis [168–170]. We determine the Bader charge transfer for naphthalene, pentacene, hexacene and heptacene. All the results are converged with respect to a fine fast Fourier transform (FFT) grid with dimensions  $400 \times 200 \times 400$ . The results of the Bader analysis are presented in Table 3.2.

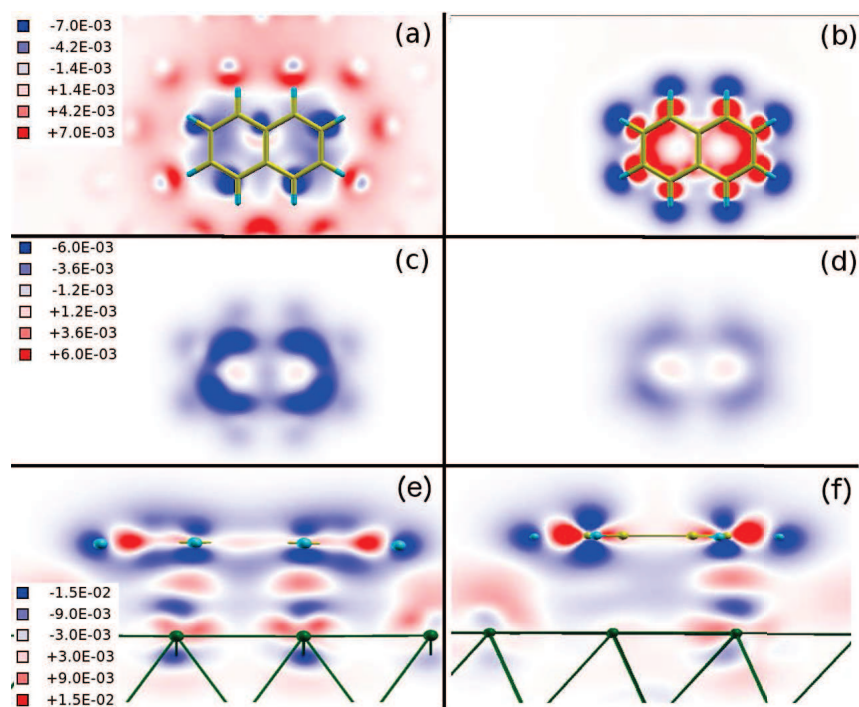


Figure 3.18.: Variation of the charge density for naphthalene adsorbed on Au(111), (a) the first plane of the metal, (b) the plane of the molecule, (c) a plane at height  $z \simeq 2 \text{ \AA}$  above the molecule, (d) a plane at height  $z \simeq 3 \text{ \AA}$  above the molecule, (e)  $(x, z)$  plane, (f)  $(y, z)$  plane.

The maximum charge transfer error is of the order of  $\pm 10^{-4} e$ .

Table 3.2.: Number of electrons of oligoacene molecules, given by Bader analysis, for the gas phase and when adsorbed on Au(111).

structure	Free molecule	@Au(111)
$C_{10}H_8$	48	47.75
$C_{22}H_{14}$	102	101.64
$C_{26}H_{16}$	120	119.59
$C_{30}H_{18}$	138	137.54

Bader analysis shows that for every structure a fraction of electron is transferred from the molecule to the substrate. This fraction varies from 0.25  $e$  in the case of naphthalene to almost 0.5  $e$  for heptacene. The direction of the charge transfer is consistent with the

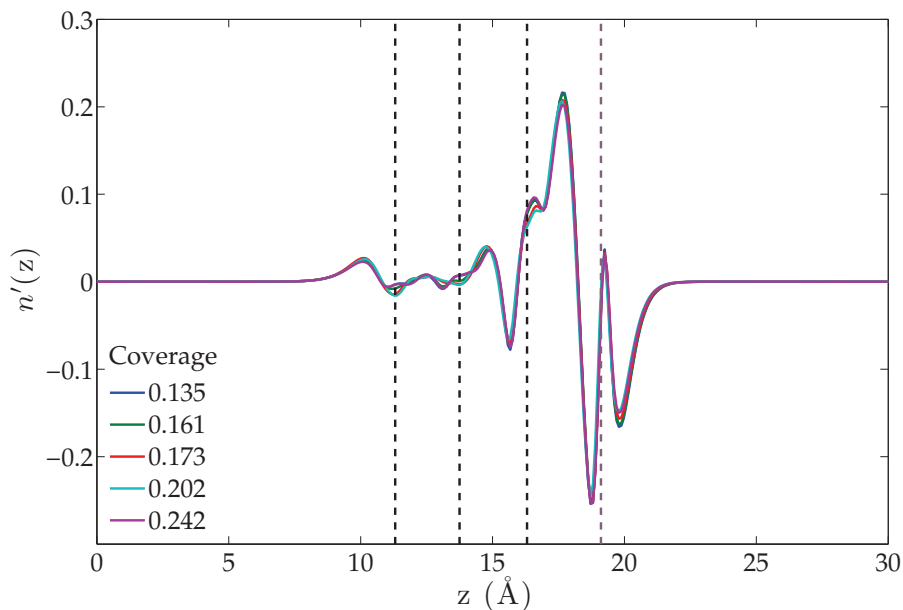


Figure 3.19.: Difference of charge density integrated along the  $x$  and  $y$  directions and represented along  $z$  direction (see Eq.3.8). We present also the dependence of this quantity for different surface coverages. The unit of  $n'(z)$  is  $-|e|$ , with  $e$  being the charge of electron.

adsorption-induced dipole moment result, as presented previously.

### 3.3.3. Density of states

The results we have presented already suggest that the electronic structure of the molecules relaxed on Au(111) should not deviate from their already reported behavior in the gas phase [5]. To justify further this statement, we show the projected density of states (PDOS) on the carbon atoms for each adsorbed molecule (Figure 3.23). The values of the band gaps obtained from these DOS are presented in detail in Table 3.3.

A point we would like to stress here is the HOMO and LUMO positions in the case of molecules in the gas phase. We need to have a relative position of the HOMO and LUMO for the free molecule with respect to the Fermi level of the substrate, so that one can have a clear picture of the shift of the molecule energy levels due to adsorption. To this end, we compared the density of states of the relaxed molecules on the surface with that of the molecule when its away from the surface by 8 Å. The molecule at 8 Å away of the metal is not expected to have any interaction with the substrate, so the density of states is the same as that of the free molecule. Thus, the DOSs show a shift towards lower energies of the molecular energy levels when the molecule is adsorbed on Au(111) surface, which

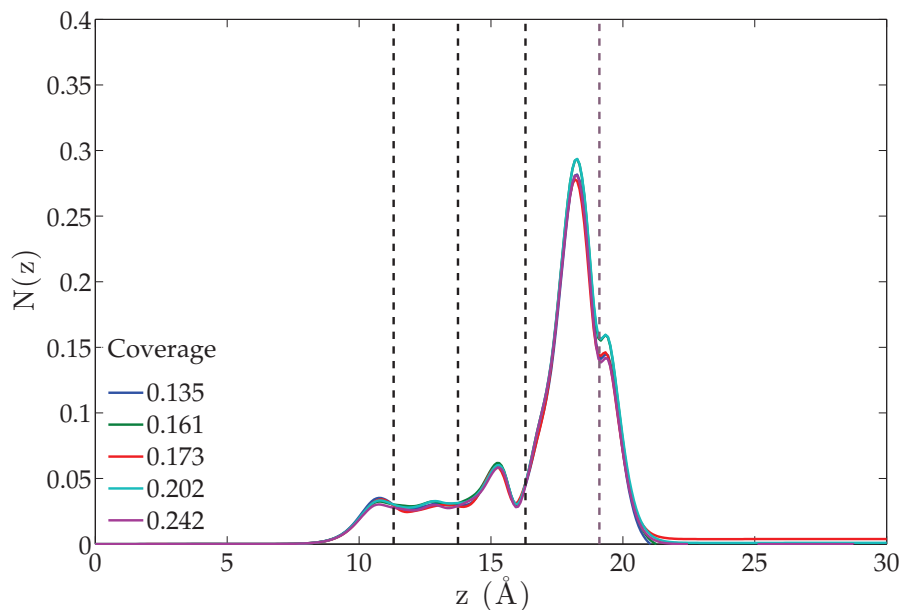


Figure 3.20.: Difference of charge density for different coverages integrated along the  $z$  direction using equation 3.9. The maximum error of this calculation is of the order of  $5 \times 10^{-3}$  e.

stabilizes the molecule.

Table 3.3.: HOMO - LUMO gaps for the molecules in the gas phase, 8 Å above the substrate and that of the molecule adsorbed on Au(111) surface.

structure	C <sub>10</sub> H <sub>8</sub>	C <sub>22</sub> H <sub>14</sub>	C <sub>26</sub> H <sub>16</sub>	C <sub>30</sub> H <sub>18</sub>
Free molecule	3.30	0.98	0.64	0.40
@Au(111)/ $Z_{(C-Au)}=8$ Å	3.30	0.98	0.64	0.40
@Au(111)/ relaxed	2.38	0.84	0.65	0.45

As one can notice directly, in Table 3.3, the band gaps of naphthalene and pentacene diminish when they interact with the surface (0.92 eV for naphthalene, 0.14 eV for pentacene). For hexacene and heptacene, however, the interaction increases the band gaps slightly (0.01 eV for hexacene, 0.05 eV for heptacene). In any case the difference is small and could not change the picture of the band gap oscillation reported for free oligoacene molecules.

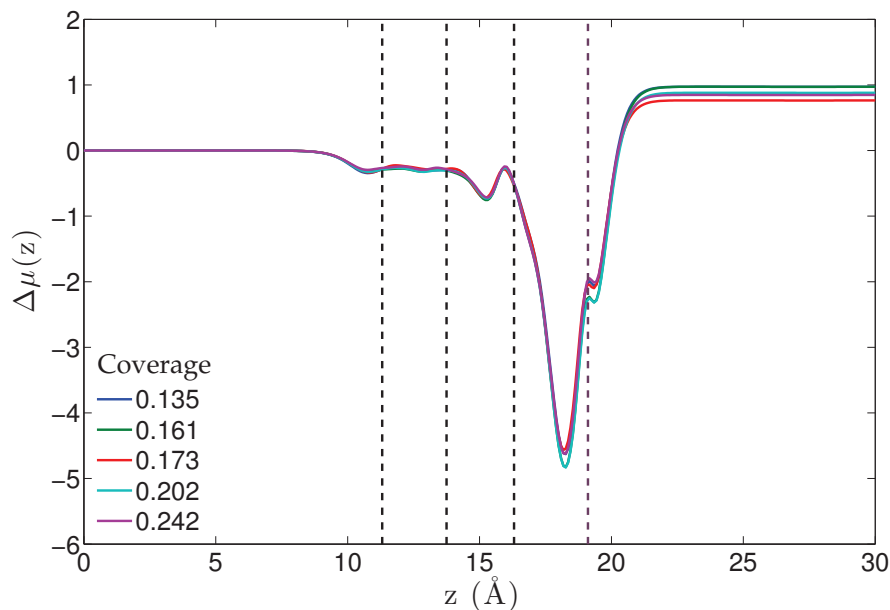


Figure 3.21.: Charge dipole moment for naphthalene adsorbed on Au(111) for different surface coverages. The units of  $\Delta\mu$  given here are  $|e|\cdot\text{\AA}$ . The electronic charge transfer from the molecule to the substrate is implied.

In the density of states it is clear that the HOMO resonances are moving towards low energies with respect to the Fermi level, when the molecules are adsorbed. On the other hand, LUMO resonances are getting closer to the Fermi level, something that brings the Fermi level in the middle of the band gap. We further studied the change in the DOS in three different cases, when the molecule is at 8 Å away of the substrate, at 4 Å and when adsorbed. The results for heptacene are presented in Figure 3.24. Notice that the molecule moves towards a stable configuration when adsorbed.

However, the problems of DFT band gap estimations compared to experiment are already reported (for example [2, 171]). For the calculations we perform, to our knowledge there are no experimental values available. Calculations with hybrid functionals can be computationally pretty demanding. To better describe the exchange energy we used the modified Becke-Johnson (MBJ) functional [172, 173]. Choosing the necessary parameter  $cmbj = 0.9$ , the HOMO-LUMO gap of Naphthalene in the gas phase is opened slightly,  $\sim 1.1\%$ . For consistency of our results, we used the same parameter for all calculations. The outcome is presented on Table 3.4, for the free and the adsorbed molecules.

The MBJ functional changes the PBE results, showing an increase of the band gaps for the relaxed molecules of .34 eV for naphthalene, .24 eV for pentacene, .07 eV for hexacene

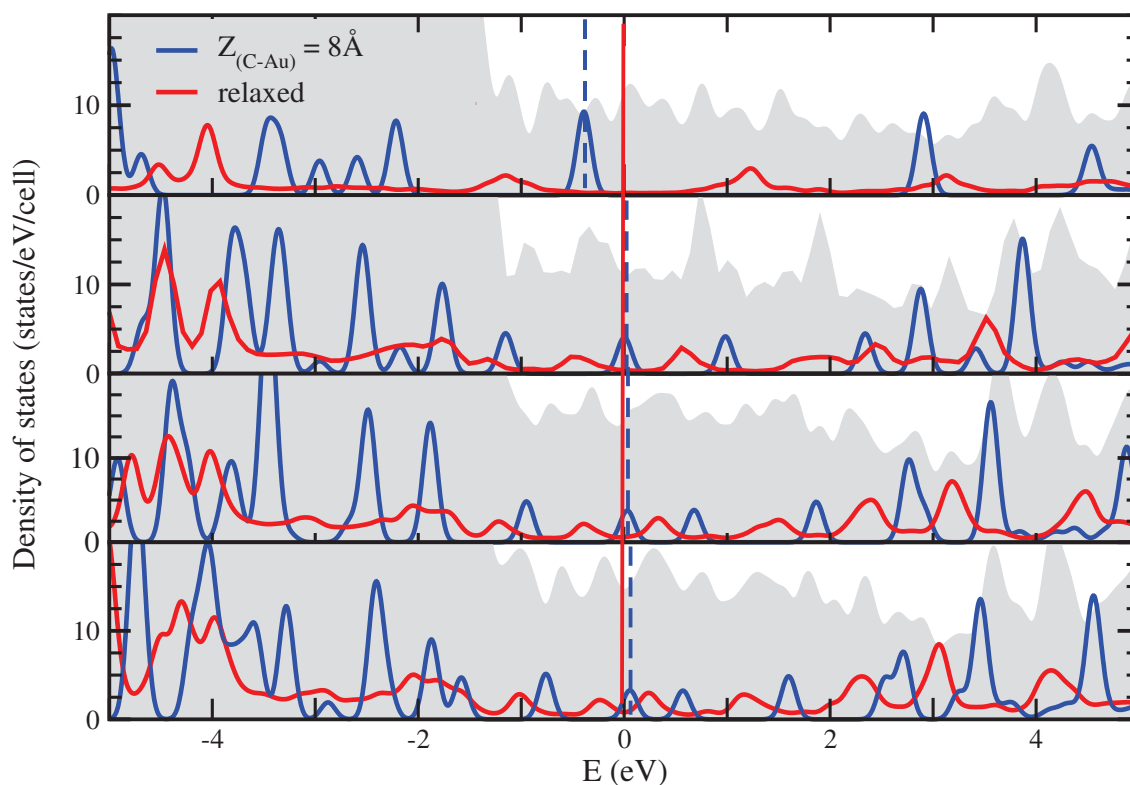


Figure 3.22.: Density of states (DOS) of oligoacene molecules. Top to bottom, projected DOS on the C atoms of naphthalene, pentacene, hexacene and heptacene. Blue represents the structures where the molecules stands 8 Å away of Au(111), while red corresponds to the adsorbed molecules. The gray shaded areas represent the DOS of the first layer of the Au(111) substrate. The Fermi level of the relaxed structures has been shifted to 0 (red solid line), while the HOMO level of the structures with  $Z_{(C-Au)}=8$  Å is represented with dashed blue lines.

Table 3.4.: MBJ functional calculated HOMO - LUMO gaps of the free and adsorbed molecules on Au(111).

structure	C <sub>10</sub> H <sub>8</sub>	C <sub>22</sub> H <sub>14</sub>	C <sub>26</sub> H <sub>16</sub>	C <sub>30</sub> H <sub>18</sub>
Free molecule	3.33	1.11	0.76	0.51
@Au(111)/ relaxed	2.72	1.08	0.72	0.48

and .03 eV for heptacene.

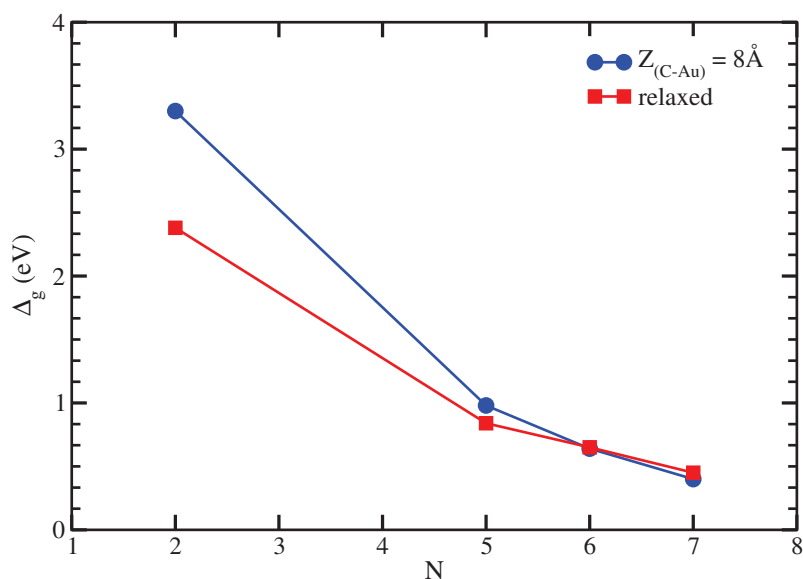


Figure 3.23.: The decay of the energy band gap for the  $C_{4N+2}H_{2N+4}$  molecules at 8 Å away from the surface (circles) and for their adsorbed counterparts (squares) (see also Table 3.3).

### 3.3.4. Calculated Scanning Tunneling Microscopy (STM) images

The calculated STM images are done using the Tersoff Hamann approximation [141]. Figure 3.25 shows these images, for each relaxed molecule adsorbed on Au(111). They are generated at a constant height of  $\sim 1.5$  Å away from the molecule. Keeping an eye for possible comparison with future experiments, we export the HOMO and LUMO STM images by setting the sample voltage appropriately. Note that there is an agreement with experimental STM images of pentacene on two monolayer NaCl on Cu(111) [46].

Our study so far showed that a metallic substrate such as Au(111) is a good candidate for possible applications using oligoacenes. The possibility to control the HOMO/LUMO band gap of these molecular chains as a function of their length would not change significantly, even under the screening environment of such a substrate. A natural continuation of this study is to change the substrate from a metal to a semiconductor or an insulator. In such a case, our target is to prove the possibility to monitor the energy band gap of the substrate by changing the adsorbed molecule.

## 3.4. Oligoacenes on SiO<sub>2</sub>

A very popular insulator among many used in device technology is silicon dioxide, SiO<sub>2</sub>. It is also used in oxide multilayers in optics, as a substrate in microelectronics, for metallic

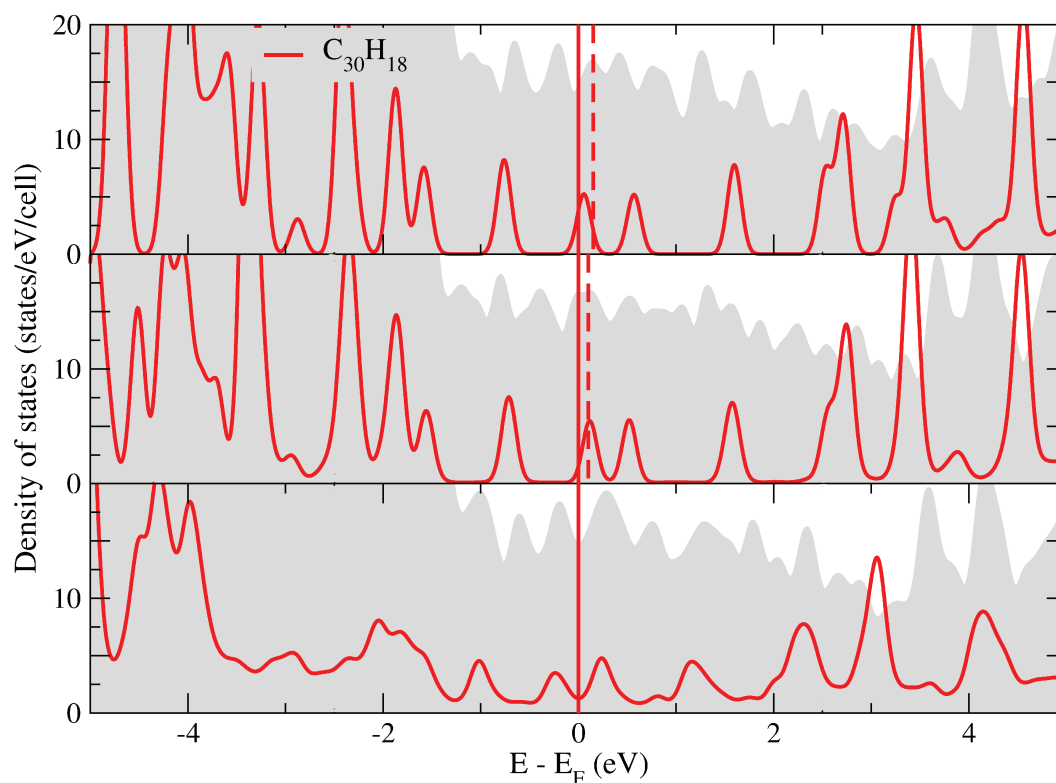


Figure 3.24.: Density of states (DOS) of heptacene at 8 Å (top), 4 Å (middle) and completely adsorbed (bottom) on Au(111) surface. The DOS of the first monolayer of Au below the molecule is represented in grey. With solid red line the Fermi level for the relaxed molecule is denoted. With dashed lines the Fermi level for the molecule at 8 Å (top), 4 Å (middle) are shown with respect to the Fermi level of the relaxed molecule.

multilayers in magnetics (see [174] for more details).  $\text{SiO}_2$  exists in many crystalline forms. The  $\alpha$ -quartz surface ( $\alpha\text{-SiO}_2$ ) has been studied extensively and it has been proved to be the most stable, with the lowest energy [175–177].

When such a substrate is to be used as a surface, inevitably there will be the appearance of dangling bonds. A dangling bond is the appearance of an unpaired valence electron, due to fewer bonding partners. This of course, leads to problems, of fundamental interest in modern semiconductor devices [178–180]. These problems are often treated with the introduction of oxygen or hydrogen in the structures to saturate the dangling bonds.

The reconstruction of the cleaved  $\alpha\text{-SiO}_2$  has been a subject of studies using ab initio

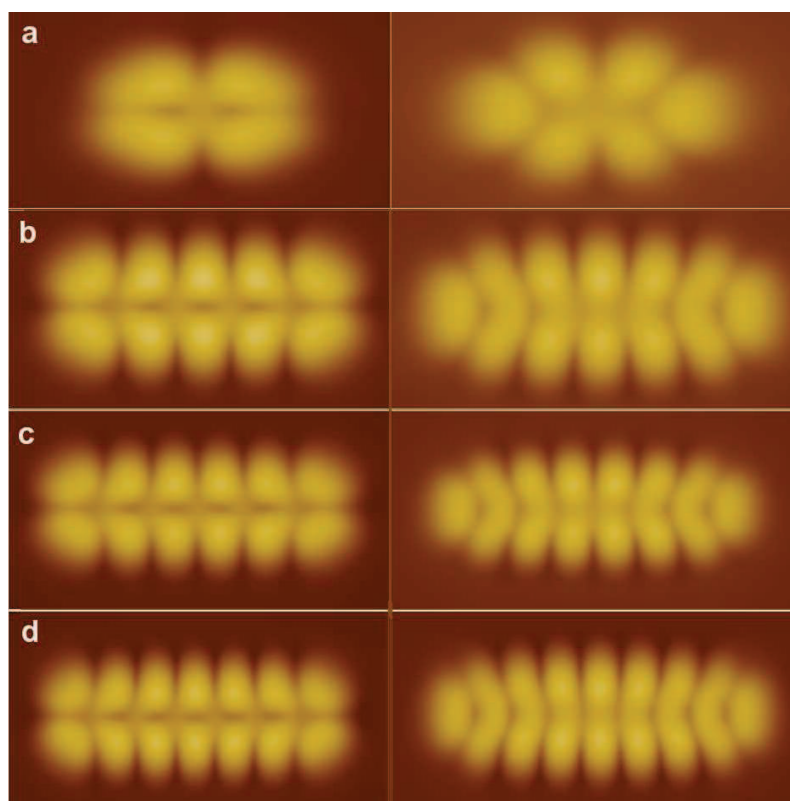


Figure 3.25.: Calculated STM images for the relaxed  $C_{4N+2}H_{2N+4}$ , for  $N = 2, 5, 6, 7$  molecules adsorbed on Au(111) surface. Top to bottom naphthalene, pentacene, hexacene and heptacene. On the left column we present the HOMO of each molecule and on the right the LUMO.

methods. Hence, it has been suggested that a “dense”, as it is called, surface is a favorable reconstruction [175, 176], i.e. the cleaved surface tends to minimize the high energy dangling bonds by surface reconstructions, [175, 176]. The “dense”  $\alpha$ -SiO<sub>2</sub> was also proposed for molecular adsorption on SiO<sub>2</sub> surfaces [181, 182] and to be considered in the interface with other materials [183–186].

More recent studies, though, using a combination of molecular dynamics and first principles calculations showed that the “dense”  $\alpha$ -SiO<sub>2</sub> surface is further reconstructed [6, 186]. In particular, in [6], it was shown using DFT calculations, that the “dense”  $\alpha$ -SiO<sub>2</sub> surface is reconstructed due to the optimization of Si-O bond length distribution and Si-Si interactions at the surface layer. The resulting reoptimized “dense” surface was proved to have a surface energy about 10% lower than the initial “dense” surface. The density of states of this surface shows no dangling bonds and has a band gap of 5.62 eV.

Therefore, in our study we used the reconstructed “dense”  $\alpha$ -SiO<sub>2</sub>, using the atomic coordinates, given in [6]. In Figure 3.26 the atomic structure of the surface is shown together with the adsorbed pentacene molecule.

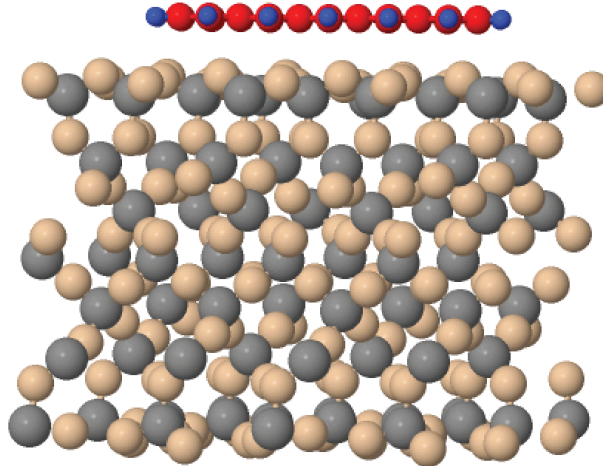


Figure 3.26.: Schematic representation of pentacene molecule adsorbed on SiO<sub>2</sub>  $\alpha$ -quartz. The carbon atoms are shown in red, the hydrogen in blue, oxygen in brown and silicon in grey. The coordinates of the substrate have been taken from [6] and are the result of molecular dynamics in the initial O-terminated structure of SiO<sub>2</sub>  $\alpha$ -quartz.

### 3.4.1. Computational Details

For this study we have also used the VASP package [98], [99], setting the energy cutoff to 500 eV for the plane waves expansion of the basis set. We have used the PBE exchange-correlation functional [78] and for the van der Waals weak interactions, we employed the semi-empirical DFT-D2 method [81]. To sample the surface Brillouin-zone we used a mesh of  $4 \times 4 \times 1$   $\mathbf{k}$  points.

To optimize the structures, we relaxed all the degrees of freedom of the molecule, while the atoms of the substrate are set to their given positions taken from [6]. The relaxation process continues until the difference of total energy between two consecutive relaxation steps is smaller than  $10^{-4}$  eV. For the relaxed structure, the absolute values of the total forces acting on the molecule are less than  $0.03$  eV/Å, while its distance from the substrate is approximately 3 Å.

We performed two different calculations, one with the molecule of pentacene relaxed on the “dense”  $\alpha$ -SiO<sub>2</sub> and the other for the infinite polyacene chain. In the case of pentacene

the unit cell given in [6] was repeated in a slab,  $2 \times 2 \times 1$ . For the band structure calculation the lattice parameter along the molecular axis for the substrate is  $10.03 \text{ \AA}$  and for the unit cell of polyacene is  $2.44 \text{ \AA}$ . In order to match the lattice parameters, the molecular unit cell was repeated 4 times and a slab  $2 \times 2 \times 1$  was used for  $\alpha\text{-SiO}_2$ . The lattice parameters change, respectively, for the molecule and for the substrate up to 1.3% (increase) and 3% (decrease).

Within this context we have to be careful to overcome the problem of the band folding of the bands into the smaller super cell Brillouin zone. The inconvenience of the band folding in the resulting band structure of the structure comes out when instead of the primitive unit cell in a periodic calculation, a super cell has to be used. Such a result is derived even for relatively small super cells and it should be avoided in order to have a clear picture of the band structure in the first Brillouin zone.

Such unfolding problems have already been encountered and confronted in several studies, for example [187–191]. For the unfolding of the band structure, in our study, we used the implementation introduced by Medeiros *et al.* [192]. The authors introduced a method of band unfolding to recover an “effective” primitive cell picture using an initial super cell calculation. Their unfolding implementation is based on the method introduced by Popescu and Zunger [191] and we consider it useful to present its basic principles.

Initially, Medeiros *et al.* define two different volumes,  $\Omega_{\text{PCBZ}}$  and  $\Omega_{\text{SCBZ}}$ , for the primitive cell Brillouin zone (PCBZ) and for the super cell Brillouin zone (SCBZ), respectively. Then, for each wave vector  $\mathbf{K}$  belonging to the SCBZ, there will be  $N_{\text{unfold}} = \Omega_{\text{PCBZ}}/\Omega_{\text{SCBZ}}$  wave vectors  $\mathbf{k}_i$  of the PCBZ such that:

$$\mathbf{k}_i = \mathbf{K} + \mathbf{G}_{\mathbf{k}_i \leftarrow \mathbf{K}}, \quad (3.11)$$

where  $i = 1, 2, 3, \dots, N_{\text{unfold}}$  the number of the wave vectors  $\mathbf{k}_i$  and  $\mathbf{G}_{\mathbf{k}_i \leftarrow \mathbf{K}}$  are vectors belonging to the super cell reciprocal lattice.

If  $|\psi_{m\mathbf{K}}^{\text{SC}}\rangle$  is an eigenstate of the Hamiltonian in the SC space and  $|\psi_{n\mathbf{k}_i}^{\text{PC}}\rangle$  the eigenstates in the PC, we have:

$$|\psi_{m\mathbf{K}}^{\text{SC}}\rangle = \sum_{\substack{n \\ \mathbf{k}_i \in \{\tilde{\mathbf{k}}_i\}}} \alpha(\mathbf{k}_i, n, \mathbf{K}, m) |\psi_{n\mathbf{k}_i}^{\text{PC}}\rangle, \quad (3.12)$$

where  $\{\tilde{\mathbf{k}}_i\}$  is the set of wave vectors  $\mathbf{k}_i$  in the PCBZ which satisfy the equation 3.11 and correspond to the PC eigenstates with the same eigenvalue with the SC eigenstates.

The probability for the  $|\psi_{m\mathbf{K}}^{\text{SC}}\rangle$  to have the same character as a PC Bloch state of wave vector  $\mathbf{k}$  is defined as the spectral weight  $P_{m\mathbf{K}}(\mathbf{k})$  and is read:

$$P_{m\mathbf{K}}(\mathbf{k}) = \sum_n |\langle \psi_{m\mathbf{K}}^{\text{SC}} | \psi_{n\mathbf{k}}^{\text{PC}} \rangle|^2 = \sum_{\mathbf{g} \in \text{PCRL}} |C_{m\mathbf{K}}^{\text{SC}}(\mathbf{g} + \mathbf{k} - \mathbf{K})|^2, \quad (3.13)$$

where PCRL stands for the primitive cell reciprocal lattice,  $\mathbf{g}$  the wave vectors belonging to it and  $C_{m\mathbf{K}}^{\text{SC}}$  the coefficients of the plane waves that span the eigenstates of the SC. The values for  $P_{m\mathbf{K}}(\mathbf{k})$  can be obtained, therefore, entirely from the coefficients  $C_{m\mathbf{K}}^{\text{SC}}$ , which means that the knowledge of the PC eigenstates is not required.

The spectral function is defined as:

$$A(\mathbf{k}; \epsilon) = \sum_m P_{m\mathbf{K}} \delta(\epsilon - \epsilon_m(\mathbf{K})), \quad (3.14)$$

where the only pairs  $(\mathbf{k}, \mathbf{K})$  included in the sum are those in which  $\mathbf{K}$  unfolds into  $\mathbf{k}$ , according to equation 3.11.

In order to accomplish finding the effective super cell (ESC) in the implementation, Medeiros *et al.* introduced the infinitesimal version  $dS_{\mathbf{k}}(\epsilon) = A(\mathbf{k}; \epsilon)d\epsilon$  of the cumulative probability function  $S_{\mathbf{k}}(\epsilon)$ . Then,  $dS_{\mathbf{k}}(\epsilon)$  represents the number of PC bands, at the PC wave vector  $\mathbf{k}$ , that cross the energy interval  $(\epsilon, \epsilon + d\epsilon)$ . Thus, a mapping of the region of interest in the  $(\mathbf{k}; \epsilon)$  space onto a  $(\mathbf{k}_i; \epsilon_j)$  grid can be done, with energy intervals of size  $\delta\epsilon$ . Therefore, a weight  $\delta N(\mathbf{k}_i; \epsilon_j)$  can be assigned to each point, given by:

$$\delta N(\mathbf{k}_i; \epsilon_j) = \int_{\epsilon_j - \delta\epsilon/2}^{\epsilon_j + \delta\epsilon/2} dS_{\mathbf{k}_i}(\epsilon) = \sum_m P_{m\mathbf{K}}(\mathbf{k}_i) \int_{\epsilon_j - \delta\epsilon/2}^{\epsilon_j + \delta\epsilon/2} \delta(\epsilon - \epsilon_m(\mathbf{K}))d\epsilon \quad (3.15)$$

Equation 3.15 gives the number of PC bands crossing  $(\mathbf{k}_i; \epsilon_j)$ . As a final step of the implementation,  $\delta N$  is averaged over wave vectors,  $\mathbf{k}_i$  related by symmetry operations of the PCBZ.

### 3.4.2. Electronic Structure

After performing the PBE calculation on the infinite chain of polyacene relaxed on the “dense”  $\alpha$ -SiO<sub>2</sub> surface, we obtain the folded band structure of the whole structure, as well as the total density of states (DOS). Then, as a post-processing method we employ the unfolding of the band structure as described above. The results for the unfolded band structure and the total DOS are presented in Figure 3.27. The different colors in the unfolded band structure graph, denote the values of  $\delta N(\mathbf{k}_i; \epsilon_i)$  as given in equation 3.15. Note the similarity of the bands, for energies around the Fermi level, with the band structure of polyacene in the gas phase, shown in Figure 3.3. The crossing of the bands is still occurring, close to the corner of the first Brillouin zone. This result is interpreted to a closed band gap in the total DOS. Note that the energy band gap of the reconstructed

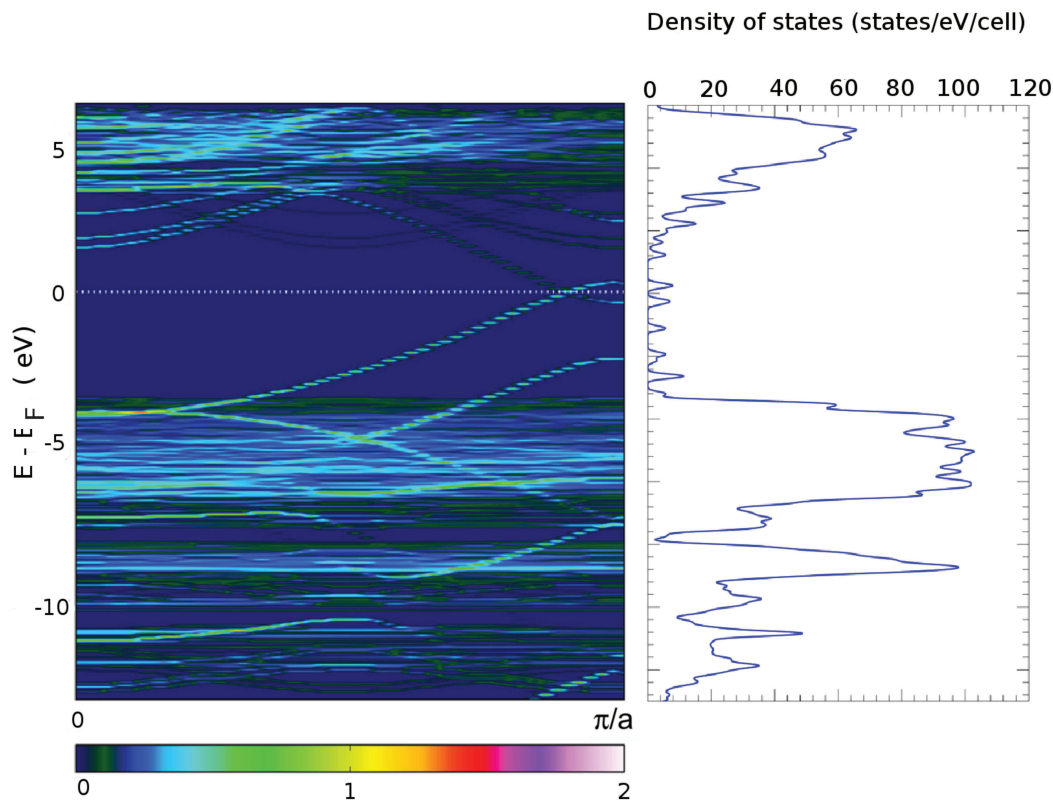


Figure 3.27.: The unfolded band structure of polyacene relaxed on the reconstructed “dense”  $\alpha$ -SiO<sub>2</sub> surface, is shown on the left. The color bar on the bottom denotes the values of  $\delta N(\mathbf{k}_i; \epsilon_i)$ , given in equation 3.15. On the right, the total DOS of the structure is presented.

“dense”  $\alpha$ -SiO<sub>2</sub> is expected to be 5.62 eV.

Since the substrate is an insulator, the type of adsorbed oligoacene molecule defines the energy band gap of the system. Considering also the fact that the band crossing is surviving even after the molecular chain’s relaxation, we expect that the band gaps oscillations will also occur for oligoacene chains when adsorbed on  $\alpha$ -SiO<sub>2</sub>. We can verify the closing of the substrate’s band gap using one of the candidate molecules, pentacene. The total DOS of the structure is shown in Figure 3.28.

Figure 3.28 presents the total DOS of pentacene adsorbed on  $\alpha$ -SiO<sub>2</sub> and shows that the energy band gap is opening with respect to the infinite molecular chain (Figure 3.27). The value of the band gap is 1.15 eV, comparable to the band gap value of 0.96 eV for the gas-phase pentacene molecule.

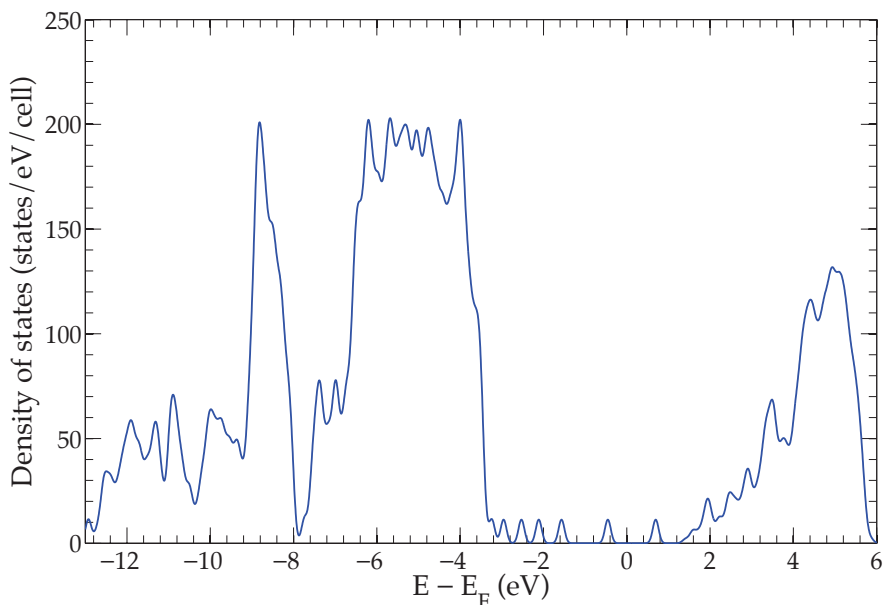


Figure 3.28.: Total density of states of pentacene relaxed on the reconstructed  $\alpha$ -SiO<sub>2</sub> surface. The HOMO-LUMO gap originated from the molecule states is about 1.15 eV.

Hence, we have proved that the band gap of the insulator SiO<sub>2</sub> can be monitored using oligoacene molecular chains. Furthermore, such a substrate forms an excellent candidate for prospective applications where the band gap oscillation property of oligoacenes can be employed.

### 3.5. Conclusions

In this chapter, we presented an investigation of oligoacene molecules properties focusing on behavior of their energy band gap with respect to their molecular length. Interestingly, we found that this band gap oscillates with a period of 11 benzene-type rings.

Employing a thorough DFT study we attributed this property to a band crossing in the band structure of the infinite molecular chain, close to the corner of the first Brillouin zone, similar to that of graphene. Moreover, we managed to verify these results with post-DFT methods, such as  $G_0W_0$  method and hybrid PBE0 functional. Furthermore, we showed that our results could be explained by Brillouin zone folding rules.

Furthermore, we used a GGA+vdW to investigate the behavior of oligoacene molecules adsorbed on a Au(111) surface. We focused on the electronic structure properties of four oligoacene molecules relaxed on a clean Au(111) surface. We attributed the adsorption-induced reduction of the workfunction to the formation of a charge dipole between the molecule and the substrate and confirmed a small charge transfer from the molecule to the substrate using Bader analysis. More importantly, studying the electronic structure of the relaxed molecules we showed that the band gap values are not modified significantly compared to the band gaps calculated for gas phase oligoacenes. Additionally, the band structure of the polyacene chain on Au(111) shows that the band crossing occurs for the bands in which the molecule contributes, with weight above 20%.

Finally, we substituted the metallic surface with an insulator, the reconstructed “dense”  $\alpha$ -SiO<sub>2</sub> surface. In such a case, we expected and we proved, that the energy band gap of the surface can be controlled and monitored by changing the adsorbed oligoacene chain.

These results demonstrate that a band gap oscillation, with increasing molecular length, remains unchanged when oligoacene chains are adsorbed on metallic surfaces and also on insulators. With these additional studies, the robustness of the property is strengthened, indicating the possibility for prospective technological applications.



# HOMO-LUMO Gaps of Molecules on Metallic Surfaces 4

---

## 4.1. Introduction

In the previous chapter the oligoacene molecular chains were studied in detail, in their gas phase and when adsorbed on substrates. At this point some important points about DFT and its performance upon the calculation of energy band gaps should be investigated. Although DFT methods succeed to describe the total energies or atomic structures, in good agreement with experiment, they tend to underestimate the experimental energy band gaps and to describe only semiquantitatively the band structures of solids and surfaces [49–51]. For the study of molecular band gaps, extensive research has been done to obtain good agreement between theory and photoemission experiments [2, 59–62]. Within such studies the adequacy of DFT using GGA and hybrid functionals is questioned. A solution to overcome the problems of DFT is to use the  $GW$  method, which takes into account a better screening electron-electron interaction and therefore gives results in good agreement with photoemission experiments. Different techniques of  $GW$  are used to study molecular band gaps ranging from the non-self-consistent  $G_0W_0$  method to the eigenvalue self-consistent  $GW$  [105] and the fully self-consistent  $GW$  [193]. In particular in the case of the perturbative  $G_0W_0$  method, the starting-point (DFT or HF) affects the calculated results for the band gaps [2, 101]. Such shortcomings of  $G_0W_0$  methodology can be overcome using the eigenvalue self-consistent  $GW$  method [96] or the fully self-consistent  $GW$  by solving the Hedin's equations [92]. However, these methods are computationally very expensive and are therefore prohibitive for big unit cells within periodic boundary conditions.

The shifts of the HOMO-LUMO levels because of adsorption or bond formation have been already studied experimentally and theoretically. More specifically Repp *et al.* [194] showed that upon the formation of a covalent bond between a pentacene molecule and a gold atom the hybridization of the orbitals leads to energetic shifts and changes in the occupation of the molecular resonances. A shift towards the Fermi energy was also observed

on gold atoms and pentacene molecules adsorbed on a NaCl film supported by a Cu surface because of the polarization of the NaCl film and the underlying metal [195, 196]. From the theoretical side, research has been done to evaluate the shifts of HOMO and LUMO within DFT and *GW* for adsorbed molecules [7, 65–67]. Neaton *et al.* showed that the energy gap of benzene adsorbed on graphite (0001) reduces significantly with respect to its gas-phase counterpart. The same result was found also by Garcia-Lastra and Thygesen for benzene and benzene-TCNE molecules adsorbed on Al(111) [67]. The authors of the above papers claimed that the adsorption-induced polarization and the HOMO-LUMO shifts are described adequately within *GW* and not DFT methods.

During adsorption certain physical phenomena are expected, that will influence the HOMO and LUMO levels of the molecules. The capture of such phenomena within DFT methods is possible to some extent. For instance, a modification in the electron density and consequently a rearrangement of the HOMO and LUMO, due to the self-consistent interaction between molecule and surface can be described sufficiently within DFT [63]. Furthermore, when a molecule is adsorbed on a surface, its discrete molecular levels are expected to be broadened to resonances and the orbital energies are shifted, a fact that was evident in oligoacene molecules adsorbed on Au(111). Such a modification takes place due to electronic coupling to the extended states in the metal. The adequacy of DFT to describe such modifications is not widely accepted [64]. A phenomenon that DFT fails at some extent to describe is the polarization of the metal substrate due to the adsorption. Indeed, during the adsorption of a molecule, an electron or a hole can be added into its orbital, due to the Coulomb interaction with the substrate. Therefore, the substrate electrons will rearrange in order to screen the added charge. This additional correlation energy further stabilizes the added hole or electron and therefore consistently reduces the molecular gap, as shown in Figure 4.1, see also [7].

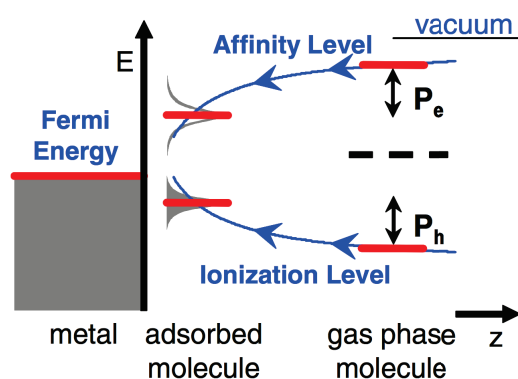


Figure 4.1.: Schematic representation of energy levels indicating the shifts of HOMO and LUMO of a gas phase molecule upon its adsorption on a metallic surface. The figure has been taken from [7].

Since, DFT does not take into account dynamical effects, like dynamical screening, a  $GW$  calculation is needed, which even in the level of the one-shot  $G_0W_0$ , can capture such electronic correlations. In this context it has been already proved, within  $GW$  methods, that the quasiparticle gap is reduced with respect to its gas phase counterpart, as shown in Figure 4.1.

Within the study presented in the following, we will also investigate the adequacy of DFT to describe the HOMO-LUMO gaps of adsorbed molecules. The difference between our study and previously mentioned work is that the molecules are chemically adsorbed on the paramagnetic surface of Cu(001). We have also investigated what happens to the QP band gap when the molecule is adsorbed on a ferromagnetic substrate. One has to study the changes in the energy band gaps due to polarization and compare the results obtained using a paramagnetic substrate. Therefore, we focused on three different organic molecules, methane ( $\text{CH}_4$ ), ethane ( $\text{C}_2\text{H}_6$ ) and ethylene ( $\text{C}_2\text{H}_4$ ) adsorbed on a Cu(001) or Co(001) substrate and calculated their spectral functions, using both DFT and  $G_0W_0$  methods.

## 4.2. Computational Details

For the calculations presented in this chapter VASP package was implemented [98], using the PAW method [99]. For the preliminary DFT calculations, the PBE functional was used, with a cutoff energy of 500 eV for the plane waves. A repeated slab model was introduced to represent the  $2\times 2$  metal surface, Figure 4.2. The slab consists of three atomic layers and a vacuum region of approximately 20 Å is inserted between them. For the sampling of the Brillouin zone a mesh of  $2\times 2\times 1$   $\mathbf{k}$ -points was used. In the case of gas-phase molecules, only the  $\Gamma$  point was used. The van der Waals dispersion interactions were taken into account using the Grimme's semi-empirical DFT-D2 method [81]. For the relaxation of the structures, the degrees of freedom for the atoms of the molecules and the substrate were fully relaxed. The relaxation steps were stopped with the criterion of the energy difference between two ionic steps to be less than  $10^{-4}$  eV. The forces in these cases were found to be less than 0.03 eV/Å. The final distances of the molecules from the surfaces are shown in Table 4.1.

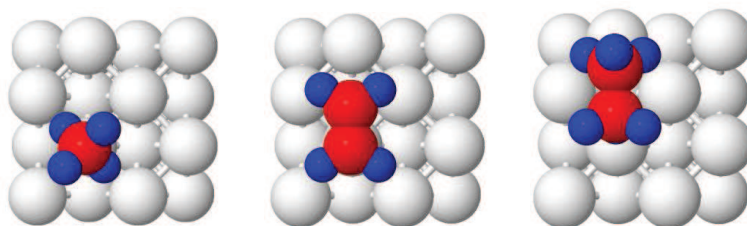


Figure 4.2.: Graphical representation of the molecules of methane, ethylene and ethane adsorbed on a Cu(001) or Co(001) substrates.

Table 4.1.: DFT-calculated distances of adsorbed molecules on Cu(001) or Co(001) substrates.

	Methane	Ethylene	Ethane
$d_{(C-Cu)}$ (Å)	2.5	2.1	3.1
$d_{(C-Co)}$ (Å)	2.5	2.0	3.0

For the  $G_0W_0$  calculations extra parameters have to be defined. Namely, the number of electronic bands, the energy cutoff for the response functions and the number of frequency points. It has to be pointed out that the increase of these parameters increases the accuracy of the calculations in most cases, but also increases the computational cost of the  $G_0W_0$  calculations. Within this study, an attempt to find the optimal values within a compromise, for the computational cost, was made. The tactics followed was the following:  $G_0W_0$  calculations were made for the gas-phase molecules, changing the above mentioned parameters and finding the best possible agreement with experimental values, when available, for the HOMO and LUMO energies. The parameters giving the optimal agreement with experiment were also used for the  $G_0W_0$  calculations of the adsorbed molecules. Hence, the values of the number of electronic bands, the energy cutoff for the response functions and the number of frequency points were, respectively, for ethane 512 bands, 60 eV and 20 points, for methane 320 bands, 60 eV and 20 points, and for ethylene 768 bands, 60 eV and 20 points. Table 4.2 shows the calculated values for HOMO and LUMO energies within PBE and  $G_0W_0$ . The HOMO energy is in good agreement with experimental values for methane and ethane. However, for ethylene the agreement with experiment is less good. A better agreement might be possible if one could increase the number of empty bands. For the study of the energy band gaps under adsorption, each molecule is positioned first at a distance of 8 Å away from the substrate. Then it approaches the substrate with a step of 2 Å until it is completely adsorbed and relaxed. This strategy will help us understand the effect of the gradual interaction of the molecule with the substrate.

Table 4.2.: DFT and  $G_0W_0$  calculated HOMO and LUMO energies for methane, ethylene and ethane molecules in the gas phase. The experimental value of the ionization potential (IE) is also given. All the energies are given in units of eV.

	HOMO (PBE)	LUMO(PBE)	HOMO( $G_0W_0$ )	LUMO ( $G_0W_0$ )	IE ( <i>Exp.</i> )
Methane	-9.41	-0.41	-12.69	0.77	12.61 ( <i>Ref. [197]</i> )
Ethylene	-6.75	-0.98	-9.22	2.98	10.51 ( <i>Ref. [198]</i> )
Ethane	-8.05	-0.43	-11.14	0.85	11.0 ( <i>Ref. [199]</i> )

### 4.3. Results

The results of the preliminary calculations are presented below. The density of states projected on the ethane molecule is presented, when the molecule is adsorbed on Cu(001) or Co(001) within DFT and  $G_0W_0$  methods. The results for methane and ethylene are shown in the appendix. In order for all the resonances to be clear, we chose the color-bar representation. Therefore, resonances with different height are shown as lines with different color ranging from zero (blue) to 0.5 (deep red). The units of DOS are given in states/eV/cell. The  $y$ -axis shows the absolute values of energy in eV. The Fermi level of the adsorbed molecules on each substrate is also indicated. In this context, the shift of the LUMO and the HOMO levels, as the molecule approaches the substrate, is indicated with red arrows (in analogy to Figure 4.1).

Upon adsorption more resonances are expected to appear in the projected DOS of each molecule due to the hybridization of the molecular orbitals with the orbitals of the substrate. Therefore, what one expects are more peaks in the projected DOS, which have a small weight on the molecular orbitals. These peaks could be interpreted as electrons being shared between the substrate and the molecule. Within our study we consider the resonances with a DOS above 0.1 states/eV/cell as important energy levels.

Focusing on ethane adsorbed on Cu(001), we find a decent agreement with previous studies when the molecule is physisorbed [7, 67].  $G_0W_0$  approximation gives a bigger HOMO-LUMO gap with respect to DFT and also captures the shifts of the corresponding resonances as the molecule is adsorbed. However, when the molecule is closer to the substrate, at a distance of 3.1 Å, DFT also captures the shifts of the HOMO and LUMO levels. Similar results are observed when the molecule is adsorbed on Co(001). The shifts of the HOMO and LUMO levels are clear within  $G_0W_0$ . However, DFT captures a reduction of the LUMO level upon adsorption at 3 Å. The spin splitting upon adsorption is observed within  $G_0W_0$  already from a distance of 4 Å far away of the substrate. DFT does not show any exchange interaction until a distance of 4 Å, however, it describes the phenomenon accurately enough upon relaxation at a distance of 3 Å.

### 4.4. Conclusions

To conclude, our results showed that the  $G_0W_0$  calculations provide a better description of the molecular adsorption effects. Shifts of the HOMO-LUMO levels are observed in the physisorption limits. We observe that upon chemisorption DFT seems to provide similar results as  $G_0W_0$ . This is true for both types of substrates, Cu(001) and Co(001). Further investigation is required, to study the performance of the two theoretical frameworks for the description of molecular adsorption. Such studies could be performed in the  $G_0W_0$ , but also using the self-consistent  $GW$  approximation and it would be interesting to see if the  $GW$  self-consistency can improve the DFT results. However,  $GW$  calculations for big

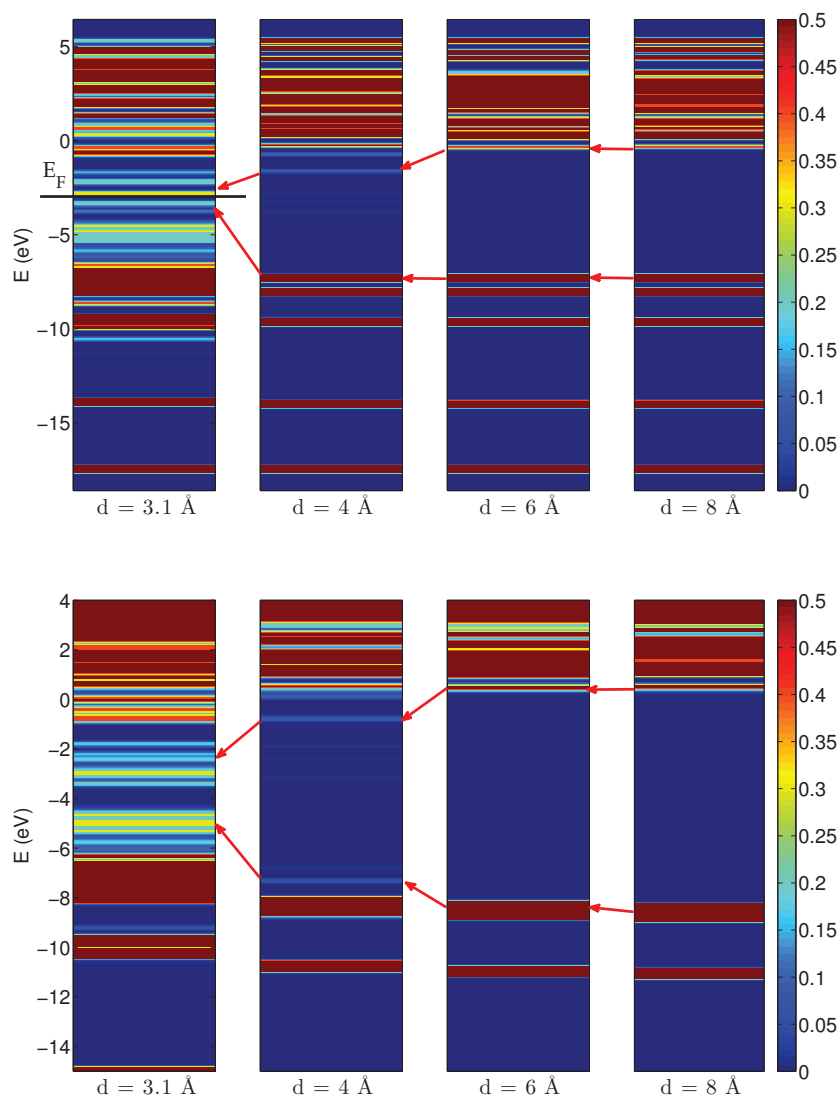


Figure 4.3.: DFT (up) and  $G_0W_0$  (down) calculated DOS for ethane adsorbed on Cu(001). The colorbar indicates the projected DOS on the molecule in states/eV/cell. The red arrows indicate the changes in HOMO and LUMO levels while the molecule approaches the substrate, from distance  $d=8$  Å to the final adsorbed configuration at  $d=3.1$  Å. The Fermi level of the adsorbed molecule within DFT is shown in a black line.

slabs is computationally prohibitive for most mainstream codes. Highly optimized codes, such as FIESTA [2] or WEST [200], use localized basis sets and may be capable of treating larger systems within the  $GW$  approximation. If the computational cost is overcome, more

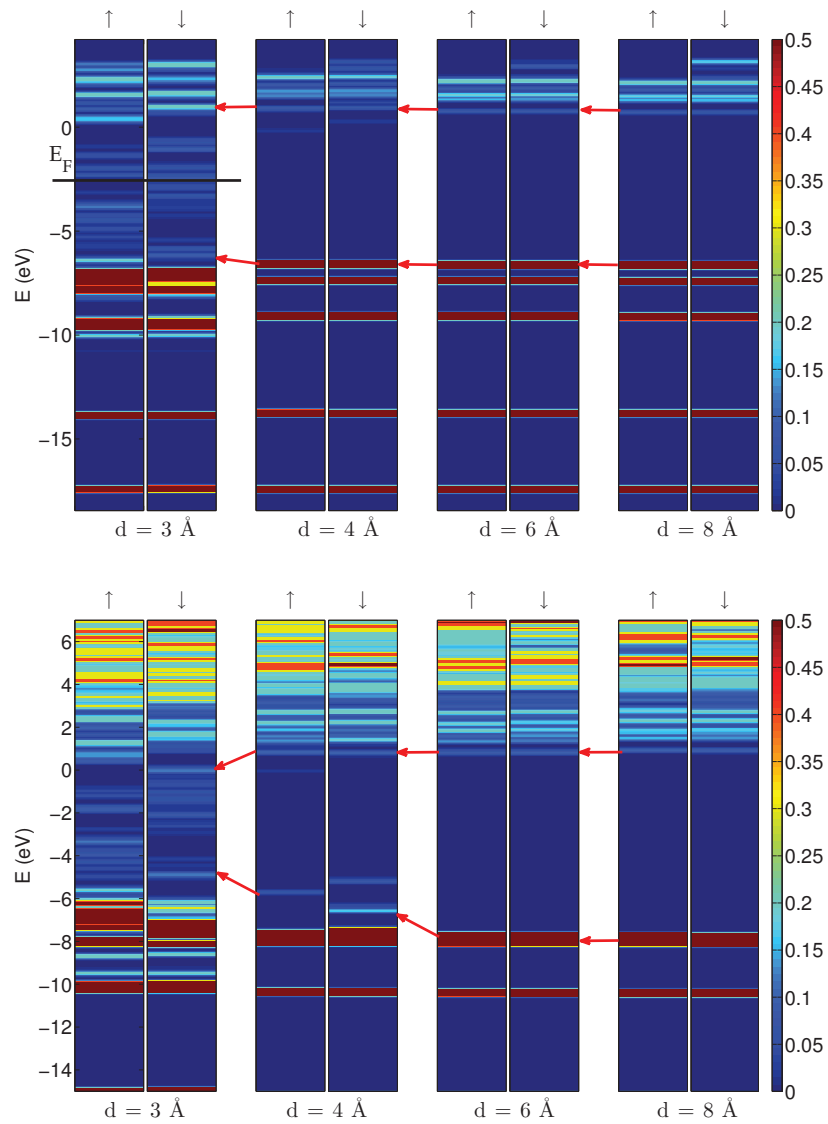


Figure 4.4.: Up downwards DFT and  $G_0W_0$  calculated DOS for ethane molecule adsorbed on Co(001), same as in Figure 4.3. The arrows  $\uparrow$  and  $\downarrow$  indicate, respectively, the up and down spins.

realistic systems could be studied and a better description of experimentally observed phenomena might be within reach.



# General Conclusions

---

The interaction of organic molecules with a supportive substrate has been an issue of extensive research in several fields in science and technology, especially in organic electronics and photovoltaics. Possible changes in the electronic structure of a molecule due to its adsorption is of high importance for possible applications where use of the molecular properties is required. In this context, we investigated different systems of organic molecules adsorbed on metallic surfaces. The electronic correlation of these systems was thoroughly studied, within DFT and *GW* methods.

The first system presented was a binuclear metal-organic complex, Ni<sub>2</sub>, adsorbed on Cu(001) substrate. The aim was to study the arising Kondo effect when two exchange coupled spins anticipating the case of single molecule magnets (SMMs). Experiments carried out at Karlsruhe Institute of Technology (KIT) showed an adsorption-site dependent behavior of the complex in the STM and STS data [4]. The measured Kondo temperature was in the order of  $\sim 10$  K, which is intriguing due to the absence of chemical bonding of the complex to the Cu surface. To explain the experimental observations we performed extensive DFT calculations. Our simulations showed that some STM images (Ni<sub>2</sub> -  $\alpha$ ) result from molecular fragments of the initial complex. Other STM images (Ni<sub>2</sub> -  $\beta$ ) can be attributed to a distorted Ni<sub>2</sub> complex with partially weakened internal chemical bonds. In both cases, our DFT calculations showed a picture of ( $S = 1$ )-type Kondo effect arising from the open  $3d$  shells of the individual Ni<sup>2+</sup> ions. Furthermore, using both the DFT-calculated spectral functions projected at the Ni atoms and the Anderson model formula for the  $S = 1$  Kondo effect, we computed the Kondo temperatures for the two configurations in good agreement with experimental values [4]. In many cases, more sophisticated methods are required to study the Kondo effect like Monte Carlo calculations [201, 202] or the dynamical mean field theory (DMFT) [203]. However, in this particular case, even the single-particle DFT could give a good prediction for the atomic configurations and good agreement with experiment for the Kondo temperatures. In general terms, binuclear complexes form an excellent candidate for studying fundamental aspects of magnetic two-impurity or double quantum dot systems. By functionalizing the bridging unit between the two dots, the super-exchange interaction between them could be enhanced and different regions of the phase diagram of the double impurity model could be accessed [204, 205]. Understanding the interaction between the spins residing on different functional regions

of the system is also vital for applications, such as quantum information storage and processing with molecules adsorbed on surfaces. Further challenges can be also identified like the possible substitution of Ising-like spins (like Tb) to study a “double molecular magnet”.

In the third chapter, motivated by several studies focused on polymers and oligomers for applications in organic electronics [39–41] and photovoltaics [36–38] we presented a thorough study of oligoacene molecules [42, 206]. We observed an oscillation of the energy band gaps as a function of the molecular length [5]. To understand the appearance of such oscillations, the band structure of the infinite chain, polyacene was invoked within DFT and  $G_0W_0$ . It was proved that the band gap oscillation originates from a band crossing at the Fermi level close to the corner of the Brillouin zone. Using a zone folding method, it can be proved that the position of the Dirac cone controls the oscillation of the HOMO-LUMO gap. The oscillating behavior of the energy band gaps was shown also to occur within the PBE0 functional. Note that in the presence of strong correlations, where *ab initio* methods tend to fail, a DMRG study by Peter Schmitteckert confirmed the oscillation phenomenon [5]. Since the extraordinary phenomenon of band gap oscillations was understood for the gas-phase molecules, our aim was to show their occurrence in the presence of the screening environment of a supportive substrate. Our extended DFT calculations showed the robustness of the property when the molecules are adsorbed on a Au(111) substrate. With an eye in prospective applications we also showed the possibility to tune the band gap of a semiconductor using oligoacene molecules of different lengths. We hope that our results will be soon confirmed by experiment since the synthesis of larger gas-phase oligoacenes is under investigation to increase their stability [43, 44]. The on-substrate synthesis provides also some hope to these achievements [45]. When their synthesis is achieved, the great progress accomplished in scanning probe microscopy [46, 47] will lead to the imaging of such organic molecules with high resolution.

In the last chapter, we focused on the performance of DFT and  $G_0W_0$  methodologies to describe the changes in the HOMO-LUMO gaps upon adsorption of molecules on substrates. Focusing on three similar-sized organic molecules, namely methane, ethane and ethylene, we demonstrated that  $G_0W_0$  can in general describe better the shifts of the HOMO and LUMO as the molecule interacts with the paramagnetic Cu(001) or the ferromagnetic Co(001) substrates. Moreover, within  $G_0W_0$  the interaction of the molecular orbitals with those of the surface can be seen more clearly by the appearance of new resonances due to hybridization. For such a study, many perspectives emerge. First of all, the performance of  $G_0W_0$  in magnetic system and especially in ferromagnetic substrates should be investigated. The possible improvement upon the shortcomings of DFT and  $G_0W_0$  using the self-consistent  $GW$  approximation should also be further studied. Furthermore, for comparison with experiment the computational cost of  $GW$  calculations should be moderated, either by the use of more powerful computers or with the use of more optimized codes. To latter direction efforts are being done, using localized basis functions for highly parallelized codes, e.g FIESTA [2] or WEST [200] codes. In this context, calculations might be feasible for realistic systems, like metal-organic interfaces. An exam-

---

ple that we currently investigate is the adsorption-induced polarization in big molecules adsorbed on a Co(001) substrate. Photoemission experiments by the group of Wolfgang Weber at IPCMS have shown the appearance of interface states (IS) at the Fermi energy of ferromagnetic metal-organic interfaces. Such highly spin-polarized IS were already observed on phthalocyanine (Pc) films on ferromagnetic Co(001) and were also explained within DFT [207]. The agreement between theory and photoemission experiment should also be confirmed within more realistic methods such as the *GW* approximation.

There are still a lot of additional calculations and developments that could be made for studying the electronic correlation of organic molecules adsorbed on metallic surfaces. Such work would have a great impact in the fields of organic electronics, organic spintronics and organic photovoltaics. First-principles calculations are expected to play an important role in such efforts. We hope the research presented in this manuscript to contribute in future theoretical and experimental efforts targeted on prospective technological applications.



# **CH<sub>4</sub> and C<sub>2</sub>H<sub>4</sub> adsorbed on metallic surfaces**

# A

---

We present here the density of states of CH<sub>4</sub> and C<sub>2</sub>H<sub>4</sub> adsorbed on a Cu(001) or Co(001) surfaces. The calculated DOS projected on the molecules, obtained within DFT and  $G_0W_0$  approximation, is presented. The results are similar to those obtained for the C<sub>2</sub>H<sub>6</sub> molecule and are discussed in chapter 4.

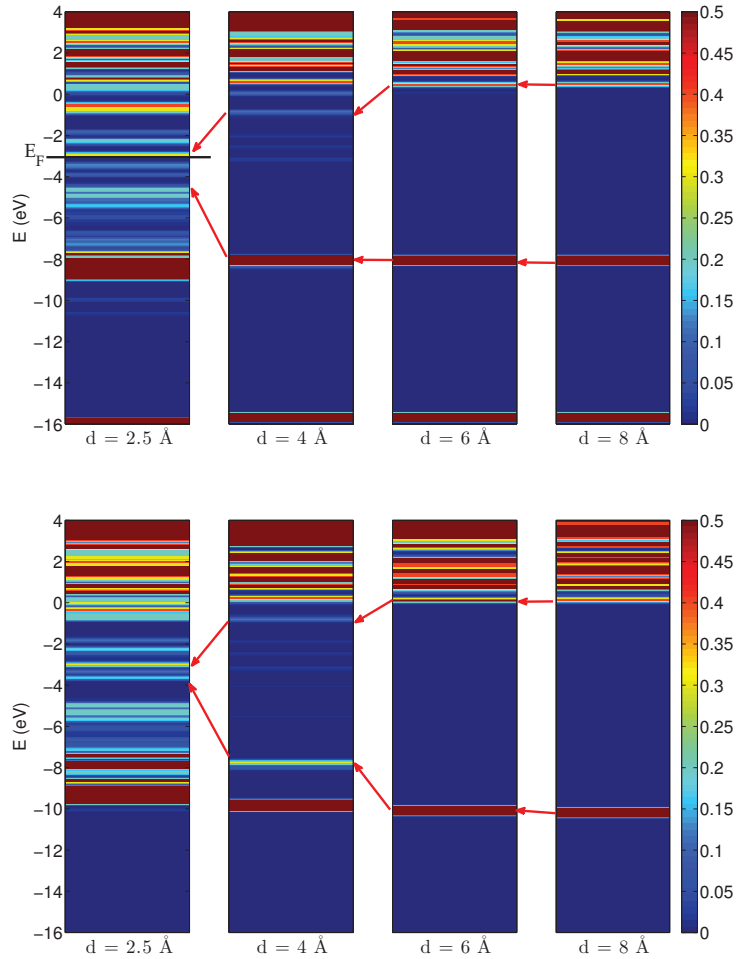


Figure A.1.: DFT and  $G_0W_0$  calculated DOS for methane adsorbed on Cu(001), respectively, first and second subfigure. The colorbar indicates the projected DOS on the molecule in states/eV/cell. The red arrows indicate the shifts in HOMO and LUMO levels while the molecule approaches the substrate, from distance  $d=8 \text{ \AA}$  to the final adsorbed configuration at  $d=2.5 \text{ \AA}$ . The Fermi level of the adsorbed molecule calculated within PBE is also shown (black line).

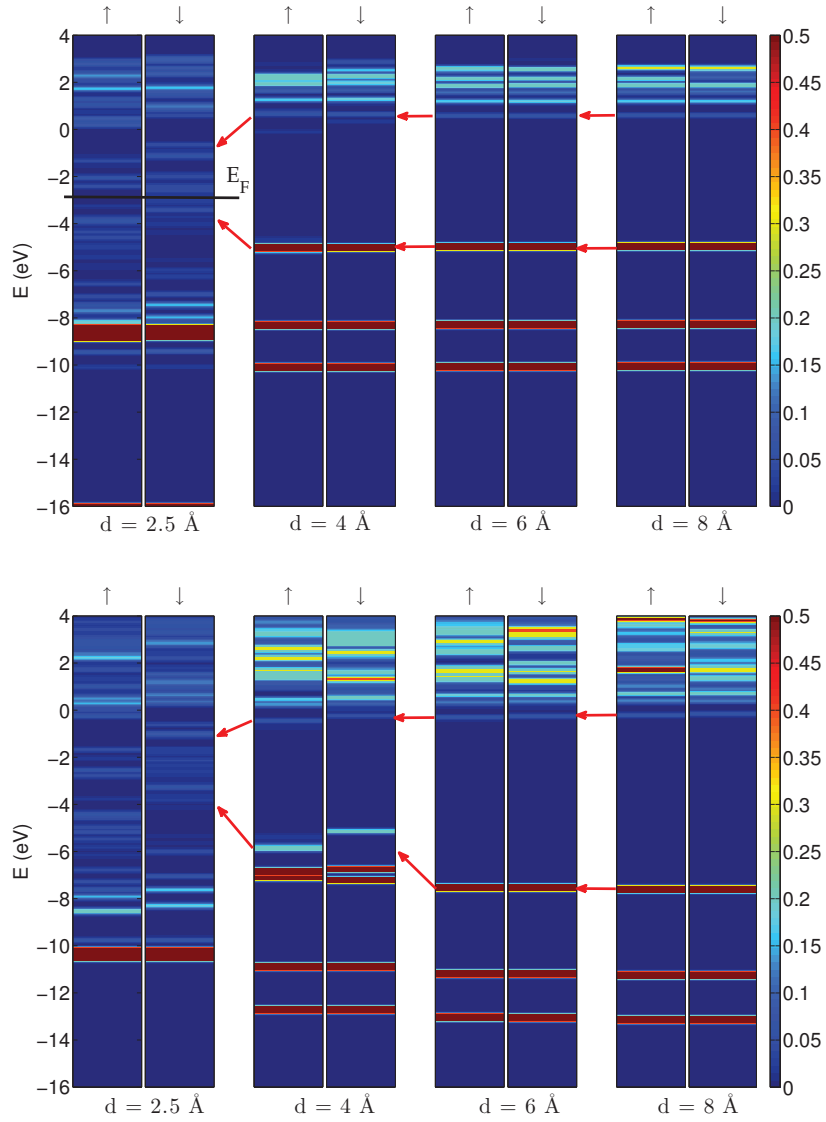


Figure A.2.: DFT and  $G_0W_0$  calculated DOS for methane adsorbed on Co(001), in analogy to Figure A.1. The arrows  $\uparrow$  and  $\downarrow$  indicate, respectively, the up and down spins.

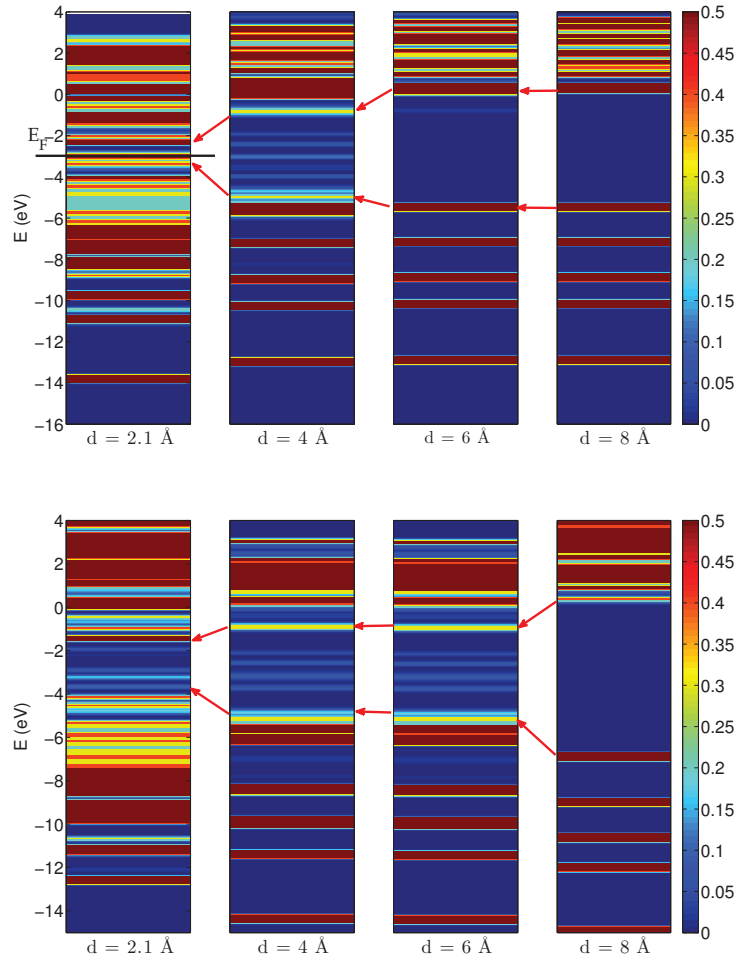


Figure A.3.: From top to bottom DFT and  $G_0W_0$  calculated PDOS for ethylene adsorbed on Cu(001). The height of the resonances is shown in different colors according to the colorbar on the right. The shifts of the HOMO and LUMO energies are indicated with red arrows and the Fermi level of the final structure with a black line (within DFT).

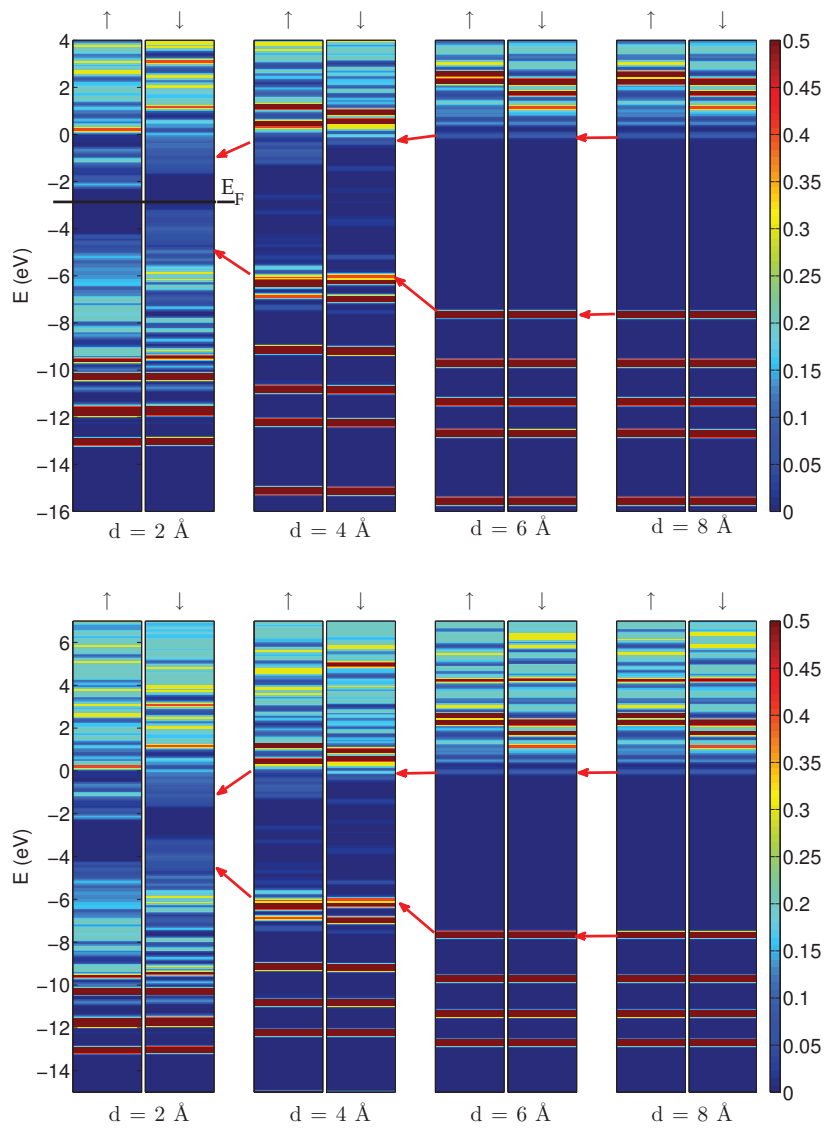


Figure A.4.: Similar to Figure A.3 for ethylene adsorbed on Co(001). The up and down spins are indicated, respectively, with  $\uparrow$  and  $\downarrow$ .



# Bibliography

---

- [1] Lapo Bogani and Wolfgang Wernsdorfer. Molecular spintronics using single-molecule magnets. *Nat. Mater.*, 7(3):179–186, 2008. [iv](#), [2](#), [3](#), [45](#), [51](#)
- [2] X. Blase, C. Attaccalite, and V. Olevano. First-principles *GW* calculations for fullerenes, porphyrins, phtalocyanine, and other molecules of interest for organic photovoltaic applications. *Phys. Rev. B*, 83:115103, Mar 2011. [iv](#), [4](#), [5](#), [32](#), [77](#), [93](#), [105](#), [110](#), [114](#)
- [3] Steffen Kahle. *Magnetic Properties of Individual Molecules Studied by Scanning Tunneling Microscopy*. PhD thesis, 2013. [iv](#), [48](#)
- [4] L. Zhang, A. Bagrets, D. Xenioti, R. Korytár, M. Schackert, T. Miyamachi, F. Schramm, O. Fuhr, R. Chandrasekar, M. Alouani, et al. Kondo effect in binuclear metal-organic complexes with weakly interacting spins. *Phys. Rev. B*, 91(19):195424, 2015. [v](#), [xi](#), [51](#), [53](#), [54](#), [55](#), [59](#), [113](#)
- [5] Richard Korytár, Dimitra Xenioti, Peter Schmitteckert, Mébarek Alouani, and Ferdinand Evers. Signature of the dirac cone in the properties of linear oligoacenes. *Nat. Commun.*, 5(5000), 2014. [vi](#), [vii](#), [4](#), [73](#), [76](#), [81](#), [91](#), [114](#)
- [6] Oleksandr I. Malyi, Vadym V. Kulish, and Clas Persson. In search of new reconstructions of (001)  $\alpha$ -quartz surface: a first principles study. *RSC Advances*, 4(98):55599–55603, 2014. [ix](#), [97](#), [98](#), [99](#)
- [7] Jeffrey B. Neaton, Mark S. Hybertsen, and Steven G. Louie. Renormalization of molecular electronic levels at metal-molecule interfaces. *Phys. Rev. Lett.*, 97(21):216405, 2006. [ix](#), [4](#), [6](#), [32](#), [106](#), [109](#)
- [8] Philipp Furche, Reinhart Ahlrichs, Christof HÄdttig, Wim Klopper, Marek Sierka, and Florian Weigend. Turbomole. *WIREs Comput. Mol. Sci.*, 4(2):91–100, 2014. [xi](#), [40](#), [54](#), [56](#), [60](#), [65](#)
- [9] Volker Blum, Ralf Gehrke, Felix Hanke, Paula Havu, Ville Havu, Xinguo Ren, Karsten Reuter, and Matthias Scheffler. Ab initio molecular simulations with nu-

- meric atom-centered orbitals. *Comput. Phys. Commun.*, 180(11):2175–2196, 2009. xi, 39, 40, 54, 56, 57, 59, 60, 64, 65, 72
- [10] S. A. Wolf, D. D. Awschalom, R. A. Buhrman, J. M. Daughton, S. von Molnár, M. L. Roukes, A. Y. Chtchelkanova, and D. M. Treger. Spintronics: A spin-based electronics vision for the future. *Science*, 294(5546):1488–1495, 2001. 1
- [11] R. Lloyd Carroll and Christopher B. Gorman. The genesis of molecular electronics. *Angew. Chem. Int. Ed.*, 41(23):4378–4400, 2002. 1
- [12] ZH Xiong, Di Wu, Z. Vally Vardeny, and Jing Shi. Giant magnetoresistance in organic spin-valves. *Nature*, 427(6977):821–824, 2004. 1
- [13] George Christou, Dante Gatteschi, David N. Hendrickson, and Roberta Sessoli. Single-molecule magnets. *Mater. Res. Soc. Bull.*, 25(11):66–71, 2000. 2
- [14] Velimir Meded, Alexei Bagrets, Andreas Arnold, and Ferdinand Evers. Molecular switch controlled by pulsed bias voltages. *Small*, 5(19):2218–2223, 2009. 2
- [15] Emanuel Lörtscher, Jacob W. Ciszek, James Tour, and Heike Riel. Reversible and controllable switching of a single-molecule junction. *Small*, 2(8-9):973–977, 2006. 2
- [16] Jiwoong Park, Abhay N Pasupathy, Jonas I Goldsmith, Connie Chang, Yuval Yaish, Jason R Petta, Marie Rinkoski, James P Sethna, Héctor D Abruña, Paul L McEuen, et al. Coulomb blockade and the kondo effect in single-atom transistors. *Nature*, 417(6890):722–725, 2002. 2, 63
- [17] Sergey Kubatkin, Andrey Danilov, Mattias Hjort, Jerome Cornil, Jean-Luc Bredas, Nicolai Stuhr-Hansen, Per Hedegaard, and Thomas Bjørnholm. Single-electron transistor of a single organic molecule with access to several redox states. *Nature*, 425(6959):698–701, 2003. 2
- [18] Edgar A Osorio, Kevin O’Neill, Nicolai Stuhr-Hansen, Ole Faurskov Nielsen, Thomas Bjørnholm, and Herre SJ van der Zant. Addition energies and vibrational fine structure measured in electromigrated single-molecule junctions based on an oligophenylenevinylene derivative. *Adv. Mater.*, 19(2):281–285, 2007. 2
- [19] Philipp Gütlich, Yann Garcia, and Harold A. Goodwin. Spin crossover phenomena in fe (ii) complexes dedicated to professor fa cotton on occasion of his 70th birthday. *Chem. Soc. Rev.*, 29(6):419–427, 2000. 2
- [20] V. Meded, A. Bagrets, K. Fink, R. Chandrasekar, M. Ruben, F. Evers, A. Bernard-Mantel, JS Seldenthuis, A. Beukman, and HSJ Van der Zant. Electrical control over the fe (ii) spin crossover in a single molecule: Theory and experiment. *Phys. Rev. B*, 83(24):245415, 2011. 2

- 
- [21] Igor Beljakov, Velimir Meded, Franz Symalla, Karin Fink, Sam Shallcross, Mario Ruben, and Wolfgang Wenzel. Spin-crossover and massive anisotropy switching of 5d transition metal atoms on graphene nanoflakes. *Nano Lett.*, 14(6):3364–3368, 2014. 2
- [22] Jiutao Li, Wolf-Dieter Schneider, Richard Berndt, and Bernard Delley. Kondo scattering observed at a single magnetic impurity. *Phys. Rev. Lett.*, 80(13):2893, 1998. 2
- [23] V. Madhavan, W. Chen, T. Jamneala, MF Crommie, and NS Wingreen. Tunneling into a single magnetic atom: Spectroscopic evidence of the kondo resonance. *Science*, 280(5363):567–569, 1998. 2, 49
- [24] HC Manoharan, CP Lutz, and DM Eigler. Quantum mirages formed by coherent projection of electronic structure. *Nature*, 403(6769):512–515, 2000. 2
- [25] Nikolaus Knorr, M Alexander Schneider, Lars Diekhöner, Peter Wahl, and Klaus Kern. Kondo effect of single co adatoms on cu surfaces. *Phys. Rev. Lett.*, 88(9):096804, 2002. 2, 59
- [26] N. Néel, J. Kröger, L. Limot, K. Palotas, WA Hofer, and R. Berndt. Conductance and kondo effect in a controlled single-atom contact. *Phys. Rev. Lett.*, 98(1):016801, 2007. 2, 59
- [27] D. Ehm, S. Hufner, F. Reinert, J. Kroha, P. Wölfle, O. Stockert, C. Geibel, and H. v Löhneysen. High-resolution photoemission study on low- $t_k$  ce systems: Kondo resonance, crystal field structures, and their temperature dependence. *Phys. Rev. B*, 76(4):045117, 2007. 2
- [28] L. Gao, W. Ji, YB Hu, ZH Cheng, ZT Deng, Q. Liu, N. Jiang, X. Lin, W. Guo, SX Du, et al. Site-specific kondo effect at ambient temperatures in iron-based molecules. *Phys. Rev. Lett.*, 99(10):106402, 2007. 2
- [29] Ying-Shuang Fu, Shuai-Hua Ji, Xi Chen, Xu-Cun Ma, Rui Wu, Chen-Chen Wang, Wen-Hui Duan, Xiao-Hui Qiu, Bo Sun, Ping Zhang, et al. Manipulating the kondo resonance through quantum size effects. *Phys. Rev. Lett.*, 99(25):256601, 2007. 2
- [30] I. Fernández-Torrente, KJ Franke, and JI Pascual. Vibrational kondo effect in pure organic charge-transfer assemblies. *Phys. Rev. Lett.*, 101(21):217203, 2008. 2
- [31] UGE Perera, HJ Kulik, V. Iancu, LGGV Dias da Silva, SE Ulloa, N Marzari, and S-W Hla. Spatially extended kondo state in magnetic molecules induced by interfacial charge transfer. *Phys. Rev. Lett.*, 105(10):106601, 2010. 2
- [32] Jesper Nygård, David Henry Cobden, and Poul Erik Lindelof. Kondo physics in carbon nanotubes. *Nature*, 408(6810):342–346, 2000. 2
-

- [33] Jens Paaske, A. Rosch, P. Wölfle, N. Mason, CM Marcus, and J. Nygård. Non-equilibrium singlet–triplet kondo effect in carbon nanotubes. *Nature Phys.*, 2(7):460–464, 2006. 2
- [34] Manuel Gruber, Fatima Ibrahim, Samy Boukari, Hironari Isshiki, Loïc Joly, Moritz Peter, Michał Studniarek, Victor Da Costa, Hashim Jabbar, Vincent Davesne, et al. Exchange bias and room-temperature magnetic order in molecular layers. *Nat. Mater.*, 2015. 2
- [35] Jun Kondo. Resistance minimum in dilute magnetic alloys. *Progr. Theoret. Phys.*, 32(1):37–49, 1964. 2, 45
- [36] Darren J. Lipomi, Benjamin CK Tee, Michael Vosgueritchian, and Zheman Bao. Stretchable organic solar cells. *Adv. Mat.*, 23(15):1771–1775, 2011. 4, 71, 114
- [37] Ismaila Dabo, Andrea Ferretti, Cheol-Hwan Park, Nicolas Poilvert, Yanli Li, Matteo Cococcioni, and Nicola Marzari. Donor and acceptor levels of organic photovoltaic compounds from first principles. *Phys. Chem. Chem. Phys.*, 15(2):685–695, 2013. 4, 71, 114
- [38] Eva Bundgaard and Frederik C. Krebs. Low band gap polymers for organic photovoltaics. *Sol. Energ. Mat. Sol. C.*, 91(11):954–985, 2007. 4, 71, 114
- [39] Kazunori Kuribara, He Wang, Naoya Uchiyama, Kenjiro Fukuda, Tomoyuki Yokota, Ute Zschieschang, Chernu Jaye, Daniel Fischer, Hagen Klauk, Tatsuya Yamamoto, et al. Organic transistors with high thermal stability for medical applications. *Nat. Commun.*, 3:723, 2012. 4, 71, 114
- [40] John E. Anthony. The larger acenes: Versatile organic semiconductors. *Angew. Chem. Int. Ed.*, 47(3):452–483, 2008. 4, 71, 114
- [41] Ching-Yao Lin, Yu-Chien Wang, Shun-Ju Hsu, Chen-Fu Lo, and Eric Wei-Guang Diau. Preparation and spectral, electrochemical, and photovoltaic properties of acene-modified zinc porphyrins. *J. Phys. Chem. C*, 114(1):687–693, 2009. 4, 71, 114
- [42] Zhe Sun, Zebing Zeng, and Jishan Wu. Benzenoid polycyclic hydrocarbons with an open-shell biradical ground state. *Chem. Asian J.*, 8(12):2894–2904, 2013. 4, 114
- [43] Marcia M. Payne, Sean R. Parkin, and John E. Anthony. Functionalized higher acenes: Hexacene and heptacene. *J. Am. Chem. Soc.*, 127(22):8028–8029, 2005. 4, 114
- [44] Irvinder Kaur, Mikael Jazdyk, Nathan N. Stein, Polina Prusevich, and Glen P. Miller. Design, synthesis, and characterization of a persistent nonacene derivative. *J. Am. Chem. Soc.*, 132(4):1261–1263, 2010. 4, 114

- 
- [45] Matthias Treier, Carlo Antonio Pignedoli, Teodoro Laino, Ralph Rieger, Klaus Müller, Daniele Passerone, and Roman Fasel. Surface-assisted cyclodehydrogenation provides a synthetic route towards easily processable and chemically tailored nanographenes. *Nat. Chem.*, 3(1):61–67, 2011. [4](#), [114](#)
- [46] Leo Gross. Recent advances in submolecular resolution with scanning probe microscopy. *Nat. Chem.*, 3(4):273–278, 2011. [4](#), [95](#), [114](#)
- [47] Leo Gross, Fabian Mohn, Nikolaj Moll, Peter Liljeroth, and Gerhard Meyer. The chemical structure of a molecule resolved by atomic force microscopy. *Science*, 325(5944):1110–1114, 2009. [4](#), [114](#)
- [48] S. Kivelson and OL. Chapman. Polyacene and a new class of quasi-one-dimensional conductors. *Phys. Rev. B*, 28(12):7236, 1983. [4](#), [73](#)
- [49] LJ Sham and M. Schlüter. Density-functional theory of the band gap. *Phys. Rev. B*, 32(6):3883, 1985. [4](#), [105](#)
- [50] Giovanni Onida, Lucia Reining, and Angel Rubio. Electronic excitations: Density-functional versus many-body green’s-function approaches. *Rev. Mod. Phys.*, 74(2):601, 2002. [4](#), [32](#), [105](#)
- [51] Ferdi Aryasetiawan and Olle Gunnarsson. The gw method. *Rep. Prog. Phys.*, 61(3):237, 1998. [4](#), [31](#), [32](#), [77](#), [105](#)
- [52] W. Bardyszewski and L. Hedin. A new approach to the theory of photoemission from solids. *Phys. Scripta*, 32(4):439, 1985. [4](#)
- [53] Lars Hedin. Effect of electron correlation on band structure of solids. *Ark. Fys.*, 30:231–558, 1965. [4](#)
- [54] Lars Hedin. On correlation effects in electron spectroscopies and the gw approximation. *J. Phys. Condens. Matter*, 11(42):R489, 1999. [4](#)
- [55] Michael Rohlfing and Steven G. Louie. Quasiparticle band structure of hgse. *Phys. Rev. B*, 57(16):R9392, 1998. [4](#), [32](#)
- [56] Hong Jiang, Ricardo I. Gomez-Abal, Patrick Rinke, and Matthias Scheffler. First-principles modeling of localized d states with the gw@lda+u approach. *Phys. Rev. B*, 82(4):045108, 2010. [4](#), [32](#)
- [57] Hong Jiang, Patrick Rinke, and Matthias Scheffler. Electronic properties of lanthanide oxides from the gw perspective. *Phys. Rev. B*, 86(12):125115, 2012. [4](#), [32](#)
- [58] M. Sabisch, P. Krüger, A. Mazur, M. Rohlfing, and J. Pollmann. First-principles calculations of  $\beta$ -sic (001) surfaces. *Phys. Rev. B*, 53(19):13121, 1996. [4](#), [32](#)
-

- [59] MJ van Setten, F. Weigend, and F. Evers. The gw-method for quantum chemistry applications: Theory and implementation. *J. Chem. Theory Comput.*, 9(1):232–246, 2012. 4, 32, 77, 105
- [60] Sivan Refaely-Abramson, Roi Baer, and Leeor Kronik. Fundamental and excitation gaps in molecules of relevance for organic photovoltaics from an optimally tuned range-separated hybrid functional. *Phys. Rev. B*, 84(7):075144, 2011. 4, 32, 105
- [61] Noa Marom, Xinguo Ren, Jonathan E. Moussa, James R. Chelikowsky, and Leeor Kronik. Electronic structure of copper phthalocyanine from g 0 w 0 calculations. *Phys. Rev. B*, 84(19):195143, 2011. 4, 32, 105
- [62] Sahar Sharifzadeh, Ariel Biller, Leeor Kronik, and Jeffrey B Neaton. Quasiparticle and optical spectroscopy of the organic semiconductors pentacene and ptcda from first principles. *Phys. Rev. B*, 85(12):125307, 2012. 4, 32, 105
- [63] Max Koentopp, Kieron Burke, and Ferdinand Evers. Zero-bias molecular electronics: Exchange-correlation corrections to landauer’s formula. *Phys. Rev. B*, 73(12):121403, 2006. 6, 106
- [64] Georg Heimel, Lorenz Romaner, Jean-Luc Brédas, and Egbert Zojer. Interface energetics and level alignment at covalent metal-molecule junctions:  $\pi$ -conjugated thiols on gold. *Phys. Rev. Lett.*, 96(19):196806, 2006. 6, 106
- [65] J. M. Garcia-Lastra and K. S. Thygesen. Renormalization of optical excitations in molecules near a metal surface. *Phys. Rev. Lett.*, 106:187402, May 2011. 6, 106
- [66] J. M. Garcia-Lastra, C. Rostgaard, A. Rubio, and K. S. Thygesen. Polarization-induced renormalization of molecular levels at metallic and semiconducting surfaces. *Phys. Rev. B*, 80:245427, Dec 2009. 6, 106
- [67] Kristian S. Thygesen and Angel Rubio. Renormalization of molecular quasiparticle levels at metal-molecule interfaces: Trends across binding regimes. *Phys. Rev. Lett.*, 102(4):046802, 2009. 6, 106, 109
- [68] Max Born and Robert Oppenheimer. Zur quantentheorie der molekeln. *Ann. Phys.*, 389(20):457–484, 1927. 8
- [69] Douglas R. Hartree. The wave mechanics of an atom with a non-coulomb central field. part i. theory and methods. In *Math. Proc. Cambridge*, volume 24, pages 89–110. Cambridge Univ Press, 1928. 9, 30
- [70] V Fock. Näherungsmethode zur lösung des quantenmechanischen mehrkörperproblems. *Z. Phys.*, 61(1-2):126–148, 1930. 9
- [71] Jorge Kohanoff. *Electronic Structure Calculations for Solids and Molecules: Theory and Computational Methods*. Cambridge University Press, 2006. 9

- 
- [72] Pierre Hohenberg and Walter Kohn. Inhomogeneous electron gas. *Phys. Rev.*, 136(3B):B864, 1964. [10](#)
- [73] W. Kohn and L. J. Sham. Self-consistent equations including exchange and correlation effects. *Phys. Rev.*, 140:A1133–A1138, Nov 1965. [12](#), [13](#)
- [74] David M. Ceperley and BJ Alder. Ground state of the electron gas by a stochastic method. *Phys. Rev. Lett.*, 45(7):566, 1980. [13](#)
- [75] John P. Perdew and Wang Yue. Accurate and simple density functional for the electronic exchange energy: Generalized gradient approximation. *Phys. Rev. B*, 33(12):8800, 1986. [14](#)
- [76] John P. Perdew, JA Chevary, SH Vosko, Koblar A. Jackson, Mark R. Pederson, DJ Singh, and Carlos Fiolhais. Atoms, molecules, solids, and surfaces: Applications of the generalized gradient approximation for exchange and correlation. *Phys. Rev. B*, 46(11):6671, 1992. [14](#)
- [77] Robert O. Jones and Olle Gunnarsson. The density functional formalism, its applications and prospects. *Rev. Mod. Phys.*, 61(3):689, 1989. [15](#)
- [78] John P. Perdew, Kieron Burke, and Matthias Ernzerhof. Generalized Gradient Approximation made Simple. *Phys. Rev. Lett.*, 77(18):3865, 1996. [15](#), [56](#), [57](#), [72](#), [83](#), [98](#)
- [79] John Hubbard. Electron correlations in narrow energy bands. In *Proc. Roy. Soc. Lond. A: Mathematical, Physical and Engineering Sciences*, volume 276, pages 238–257. The Royal Society, 1963. [16](#)
- [80] SL Dudarev, GA Botton, SY Savrasov, CJ Humphreys, and AP Sutton. Electron-energy-loss spectra and the structural stability of nickel oxide: An lsd+ u study. *Physical Review B*, 57(3):1505, 1998. [17](#), [63](#)
- [81] Stefan Grimme. Semiempirical gga-type density functional constructed with a long-range dispersion correction. *J. Comp. Chem.*, 27(15):1787–1799, 2006. [19](#), [60](#), [65](#), [83](#), [98](#), [107](#)
- [82] Alexandre Tkatchenko and Matthias Scheffler. Accurate molecular van der waals interactions from ground-state electron density and free-atom reference data. *Phys. Rev. Lett.*, 102(7):073005, 2009. [19](#), [57](#), [60](#), [65](#)
- [83] Erich Runge and Eberhard KU Gross. Density functional theory for time-dependent systems. *Phys. Rev. Lett.*, 52(12):997, 1984. [19](#)
- [84] E KU Gross and W. Kohn. Time-dependent density functional theory. *Adv. Quant. Chem*, 21:255–291, 1990. [19](#)
-

- [85] T. Koopmans. Ordering of wave functions and eigenenergies to the individual electrons of an atom. *Physica*, 1(1):104–113, 1933. [20](#), [77](#)
- [86] JF Janak. Proof that  $\frac{\partial \epsilon}{\partial n_i} = \epsilon$  in density-functional theory. *Phys. Rev. B*, 18(12):7165, 1978. [20](#)
- [87] Alexander L. Fetter and John Dirk Walecka. *Quantum theory of many-particle systems*. Courier Corporation, 2003. [21](#)
- [88] G. Strinati. Application of the green’s functions method to the study of the optical properties of semiconductors. *Riv. Nuovo Cimento*, 11(12):1–86, 1988. [22](#)
- [89] E.K.U. Gross, E. Runge, and O. Heinonen. Manyparticle theory (adam hilger, bristol, 1991). Technical report, ISBN 0-7503-0155-4. [22](#)
- [90] Richard D. Mattuck. *A Guide to Feynman Diagrams in the Many-body Problem*. Courier Corporation, 2012. [24](#)
- [91] H. Lehmann. Über eigenschaften von ausbreitungsfunktionen und renormierungskonstanten quantisierter felder. *Nuovo Cimento*, 11(4):342–357, 1954. [25](#)
- [92] Lars Hedin. New method for calculating the one-particle green’s function with application to the electron-gas problem. *Phys. Rev.*, 139(3A):A796, 1965. [25](#), [77](#), [105](#)
- [93] Julian Schwinger. On the green’s functions of quantized fields. *Proc. Natl. Acad. Sci.*, 37(7):452–455, 1951. [25](#)
- [94] Fabien Bruneval. Exchange and correlation in the electronic structure of solids, from silicon to cuprous oxide: Gw approximation and beyond. *PhD Thesis*, 2005. [31](#)
- [95] L. Hedin, A. Johansson, BI Lundqvist, S. Lundqvist, and V. Samathiyakanit. Effects of electron–electron interaction on the one-electron properties of atoms and solids. Technical report, Inst. of Theoretical Physics, Goteborg, 1969. [31](#)
- [96] Mark S. Hybertsen and Steven G. Louie. Electron correlation in semiconductors and insulators: Band gaps and quasiparticle energies. *Phys. Rev. B*, 34(8):5390, 1986. [31](#), [32](#), [105](#)
- [97] Mark S. Hybertsen and Steven G. Louie. First-principles theory of quasiparticles: Calculation of band gaps in semiconductors and insulators. *Phys. Rev. Lett.*, 55(13):1418, 1985. [31](#)
- [98] G. Kresse and J. Furthmüller. Software vasp, vienna (1999). *Phys. Rev. B*, 54(11):169, 1996. [32](#), [40](#), [41](#), [60](#), [65](#), [72](#), [83](#), [98](#), [107](#)
- [99] P. E. Blöchl. Projector augmented-wave method. *Phys. Rev. B*, 50:17953–17979, Dec 1994. [32](#), [40](#), [41](#), [60](#), [72](#), [83](#), [98](#), [107](#)

- 
- [100] F. Fuchs, J. Furthmüller, F. Bechstedt, M. Shishkin, and G. Kresse. Quasiparticle band structure based on a generalized kohn-sham scheme. *Phys. Rev. B*, 76(11):115109, 2007. [32](#)
- [101] Fabien Bruneval and Miguel AL Marques. Benchmarking the starting points of the gw approximation for molecules. *J. Chem. Theory Comp.*, 9(1):324–329, 2012. [32](#), [105](#)
- [102] Gordon Baym and Leo P. Kadanoff. Conservation laws and correlation functions. *Phys. Rev.*, 124(2):287, 1961. [32](#)
- [103] Leo P. Kadanoff and Gordon A. Baym. *Quantum Statistical Mechanics Green's Function Methods in Equilibrium Problems*. Benjamin, 1962. [32](#)
- [104] M. Shishkin and G. Kresse. Self-consistent gw calculations for semiconductors and insulators. *Phys. Rev. B*, 75(23):235102, 2007. [32](#), [41](#)
- [105] Noa Marom, Fabio Caruso, Xinguo Ren, Oliver T. Hofmann, Thomas Körzdörfer, James R. Chelikowsky, Angel Rubio, Matthias Scheffler, and Patrick Rinke. Benchmark of gw methods for azabenzenes. *Phys. Rev. B*, 86(24):245127, 2012. [32](#), [105](#)
- [106] Sergey V. Faleev, Mark van Schilfgaarde, and Takao Kotani. All-electron self-consistent gw approximation: Application to si, mno, and nio. *Phys. Rev. Lett.*, 93(12):126406, 2004. [33](#)
- [107] Mark van Schilfgaarde, Takao Kotani, and S. Faleev. Quasiparticle self-consistent gw theory. *Phys. Rev. Lett.*, 96(22):226402, 2006. [33](#)
- [108] Athanasios N. Chantis, Mark van Schilfgaarde, and Takao Kotani. Quasiparticle self-consistent gw method applied to localized 4 f electron systems. *Phys. Rev. B*, 76(16):165126, 2007. [33](#)
- [109] Axel Svane, Niels Egede Christensen, M. Cardona, AN Chantis, M. Van Schilfgaarde, and T. Kotani. Quasiparticle self-consistent gw calculations for pbs, pbse, and pbte: Band structure and pressure coefficients. *Phys. Rev. B*, 81(24):245120, 2010. [33](#)
- [110] Adrian Stan, Nils Erik Dahlen, and Robert Van Leeuwen. Fully self-consistent gw calculations for atoms and molecules. *EPL*, 76(2):298, 2006. [33](#)
- [111] Wolf-Dieter Schöne and Adolfo G. Eguiluz. Self-consistent calculations of quasiparticle states in metals and semiconductors. *Phys. Rev. Lett.*, 81(8):1662, 1998. [33](#)
- [112] HJ De Groot, PA Bobbert, and W. Van Haeringen. Self-consistent gw for a quasi-one-dimensional semiconductor. *Phys. Rev. B*, 52(15):11000, 1995. [33](#)
- [113] Bengt Holm. Total energies from gw calculations. *Phys. Rev. Lett.*, 83(4):788, 1999. [33](#)
-

- [114] Andrey Kutepov, Sergey Y Savrasov, and Gabriel Kotliar. Ground-state properties of simple elements from gw calculations. *Phys. Rev. B*, 80(4):041103, 2009. [33](#)
- [115] David J. Singh and Lars Nordstrom. *Planewaves, Pseudopotentials, and the LAPW method*. Springer Science & Business Media, 2006. [34](#)
- [116] Peter E. Blöchl. Projector augmented-wave method. *Phys. Rev. B*, 50(24):17953, 1994. [35](#)
- [117] Xinguo Ren, Patrick Rinke, Volker Blum, Jürgen Wieferink, Alexandre Tkatchenko, Andrea Sanfilippo, Karsten Reuter, and Matthias Scheffler. Resolution-of-identity approach to hartree–fock, hybrid density functionals, rpa, mp2 and gw with numeric atom-centered orbital basis functions. *New J. Phys.*, 14(5):053020, 2012. [40](#)
- [118] M. Shishkin and G. Kresse. Implementation and performance of the frequency-dependent gw method within the paw framework. *Phys. Rev. B*, 74(3):035101, 2006. [41](#), [43](#), [44](#)
- [119] Xinguo Ren, Patrick Rinke, Christian Joas, and Matthias Scheffler. Random-phase approximation and its applications in computational chemistry and materials science. *J. Mater. Sci.*, 47(21):7447–7471, 2012. [41](#)
- [120] Dante Gatteschi and Roberta Sessoli. Quantum tunneling of magnetization and related phenomena in molecular materials. *Angew. Chem. Int. Ed.*, 42(3):268–297, 2003. [45](#)
- [121] Wenjie Liang, Matthew P. Shores, Marc Bockrath, Jeffrey R. Long, and Hongkun Park. Kondo resonance in a single-molecule transistor. *Nature*, 417(6890):725–729, 2002. [45](#)
- [122] Stefan Wagner, Ferdinand Kisslinger, Stefan Ballmann, Frank Schramm, Rajadurai Chandrasekar, Tilmann Bodenstern, Olaf Fuhr, Daniel Secker, Karin Fink, Mario Ruben, et al. Switching of a coupled spin pair in a single-molecule junction. *Nat. Nanotechnol.*, 8(8):575–579, 2013. [45](#)
- [123] W. Meissner and B. Voigt. Messungen mit hilfe von flüssigem helium xi widerstand der reinen metalle in tiefen temperaturen. *Ann. Phys.*, 399(8):892–936, 1930. [45](#)
- [124] WJ De Haas, J. De Boer, and GJ Van den Berg. The electrical resistance of gold, copper and lead at low temperatures. *Physica*, 1(7):1115–1124, 1934. [45](#)
- [125] Jun Kondo. Effect of ordinary scattering on exchange scattering from magnetic impurity in metals. *Phys. Rev.*, 169(2):437, 1968. [45](#)
- [126] Philip Warren Anderson. Localized magnetic states in metals. *Phys. Rev.*, 124(1):41, 1961. [46](#)

- 
- [127] JR Schrieffer and PA Wolff. Relation between the anderson and kondo hamiltonians. *Phys. Rev.*, 149(2):491, 1966. [46](#), [47](#)
- [128] Alexander Cyril Hewson. *The Kondo Problem to Heavy Fermions*, volume 2. Cambridge university press, 1997. [47](#)
- [129] Gerd Binnig and Heinrich Rohrer. Scanning tunneling microscopy. 1982. [48](#)
- [130] Gerd Binnig, Heinrich Rohrer, Ch. Gerber, and E. Weibel. Surface studies by scanning tunneling microscopy. *Phys. Rev. Lett.*, 49(1):57, 1982. [48](#)
- [131] Gerd Binnig, Heinrich Rohrer, Ch. Gerber, and Eddie Weibel. Tunneling through a controllable vacuum gap. *Appl. Phys. Lett.*, 40(2):178–180, 1982. [48](#)
- [132] Gerd Binnig, Heinrich Rohrer, Ch. Gerber, and Eduard Weibel.  $7 \times 7$  reconstruction on si (111) resolved in real space. *Phys. Rev. Lett.*, 50(2):120, 1983. [48](#)
- [133] Donald M. Eigler and Erhard K. Schweizer. Positioning single atoms with a scanning tunnelling microscope. *Nature*, 344(6266):524–526, 1990. [48](#)
- [134] S. Heinze, M. Bode, A. Kubetzka, O. Pietzsch, X. Nie, S. Blügel, and R. Wiesendanger. Real-space imaging of two-dimensional antiferromagnetism on the atomic scale. *Science*, 288(5472):1805–1808, 2000. [48](#)
- [135] AJ Heinrich, JA Gupta, CP Lutz, and DM Eigler. Single-atom spin-flip spectroscopy. *Science*, 306(5695):466–469, 2004. [49](#)
- [136] Sebastian Loth, Kirsten von Bergmann, Markus Ternes, Alexander F. Otte, Christopher P. Lutz, and Andreas J. Heinrich. Controlling the state of quantum spins with electric currents. *Nature Phys.*, 6(5):340–344, 2010. [49](#)
- [137] Stefan Heinze. *First-Principles Theory of Scanning Tunneling Microscopy Applied to Transition-Metal Surfaces*. PhD thesis, 2000. [49](#)
- [138] C. Julian Chen. *Introduction to Scanning Tunneling Microscopy*. Oxford University Press, 2008. [49](#)
- [139] Ernst Meyer, Hans Josef Hug, and Roland Bennewitz. Introduction to scanning tunneling microscopy. In *Scanning Probe Microscopy*, pages 15–44. Springer, 2004. [49](#)
- [140] John Bardeen. Tunnelling from a many-particle point of view. *Phys. Rev. Lett.*, 6(2):57, 1961. [49](#)
- [141] J. Tersoff and DR Hamann. Theory and application for the scanning tunneling microscope. *Phys. Rev. Lett.*, 50(25):1998, 1983. [50](#), [60](#), [65](#), [95](#)
- [142] J. Tersoff and D. R. Hamann. Theory of the scanning tunneling microscope. *Phys. Rev. B*, 31:805–813, 1985. [50](#)
-

- [143] Ugo Fano. Effects of configuration interaction on intensities and phase shifts. *Phys. Rev.*, 124(6):1866, 1961. [51](#)
- [144] O. Újsághy, J. Kroha, L. Szunyogh, and A. Zawadowski. Theory of the fano resonance in the stm tunneling density of states due to a single kondo impurity. *Physical Rev. Lett.*, 85(12):2557, 2000. [51](#)
- [145] J. Merino and O. Gunnarsson. Simple model for scanning tunneling spectroscopy of noble metal surfaces with adsorbed kondo impurities. *Phys. Rev. B*, 69(11):115404, 2004. [51](#)
- [146] M. Plihal and JW Gadzuk. Nonequilibrium theory of scanning tunneling spectroscopy via adsorbate resonances: Nonmagnetic and kondo impurities. *Phys. Rev. B*, 63(8):085404, 2001. [51](#)
- [147] K. Nagaoka, T. Jamneala, M. Grobis, and MF Crommie. Temperature dependence of a single kondo impurity. *Phys. Rev. Lett.*, 88(7):077205, 2002. [51](#)
- [148] Ansgar Schäfer, Hans Horn, and Reinhart Ahlrichs. Fully optimized contracted gaussian basis sets for atoms li to kr. *J. Chem. Phys.*, 97(4):2571–2577, 1992. [56](#)
- [149] Karin Eichkorn, Oliver Treutler, Holger Öhm, Marco Häser, and Reinhart Ahlrichs. Auxiliary basis sets to approximate coulomb potentials. *Chem. Phys. Lett.*, 240(4):283–290, 1995. [56](#)
- [150] A. Arnold, F. Weigend, and F. Evers. Quantum chemistry calculations for molecules coupled to reservoirs: Formalism, implementation, and application to benzenedithiol. *J. Chem. Phys.*, 126(17):174101, 2007. [58](#), [60](#), [65](#)
- [151] Jan Wilhelm, Michael Walz, Melanie Stendel, Alexei Bagrets, and Ferdinand Evers. Ab initio simulations of scanning-tunneling-microscope images with embedding techniques and application to c 58-dimers on au (111). *Phys. Chem. Chem. Phys.*, 15(18):6684–6690, 2013. [58](#), [60](#)
- [152] Alexei Bagrets. Spin-polarized electron transport across metal–organic molecules: A density functional theory approach. *J. Chem. Theory Comput.*, 9(6):2801–2815, 2013. [58](#)
- [153] Hermann Grabert and Michel H. Devoret. *Single Charge Tunneling: Coulomb Blockade Phenomena in Nanostructures*, volume 294. Springer Science & Business Media, 2013. [63](#)
- [154] Matthew J. Allen, Vincent C. Tung, and Richard B. Kaner. Honeycomb carbon: a review of graphene. *Chem. Rev.*, 110(1):132–145, 2009. [71](#)
- [155] Wonbong Choi, Indranil Lahiri, Raghunandan Seelaboyina, and Yong Soo Kang. Synthesis of graphene and its applications: a review. *Crit. Rev. Solid State Mater. Sci.*, 35(1), 2010. [71](#)

- 
- [156] Toshiaki Enoki, Yousuke Kobayashi, and Ken-Ichi Fukui. Electronic structures of graphene edges and nanographene. *Int. Rev. Phys. Chem.*, 26(4):609–645, 2007. [71](#)
- [157] S. Kivelson and O. L. Chapman. Polyacene and a new class of quasi-one-dimensional conductors. *Phys. Rev. B*, 28:7236–7243, Dec 1983. [71](#)
- [158] Kenneth B. Wiberg. Properties of some condensed aromatic systems. *J. Org. Chem.*, 62(17):5720–5727, 1997. [71](#)
- [159] Michael Bendikov, Fred Wudl, and Dmitrii F. Perepichka. Tetrathiafulvalenes, oligoacenenes, and their buckminsterfullerene derivatives: The brick and mortar of organic electronics. *Chem. Rev.*, 104(11):4891–4946, 2004. [71](#)
- [160] Zhe Sun, Qun Ye, Chunyan Chi, and Jishan Wu. Low band gap polycyclic hydrocarbons: from closed-shell near infrared dyes and semiconductors to open-shell radicals. *Chem. Soc. Rev.*, 41(23):7857–7889, 2012. [71](#)
- [161] Erik van Lenthe, Evert-Jan Baerends, and Jaap G. Snijders. Relativistic total energy using regular approximations. *J. Chem. Phys.*, 101(11):9783–9792, 1994. [72](#)
- [162] Paula Mori-Sánchez. A fractional view of the exchange-correlation functional in density-functional theory. 2010. [79](#)
- [163] Kenji Toyoda, Ikutaro Hamada, Kyuho Lee, Susumu Yanagisawa, and Yoshitada Morikawa. Density functional theoretical study of pentacene/noble metal interfaces with van der waals corrections: Vacuum level shifts and electronic structures. *J. Chem. Phys.*, 132(13):134703, 2010. [83](#), [84](#)
- [164] CB France, PG Schroeder, JC Forsythe, and BA Parkinson. Scanning tunneling microscopy study of the coverage-dependent structures of pentacene on au (111). *Langmuir*, 19(4):1274–1281, 2003. [84](#)
- [165] Wei Liu, Victor G Ruiz, Guo-Xu Zhang, Biswajit Santra, Xinguo Ren, Matthias Scheffler, and Alexandre Tkatchenko. Structure and energetics of benzene adsorbed on transition-metal surfaces: Density-functional theory with van der waals interactions including collective substrate response. *New J. Phys.*, 15(5):053046, 2013. [84](#)
- [166] Paul A. Anderson. Work function of gold. *Phys. Rev.*, 115:553–554, Aug 1959. [86](#)
- [167] Sebastijan Peljhan and Anton Kokalj. Adsorption of chlorine on cu (111): A density-functional theory study. *J. Phys. Chem. C*, 113(32):14363–14376, 2009. [86](#)
- [168] Richard FW Bader. Atoms in molecules: a quantum theory. international series of monographs on chemistry 22, 1990. [89](#)
- [169] W. Tang, E. Sanville, and G. Henkelman. A grid-based bader analysis algorithm without lattice bias. *J. Phys. Cond. Mat.*, 21(8):084204, 2009. [89](#)
-

- [170] Edward Sanville, Steven D. Kenny, Roger Smith, and Graeme Henkelman. Improved grid-based algorithm for bader charge allocation. *J. Comp. Chem.*, 28(5):899–908, 2007. [89](#)
- [171] L. J. Sham and M. Schlüter. Density-functional theory of the band gap. *Phys. Rev. B*, 32:3883–3889, Sep 1985. [93](#)
- [172] Axel D. Becke and Erin R. Johnson. A simple effective potential for exchange. *J. Chem. Phys.*, 124(22):221101, 2006. [93](#)
- [173] Fabien Tran and Peter Blaha. Accurate band gaps of semiconductors and insulators with a semilocal exchange-correlation potential. *Phys. Rev. Lett.*, 102(22):226401, 2009. [93](#)
- [174] BE Deal and C. Robert Helms. *The physics and chemistry of SiO<sub>2</sub> and the Si-SiO<sub>2</sub> interface*. Springer Science & Business Media, 2013. [96](#)
- [175] G-M Rignanese, Alessandro De Vita, J-C Charlier, Xavier Gonze, and Roberto Car. First-principles molecular-dynamics study of the (0001)  $\alpha$ - quartz surface. *Phys. Rev. B*, 61(19):13250, 2000. [96](#), [97](#)
- [176] TPM Goumans, Adrian Wander, Wendy A Brown, and C Richard A Catlow. Structure and stability of the (001)  $\alpha$ -quartz surface. *Phys. Chem. Chem. Phys.*, 9(17):2146–2152, 2007. [96](#), [97](#)
- [177] Nora H de Leeuw, F Manon Higgins, and Stephen C Parker. Modeling the surface structure and stability of  $\alpha$ -quartz. *J. Phys. Chem. B*, 103(8):1270–1277, 1999. [96](#)
- [178] BP Lemke and D. Haneman. Dangling bonds on silicon. *Phys. Rev. B*, 17(4):1893, 1978. [96](#)
- [179] JT Yates Jr. Surface chemistry of silicon-the behaviour of dangling bonds. *J. Phys.: Condens. Matter*, 3(S):S143, 1991. [96](#)
- [180] Peter Broqvist, Audrius Alkauskas, and Alfredo Pasquarello. Defect levels of dangling bonds in silicon and germanium through hybrid functionals. *Phys. Rev. B*, 78(7):075203, 2008. [96](#)
- [181] Nikita I Vakula, Gulnara M Kuramshina, Leonid G Gorb, Frances Hill, and Jerzy Leszczynski. Adsorption and diffusion of a silver atom and its cation on  $\alpha$ -sio<sub>2</sub> (001): Comparison of a pure surface with a surface containing an al defect. *Chem. Phys. Lett.*, 567:27–33, 2013. [97](#)
- [182] G-M Rignanese, J-C Charlier, and Xavier Gonze. First-principles molecular-dynamics investigation of the hydration mechanisms of the (0001)  $\alpha$ -quartz surface. *Phys. Chem. Chem. Phys.*, 6(8):1920–1925, 2004. [97](#)

- 
- [183] Thanh Cuong Nguyen, Minoru Otani, and Susumu Okada. Semiconducting electronic property of graphene adsorbed on (0001) surfaces of sio 2. *Phys. Rev. Lett.*, 106(10):106801, 2011. [97](#)
- [184] Konstantin S. Novoselov, VI Fal, L. Colombo, PR Gellert, MG Schwab, K. Kim, et al. A roadmap for graphene. *Nature*, 490(7419):192–200, 2012. [97](#)
- [185] P. Havu, M. Ijäs, and A. Harju. Hydrogenated graphene on silicon dioxide surfaces. *Phys. Rev. B*, 84(20):205423, 2011. [97](#)
- [186] Jian-Hao Chen, Chaun Jang, Shudong Xiao, Masa Ishigami, and Michael S Fuhrer. Intrinsic and extrinsic performance limits of graphene devices on sio2. *Nat. Nanotechnol.*, 3(4):206–209, 2008. [97](#)
- [187] Wei Ku, Tom Berlijn, Chi-Cheng Lee, et al. Unfolding first-principles band structures. *Phys. Rev. Lett.*, 104(21):216401, 2010. [99](#)
- [188] Yong Zhang and Lin-Wang Wang. Global electronic structure of semiconductor alloys through direct large-scale computations for iii-v alloys  $ga_x in 1-x p$ . *Phys. Rev. B*, 83(16):165208, 2011. [99](#)
- [189] Timothy B. Boykin and Gerhard Klimeck. Practical application of zone-folding concepts in tight-binding calculations. *Phys. Rev. B*, 71(11):115215, 2005. [99](#)
- [190] Timothy B. Boykin, Neerav Kharche, Gerhard Klimeck, and Marek Korkusinski. Approximate bandstructures of semiconductor alloys from tight-binding supercell calculations. *J. Phys.: Condens. Matter*, 19(3):036203, 2007. [99](#)
- [191] Voicu Popescu and Alex Zunger. Extracting  $e$  versus  $k$  effective band structure from supercell calculations on alloys and impurities. *Phys. Rev. B*, 85(8):085201, 2012. [99](#)
- [192] Paulo VC Medeiros, Sven Stafström, and Jonas Björk. Effects of extrinsic and intrinsic perturbations on the electronic structure of graphene: Retaining an effective primitive cell band structure by band unfolding. *Phys. Rev. B*, 89(4):041407, 2014. [99](#)
- [193] Fabio Caruso, Patrick Rinke, Xinguo Ren, Matthias Scheffler, and Angel Rubio. Unified description of ground and excited states of finite systems: The self-consistent gw approach. *Physical Review B*, 86(8):081102, 2012. [105](#)
- [194] Jascha Repp, Gerhard Meyer, Sami Paavilainen, Fredrik E Olsson, and Mats Persson. Imaging bond formation between a gold atom and pentacene on an insulating surface. *Science*, 312(5777):1196–1199, 2006. [105](#)
- [195] J. Repp and G. Meyer. Scanning tunneling microscopy of adsorbates on insulating films. from the imaging of individual molecular orbitals to the manipulation of the charge state. *Appl. Phys. A*, 85(4):399–406, 2006. [106](#)
-

- [196] Jascha Repp, Gerhard Meyer, Sladjana M. Stojković, André Gourdon, and Christian Joachim. Molecules on insulating films: Scanning-tunneling microscopy imaging of individual molecular orbitals. *Phys. Rev. Lett.*, 94(2):026803, 2005. [106](#)
- [197] J. Berkowitz, JP Greene, H. Cho, and B. Ruscić. The ionization potentials of ch<sub>4</sub> and cd<sub>4</sub>. *J. Chem. Phys.*, 86(2):674–676, 1987. [108](#)
- [198] Jennifer W. Au, Glyn Cooper, and CE Brion. The molecular and dissociative photoionization of ethane, propane, and n-butane: absolute oscillator strengths (10–80 ev) and breakdown pathways. *Chem. Phys.*, 173(2):241–265, 1993. [108](#)
- [199] Koichi Ohno, Kohji Okamura, Hideo Yamakado, Shigeo Hoshino, Tomohide Takami, and Masayo Yamauchi. Penning ionization of hcho, ch<sub>2</sub>ch<sub>2</sub>, and ch<sub>2</sub>chcho by collision with he (23s) metastable atoms. *J. Phys. Chem.*, 99(39):14247–14253, 1995. [108](#)
- [200] Marco Govoni and Giulia Galli. Large scale gw calculations. *Journal of Chemical Theory and Computation*, 2015. [110](#), [114](#)
- [201] RM Fye, JE Hirsch, and DJ Scalapino. Kondo effect versus indirect exchange in the two-impurity anderson model: A monte carlo study. *Physical Review B*, 35(10):4901, 1987. [113](#)
- [202] Jorge E. Hirsch and R. Martin Fye. Monte carlo method for magnetic impurities in metals. *Physical review letters*, 56(23):2521, 1986. [113](#)
- [203] S. Biermann, F. Aryasetiawan, and A. Georges. First-principles approach to the electronic structure of strongly correlated systems: Combining the gw approximation and dynamical mean-field theory. *Physical review letters*, 90(8):086402, 2003. [113](#)
- [204] C. Jayaprakash, HR Krishna-Murthy, and JW Wilkins. Two-impurity kondo problem. *Physical Review Letters*, 47(10):737, 1981. [113](#)
- [205] Walter Hofstetter and Herbert Schoeller. Quantum phase transition in a multilevel dot. *Physical review letters*, 88(1):016803, 2001. [113](#)
- [206] Holger F. Bettinger. Electronic structure of higher acenes and polyacene: The perspective developed by theoretical analyses. *Pure Appl. Chem.*, 82(4):905–915, 2010. [114](#)
- [207] F. Djeghloul, F. Ibrahim, M. Cantoni, M. Bowen, L. Joly, S. Boukari, P. Ohresser, F. Bertran, P. Le Fevre, P. Thakur, et al. Direct observation of a highly spin-polarized organic spinterface at room temperature. *Scientific reports*, 3, 2013. [115](#)



Dimitra XENIOTI

## Effect of electronic correlation on molecules adsorbed on metallic surfaces

### Résumé en français

La combinaison de la spintronique et de l'électronique organique est censée conduire à une nouvelle gamme d'applications en la domaine de spintronique organique. Ce travail se concentre sur la physique des molécules organiques adsorbées sur des surfaces métalliques et les changements de leurs structures électroniques en raison de l'effet important du substrat métallique. Nous avons étudié le complexe  $\text{Ni}_2$  adsorbé sur le  $\text{Cu}(001)$  qui montre un effet Kondo à basses températures. Nous avons ensuite étudié des chaînes d'oligoacènes (anneaux de benzène fusionnés) qui présentent une propriété prédite: une oscillation de la bande interdite d'énergies en fonction de la longueur de la molécule. Cette propriété peut survivre même lorsque la molécule est adsorbée sur une surface, comme l' $\text{Au}(111)$  ou le  $\text{SiO}_2$ . Pour terminer, nous avons étudié des petites molécules, telles que l'éthane ou l'éthylène, adsorbées sur un substrat de  $\text{Cu}(001)$  et de  $\text{Co}(001)$ . La différence d'énergie entre l'orbitale vide la plus basse (LUMO) et l'orbitale moléculaire occupée la plus élevée (HOMO) est étudiée dans les approximations de la théorie de la fonctionnelle de la densité (DFT) et la méthode  $\text{GW}$ .

**Mots-Clés:** *ab initio*, DFT,  $\text{GW}$ , électronique organique, spintronique, Kondo, oligoacènes

### Résumé en anglais

The combination of spintronics and organic electronics, is believed to lead to a new generation of spin based devices, which would likely open a new broad range of applications in the field of organic spintronics. In this context, this work focuses on organic molecules adsorbed on metallic surfaces and their electronic structure changes due to the important screening of the metallic environment. We have studied different systems, starting with a  $\text{Ni}_2$  complex adsorbed on  $\text{Cu}(001)$ , where Kondo effect sets in. This study is followed by oligoacene chains (fused benzene rings) where an extraordinary property is seen: an oscillation of the energy band gap with respect to the molecular length. This property is proved to survive under the screening of surfaces such as  $\text{Au}(111)$  and  $\text{SiO}_2$ . We finally focused on small molecules, like ethane and ethylene, adsorbed on  $\text{Cu}$  and  $\text{Co}$ . The difference of energy between the lowest unoccupied molecular orbital (LUMO) and the highest occupied molecular orbital (HOMO) is studied using density functional theory (DFT) and  $\text{GW}$  methodologies.

**Mots-Clés:** *ab initio*, DFT,  $\text{GW}$ , organic electronics, spintronics, Kondo, oligoacenes



---

ÉCOLE DOCTORALE DE PHYSIQUE ET CHIMIE-PHYSIQUE

DOMAINE DE RECHERCHE : PHYSIQUE

**Dimitra XENIOTI**

---

**Effet de corrélation électronique sur les molécules  
adsorbées sur des surfaces métalliques**

---

---

Aujourd'hui, il est tout à fait clair que la technologie basée sur la microélectronique du silicium a atteint ses limites de performance, conduisant les chercheurs à l'élaboration de nouveaux paradigmes électroniques, technologiques et informatiques. Après la découverte de la magnétorésistance tunnel (TMR) et de la magnétorésistance géante (GMR), nous sommes confrontés à une grande révolution de la mémoire informatique et des capacités de stockage magnétiques des disques durs modernes, à un rythme sans cesse croissant. En même temps, l'attention des chercheurs est aujourd'hui focalisée sur des matériaux organiques pour substituer la microélectronique du silicium, car ces matériaux ne coûtent pas cher à produire, et sont de plus flexibles et diversifiés dans leurs applications. La combinaison de la spintronique et de l'électronique organique est censée conduire à une nouvelle génération de dispositifs à base de spin, susceptible d'ouvrir une nouvelle gamme d'applications et une nouvelle génération de produits en spintronique organique.

Un autre grand défi pour les chercheurs serait de remplacer dans un futur proche, les transistors à base de silicium par des transistors moléculaires. Pour ce faire, beaucoup d'efforts expérimentaux et théoriques ont déjà été accomplis. Les simples magnets moléculaires (SMM) ont attiré beaucoup d'attention, car le temps de relaxation magnétique à basses températures peut être de l'ordre de plusieurs années. Cependant, pour des applications comme le stockage de données magnétiques, les SMM doivent être déposés sur un substrat de soutien. De plus, une bonne compréhension de l'interaction entre les molécules et les fils métalliques est indispensable pour accéder à de nouveaux progrès dans ce domaine.

Dans ce contexte, ce travail se concentre sur la physique des molécules organiques adsorbées sur des surfaces métalliques, en mettant l'accent plus particulièrement sur les changements de leurs structures électroniques en raison de l'effet important du substrat métallique. Nous avons d'abord étudié le complexe  $\text{Ni}_2$  adsorbé sur le  $\text{Cu}(001)$  qui montre un effet Kondo à basses températures. Nous avons ensuite étudié des chaînes d'oligoacènes (anneaux de benzène fusionnés) qui présentent une propriété prédite, pour la première fois, par nos calculs, à savoir une oscillation de la bande interdite d'énergies en fonction de la longueur de la macro-molécule. Nous avons ensuite montré que cette propriété peut survivre même lorsque la molécule est adsorbée sur une surface métallique, telle que celle de l' $\text{Au}(111)$  ou de  $\text{SiO}_2(001)$ . Pour terminer cette thèse, nous avons montré que le calcul des quasiparticules dans l'approximation GW permet de corriger la différence d'énergie entre l'orbitale vide la plus basse (LUMO) et l'orbitale moléculaire occupée la plus élevée (HOMO), et que les résultats sont en très bon accord avec l'expérience. Comme la méthode GW

---

est très coûteuse en temps de calcul, nous avons uniquement étudié les petites molécules, telles que l'éthane ou l'éthylène. Nos calculs montrent également que lorsque les molécules sont adsorbées sur un substrat de Co(001), ces molécules sont polarisées en spin et la différence d'énergie entre la LUMO et la HOMO est réduite d'une manière significative.

Il est bien connu que, selon les lois de la physique quantique, les molécules confinent les électrons dans les niveaux discrets d'énergies, tandis que les métaux offrent un continuum d'états possibles pour le nuage électronique. La forte hybridation des états moléculaires avec les électrons d'un substrat métallique peut, sous certaines conditions, conduire à l'effet Kondo. Cette physique de premier plan de la physique des électrons corrélés a été observée tout d'abord dans les métaux avec une petite quantité d'impuretés magnétiques, où l'effet Kondo conduit à une résistivité anormale à basses températures. En même temps, les moments magnétiques des impuretés sont écrantés par des électrons itinérants du métal dans lequel les impuretés sont implantées. L'effet Kondo, de nos jours, a été relancé dans le cadre de systèmes mésoscopiques et dans les nanosciences, en particulier, dans les adsorbats moléculaires et jonctions moléculaires. Lorsque la molécule est dans une configuration "break-jonction" ou dans un "setup" STM (microscopie à effet tunnel), le transport à basse température à faible polarisation est régi par l'effet Kondo, qui donne lieu à une résonance Kondo forte dans le spectre de la conductance différentielle, ouvrant ainsi une nouvelle façon de transport cohérent dans l'électronique moléculaire.

De nos jours, il est possible de régler le système de façon contrôlée, à partir du régime Kondo, à un régime où les électrons sont décorrélés. Par exemple, ce réglage peut être réalisé en modifiant la conformation moléculaire sans altérer la composition chimique. Faire apparaître ou disparaître l'effet Kondo fournit des moyens d'exercer un contrôle de spin qui est de plus grand intérêt pour la spintronique.

Notre travail est motivé par des mesures STM à basses températures effectuées sur une molécule organique de métal-binucléaire, dite Ni(hexafluoro-acétylacétonate)<sub>2</sub>-bipyrimidine<sub>2</sub>(Ni<sub>2</sub>), déposée sur une surface de Cu(001) Fig. 0.1.

L'expérience révèle que ce système présente un effet Kondo, avec un spin localisé à proximité des atomes de Ni, et une température Kondo  $T_K$  de l'ordre de  $\sim 10\text{K}$ ; et cette température varie en fonction du type d'adsorption. La physique mise en jeu est intrigante, parce que l'effet Kondo a lieu en présence de deux spins portés par l'ion Ni<sup>2+</sup>, qui sont en concurrence pour l'écrantage par les électrons de conduction.

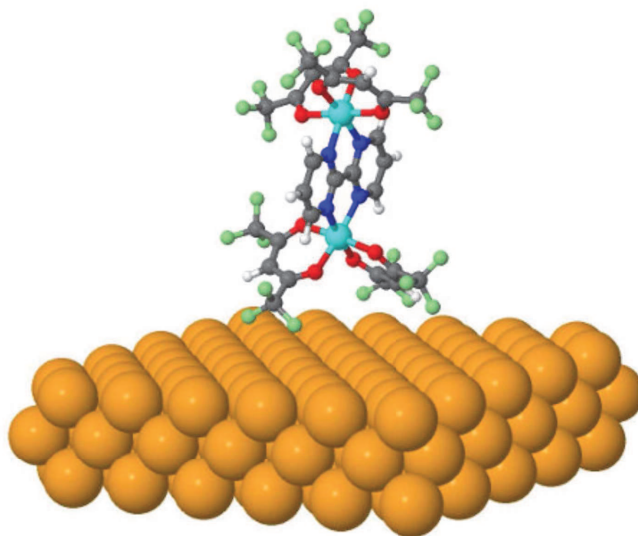


FIGURE 0.1 – Complexe de  $\text{Ni}_2$  adsorbé sur la surface de  $\text{Cu}(001)$ .

En outre, la molécule synthétisée ne possède pas de groupe d’ancrage, qui pourrait être responsable de la formation d’une liaison chimique avec la surface de cuivre. Sans cette liaison chimique avec le substrat, il est très difficile de justifier cette température de Kondo relativement élevée. Motivé par cette énigme, nous avons présenté une analyse fondée sur la théorie de la fonctionnelle de la densité (DFT) pour comprendre la structure électronique des complexes organo-métalliques à base de nickel déposés sur la surface  $\text{Cu}(001)$ . Nos résultats montrent que pour l’une des géométries, une température Kondo relativement grande ( $T_K \sim 10$  K) peut être obtenue et attribuée aux complexes  $\text{Ni}_2$  déformés, et par conséquent chimiquement liés à la surface par le groupe bipyrimidine de la molécule (Fig. 0.2).

La seconde géométrie, observée par les expériences STM, est attribuée à la fragmentation de la molécule (Fig. 0.3).

Nous avons admis que la molécule originale binucléaire se décompose en deux parties. la moitié formée par le  $\text{Ni}(\text{hexafluoroacétylacétonate})_2$  se lie au substrat de cuivre. Pour les deux géométries, nos calculs montrent un effet Kondo de spin ( $S = 1$ ) qui émerge en raison de la couche 3d ouverte des ions  $\text{Ni}^{2+}$ . L’utilisation du modèle d’Anderson et la densité des états projetés sur les atomes Ni de la structure, permettent d’estimer des températures Kondo, en bon accord avec les valeurs expé-

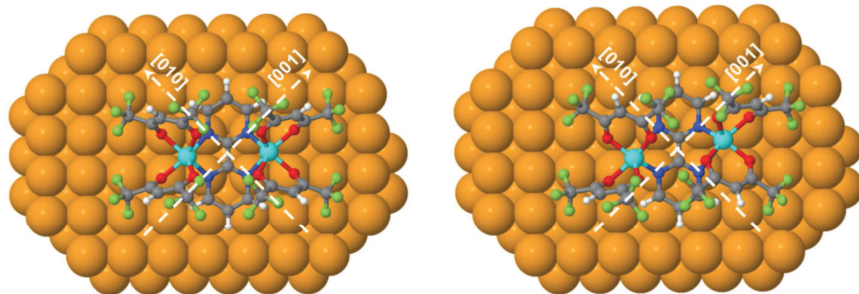


FIGURE 0.2 – Les représentations graphiques des deux configurations moléculaires "déformées" de  $\text{Ni}_2$  adsorbé sur  $\text{Cu}(001)$ . La liaison entre la molécule et le substrat a lieu par l'intermédiaire de l'unité bpym central. (a) montre la structure presque symétrique,  $C_{2v}$  - type de structure avec deux plans de symétrie du complexe tournée de  $45^\circ$  par rapport à la direction fcc  $[001]$  et  $[010]$ , (b) montre la structure correspondant à la symétrie cassée locale qui est énergétiquement plus favorable.

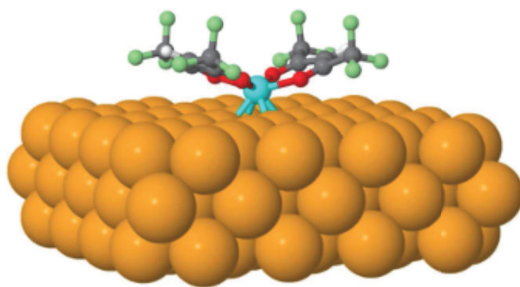


FIGURE 0.3 – Structure de fragmentation  $\text{Ni}(\text{hfacac})_2$  lié à  $\text{Cu}(001)$  par l'atome de Ni.

rimentales.

Aujourd'hui il est bien connu qu'une grande variété de molécules organiques sont disponibles pour la conception des matériaux, qui peuvent être utilisés pour des applications de l'électronique organique. Par exemple, les polymères et les oligomères semblent être très prometteurs, car ils montrent une souplesse mécanique et leurs gaps optiques peuvent être manipulés par la variation du nombre  $N$  d'unités fusionnées. Dans cette deuxième étude, nous considérons un groupe de ces polymères, la

---

famille de chaînes d'oligoacène, qui a fait l'objet d'intenses discussions en raison des effets de corrélations électroniques très prononcés. Les oligoacènes sont des chaînes linéaires constituées d'un noyau benzénique répété, et jouent un rôle dominant pour des applications dans le photovoltaïque organique (OPV), mais aussi pour des applications dans l'électronique et la médecine.

Dans nos calculs, nous avons considéré des chaînes linéaires d'oligoacènes, constituées d'un anneau répété de benzène. Comme la longueur augmente, nous nous attendons à ce que le gap optique s'approche d'une constante (si la chaîne infinie est un isolant de bande) ou à disparaître complètement (si la chaîne est un métal). Le comportement métallique se manifeste généralement par au moins une bande qui coupe le niveau de Fermi. Cette bande serait ensuite partiellement remplie et les gaps de chaînes de longueurs finies devraient tendre vers zéro quand la longueur de ces chaînes augmente, comme  $1/N$ ,  $N$  étant le nombre d'unités répétées. Le comportement en  $1/N$  reflète l'espacement des niveaux d'énergies d'une particule dans une boîte. Par conséquent, nous nous attendons d'une décroissance monotone. Or, l'étude nous montre que la bande interdite d'énergie des oligoacènes décroît d'une façon non-monotone, avec de fortes oscillations incommensurables Fig. 0.4.

Nos calculs fondés sur la DFT montrent que la bande interdite  $\Delta_g^N$  des 10 premières oligoacènes chute rapidement à zéro, puis augmente et chute de nouveau à plusieurs reprises, avec une périodicité de 11 unités (anneaux de benzène). Ce comportement n'a pas été signalé avant, en dépit de la recherche intensive sur ces molécules. La forme de la bande interdite des oligoacènes indique qu'un franchissement orbitalaire se produit au niveau des points extrêmes de la fonction écart énergétique au niveau de Fermi. Nous confirmons cela en inspectant les spectres de valeurs propres de Kohn-Sham. Pour comprendre l'origine des oscillations et des passages à niveau, nous invoquons la structure de bande de la chaîne infinie, appelée polyacène. Comme on passe du point  $\Gamma$  de haute symétrie vers le coin de la zone de Brillouin, nous rencontrons un croisement des bandes de valence et de conduction au point  $k_D = 0.9192 \pi/a$ , qui est similaire à des cônes de Dirac observés dans le graphène (Fig. 0.5). Nous avons réussi à vérifier ces résultats avec des calculs au delà de la DFT, tels que le calcul  $G_0W_0$ , dans lequel les bandes interdites d'énergies sont en meilleur accord avec les expériences, car cette méthode décrit mieux l'échange électronique.

Cette étude est étendue, aux molécules d'oligoacènes adsorbées sur des surfaces métalliques ou isolantes, telles que les surfaces de Au(111) ou du SiO<sub>2</sub>(001). Nos calculs

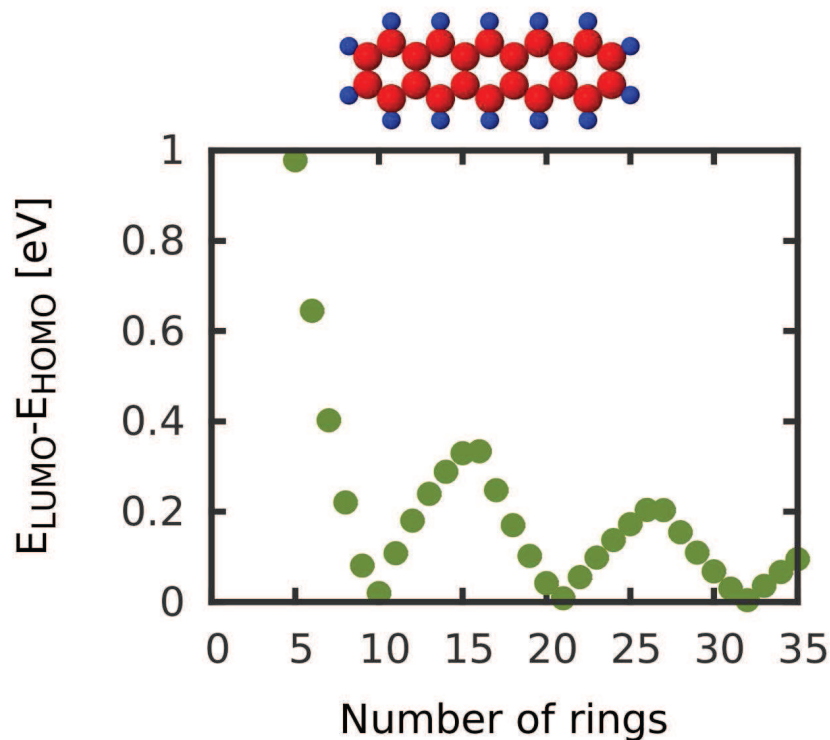


FIGURE 0.4 – Oscillation de la bande interdite des oligoacènes en fonction du nombre d’anneaux de benzènes répétés.

montrent une physisorption des oligoacènes sur ces substrats et un faible transfert de charge de la molécule vers le substrat. L’étude de la structure électronique des molécules adsorbées montre que les valeurs des bandes interdites ne changent pas de manière significative par rapport à celles de la phase gazeuse des molécules. En outre, la structure de bande de la chaîne de polyacène montre que le croisement des bandes au niveau de Fermi n’est pas altéré.

Ces résultats démontrent que les oscillations de la bande interdite en fonction de la longueur de la molécule restent inchangées lorsque les chaînes d’oligoacènes sont adsorbées sur certaines surfaces métalliques ou isolantes, comparées à celle de la phase gazeuse. Cette nouvelle étude permet de confirmer la robustesse de cette propriété, et indique des possibilités pour les applications technologiques potentielles.

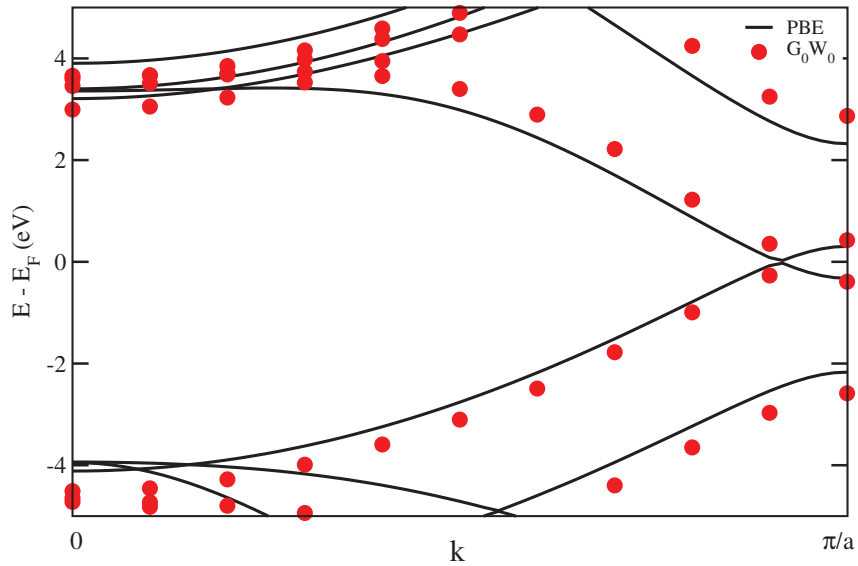


FIGURE 0.5 – La structure de bande de la chaîne infinie, calculée par un fonctionnelle PBE et par la méthode des quasiparticules  $G_0W_0$ . Comme on passe du point  $\Gamma$  de haute symétrie vers le coin de la zone de Brillouin, nous rencontrons un croisement des bandes de valence et de conduction au point  $k_D = 0.9192 \pi/a$ .

TABLE 0.1 – Les énergies HOMO-LUMO pour les molécules de la phase gazeuse, 8 Å au-dessus du substrat et celles de la molécule adsorbée sur Au(111)

structure	$C_{10}H_8$	$C_{22}H_{14}$	$C_{26}H_{16}$	$C_{30}H_{18}$
Molécule libre	3.30	0.98	0.64	0.40
@Au(111)/ $Z_{(C-Au)}=8$ Å	3.30	0.98	0.64	0.40
@Au(111)/ adsorbée	2.38	0.84	0.65	0.45

Enfin, nous avons étendu nos recherches à un substrat ferromagnétique, Co(001), et nous avons étudié plusieurs molécules différentes, en se concentrant sur le magnétisme induit à l'interface entre molécule et substrat et la variation de la bande d'énergie interdite. Des molécules telles que l'octane, l'éthane, l'éthylène mais également  $H_2O$  et  $NH_3$  ont été analysées avec les méthodes DFT et  $G_0W_0$ . Nos résultats indiquent une réduction de la différence entre la LUMO et la HOMO et lorsque les

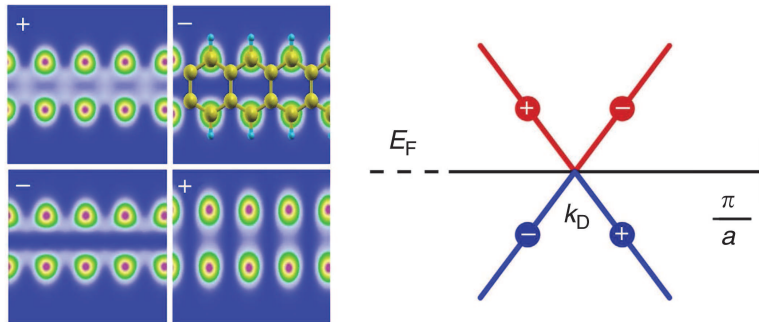


FIGURE 0.6 – La densité de charge aux points  $\mathbf{k}$  situés autour des points où les bandes se croisent,  $k_D$ . La bande de valence qui augmente l'énergie, a une symétrie impaire, alors que la conduction, ce qui diminue l'énergie, présente une symétrie paire le long de l'axe moléculaire.

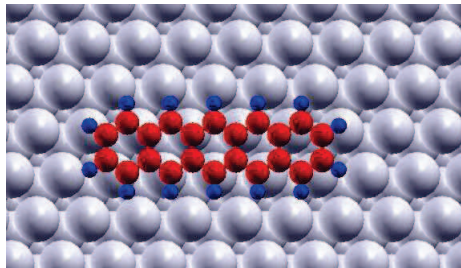


FIGURE 0.7 – Cellule unitaire de pentacène adsorbé sur Au(111).

molécules se rapprochent du substrat, un magnétisme induit pour certains d'entre eux, en fonction de la nature de la molécule (organique/inorganique) et en fonction de sa longueur.

Pour résumer, cette thèse a porté sur l'étude de la corrélation électronique dans les molécules organiques adsorbées sur des surfaces métalliques. Nous espérons que cette recherche inspirera d'autres travaux théoriques et expérimentaux surtout concernant les applications technologiques potentielles dans le domaine de la spintronique ou du photovoltaïque organique.

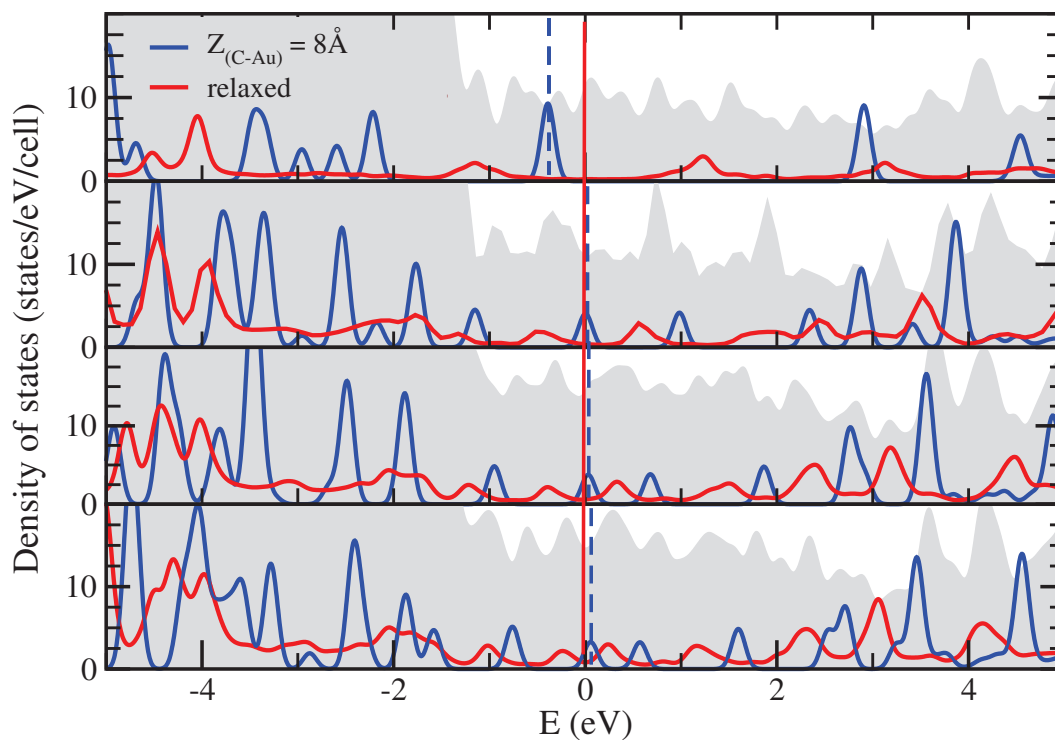


FIGURE 0.8 – Densité d' états (DOS) de molécules d' oligoaène. De haut en bas, projetée DOS sur les atomes de carbone du naphthalène, pentacène, hexacène et heptacène. Le bleu représente les structures où les molécules se trouvent à une distance de  $8\text{\AA}$  au-dessus de Au(111). Le rouge correspond aux molécules adsorbées sur Au(111). Les zones grisées représentent la DOS de la première couche du substrat. Le niveau de Fermi des structures détendue a été décalé à 0 (ligne rouge solide). Le niveau de HOMO des structures avec  $Z_{(C-Au)} = 8\text{\AA}$  est représenté par des lignes pointillés bleus.

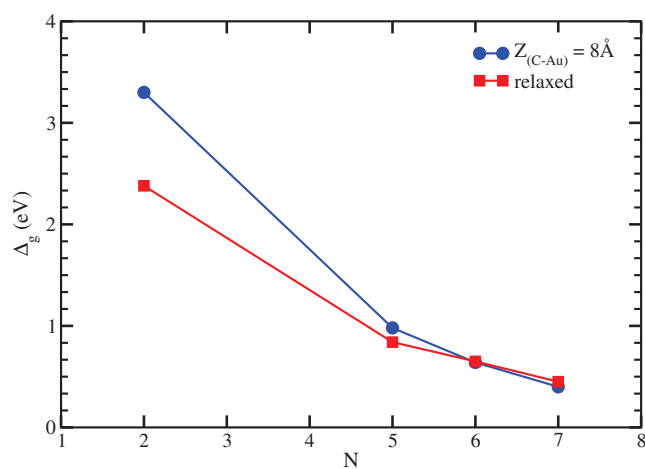


FIGURE 0.9 – La décroissance de la bande d'énergie pour les molécules  $C_{4N+2}H_{2N+4}$  à 8 Å au-dessus de la surface (cercles) comparée avec leurs homologues adsorbées (carrés) (voir également le tableau 0.1).

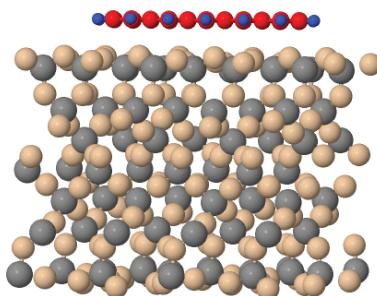


FIGURE 0.10 – Représentation schématique de la molécule de pentacène adsorbé sur  $SiO_2$   $\alpha$ -quartz. Les atomes de carbone sont indiquées en rouge, l'hydrogène en bleu, l'oxygène et le silicium en brun et en gris. Les coordonnées du substrat sont le résultat de la dynamique moléculaire dans la structure de  $SiO_2$   $\alpha$ -quartz O-terminé initiale.

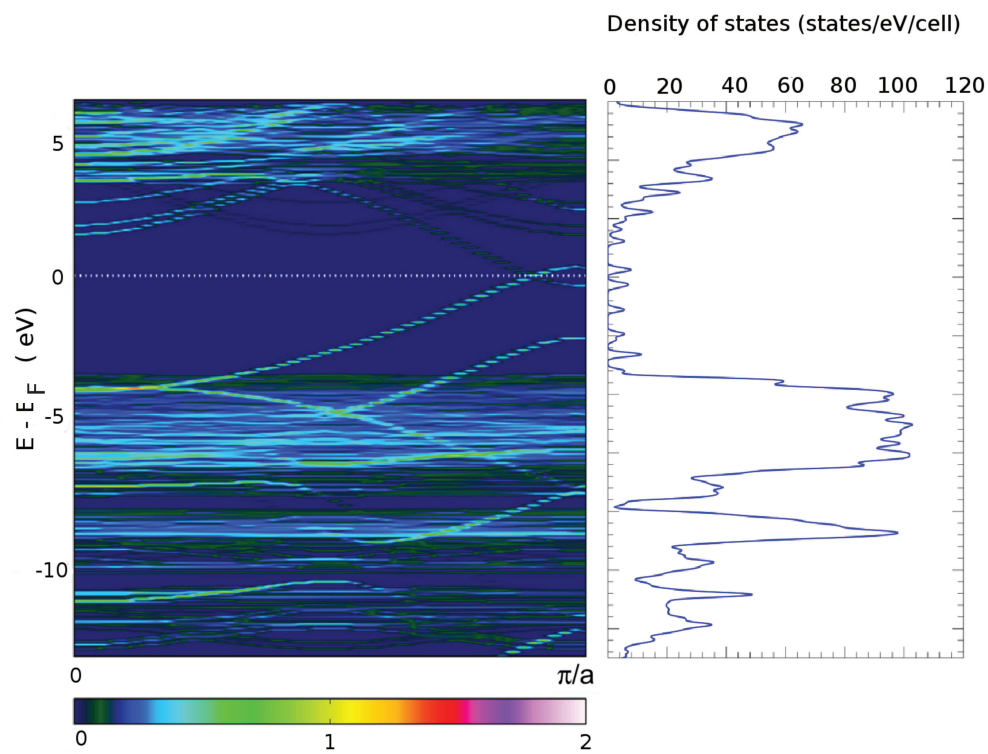


FIGURE 0.11 – La structure de bande dépliée de polyacène détendu sur le reconstruite "dense"  $\alpha$ -SiO<sub>2</sub> surface, est indiqué sur la gauche. Sur la droite, la DOS totale de la structure est présentée.

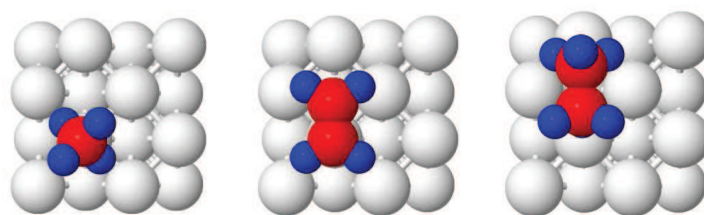


FIGURE 0.12 – Représentation graphique des molécules de méthane, d'éthane et d'éthylène adsorbées sur les substrats de Cu(001) ou de Co(001).

---

TABLE 0.2 – DFT-calculées distances des molécules adsorbées sur Cu(001) ou Co(001).

	Méthane	Éthylène	Éthane
$d_{(C-Cu)}$ (Å)	2.5	2.1	3.1
$d_{(C-Co)}$ (Å)	2.5	2.0	3.0

TABLE 0.3 – HOMO et LUMO calculées par DFT et  $G_0W_0$  pour les énergies de méthane, éthane et éthylène dans la phase gazeuse. La valeur expérimentale du potentiel d’ionisation (IE) est également donnée. Toutes les énergies sont exprimées en unités d’eV.

	HOMO (PBE)	LUMO(PBE)	HOMO( $G_0W_0$ )	LUMO ( $G_0W_0$ )	IE ( <i>Exp.</i> )
CH <sub>4</sub>	-9.41	-0.41	-12.69	0.77	12.61
C <sub>2</sub> H <sub>4</sub>	-6.75	-0.98	-9.22	2.98	10.51
C <sub>2</sub> H <sub>6</sub>	-8.05	-0.43	-11.14	0.85	11.01

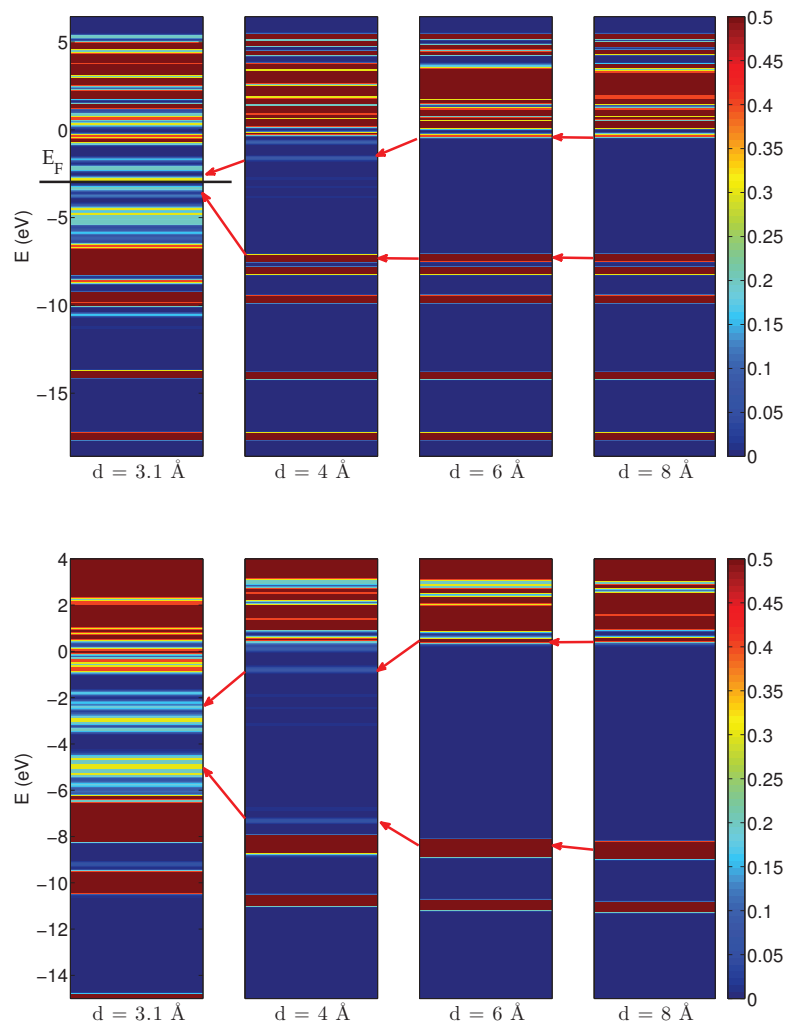


FIGURE 0.13 – DFT (en haut) et  $G_0W_0$  (en bas) DOS pour l'éthane adsorbée sur Cu(001). Les couleurs différentes indiquent le DOS projetée sur la molécule en unités de états/eV/cellule. Les flèches rouges indiquent les changements dans les niveaux HOMO et LUMO de la molécule quand elle rapproche le substrat, à partir de la distance  $d = 8 \text{ \AA}$  à la configuration finale adsorbée à  $d=3.1 \text{ \AA}$ . Le niveau de Fermi de la molécule adsorbé sur DFT est représenté en ligne noire.

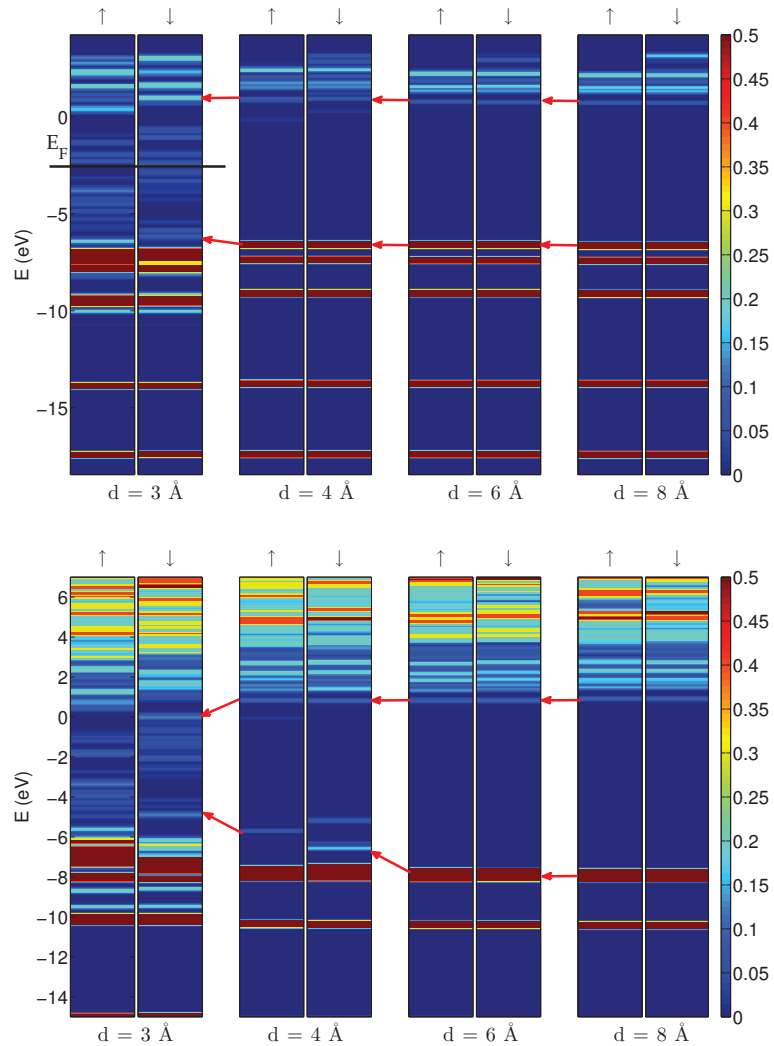


FIGURE 0.14 – DFT (en haut) et  $G_0W_0$  (en bas) DOS pour l'éthane adsorbée sur Co(001), comme dans la figure 0.13. Les flèches  $\uparrow$  et  $\downarrow$  indiquent, respectivement, le spin-up et spin-down.

---

## Publication List

1. *Signature of the Dirac cone in the properties of linear oligoacenes*, Korytár, R., Xenioti, D., Schmitteckert, P., Alouani, M., & Evers, F. Nat. Comm., **5**, 5000 (2014)
2. *Kondo effect in binuclear metal-organic complexes with weakly interacting spins*, Zhang, L., Bagrets, A., Xenioti, D., Korytár, R., Schackert, M., Miyamachi, T., ... & Evers, F., Phys. Rev. B, **91**, 19 (2015)
3. *Electronic structure of oligoacene molecules interacting with a metallic surface*, Xenioti, D., Korytár, R., Evers, F. & Alouani, M., (en préparation)
4. *Highly spin-polarized electronic interface states : a common feature of ferromagnetic metal-organic interfaces*, Djeghloul, F., Gruber, M., Urbain, E., D. Xenioti, Joly, L., Boukari, S., Arabski, J., Bulou, H., Scheurer, F., Bertran, F., Le Fèvre, P., Taleb-Ibrahimi, A., Wulfhekel, W., Garreau, G., Hajjar-Garreau, S., Wetzels, P., Alouani, M., Beaurepaire, E., Bowen, M., & Weber, W., (en préparation)
5. *Monitoring the energy band gap of SiO<sub>2</sub> using oligoacene molecules*, Xenioti, D. & Alouani, M., (en préparation)
6. *Effect of electronic correlation on molecules adsorbed on metallic surfaces*, Xenioti, D. & Alouani, M., (en préparation)

## Formation Scientific

1. Introduction to Numerical Simulations : From materials science to biochemistry with a look at modern high performance computing platforms, Prof. M. Boero, 9,12, 16 Décembre 2013 et 10,13,16 Janvier 2014, Strasbourg, France
2. UFA-Winter School "Surface-Confined Synthesis of Nanostructures", organisée par l' Université franco-allemande (UFA), Février 17-20, 2014, Baden-Baden, Allemagne
3. 45<sup>th</sup> IFF Spring School "Computing Solids : Models, ab-initio methods and supercomputing", 10-21 Mars, Jülich, Allemagne

- 
4. Spontaneous Symmetry Breaking : From Condensed Matter Systems to Particle Physics, Dr. N. Mohammadi, 21-29 Mai 2015, Strasbourg, France

## Communications et conférences

- International school Magnetism and Spintronics in molecular nanostructures, 16-22 Septembre 2012, Porquerolles, France
- Recent progress in Dynamical Mean-Field Theory and GW calculations, and hands-on school on full-potential LMTO (RSPT code), 17-20 Décembre 2012, Strasbourg, France
- Hands-on Density Functional Theory and Beyond : Computational Materials Science for Real Materials, 6-15 Août 2013, ICTP, Trieste, Italy – *Présentation d' un poster : "Kondo effect in binuclear metal-organic complexes"*
- UFA-Winter School "Surface-Confined Synthesis of Nanostructures", 17-20 Février 2014, Baden-Baden, Allemagne – *Présentation d' un poster : "Kondo effect in binuclear metal-organic complexes"*
- 45<sup>th</sup> IFF Spring School "Computing Solids : Models, ab-initio methods and supercomputing", 10-21 Mars, Jülich, Allemagne, *Présentation d' un poster : "Kondo effect in binuclear metal-organic complexes"*
- Deutsche Physikalische Gesellschaft (DPG) Meeting, 30 Mars-4 Avril, Dresden, Allemagne – *Exposé oral : "Kondo effect in binuclear metal-organic complexes"*
- Présentation à mi-parcours à l'IPCMS, 1 Juillet 2014, Strasbourg
- XXIII<sup>e</sup> Congrès Général, Société Française de Physique, Strasbourg – *Exposé oral : "Signature of the Dirac cone in the properties of linear oligoacenes"*